University of Trento
Department of Physics

Free-fall of LISA Test Masses: a new torsion pendulum to test translational acceleration

Dissertation

to Partial Fulfillment of the Work
for the Academic Degree of Doctor of Philosophy in Physics

Submitted

by the candidate:
Giacomo Ciani
Cycle: XX

Tutors:
Dr. Rita Dolesi
Prof. Stefano Vitale

February 2008

Ad Antonella, Daniele, Mauro, Karine, Renato, Giovanni e tutti gli altri del gruppo Basse Temperature,

nel quale non solo si lavora,
si impara e si fa bella scienza, ma anche ci si diverte, si scherza e si vive.

A Peter,

soprattutto, ma non solo,
per il prezioso lavoro di eroica difesa della grammatica Inglese.

A Ludovico,

per le energie, il sudore, i pensieri e le ore spese sull'esperimento,
lavorando fianco a fianco con me per gran parte della sua costruzione.

A Bill,

la cui "voglia di capire" è stata, ed è, uno stimolo
costante e una critica costruttiva ad ogni affermazione e ragionamento scientifico.

A Stefano,

timoniere e trascinatore pragmatico, e riferimento scientifico di raro valore.

A Rita,

per la guida costante e infaticabile, e per le infinite,
preziose e animate discussioni scientifiche; sempre concluse con una risata.

A David,

amico che ha condiviso con me tre anni di avventure e disavventure,
soddisfazioni e sacrifici, successi e fallimenti di ogni sorta, lavorativi e non.

A Ilaria,

per l'insostituibile supporto morale e materiale durante i lunghissimi mesi
di stesura della tesi. E per la felicità che mi regala in tutti gli altri momenti.

Ai miei genitori e alla mia famiglia,

senza i cui stimoli e la cui educazione
questo percorso non sarebbe forse mai iniziato. E senza il cui
affetto, supporto e apprezzamento non sarebbe sicuramente giunto fin qui.

Alla fisica,

che ogni giorno soddisfa una mia curiosità;
instillandomene altre cento, e continuando a farmi divertire.

Grazie!

Abstract

Scientific community excitement about gravitational waves is growing year on year: availability of next generation experiments with improved sensitivity and bandwidth, together with the new astronomical observation capabilities gravitational waves could provide are a promise of new, amazing science.

Among the many complementary operative or proposed gravitational wave experiments, LISA [1] stands out as the first high sensitivity, low frequency interferometric space-borne gravitational wave observatory. It promises wonderful possibilities in terms of number and variety of observable sources, many of which will provide a stable signal in the LISA band with huge Signal-to-Noise Ratio. Moreover, exciting new science is a probable outcome of its observations.

However, the strain sensitivity LISA scientific goal ($10 \cdot 10^{-21}$ 1/Hz$^{1/2}$ at 1 mHz) is pushing the technological limits of almost all its subsystems. Among them, the Gravitational Reference Sensor (*GRS*) plays a crucial role in fulfilling the $3 \cdot 10^{-15}$ m/(s^{2}Hz$^{1/2}$) requirement in terms of purity of geodesic motion of LISA reference free falling Test Masses (*TM*), that sets the instrument sensitivity limit below about 1 mHz. The GRS must assure at the same time high readout sensitivity and low disturbances on the measured TM.

Given the unprecedented level of performance needed, thorough testing is required. While a dedicated space mission, the Lisa Technology Package [2, 3] technological demonstration experiment, is at present scheduled to be launched in 2010, extensive ground testing is mandatory to exclude the most threatening sources of disturbances and give a preliminary characterization of the noise model on which the missions concepts and noise budget apportioning are based.

Measuring disturbances below 10 fN/Hz$^{1/2}$ on Earth in the LISA measurement bandwidth from $3 \cdot 10^{-5}$ to 0.1 Hz is a demanding experimental task, and required the design and commissioning of dedicated facilities. The torsion pendulum currently used by the Trento LISA group has demonstrated the possibility to effectively characterize the GRS and place relevant upper limits to the GRS related force disturbance.

Nevertheless, torsion pendulums used so far have some intrinsic limitations due to the model dependent conversion of the measured torque noise into corresponding force disturbance, and risk being insensitive to some force contribution that could

be potentially important.

The object of the work presented here has been the building and commissioning of a new concept torsion pendulum facility, directly sensitive to forces exerted by the GRS on the TM, thus reducing significantly the possibility of missing important contributions to the force noise and allowing for simpler, more solid estimation of force-disturbance upper-limits. The facility is now operating and although further debugging and improvement is possible, it has already been used for some preliminary measurement. As well as providing a more representative confirmation of previously obtained results, it has significantly improved the force-noise upper-limit, reaching the level required by LTP down to about 1 mHz.

We give here an overview of the this thesis, pointing out the relevant topics and how they are organized among the ten chapters.

In Chapter 1 we will briefly introduce gravitational waves, their sources and the exciting science that can derive from their observation. We will then describe the Laser Interferometer Space Antenna (*LISA*) mission, its scope and the technological challenges it poses: the LISA sensitivity goal and the consequent requirements will be presented, leading us to the need for LTP, the technological demonstration mission, and for extensive ground testing.

In Chapter 2 we will then focus on one of the core parts of the LISA mission, the capacitive Gravitational Reference Sensor (*GRS*) which has been designed and is currently being tested in Trento. Along with an introduction to the operating principles and a closer look at its design, we will enumerate the known sources of force noise related to the GRS and describe those which are most threatening. From this, the need for a representative ground testing campaign will clearly arise.

Chapter 3 will present the torsion pendulum as a suitable GRS ground testing facility. We will briefly describe the "single Test Mass" (*1-TM*) facility used in Trento for several years and give a general introduction to the techniques employed to characterize the disturbances that the sensor can exert on a LISA Test Mass (*TM*) suspended inside it. Beside this facility's successes, we will then point out its limits, being sensitive only to torques acting on the TM. An evolution of the design, directly sensitive to forces acting on the TM and capable of performing more representative measurements, will then be proposed. The achievable results and their interpretation will be discussed.

In the following chapter, the detailed design of the core parts of new "four Test Mass" (*4-TM*) testing facility will be presented along with its expected performance. Two different implementations of the pendulum inertial member+capacitive sensors assembly (one for preliminary instrument debug, the other for actual GRS testing) will be introduced, to be further discussed in the following chapters along with experimental results obtained. Facility features and subsystems common to both implementations, including the suspension system, vacuum system, thermal stabilization and diagnostics will then be described.

In Chapter 5 we will describe the preliminary, simplified implementation of the proposed 4-TM torsion pendulum. While it was not suitable for GRS testing, it served as a test of feasibility as well as a guideline for the setup of the final facility, including subsystems. It shared the base geometry and fundamental aspect of the final project, and it was also used to probe achievable performance and give a rough estimate of laboratory gravitational noise background. We will present results that show a nearly thermal noise-limited background and measurement proving that gravitational noise would not have represented a limiting factor for the GRS facilities performance.

Chapter 6 will then be dedicated to the 4-TM torsion pendulum configuration for GRS testing. While most of the core and diagnostic subsystems are common with the preliminary facility, we will mention the minor upgrades and provide detailed description of the two main changes: the inertial member, made up of four LISA like hollow TM, and the so called STiffness Compensator (STC), an additional sensor designed and built in Trento as a support for readout enhancement and stiffness cross-talk minimization.

The first-ever upper limit set by directly measuring the force noise exerted by the GRS on a LISA-like TM inside it, in a flight representative configuration, will be presented in Chapter 7. Data analysis techniques and related issues will be extensively discussed before showing their application to some noise runs, as well as to a statistical average among two different sets of them, corresponding to two functionality status of the facility. The measured excess noise with respect to the expected background, although not null, will be shown to be low enough to set upper limits on the force noise at the level of LTP requirements, and a factor 10 from LISA, at about 1 mHz.

In Chapter 8 and Chapter 9 we describe preliminary measurements of two of the GRS related effects that need on ground investigation and characterization: GRS-TM springlike coupling and stray voltages imbalances. These serve both to verify the sensor electrostatic model and to study potentially threatening electrostatic properties. After introducing the measurement techniques, we will present partial characterizations of the relevant parameters, which are found to be in agreement with previous results obtained with the 1-TM facility, but much more representative of the interactions that can produce potentially disturbing effects along the TM X axis, used in-flight for interferometric measurement aimed at detecting gravitational waves.

Finally, Chapter 10 will summarize the most interesting and innovative aspect of the work presented throughout this thesis: the building, commissioning and first valuable investigation campaigns of a new generation torsion pendulum able to set upper limits of unprecedented representativity by directly measuring the force acting on a LISA like TM inside the GRS. Besides the obtained results, the work presented resulted in the availability of a new instrument that will help in reducing the risk of failure of an innovative, exciting scientific mission such as LISA.

In the appendix section, extended explanations about some experimental details linked to the construction, assembly and operation of the complex, high precision 4-TM torsion pendulum facility can be found, along with an explanation of the electrostatic model used to calculate relevant GRS operating parameters.

Contents

Abstract **i**

1 The LISA and LTP challenge **1**

1.1 A cosmic sea . . . 1

1.1.1 What are gravitational waves? . . . 1

1.1.2 A new astronomy within reach . . . 2

1.2 Detecting gravitational waves . . . 2

1.3 LISA Mission . . . 3

1.3.1 Mission overview . . . 3

1.3.2 LISA TM geodesic motion requirements . . . 5

1.3.3 Drag free navigation . . . 7

1.4 LTP . . . 8

2 The Gravitational Reference Sensor: design and noise model **11**

2.1 Sensing and actuation scheme . . . 12

2.2 GRS noise model . . . 15

2.2.1 Electrostatic interactions . . . 16

2.2.2 Thermal effects . . . 24

2.2.3 Miscellaneous . . . 27

2.2.4 Unknown sources . . . 27

2.3 GRS Design details . . . 28

3 Testing GRS performances on-ground **33**

3.1 Torsion pendulums as test benches: the single TM facility . . . 34

3.2 GRS characterization techniques . . . 38

3.3 1-TM facility limitations . . . 40

3.4 4-TM facility concept . . . 42

4 4-TM facility **47**

4.1 Torsion pendulum implementation . . . 47

4.2 Auxiliary systems . . . 50

4.2.1 Vacuum system . . . 50

4.2.2 Suspension system . . . 51

4.2.3 Micro-positioning 51
4.2.4 Charge Management Control 52
4.2.5 Thermal stabilization 53
4.2.6 Diagnostics 53
4.2.7 Data acquisition system 55
4.2.8 Clean environment 55

5 Preliminary 4-TM facility 57

5.1 Inertial member 57
5.2 Capacitive readout 59
5.2.1 Sensors 59
5.2.2 Electronics 60
5.3 Experimental results 62
5.3.1 Ultimate noise performances 62
5.3.2 Estimating gravitational background 66

6 4-TM GRS testing facility 69

6.1 Inertial member 69
6.2 Capacitive readout 71
6.3 Stiffness Compensator 74
6.4 Electrostatic shielding 79
6.5 Electronics 81

7 Upper limits on GRS related force noise 83

7.1 Data taking 84
7.2 Data analysis 85
7.2.1 Power spectral density estimation 85
7.2.2 Data interpolation, per-filtering and decimation 88
7.2.3 Conversion into torque 88
7.2.4 Analysis of external disturbances 93
7.2.5 Readout noise reduction 96
7.2.6 Accurate spectrum estimation 100
7.3 Setting upper limits on GRS related noise sources 102
7.4 Experimental results 104
7.4.1 Single run torque noise analysis 104
7.4.2 Estimation of the average torque noise 108
7.4.3 Conclusion 114

8 GRS related force gradient: the "stiffness" 119

8.1 Electrostatic model and the origin of the electrostatic stiffness 120
8.1.1 Sensing stiffness 121
8.1.2 TM charge 122

8.1.3 DC Biases 122
8.2 Measurement technique 122
8.2.1 Global stiffness 123
8.2.2 Sensing stiffness 125
8.2.3 Charge related stiffness 126
8.3 Results 126

9 Stray electrostatics inside GRS: DC-Biases 131
9.1 DC bias as a noise source 132
9.2 Measurement technique 135
9.3 Results 139

10 Conclusions 147

A Electrostatic Model 151

B Calibrations 155
B.1 Preliminary facility 156
B.2 GRS testing facility 160

C ORO 167
C.1 Operating concept 167
C.2 Integration of ORO in the 4-TM facility 168

D Alignments 171
D.1 On-bench assembling and centering procedures 171
D.1.1 Inertial member 171
D.1.2 GRS 176
D.1.3 STC 176
D.1.4 ORO 177
D.1.5 Sensors assembly 177
D.2 In-operation centering procedures 178
D.2.1 GRS 178
D.2.2 ORO 180

List of Figures

1.1 LISA configuration scheme 4
1.2 LISA orbit 4
1.3 LISA sensitivity and LISA/LTP acceleration requirements 6
1.4 LTP 3D design 9

2.1 GRS sensing capacitive bridge scheme 12
2.2 GRS sensing bridges arrangement to discriminate rotational and translational DOF 14
2.3 6-DOF sensing bridges arrangement 14
2.4 Free-fall requirements comparison between space missions 28
2.5 GRS faces detail 29
2.6 Electrodes design 30
2.7 GRS Engineering Model Replica 31

3.1 1-TM facility scheme 35
3.2 1-TM pendulum transfer function 36
3.3 1-TM facility sensitivity curves 38
3.4 Example of thermal measurement in rotational configuration 41
3.5 Examples of force patterns to which the 1-TM facility is insensitive . 42
3.6 Force sensitive torsion pendulum concept 43
3.7 4-TM facility conceptual design 46

4.1 Autocollimator readout noise 49
4.2 4-TM pendulum expected performances 49
4.3 Vacuum vessel and early integration stage 50
4.4 Autocollimator mounting 51
4.5 Suspension system 52
4.6 Thermal room 54

5.1 Preliminary inertial member 58
5.2 Preliminary pendulum assembly scheme 60
5.3 Preliminary pendulum assembly pictures 61
5.4 Electronics scheme 61
5.5 Electronics box 61

5.6 Preliminary pendulum noise performances 65
5.7 Preliminary pendulum gravitational noise estimate 67

6.1 TM mock-up 70
6.2 TM mock-up 72
6.3 GRS facility capacitive sensors arrangement 73
6.4 GRS facility estimated tilt-stiffness induced torque noise 75
6.5 STC Sensor overview 77
6.6 Extended capacitive model 78
6.7 Inertial member conductive external shields 80
6.8 Inertial member conductive shields details 81

7.1 Run #20070929 angular data PSD 87
7.2 Data decimation: result comparison 89
7.3 Time torque application example 91
7.4 Torque estimation techniques comparison 92
7.5 Cross-coherence plot examples 96
7.6 Torque estimated PSD example 97
7.7 Application of some spectrum average techniques 105
7.8 Fitting the noise spectrum: comparison between two models 107
7.9 A check of the relative error of averaged PSD points 109
7.10 Average torque noise PSD (Set1) 110
7.11 Excess noise from capacitive sensors data (Set1) 111
7.12 Excess noise from cross spectral density analysis (Set1) 112
7.13 Average torque noise PSD (Set2) 115
7.14 Excess noise from PSD and CSD analysis (Set2) 116
7.15 Upper limits to GRS related force noise: LTP/LISA requirement comparison 117

8.1 Stiffness measure: GRS signal correction 127
8.2 Stiffness measure: Force vs Displacement 128
8.3 Stiffness measure: Stiffness vs Injection Bias 129

9.1 DC-bias example configurations 133
9.2 DC-biases measure example time series 140
9.3 DC-biasese measurement $2\omega_m$ fit 141
9.4 DC-biasese measurement and compensation 144

B.1 Capacitive signal combination 157
B.2 GRS testing facility calibration example 161

C.1 ORO operating principle examples 168
C.2 ORO installation on STC 169

D.1 GRS testing facility inertial member central support 172
D.2 GRS testing facility inertial member assembly mask 173
D.3 GRS testing facility inertial member assembly procedure 174

List of Tables

4.1 List of preliminary facility experimental signals 55
4.2 List of GRS testing facility experimental signals 56

6.1 STC electrostatic model 79

7.1 Comparison between fits to torque noise PSD and CSD 113

B.1 DOFs calibration 163

D.1 Inertial member accuracy measurement results 176

Chapter 1

The LISA and LTP challenge

1.1 A cosmic sea

1.1.1 What are gravitational waves?

Einstein's General Relativity Theory (GR) proposed a completely new interpretation of the gravitational interaction, seen as a geometrical distortion of the space-time, the 4-fold space in which things live, and thus affecting each object's motion the same way [4]. For a particle not subject to any force, straight trajectories in the flat Newtonian space become geodesics in curved space-time which shape is modeled by mass and energy distributions. This new interpretation was able to explain many of the unresolved mysteries of gravitational interaction, for example the observed deflection of photons (that are massless and should not undergo gravitational interaction according to Newtonian theory) by massive celestial bodies.

In this picture, an inertial frame can only be defined locally as the one that follows the local geodesic, and small particles subject only to gravitational interaction can be used as references.

Moreover according to GR, as a consequence of the finite propagation velocity of any signal, gravitational "distortion" travels at light-speed in space-time as waves in a medium: mass configurations that change periodically in time produce a fluctuating distortion that propagates indefinitely in space and time, resulting in what is called a Gravitational Wave (GW).

Far away from the source, the effect of a GW propagating in direction $\vec{r}$ is that of alternately squeezing a and stretching space-time in directions orthogonal to $\vec{r}$, with two possible polarizations: a gravitational wave "strength" is thus characterized by the relative change, or *strain* h, it induces in the separation of objects on a plane perpendicular to its propagation vector.

1.1.2 A new astronomy within reach

The existence of gravitational waves has been indirectly proved by Hulse and Taylor (Nobel Prize 1993) from the observation of the energy loss of the binary system PSR1913+16 [5] . Nevertheless, they have never been directly observed: being able to detect and measure gravitational waves will thus provide definitive proof of their existence and a verification of the theory of general relativity.

Although this would be a precious result, the scientific value of such an observation can be even more rich and exciting: it would open up a completely new field of gravitational wave astronomy.

With respect to electromagnetic radiation, GW offer a complementary tool for investigating the Universe: many possible sources of gravitational waves are expected to exist, among them celestial objects that cannot be observed by conventional electromagnetic astronomy, such as black holes. Gravitational waves coming from binaries of compact objects, merging black holes, Extreme Mass Ratio Inspirals and a variety of other systems with time-varying mass distributions can bring precious information about them and the gravitational interaction that drive their motion. Observing frequency, amplitude, polarization, direction and time evolution of gravitational waves would provide further clues on source numbers, characteristics and positions in the sky. Moreover, as GW scarcely interacts with matter, they propagate far beyond electromagnetic radiation, allowing us to observe the universe far away both in space and in time.

1.2 Detecting gravitational waves

A lot of effort has been devoted in the past decades to detecting gravitational waves, but they have not been successful yet: unfortunately, significantly distorting spacetime requires a huge amount of energy, and even powerful gravitational waves sources produce exceedingly small relative strains that are very hard to detect.

Among the different techniques proposed and employed to build gravitational wave detectors, the current best in terms of both sensitivity and bandwidth is the interferometric measure of the distance between far away reference particles nominally subject only to the large-scale gravitational field (at least along the measurement axis). Any GW propagating along a direction not exactly parallel to their separation would modulate their distance at its characteristic frequency, inducing a relative displacement proportional to the wave amplitude. The Michelson-like interferometric readout between two orthogonal arms provides a “self reference” to discriminate coherent orthogonal distances distortion caused by a gravitational wave signal.

As GW induce relative distance changes, it is clear that given an instrument displacement accuracy, measuring longer distances would result in better GW sensitivity[1]: at present, several km-size interferometers operate on Earth in search for GW signals [6, 7]. However, they are limited by the local gravitational field noise to signals of frequency higher than few Hz, up to several kHz. Unfortunately, this greatly reduces the number and the duration of the observable sources, as the most stable and numerous are expected to emit signals in the 10 mHz region and below.

1.3 LISA Mission

1.3.1 Mission overview

Aimed at complementing the Earth based interferometers observations in a much lower frequency band[2], the LISA (Laser Interferometer Space Antenna) mission has been proposed [1]. It will be the first space-based interferometric gravitational wave observatory, and is currently under development by a joint collaboration of NASA and ESA [8].

The principle is still that of measuring the distance between reference Test Masses (*TM*) in nominal free-fall, but exploiting the gravitationally much quieter space environment and the possibility of much bigger TM separations. The TM used as reference for the interferometric readout will be at the corners of a nearly equilateral triangle roughly $5 \cdot 10^6$ km in size, of order one million times bigger than the instruments built on Earth. Each side will thus be used as an interferometer arm, obtaining the equivalent of two semi-independent interferometers when combining all the signals. The experiment concept is sketched in Figure 1.1.

The TM orbits are chosen in such a way that the triangle will follow the Earth's path around the Sun, about 20° behind it, maintaining a constant inclination of 60° with respect to the ecliptic (see Figure 1.2). Along the orbit, the triangle will both change its velocity direction and "look" in different directions in the sky; the induced modulation in each source signal will provide the ability to acquire additional information and determine its position with a resolution up to 1 arcminute in the most favorable conditions.

As LISA sensitive frequency band is much lower than that of Earth-based interferometers, GW emission by a number of already known binary systems is expected to be detected, allowing for their usage as testing and calibration references for the

[1] Strictly speaking, this is true as long as we are interested in GW with wavelength much longer than the distance we are measuring; otherwise the time-of-flight of photons between the target particles will be longer than the period of the GW, resulting in reduced, or even null for certain frequencies, sensitivity.

[2] Sensitivity is not the only quantity that matters when observing gravitational wave signals: different frequencies mean different sources and different phases of their evolution. Although the chances of LISA observing gravitational waves should be much higher than those of terrestrial observatories both for probability (provided General Relativity previsions are right, it is guaranteed to see more than one signal once "switched on"), number and duration, their observations are complementary and essential to reconstruct a complete picture of all possible sources and their evolution over time.

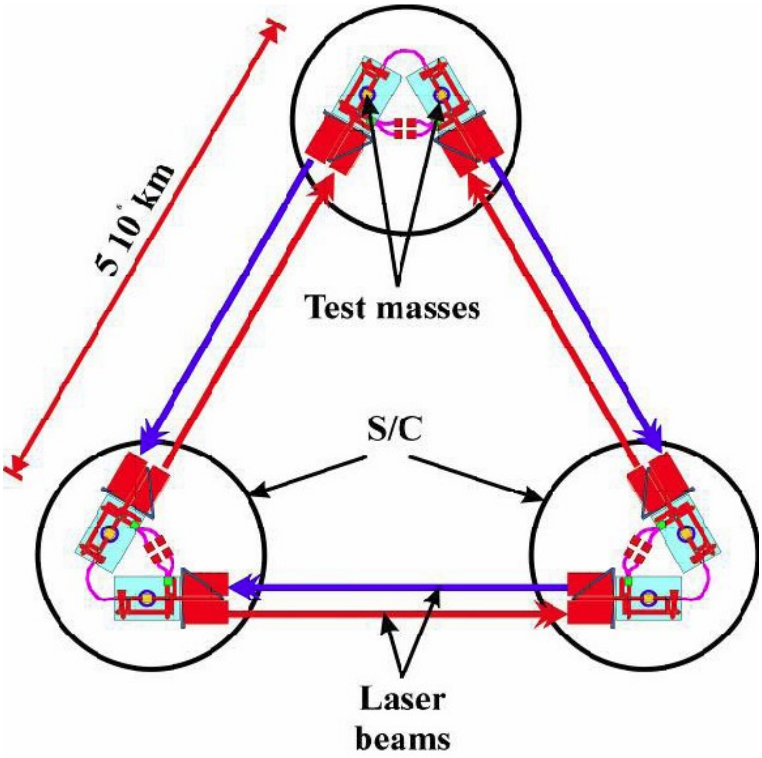

Figure 1.1 – A simple picture of the LISA interferometric configuration. The three satellites, each hosting two TMs, occupy the corner of a nearly equilateral triangle $5 \cdot 10^6$ km in size. Each side of the triangle is the arm of an interferometer, and the combination of them is equivalent to two semi-independent interferometers.

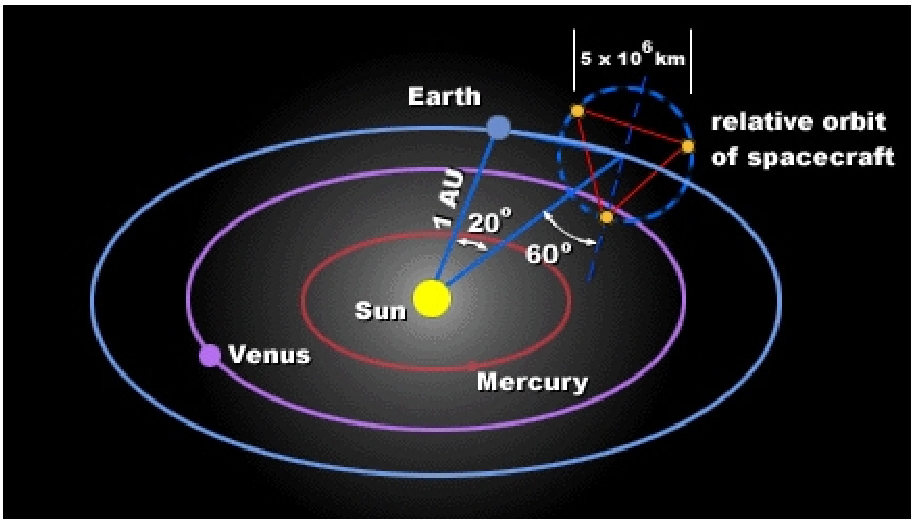

Figure 1.2 – Sketch of the LISA orbit: it will follow the Earth orbit around the Sun 20° behind, or approximatively 50 million km. Velocity and orientation modulation during the year will provide additional information about the detected sources.

instrument. On the contrary, if these signals were not detected once LISA became operational, it would shake the very foundations of the General Relativity Theory. In any case, the potential and scientific value of LISA observations will be amazing.

To reach its scientific goal, LISA aims to detect strains of order 10^{-23} in a one year integration time, measuring variations of the distance between two TMs 10^6 km apart at the pm level, in the measurement bandwidth from 0.1 mHz to 100 mHz.

1.3.2 LISA TM geodesic motion requirements

For the instrument to reach the required sensitivity, each TM stray residual acceleration with respect to the local inertial frame should be strongly reduced. In the limit of long wavelength and small GW signal, for the distance $\Delta X(t)$ between two TM (at the ends of one interferometer arm) the following relation holds:

$$m\frac{d^2\Delta X}{dt^2} = \Delta F_X + mL\frac{d^2 h}{dt^2} \tag{1.1}$$

where m is the mass of the two TMs (supposed to be equal), L their average separation, h the strain signal of the passing GW and ΔF_X any residual, spurious differential acceleration between the TM not due to the large scale gravitational field. It is easy to show, from the above equation, that any residual spurious acceleration with spectral density $S^{1/2}_{\Delta F_X}$ would mimic a GW signal

$$S_h^{1/2} = \frac{S^{1/2}_{\Delta F}}{mL\omega^2} = \frac{S^{1/2}_{\Delta a}}{L\omega^2} \tag{1.2}$$

The $1/\omega^2$ frequency dependence suggests that, while at high frequency LISA would be limited by the interferometric readout with displacement sensitivity of 40 pm/Hz$^{1/2}$), at low frequency residual TM acceleration due to spurious forces would set the sensitivity floor of the instrument.

Given the LISA target sensitivity of $S_h^{1/2} = 10^{-21}$ per root Hz at 3 mHz and increasing as $1/\omega^2$ at lower frequencies down to 30 μHz, this translates in an acceleration noise requirement of $S_a^{1/2} \leq 3 \cdot 10^{-15}$ m/s^2. The overall acceleration requirement is expressed as a function of the frequency as:

$$S_a^{1/2}(\omega) \leq 3 \cdot 10^{-15} \left(1 + \left(\frac{f}{3\ \mathrm{mHz}}\right)^2\right)^{1/2} \frac{\mathrm{m}}{\mathrm{s^2Hz^{1/2}}} \tag{1.3}$$

for 10^{-4} Hz $< f < 10^{-1}$ Hz.

To satisfy the extremely low required residual acceleration with respect to the local inertial frame (see Figure 1.3), the TM has to be shielded against external disturbances such as, for example, the Sun light pressure (and, even more, its fluctuations in the requirement bandwidth). The TM must thus be surrounded by a satellite that, as well as hosting all the necessary instrumentation, should act as a

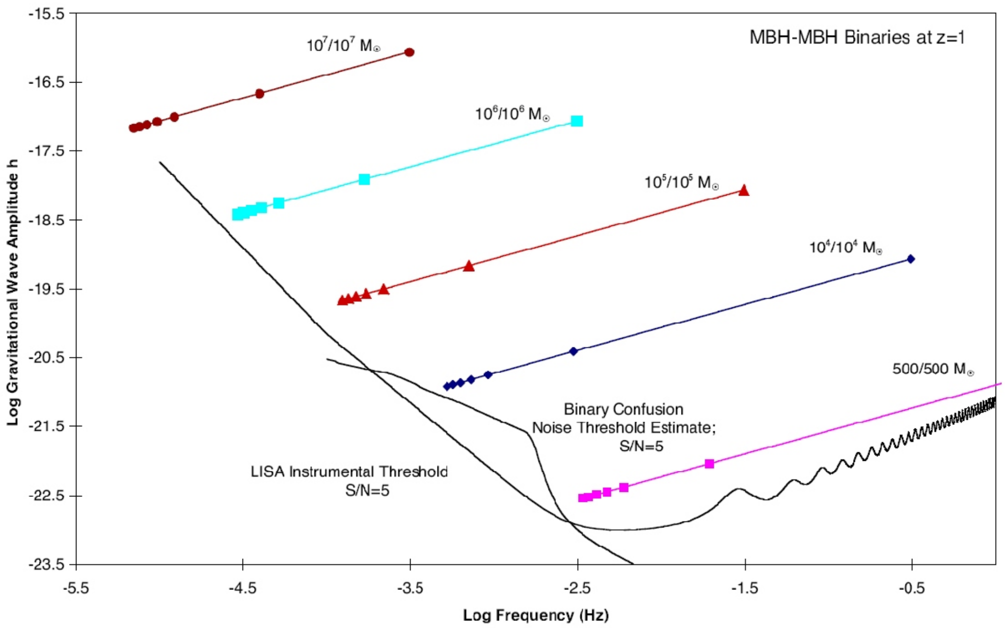

(a)

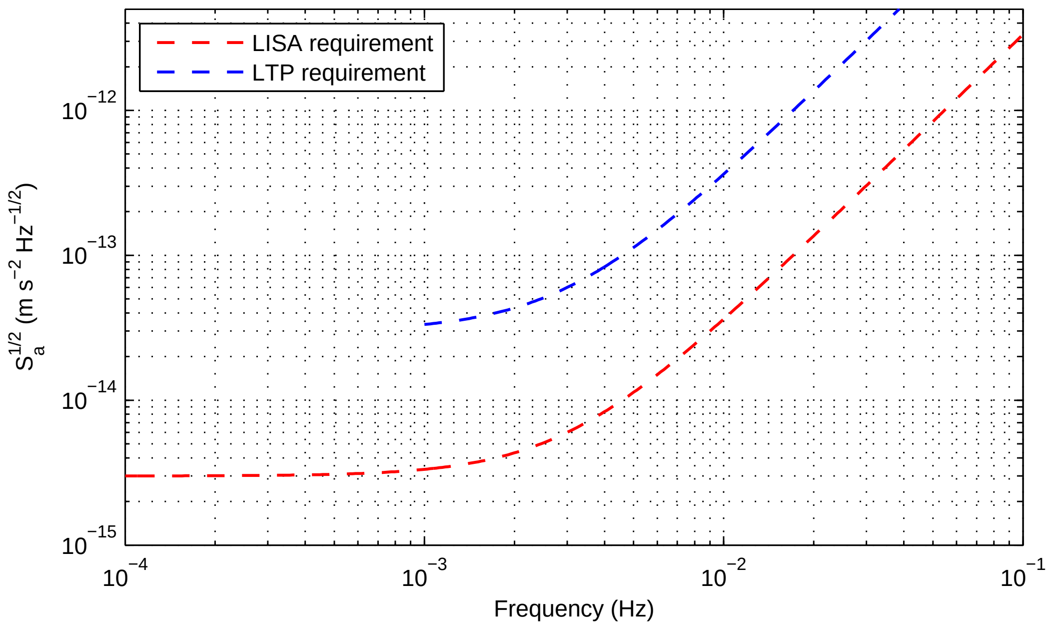

(b)

Figure 1.3 – In in (a), LISA sensitivity curve is plotted along with estimated signals from merging massive black holes (MBH) during the last year before coalescence (at the right end of each curve). Consequent acceleration requirement for LISA and LTP, its precursor demonstration mission, are plotted in (b). The flat low frequency acceleration noise would translate for LISA in a strain sensitivity rising as $1/f^2$. Note that TM weight is about 2 kg, and represents the conversion factor between acceleration and force requirements.

shield, following the TM in a drag-free navigation scheme.

1.3.3 Drag free navigation

Drag-free navigation consists of the TM floating inside the satellite without touching it. A "gravitational reference sensor" (GRS) will continuously sense the TM-Spacecraft relative displacement and feed an high gain control loop to force the satellite to remain centered with respect to the TM, using high precision micro-Newton thrusters to compensate external forces that would make the spacecraft deviate from the reference TM free-fall trajectory.

Unfortunately, while shielding external disturbances, the satellite and the position sensor themselves can introduce disturbances on the TM. Let us consider only the X axis, that is the GW sensitive one along which the interferometric measure is performed. As the aim of the drag free system is to keep the TM centered in the GRS, we can expand the overall interaction $f(x)$ between the TM and the spacecraft (including the GRS and all other experimental and navigation instrumentation) to first order in the TM displacement $\tilde{x}$, obtaining a force term acting on a centered TM $f_{str} = f(0)$ plus a spring-like term $-k\tilde{x} = f'(0)\tilde{x}$. Writing down the equation of motion of a TM of mass m inside a spacecraft of mass M, with a relative displacement control loop with gain G:

$$\begin{cases} mx''(t) + k\Big(x(t) - X(t)\Big) = f_{str}(t) \\ MX''(t) - k\Big(x(t) - X(t)\Big) - G\Big(x(t) + x_n(t) - X(t)\Big) = -f_{str}(t) + F_{ext}(t) \end{cases} \tag{1.4}$$

In the above equations, $x(t)$ and $X(t)$ are the TM and satellite positions in the local inertial reference frame (note that $\tilde{x}(t) = x(t) - X(t)$), $F_{ext}(t)$ is the external force acting on the spacecraft and $x_n(t)$ is the noise in the position signal that drives the displacement control loop. External not (completely) shielded forces acting on the TM alone have not been considered here as their effect is not related to the spacecraft and can thus be summed up independently.

Moving to the frequency domain via the Laplace transform:

$$a_n(s) = \frac{\omega_{fb}^2}{\omega_0^2(1+\mu) + s^2 + \omega_{fb}^2}\left(\frac{f_{str}(s)}{m}\left(1 + \frac{s^2}{\omega_{fb}^2}\right) + \omega_0^2\left(x_n(s) + \frac{F_{ext}}{M\omega_{fb}^2}\right)\right) \tag{1.5}$$

where we define $\mu = m/M$, $\omega_{fb}^2 = G/M$ and $\omega_0^2 = k/m$. In the limit of high control loop gain ($\omega_{fb}^2 >> \omega_0^2$) this expression reduces to:

$$a_n(s) = \frac{f_{str}(s)}{m} + \omega_0^2\left(x_n(s) + \frac{F_{sc}}{M\omega_{fb}^2}\right) \tag{1.6}$$

To fulfill the acceleration noise requirements, stringent limits are set on all the terms of the above equation: residual noisy forces, TM-satellite spring-like "stiffness", and position readout noise. As the GRS is both the position sensor and the closest structure to the TM, it contributes to all the above terms and it is required to provide both a small interaction and a low readout noise.

Moreover, each corner of the LISA constellation triangle will actually be constituted by a single spacecraft hosting two TM, representing the ending points of the two interferometric arms converging in the satellite position (see Figure 1.1). Each satellite will follow both its TM in drag-free navigation along the two interferometric sensitive axes, while exploiting TM position actuation along the orthogonal directions to keep them together. The GRS capacitive sensor has thus also been designed to provide actuation capabilities.

As we will see in the next Chapter, these requirements set the design guidelines of the capacitive GRS developed by the LISA group in Trento and currently baselined for LISA.

1.4 LTP

To ensure the maximum scientific revenue from a challenging mission such as LISA, requirements in terms of purity of TM geodesic motion, as well as other subsystems performance, have been set to unprecedented levels.

Given the overall cost of the LISA mission and the risks related achieving its design performance, the need for a demonstration mission was recognized very early, and resulted in the formulation of the Lisa Technology Package (*LTP*) mission [2, 3], to be flown by ESA aboard the LISA Pathfinder spacecraft scheduled for launch in 2010.

The idea is that of squeezing a LISA interferometric arm in a single satellite, placing inside it two TM and reading their relative position (see Figure 1.4): while this design will obviously be insensitive to GW (the arm is too short) it will still allow for testing GRS performance, drag-free loop control laws and a series of additional subsystem and possible sources of disturbance, providing the ability to check and characterize the overall noise model for LISA.

As the two TM have to stay inside the spacecraft, they cannot be left to drift freely even on the measurement axis: one of them will be used as a reference for the drag-free navigation driving the spacecraft, while the other will be forced to follow the satellite by means of capacitive actuation. System performances will then be evaluated measuring the residual spurious acceleration between the two TM, measured via interferometric readout.

Although the GRS design has been driven by the LISA requirements, on board of LTP overall performance has been relaxed a factor 10 both in acceleration and in frequency mainly because the additional force noise and stiffness introduced on the TM subject to electrostatic suspension. The TM free-fall purity the mission aims

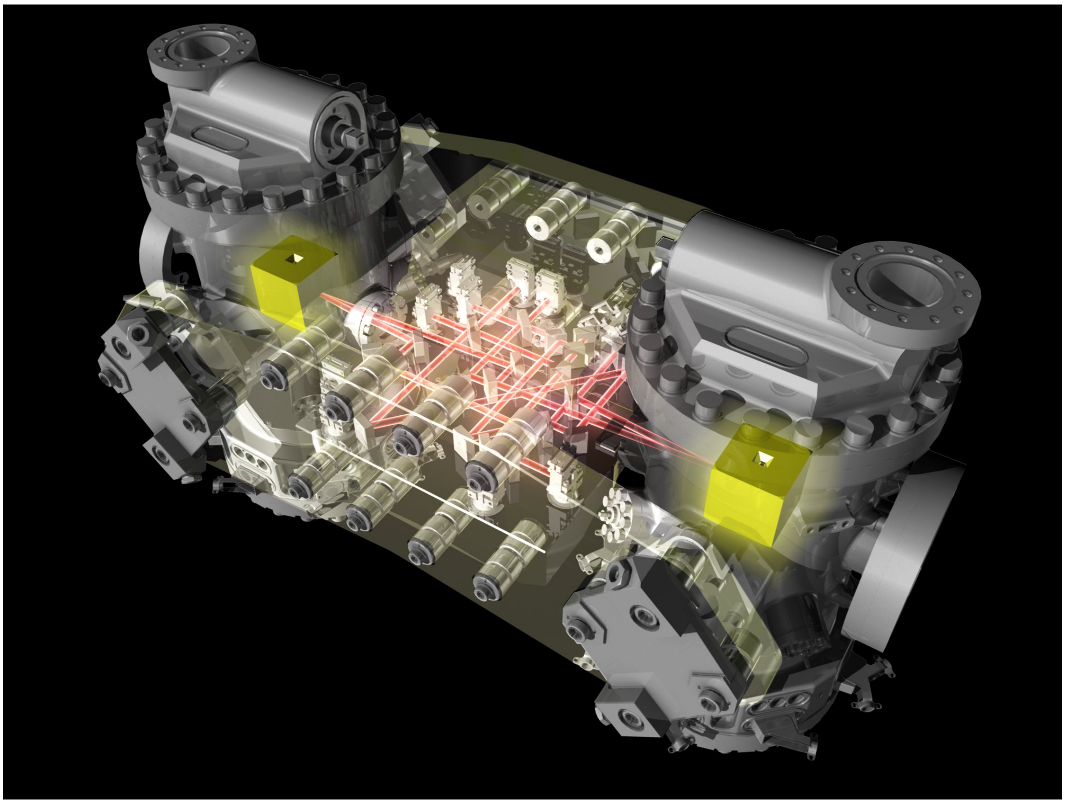

Figure 1.4 – A 3D representation of the LTP experiment. In between the two TM is the optical bench with laser path indicated in red (Courtesy of European Space Agency).

to demonstrate is thus:

$$S_a^{1/2}(\omega) \leq 3 \cdot 10^{-14} \left(1 + \left(\frac{f}{3\ \text{mHz}}\right)^2\right)^{1/2} \tag{1.7}$$

for 10^{-3} Hz $< f < 3 \cdot 10^{-2}$ Hz.

Chapter 2

The Gravitational Reference Sensor: design and noise model

As explained in the previous section, achieving high-purity free-fall of LISA and LTP TMs requires the spacecraft to act as a shield against external disturbances. Along with reducing stray forces and residual position dependent couplings between the satellite and the TM below given budgets, the relative displacement noise between the two is required to be kept within a suitable limit so as not to induce a force noise large enough to jeopardize the mission. The Gravitational Reference Sensor (*GRS*) that reads the spacecraft-TM relative displacement and drives the drag-free control loop is thus required to measure precisely the TM position while exerting on it extremely small forces.

Moreover, in both missions each spacecraft contains two TMs, and some actuation capability is required to keep them together.

In the following sections we will describe in some detail the capacitive sensor developed in Trento [9–14], that has both sensing and actuation capabilities and represents the current solution to be employed in both missions. It is constituted by one cubic LISA TM enclosed in a cubic shell with mm-size gaps between the two along all the directions. The cubic shell hosts the sensing and injection electrodes needed for capacitive sensing (and is thus called the "Electrode Housing", concisely *EH*), as long as a number of features such as holes for laser readout and caging mechanism[1]. After introducing the sensing and actuation scheme working principles, we will present the noise model that sets most of the design guidelines, accounting for all the possible source of noise (both in readout and in force) and their estimated contributions. Finally, we will give a detailed description of the sensor geometry and

[1]TM will experience very hard shaking during the launch phase, and cannot be left free to hit the EH without causing major damages. Designing a caging system capable of holding them firmly during the heavy shock phase while retaining the ability to release them in space with very little kinetic energy (small enough to allow electrostatic actuation system to stop them before they hit the EH) has been a difficult task for the industrial partners involved in the project, and required special geometrical feature on both the TM and the EH

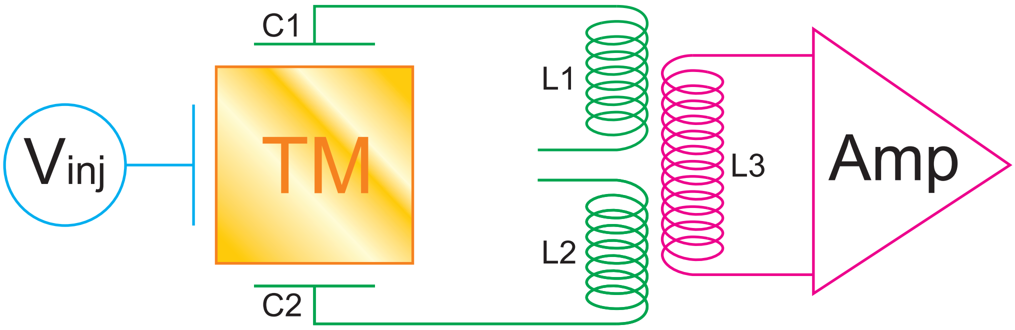

Figure 2.1 – A simple scheme that shows how capacitive sensing works along a single translational DOF. An oscillating injection voltage V_{inj} is used to polarize the TM, whose impedance toward ground depends on its position through the capacitances $C1$ and $C2$ that change as the TM move closer to one or the other electrode. The currents flowing in the two inductances $L1$ and $L2$, that are equal when the TM is centered, become different as it moves and the magnetic fields they induce in the overlapping inductances $L1$ and $L2$ no longer cancel, thus inducing a current in $L3$ that is suitably amplified.

implementation.

2.1 Sensing and actuation scheme

The GRS is a 6-DOF sensor capable of measuring TM position along three rotational and three translational DOF. The whole sensing scheme is however based on capacitive bridges that measure distances, and angular DOF are reconstructed by differential displacement at a known distance.

As an example, a single capacitive bridge scheme is represented in Figure 2.1. The position measurement is based on the comparison of the TM capacitances toward the two sensing electrodes, that are functions of the gaps. Applying a sinusoidal signal $V_{inj} \sin(\omega_{inj} t)$ to the injections electrode C_{inj}, the TM voltage oscillates at the same frequency with amplitude $V_{TM} = \alpha V_{inj}$, where $\alpha = C_{inj}/C_{tot}$ is the ratio between the injection electrode capacitance toward the TM and the TM capacitance toward all the surrounding surfaces.

The electrical impedance from the TM to the electrical ground along the two bridge branches is a function of the electrodes capacitance toward the TM, the remaining part of the branches being equal. Thus, if the TM is centered (and supposing a perfectly symmetric geometry), the capacitance and so the currents flowing in the two branches would be equal. On the contrary, as the TM moves closer to one electrode, the corresponding current will increase, while the opposite one will be reduced. By comparing the currents flowing in the two branches it is thus possible to measure the TM position.

The difference between the two currents is measured by means of an inductive transformer in which the two currents flows in opposite directions in two equal inductances that share the same magnetic core: if the two currents are equal, the induced magnetic fields cancel each other and there is no net variation of the magnetic field flux. However, if the two currents are different an oscillating magnetic field at angular frequency ω_{inj} arises, inducing a signal on a “secondary” winding sharing the same magnetic core of the first two. This signal is finally amplified and the noise efficiently suppressed by means of coherent signal detection at the injection frequency. This signal turns out to be proportional to the difference in the two currents, thus also proportional to the difference in the two electrodes capacitance toward the TM which, in turn, is proportional, to first order, to TM displacement; once calibrated, it constitutes the displacement readout.

Still considering the simplified example of Figure 2.1, the voltage drop ΔV between the TM and each surrounding surface, induced by the injection bias, gives rise to an attractive force proportional to its RMS value ΔV^2 (this is the well known attractive force between the plates of a capacitor). Along the sensing axis, the attractive forces toward the different surfaces cancels out for a centered TM thanks to the symmetry of the system, while a first order term in the TM displacement from the center remains and can be approximated as a pseudo-elastic term (a more comprehensive explanation of this effect and its role in the GRS-TM interaction will be given in Chapter 8).

If the voltage drop is not symmetric, however, this attractive force can be exploited to obtain actuation capabilities: purposely changing the voltage of one of the sensing electrodes, we increase its RMS voltage drop toward the TM and a net force arises. Moreover, if the applied voltage is of the form $V_{act}\sin(\omega_{act}t)$, the corresponding average TM polarization will be null and the applied force, proportional to

$$(V_{act}\sin(\omega_{act}t))^2 = \frac{V_{act}^2}{2}\,(1+\cos(2\omega_{act}t))$$

will have a constant component and an high frequency oscillating one; with an appropriate choice of ω_{act}, the latter would have actually no appreciable effect on the TM motion because of its inertia. We are thus able to actuate the TM at low frequency in both directions, without polarizing it or disturbing the sensing measurement, by simply applying suitable sinusoidal signals to appropriate electrodes.

To be able to discriminate all the six DOF of a free TM, the actual GRS design foresees six of the capacitive bridges described above, two for each pair of opposing faces. In Figure 2.2 an example of the layout of two of them along the same translational DOF is given: it is easy to see that while the mean of their calibrated readouts measures the net TM translation, their difference is proportional, via the distance separating the electrodes, to the TM rotation around the axis perpendicular to the sheet .

Combining all the six bridges as shown in Figure 2.3 finally allows for complete discrimination of all the 6 DOF of a free TM.

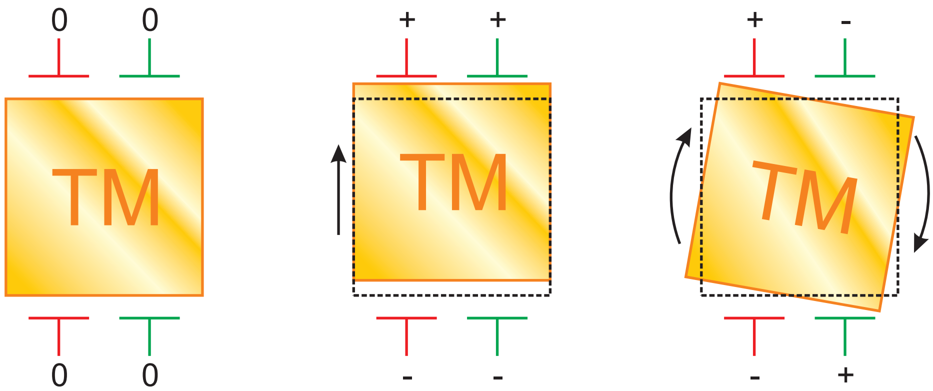

Figure 2.2 – An example scheme of sensing bridges arrangement on a pair of face to discriminate both a translational and a rotational DOF. Electrodes belonging to the same capacitive bridge are colored the same, while the symbol near them indicates their capacitance variation upon the considered TM motion. It can be seen that, if the TM translates the capacitance imbalance have the same sign on the two bridges, while if the TM rotates the imbalance is opposite on the two bridges. This allows for discrimination of the two DOF.

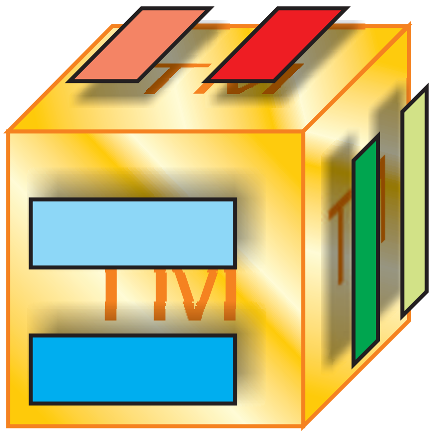

Figure 2.3 – A scheme of the arrangement of the six sensing capacitive bridge employed on the GRS to discriminate all the 6 DOFs of the TM. Each represented electrode has a corresponding one on the opposite face, not visible in the picture. Each pair of bridges, represented by light or dark shading of the same color, works together as explained in Figure 2.2 to discriminate 2 DOF.

2.2 GRS noise model

The presence of the spacecraft (including GRS), although necessary to hold all the necessary instrumentation and to shield the TM from external disturbances as the Sun light pressure, is by itself a source of noise for the free falling TM because of a number of interactions. Approximating each force f_i between the satellite and the TM to the first order in the TM displacement x from its nominal center position along the sensitive axis X, we obtain

$$f_i(x) \approx f_i(0) + f_i'(0)x \equiv f_i(0) - k_i x \tag{2.1}$$

Although a huge amount of work has been done to reduce each $f_i(0)$ as much as possible, because of the noisy nature of the different contributions and the presence of a number of unknown sources, a residual noisy stray force f_{str}, is expected to act on the TM. Moreover, analogous reduction of the single k_i could be in general even harder, thus resulting in a net gradient (the noisy part of k_i can be neglected in this case, being much smaller than the average value) of the force experienced by the TM. This can be summarized as a global spring constant k coupling with the noisy TM-spacecraft relative displacement Δx to produce again a noisy force.

In the local inertial frame, the noisy acceleration a_n of the TM, mass m, due to spacecraft related effects[2] can thus be expressed as the combined effects of a number of stray position independent forces and a number of spring-like interactions proportional to the TM-Spacecraft displacement:

$$a_n = \frac{f_{str}}{m} - \frac{k\Delta x}{m} \tag{2.2}$$

Comparing Equation 2.2 with Equation 1.6, we can see that the residual displacement between the TM and the spacecraft, that introduces a noisy acceleration by means of the spring-like coupling interactions mentioned above, is contributed by both the readout noise x_n of the GRS that feeds the control loop and the residual motion of the satellite $F_{ext}/(M\omega_{sc})$ due to imperfect compensation of external forces because of the finite gain G.

The GRS plays an important role here, as in addition to being directly responsible for x_n, it gives contributions in both f_{str} and k, because it is the structure closest to the TM and constitutes its surrounding environment. We note that the need to reduce as much as possible a_n requires high sensitivity and low exerted force at the same time. Finding the best compromise between the two is a part of the complex task of total noise budget apportioning for both LISA and LTP missions,

[2] This is only part of the total acceleration noise, as not (completely) shielded forces originating outside the spacecraft can also contribute. Anyway, as we are interested in the forces related to the spacecraft, and the GRS in particular, we will not mention external ones acting directly on the TM (while still considering those acting on the satellites, because, as we will show, by shaking it they have an effect on the TM because of the stiffness coupling).

while meeting these requirements has been the aim of the design optimization of the GRS, that arrived at the current solution.

At present, the requirement for readout noise is set to 1.8 nm/Hz$^{1/2}$ along the sensitive X axis. This, together with the limit imposed to the injection bias not to exceed the budget of 10^{-7} N/m for the induced stiffness (see 8.1.1), implies constraints on the readout electronic noise and gain, and on the sensor geometry (affecting capacitances values) [10].

The force noise and stiffness sources panorama is much more populated and complicate. In the following we list, among all the foreseen source of interaction between the GRS and the TM, those that have been identified as the most important in the measurement bandwidth, and are thus apportioned a bigger part of the allowed force noise. Although the presented arguments are in general valid for all DOF, we will mainly refer to the stiffness and acceleration noise along the X direction, as it is the interferometric readout sensitive axis and so the one that sets the more stringent requirement about disturbances [10].

2.2.1 Electrostatic interactions

From the well known formula of the attractive force between the plates of a capacitor and considering that each surface surrounding the TM has a capacitance C_i toward it, the formula for the overall electrostatic force acting on the TM along the X axis follows:

$$F_X = \frac{1}{2}\sum_i \frac{\partial C_i}{\partial x}\left(V_{TM} - V_i\right)^2 \tag{2.3}$$

Where V_i is the i-th surface voltage and V_{TM} the TM potential. The sum over i is in principle extended to all the surfaces surrounding the TM, that can be grouped based on similar electrical characteristics depending on the considered effect (ranging from a rough division in TM and internal EH faces for effects like the sensing stiffness, to fine subdivision in domains of the order of mm^2 for "DC-bias" related effects). In the infinite parallel plate model presented in Appendix A, however, the only surfaces that have $\frac{\partial C_i}{\partial x} \neq 0$ are those distributed on the X faces.

In the following, we will describe the main contribution to the voltages involved in Equation 2.3:

TM voltage (V_{TM}) :

- *Polarization due to surrounding voltages:* each surface induces a polarization of the TM equal $V_i C_i / C_{tot}$. Thus the total polarization of the TM due to surrounding potential is

$$V_{TM,V_j} = \sum_j \frac{C_j}{C_{tot}} V_j \tag{2.4}$$

Note that, opposite to what have been said about Equation 2.3, here the sum is extended to all the surfaces of the EH, as the capacitance is always different from 0.

- *Injection bias:* a polarizing signal V_{inj} is applied to suitable injection electrodes as part of the sensing scheme described in the previous section. Although it is part of the polarization effect just described, it is useful to deal with it separately: for the injection electrodes we can define the total voltage as the sum of the injection voltage considered here and a residual one, included in the above summation[3]. Thus, the TM voltage is also contributed by the term:

$$V_{TM,inj} = \sum_{j \in inj} \frac{C_j}{C_{tot}} V_{inj} \sin(\omega_{inj} t) = \alpha V_{inj} \sin(\omega_{inj} t) \tag{2.5}$$

where the sum is restricted to the injection electrodes. In LTP and LISA $\omega_{inj} = 100$ kHz, and V_{inj} is calculated so as to give $\alpha V_{inj} \approx 0.6$ V, as a compromise between sensitivity and induced stiffness (see the following).

- *TM charge:* due to impacting cosmic rays, TM charging will happen in space. It is a random process and affect the TM voltage with a noisy contribution

$$V_{TM,Q} = \frac{Q(t)}{C_{tot}} \tag{2.6}$$

where C_{tot} is the total capacitance of the TM toward surrounding surfaces and the $Q(t)$ is the net charge. TM charging is a Poisson process with estimated net charging rate for LISA $e\lambda_{net} \approx 50\frac{e}{\mathrm{s}}$ and $S_Q^{1/2} = \frac{e\sqrt{2\lambda_{eff}}}{\omega} \approx \frac{25}{\omega} e$ Hz$^{1/2}$ [10, 15], with e the elementary charge. Note that λ_{net} and λ_{eff} differ because charges of both signs are released on the TM by cosmic rays: thus, while the charge noise associated with the random arrival process concerns the total number of charges of both signs, the net charge accrual is smaller as it is obtained from the difference between the two.

Surrounding surfaces potential (V_i) :

- *Stray biases:* Although gold coated and grounded, surfaces surrounding the TM can show spatially-varying potential due to work function inhomogeneities[4] [16, 17] (see Section 9 for details). They are expected to

[3] Actually, this is not strictly true as the "only stray biases contributed" V_j just defined doesn't coincide with the V_i used in 2.3, where the total bias has to be considered. As already said, however, if we assume the electrostatic model introduced in Appendix A to be valid, the capacitances derivative along X of injection electrodes on Y and Z faces is null. Thus, Y and Z faces (here including the electrodes) only contribute to the force via the polarization effect (they change V_{TM}), and we recover the validity of the division being done here

[4] Note that in principle a local potential variation can happen also on the TM surface. However, as it contributes to the voltage drop between the TM and the corresponding facing i-th surface, it can be attributed to the latter thus simplifying the modeling

contribute with values of order tens of mV (up to 100 mV) and can also vary over time. At present, models and estimates about DC-biases are few and unreliable, also considering the strong dependence on the history and peculiar characteristics of the sample, and an experimental investigation before flight the missions is mandatory.

- *Readout back-action:* given the scheme presented in 2.1, it can be shown that a fluctuation in the voltage drop across the main inductance of the inductive transformer generates corresponding voltage drops of opposite sign in the secondary windings [13]. Since these are connected to opposing electrodes, they fluctuate in phase with opposing sign, thus generating a net fluctuating electric field across the sensor. Actually, the thermal fluctuations on the primary winding are expected to be strongly suppressed by the feedback loop of the amplifier, and this effect should be negligible [18]. It however requires testing and confirmation on ground.

- *Voltage thermal noise:* dielectric losses in the TM surroundings surface give rise to a voltage thermal noise according to the fluctuation-dissipation theorem, with spectral density [19]

$$S_{V_{th}}^{1/2} = \sqrt{4K_bT\frac{\delta}{2\pi f C_i}}$$

  with K_b is the Boltzmann constant, T the ambient temperature, C_i the surface capacitance toward the TM and δ the loss angle in the dissipative medium, estimated to be of order 10^{-5} in the measurement bandwidth making this contribution negligible.

- *Actuation noise:* actuation circuitry is directly connected to electrodes, and voltage noise originating in the electronics would translate in a corresponding electrodes voltage noise summing to those above. This required a limit of 10 μV to be imposed on maximum actuation circuitry voltage noise.

Due to the listed effects, both V_{TM} and V_i fluctuates over time, and can be thought as formed by the sum of a “DC” term (meaning an average value that fluctuates with frequencies below the measurement band) and an in-band contribution. Moreover, we note that because of term V_{TM,V_j}, V_{TM} turns out to be a function of the X TM position through the capacitances C_j; further on, we will use the definition

$$V_{TM,0} \equiv V_{TM,inj} + V_{TM,Q} \quad \Rightarrow \quad V_{TM} = V_{TM,0} + \sum_j \frac{C_j V_j}{C_{tot}}$$

to explicitly express this dependence.

According to what has been said in the previous section, we are interested in evaluating the electrostatic contribution to both the net force and the stiffness experienced by an almost centered TM ($x = 0$). To do that, we will expand the various terms up to first order in the TM displacement x, so as to be able to separate their contributions to both stiffness and force.

Evaluating the square in Equation 2.3 and separating the various terms, we find:

$$F_X = \frac{1}{2}\sum_i \frac{\partial C_i}{\partial x} V_{TM}^2 + \frac{1}{2}\sum_i \frac{\partial C_i}{\partial x} V_i^2 - \sum_i \frac{\partial C_i}{\partial x} V_{TM} V_i \tag{2.7}$$

To simplify the notation, we observe that the C_i, their first and second derivatives and V_{TM} (through C_j in the term $\sum_j C_j Vj/C_{tot}$) are all and the only functions of x in this model (C_{tot} is constant at the first order in x because the TM is surrounded by the EH, and opposite surfaces derivatives have opposite sign, compensating each other upon TM displacement). As we are performing series expansion around zero, we will assume that all these quantities as they appear in the following equations are computed for $x = 0$, while keeping account of their dependence on x when performing derivatives and series expansions. Moreover, we will use the electrostatic model introduced in Appendix A, and in particular relations A.1 and the σ_i function introduced in Equation A.2 to account for different sign of capacitance first derivatives of surfaces belonging to different X faces ($\sigma = +1$ on $X+$ faces, and $\sigma = -1$ on $X-$ ones).

It can be noted that the expansion of the first term of Equation 2.7 only gives rise to a stiffness contribution:

$$\begin{aligned} \frac{1}{2}\sum_i \frac{\partial C_i}{\partial x} V_{TM}^2 \approx \frac{1}{2} V_{TM}^2 \sum_i \frac{\partial C_i}{\partial x} + \frac{1}{2}\frac{\partial \left(V_{TM}^2\right)}{\partial x} \sum_i \frac{\partial C_i}{\partial x} x + \frac{1}{2} V_{TM}^2 \sum_i \frac{\partial^2 C_i}{\partial x^2} x \approx \\ \approx \frac{V_{TM}^2}{2} \sum_i \frac{2C_i}{d^2} x = 2V_{TM}^2 \frac{C_{Xf}}{d^2} x \end{aligned} \tag{2.8}$$

where we used that nominally $\sum_i \frac{\partial C_i}{\partial x}\Big|_0 = 0$ and $\sum_i C_i\Big|_0 = C_{Xf}$, with C_{Xf} the capacitance of the single X face when the TM is centered.

When expanding in series second term of Equation 2.7, we get both a contribution to the net force

$$\frac{1}{2}\sum_i \sigma_i \frac{C_i}{d} V_i^2 \tag{2.9}$$

and one to the stiffness

$$\sum_i \frac{C_i}{d^2} V_i^2 x \tag{2.10}$$

Finally, using the definition of $V_{TM,0}$ given above, we can rewrite the third term of Equation 2.7 as:

$$-\sum_i \frac{\partial C_i}{\partial x} V_{TM} V_i = -V_{TM,0} \sum_i \frac{\partial C_i}{\partial x} V_i - \left(\sum_j \frac{C_j V_j}{C_{tot}} \right) \sum_i \frac{\partial C_i}{\partial x} V_i \tag{2.11}$$

Once again, expanding the first term of this equation give rise to both a force

$$-V_{TM,0} \sum_i \sigma_i \frac{C_i}{d} V_i \tag{2.12}$$

and a stiffness

$$-2V_{TM,0} \sum_i \frac{C_i}{d^2} V_i x \tag{2.13}$$

The same holds for the second term, that however has a dependence on x in both factors, thus leading to one force term

$$-\left(\sum_j \frac{C_j V_j}{C_{tot}} \right) \sum_i \sigma_i \frac{C_i}{d} V_i \tag{2.14}$$

and two stiffness ones:

$$-\left(\left(\sum_j \frac{\frac{\partial C_j}{\partial x} V_j}{C_{tot}} \right) \sum_i \sigma_i \frac{C_i}{d} V_i + 2 \left(\sum_j \frac{C_j V_j}{C_{tot}} \right) \sum_i \frac{C_i}{d^2} V_i \right) x \tag{2.15}$$

Summing up all the different contributions, we can express the general form of the net position independent force.

$$\begin{aligned} F_X(0) &= \frac{1}{2} \sum_i \sigma_i \frac{C_i}{d} V_i^2 - V_{TM,0} \sum_i \sigma_i \frac{C_i}{d} V_i - \left(\sum_j \frac{C_j V_j}{C_{tot}} \right) \sum_i \sigma_i \frac{C_i}{d} V_i = \\ &= \frac{1}{2} \sum_i \sigma_i \frac{C_i}{d} V_i^2 - \left(V_{TM,0} + \sum_j \frac{C_j V_j}{C_{tot}} \right) \sum_i \sigma_i \frac{C_i}{d} V_i \end{aligned} \tag{2.16}$$

and that of the stiffness constant:

$$
\begin{aligned}
F'_X(0) = 2V_{TM}^2 \frac{C_{Xf}}{d^2} &+ \sum_i \frac{C_i}{d^2} V_i^2 - 2V_{TM,0} \sum_i \frac{C_i}{d^2} V_i - \\
&- \left(\sum_j \frac{\frac{\partial C_j}{\partial x} V_j}{C_{tot}} \right) \sum_i \sigma_i \frac{C_i}{d} V_i - 2 \left(\sum_j \frac{C_j V_j}{C_{tot}} \right) \sum_i \frac{C_i}{d^2} V_i = \\
&= 2 \left(V_{TM,0}^2 + \left(\sum_j \frac{C_j V_j}{C_{tot}} \right)^2 + 2V_{TM,0} \left(\sum_j \frac{C_j V_j}{C_{tot}} \right) \right) \frac{C_{Xf}}{d^2} \\
- 2 \left(V_{TM,0} + \sum_j \frac{C_j V_j}{C_{tot}} \right) \sum_i \frac{C_i}{d^2} V_i &- \left(\sum_j \frac{\frac{\partial C_j}{\partial x} V_j}{C_{tot}} \right) \sum_i \sigma_i \frac{C_i}{d} V_i + \sum_i \frac{C_i}{d^2} V_i^2
\end{aligned} \tag{2.17}
$$

so that

$$F_X(x \sim 0) \approx F_X(0) + F'_X(0)x$$

Before commenting on the single contributions that correspond to the various terms in the above expressions, it is useful to further expand the term $V_{TM,0}^2$:

$$
\begin{aligned}
V_{TM,0}^2 = \left(\frac{Q}{C_{tot}} + \alpha V_{inj} \sin(\omega_{inj} t) \right)^2 &= \\
= \left(\frac{Q}{C_{tot}} \right)^2 &+ \alpha^2 V_{inj}^2 \sin^2(\omega_{inj} t) + 2 \frac{Q}{C_{tot}} \alpha V_{inj} \sin(\omega_{inj} t)
\end{aligned} \tag{2.18}
$$

In the above expression, $(Q/C_{tot})^2$ is the RMS TM voltage due to its charge. The second term can be rewritten as

$$\frac{\alpha^2 V_{inj}^2}{2} (1 - \cos(2\omega_{inj} t))$$

and thus contributes with a DC force term plus a 2ω one that can be neglected being by far from measurement band and whose effects are strongly suppressed by the TM inertia.

About the remaining mixed product, we note that the multiplication of a signal χ (the TM charge in this case) by a pure sinusoid of frequency ω_{inj} has the effect of shifting its spectrum by $\pm\omega_{inj}$ (in the case of the injection signal itself, it exactly corresponds to bring it to frequency zero, resulting in the DC component shown above):

$$S_{\chi \sin(\omega_{inj} t)}^{1/2}(\omega) = \frac{1}{2} \left(S_\chi^{1/2}(w + w_{inj}) + S_\chi^{1/2}(w - w_{inj}) \right) \tag{2.19}$$

This means that interaction with the injection voltage *down-converts* to the measurement band disturbance fluctuations that are about 100 kHz above, and are thus expected to be negligible. The mixed product in Equation 2.18, for example, brings into the measurement band charge fluctuations at about 100 kHz, that are very small considering that the charge noise is expected to decrease as ω^{-1}. This applies also to the interaction of $V_{TM,inj}$ with fluctuating V_i: all the effects contributing to V_i are expected to have negligible fluctuation at 100 kHz if they satisfy noise requirements in the measurement band, the only exception being the readout back action. As the fluctuations on opposite electrodes are in phase, it does contribute a net field with a white spectrum whose $\sim$ 100 kHz component couples with the oscillating TM voltage down-converting to an in-band net force term. Though according to the readout circuitry model this contribution should be negligible, it needs experimental confirmation.

Keeping in mind this, and assuming the readout back-action to be negligible (as long as no experimental results contradict this hypothesis), we can consider negligible any term linear in $V_{TM,inj}$ and consider $V_{TM,0}$ to be only due to the TM charge $V_{TM,0} = V_{TM,Q} = Q/C_{tot}$, except that in the case of V_{TM}^2 in which we should account also for a DC contribution $\alpha^2 V_{inj}^2/2$ as shown by Equation 2.18.

We can thus rewrite the expressions for the stiffness as:

$$
\begin{aligned}
F'_X(0) = \\
&\alpha^2 V_{inj}^2 \frac{C_{Xf}}{d^2} && \text{(2.20a)}\\
&+ 2\left(\frac{Q}{C_{tot}}\right)^2 \frac{C_{Xf}}{d^2} + 2\frac{Q}{C_{tot}}\left(2\left(\sum_j \frac{C_j V_j}{C_{tot}}\right)\frac{C_{Xf}}{d^2} - \sum_i \frac{C_i}{d^2} V_i\right) && \text{(2.20b)}\\
&+ 2\left(\sum_j \frac{C_j V_j}{C_{tot}}\right)^2 \frac{C_{Xf}}{d^2} - 2\left(\sum_j \frac{C_j V_j}{C_{tot}}\right)\sum_i \frac{C_i}{d^2} V_i \\
&\qquad - \left(\sum_j \frac{\frac{\partial C_j}{\partial x} V_j}{C_{tot}}\right)\sum_i \sigma_i \frac{C_i}{d} V_i + \sum_i \frac{C_i}{d^2} V_i^2 && \text{(2.20c)}
\end{aligned}
$$

The maximum allowed value for the stiffness contribution expressed in the above equation sets constraints both on V_{inj} (fixed to the previously mentioned value to induce a stiffness $\approx 10^{-7}$ N/m) and on Q not to exceed $\approx 10^7 e$ (to limit the induced stiffness below $2 \cdot 10^{-9}$ N/m, roughly 0.1% of the total LTP stiffness budget of $\approx 25 \cdot 10^{-7}$ N/m) [10]. To fulfill the need to keep the TM charge below a given limit, an UV light charge management system has been designed for both LTP and LISA [20](see 4.2.4).

Although terms depending on the V_i distribution in the above equation are currently estimated not to be dominating, experimental investigation is ongoing.

We can rewrite the expression for the force as:

$$F(0) =$$

$$-\frac{Q}{C_{tot}}\sum_i \sigma_i \frac{C_i}{d} V_i \tag{2.21a}$$

$$-\sum_j \frac{C_j V_j}{C_{tot}} \sum_i \sigma_i \frac{C_i}{d} V_i \tag{2.21b}$$

$$+\frac{1}{2}\sum_i \sigma_i \frac{C_i}{d} V_i^2 \tag{2.21c}$$

The first term represents the force experienced by a charged TM in the net electric field induced by asymmetric distribution of the V_i among the two X faces.

The quantity $\sum_i \sigma_i \frac{C_i}{d} V_i$ (or, more generically, $\sum_i \frac{\partial C_i}{\partial x} V_i$) measure the stray voltage imbalance between the X faces: note that if the V_i were all equal, this quantity will be null. On the other hand, V_i of opposite sign on opposite faces would maximize the absolute value of this quantity. As will be shown in Chapter 9, a more convenient way of expressing this quantity is in terms of a suitable voltage $+\tilde{V}$ applied to the $X+$ electrodes and $-\tilde{V}$ applied to the $X-$ one to obtain the same effect. In this case we can rewrite term 2.21a as:

$$-\frac{Q}{C_{tot}}\sum_i \sigma_i \frac{C_i}{d} V_i = -\frac{Q}{C_{tot}} 4 \frac{C_{Xe}}{d}\tilde{V} \tag{2.22}$$

where C_{Xe} is the capacitance of a single X electrode. Calling $\Delta X = 4\tilde{V}$, we can use it to express the imbalance of a generic stray voltage distribution. From the above equation:

$$\Delta X \equiv 4\tilde{V} = -\frac{1}{2}\frac{Q}{C_{tot}}\sum_i \sigma_i \frac{C_i}{d} V_i \left(-\frac{1}{2}\frac{Q}{C_{tot}}\frac{C_{Xe}}{d}\right)^{-1} = \frac{d}{C_{Xe}}\sum_i \sigma_i \frac{C_i}{d} V_i \tag{2.23}$$

Term 2.21a can show in-band variations due to both charge fluctuations

$$-\frac{S_Q^{1/2}(\omega)}{C_{tot}}\frac{C_{Xe}}{d}\Delta X \tag{2.24a}$$

or surface potential noise due to the variety of effects listed at the beginning of this section:

$$-\frac{Q}{C_{tot}}\frac{C_{Xe}}{d} S_{\Delta X}^{1/2}(\omega) \tag{2.24b}$$

Given the expected value of $S_Q^{1/2} \approx 6 \cdot 10^{-15}$ C/Hz$^{1/2}$ at 0.1 mHz, ΔX should be less than 5 mV (about 1 mV per electrode) not to exceed the allocated noise budget for LISA: as the measured ΔX is usually much bigger, this would require compensation capabilities (see Chapter 9). Moreover, according to the maximum value of the charge set by the induced excess stiffness, it should hold $S_{\Delta X}^{1/2} \lesssim 5 \cdot$

10^{-5} V/Hz$^{1/2}$).

Finally, terms 2.21b and 2.21c describe stray voltage self-interaction

2.2.2 Thermal effects

Thermal gradients across the GRS structure are responsible for a number of effects that can result in a noisy force acting on the TM. In particular, three mechanism have been identified that can spoil the purity of TM geodesic motion at the level required for LISA and LTP [21]:

Radiation pressure: thermal photons emitted by internal GRS surfaces hit the TM transferring momentum when absorbed or reflected. Frequency (i.e. momentum) distribution and number of photon depends on the surface temperature, and so the total momentum transferred to the TM by each of the facing surface: if the GRS internal $X+$ face has a higher temperature than the $X-$ one, the radiation pressure exerted by emitted photons that hit the TM will be correspondingly higher and a net force would arise along the X axis (in this case in the negative direction). If the temperature difference among the two GRS faces is noisy, the resulting force would also be noisy and affect the free fall purity in the measurement bandwidth.

Trying to give a quantitative estimate to the effect, we can build a simplified model. In the approximation of two homogeneous infinite parallel planes one of which (the TM) is isothermal, the force exerted on it by radiation coming from an opposing infinitesimal surface dA at temperature T is perpendicular to the plane and can be written as

$$dF_{RP} = \frac{2\sigma}{3c} T^4 dA \tag{2.25}$$

with σ the Stefan-Boltzmann constant and c the speed of light. One can integrate Equation 2.25 over the internal surface of the GRS to have a first order estimate of the force acting on the TM for a given internal temperature profile. In the simple case of an uniform difference ΔT between the $X+$ and $X-$ faces we get:

$$F_{RP} \approx A \frac{8\sigma}{3c} T_0^3 \Delta T \tag{2.26a}$$

where A is the area of one TM face and T_0 average TM temperature.

Despite the simplicity of the above formula, applicability of these approximations to the actual GRS geometry is hard to predict. Effects of temperature inhomogeneities together with border effects can mix to produce potentially strong deviations: asymmetries in the number of emitted photons propagating in different directions from a single point that hit the TM can cause tangential forces to arise, high reflectivity of surfaces can make the photons travel relatively long distances affecting surfaces far from their origin and thus smoothing the temperature distribution, etc... We can introduce in Equation 2.26a a correction factor K_{RP} that accounts for the mentioned effects, an write the expected force derivative with respect ΔT:

$$\frac{\partial F_{RP}}{\partial \Delta T} \approx K_{RP} A \frac{8\sigma}{3c} T_0^3 \approx 27 \ \frac{\mathrm{pN}}{\mathrm{K}} K_{RP} \left(\frac{T_0}{293 \ \mathrm{K}} \right)^3 \tag{2.26b}$$

Simulations performed to evaluate the effect in the real GRS configuration resulted in an estimate of $K_{RP} \approx 1/3$, thus representing a noticeable, although not order-of-magnitude, reduction of the estimated force noise due to this source [21].

However a confirmation via ground testing is mandatory.

Radiometer effect: in a similar way to thermal photons, residual gas particles trapped in the gaps hit the TM and transfer to it their momentum. At the expected operating pressure of 10^5 Pa the mean free path of particles is much larger than the system dimensions, and the kinetic energy they carry is a function of the temperature of the surface they just left (at least partially, with other contributions coming perhaps from the history of the particle). Particles trapped in a gap delimited by GRS surfaces at higher temperatures would thus carry an higher momentum and exert more force on the TM. If the temperature difference between opposing surfaces fluctuates, it will result in a noisy force acting on the TM.

As in the case of radiation pressure, we can try to estimate the effect applying a simplified model of infinite parallel planes at uniform temperature T_0 and $T0 + \Delta T$, with $\Delta T << T_0$; we arrive at the following formula for the force exerted on one plane by particles coming from a facing surface dA:

$$dF_{RE} = \frac{P_0}{2} \left(1 + \sqrt{\frac{T}{T_0}} \right) dA \tag{2.27}$$

where P_0 is the pressure if both planes were at temperature T_0. Integrating in the simple case of $X+$ and $X-$ faces at uniform temperatures with difference ΔT and TM temperature T_0 we get:

$$F_{RE} \approx A \frac{P_0}{4} \frac{\Delta T}{T_0} \tag{2.28a}$$

This model in however affected by a number of source of uncertainty deriving from the molecules-surface dynamics (absorption, emission direction and energy distributions, level of thermalization, etc...). We can once again write the force derivative with respect to ΔT:

$$\frac{\partial F_{RE}}{\partial \Delta T} \approx K_{RE} A \frac{P_0}{4T_0} \approx 18 \ \frac{\text{pN}}{\text{K}} K_{RE} \left(\frac{P_0}{10^5 \ \text{Pa}}\right)\left(\frac{293 \ \text{K}}{T_0}\right) \tag{2.28b}$$

introducing the parameter K_{RE} to account mainly for effects coming from geometrical factors. Numerical simulations estimated $K_{RE} \approx 1.25$, substantially confirming the validity of the model [21]. However, ground testing would be crucial to have a more reliable estimation of the force noise the TM could experience in space.

Thermal activated outgassing: among all thermal gradient related effects, this is the most subtle, least well understood and most difficult to model. GRS surfaces will adsorb a number of impurities and species during production, assembly and storage. Once in vacuum, these will outgass (i.e. desorb) from the surfaces modifying the local pressure. Because the outgassing process is likely driven by temperature, thermal differences among surfaces would lead to different outgassing rates, and thus a net noisy force will derive from noisy temperature differences. Unfortunately, the picture is even worst: the contamination distribution may not be uniform and different species outgassing will probably have different outgassing dependence on the temperature, making it very hard to produce a model for the effect. The simple model of a single species outgassing flux Q driven by an exponential law $Q(T) = Q_0 \exp^{-\Theta/T}$ with an activation temperature Θ gives, again in the simple approximation used above, a very rough estimate of the differential pressure:

$$\Delta P_{OG} \approx \frac{Q(T)\Theta\Delta T}{C_{eff} T^2} \tag{2.29}$$

where C_{eff} takes into account the conductances between the two X sides of the sensor through paths around the TM as well as conductances toward the exterior through holes in the EH. It has been estimated that

$$\frac{\partial F_{OG}}{\partial \Delta T} \approx A \frac{Q(T_0)}{C_{eff}} \frac{\Theta}{T^2} \approx 40 \ \frac{\text{pN}}{\text{K}} \left(\frac{Q(T_0)}{1.4 \ \text{nJ/s}}\right)\left(\frac{\Theta}{3 \cdot 10^4 \ \text{K}}\right)\left(\frac{293 \ \text{K}}{T_0}\right)^2 \tag{2.30}$$

However, even if applied to more than one species simultaneously, this basic model together with the scarce knowledge about Θ appears to be inadequate for a reliable estimate of the effect and ground testing is absolutely needed.

The three source of noise described above sum up coherently, and their estimated combined effect requires to limit temperature fluctuations between GRS X faces below 10^{-5} K/Hz$^{1/2}$.

From the above discussion, it is clear that thermal gradient related effects are among the more dangerous and the least reliably estimated source of noise jeopardizing LTP and LISA mission, and on ground investigation is thus a great advantage.

2.2.3 Miscellaneous

A number of other effects not listed above are foreseen as possible sources of force noise or stiffness [3, 10]. They include:

- Gravitational: in both LTP and LISA, an accurate mass distribution balancing procedure have been studied to reduce as much as possible the net gravitational interaction between TMs and spacecraft, that can translate into a noisy force by means of variation induced by thermal distortion of the structure. However it remains one relevant source of noise, and on LTP it accounts for about 10% of the total noise budget ($\sim 3 \cdot 10^{-15}$ m/(s^{2}Hz$^{1/2}$), or ~ 1.5 fN/Hz$^{1/2}$). Moreover, gravitational force gradient mainly due to the presence of the satellite is by far the biggest contribution to the total allowable stiffness, representing roughly 50% of the total.

- Stringent limits on the on board magnetic fields, as well as requirement on the TM alloy magnetic properties, have been set considering that TM permanent and induced magnetic moment can interact with the local (i.e. generated inside the spacecraft) and interplanetary magnetic fields and fields gradient, resulting once again in a noise force and a stiffness term. Nevertheless, while the latter is accounted for a small fraction of the total stiffness, near a third of the noise budget in reserved for the former. Note that, although in principle the TM charge could couple with the interplanetary magnetic field, this contribution is negligible.

- TM motion damping by means of random residual gas molecules impact can result in a noisy force. However, at operating pressure of 10^{-5} Pa this contribution turns out to be very small, although not negligible.

- Leakage in the sensitive X axis of interaction nominally affecting only orthogonal DOFs is another non negligible source of noise. We include here actuation cross-talks and a variety of other effects.

2.2.4 Unknown sources

LISA and its technological demonstration mission LTP are pushing the limit of requested purity of geodesic motion for a nominally free falling proof mass well beyond any level previously achieved (see Figure 2.4]. In addition to the list of the major known sources of noise given in this chapter, a main threat for the missions comes from unknown and unmodeled sources of noise that can show up when the experiments become operational in space, excluding any possibility of intervention and correction. It is thus of fundamental importance to be able to place a relevant

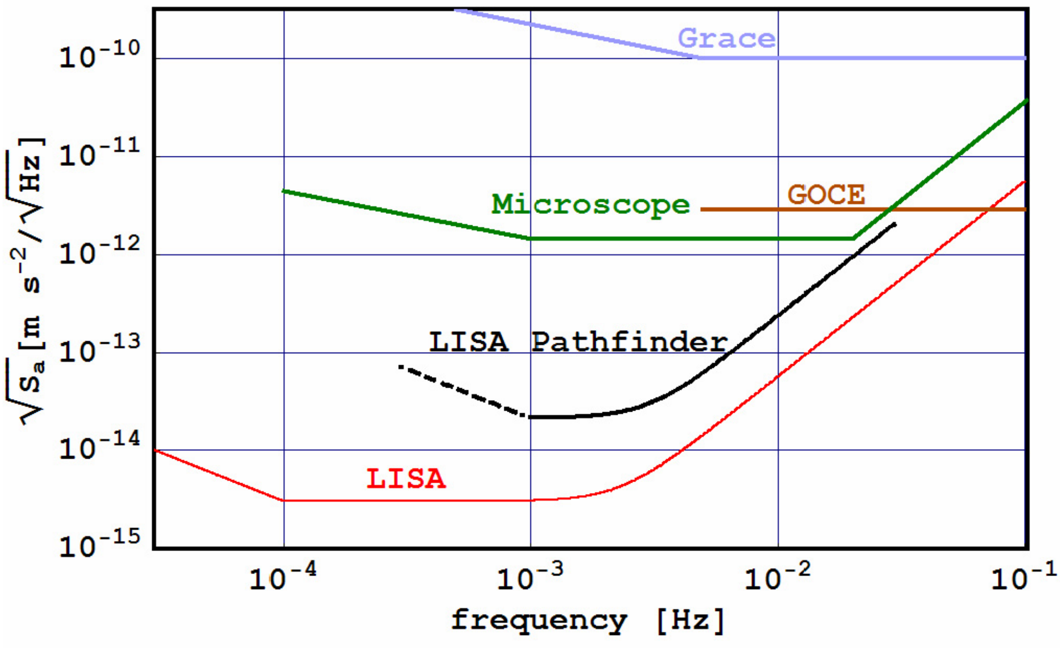

Figure 2.4 – Comparison of LISA and LTP free-fall requirements with those of other space missions. Even LTP requirements, relaxed a factor 10 with respect to LISA, are two order of magnitude below those of other missions.

upper limit on the force noise exerted by these unexpected sources, as close as possible to the LISA requirement to achieve full sensitivity. This is one of the main task of the on-ground testing campaign.

2.3 GRS Design details

The present sensor design, that is the current baseline GRS for the LTP and LISA missions, is the product of a long and complex optimization process, driven by the noise model described above and partially aided by ground testing campaigns on prototype sensors [9–14]. Here we will refer to the Engineering Model (*EM*) that has been tested so far in the facilities we are going to describe. A variation with sapphire electrodes instead of Shapal ones is also currently under testing, while a replica of the actual Flight Model is expected be available for testing within first half of 2008. Although different in some construction and materials, they all share the same geometry and electrode configuration.

Because most of the disturbing effects described in the previous section are expected to scale as the inverse of the distance at some power, trying to obtain gaps as large as possible fulfilling at the same time the sensitivity requirements has been one of the main objectives, successfully achieved, of the optimization procedure: the GRS design currently foresees 4 mm gaps along the interferometer-sensitive X axis, and slightly smaller along the orthogonal DOFs (3.5 mm along Z and 2.9 mm along Y).

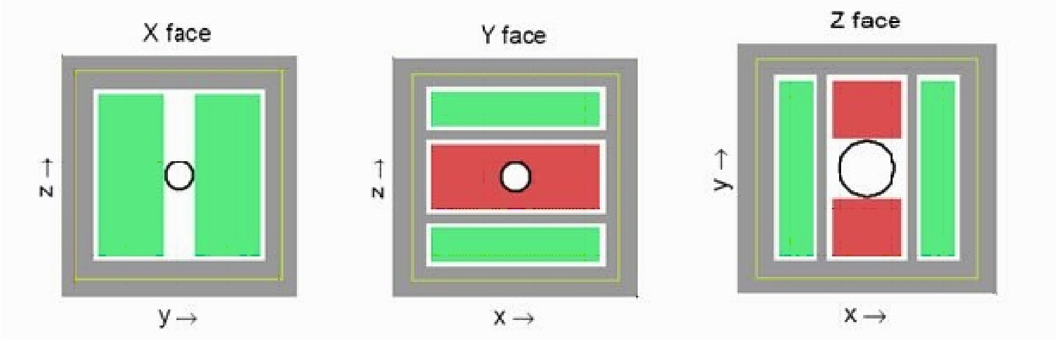

Figure 2.5 – A scheme of the disposition of electrodes and other main features on the GRS internal faces. You can see injection electrodes filled in red, and sensing ones filled in green, while the thin yellow line represent the projection of the TM face.

It has a total of twelve sensing electrodes, arranged in pairs as in Figure 2.3, and six injection ones. Figure 2.5 shows a drawing of X, Y and Z faces (both faces along the same DOF are equal) with electrode layout and other main features.

X faces host only two sensing electrodes 14.5x36 mm in size, for an estimated capacitance toward the centered TM of about 1.15 pF each. Between the two electrodes there is a 6 mm diameter hole to allow light for interferometric readout to reach the TM.

Each Y face hosts two smaller sensing electrodes 7.1x38.2 mm in size (0.83 pF each) along with a central injection one (1.24 pF).

Z faces hosts 2 sensing and 2 injection electrodes. The first have an estimated capacitance of about 0.6 pF, the second 0.42 pF.

Except for a 1 mm groove around each electrode, the remaining EH internal surface is constituted by grounded guard-rings that aim to reduce direct cross-talk between electrodes, both sensing and injection.

On all faces, the design guideline for electrode layout and sizing was that of maximizing electrodes size (to increase sensitivity) while maintaining their overall extension inside a safe-frame smaller than the TM face. In this way, border effects are negligible and each electrode capacitance toward the TM does not change appreciably when the TM moves parallel to the electrode itself. According to a model in which field lines extends from the border of a surface as arcs of circumference, and maintaining an additional margin, the safe-frame has been reduced by the size of the gap plus 1 mm on each side, thus yielding a maximum available electrode area on each X face of $(46 - 2 \times 4 - 2)^2$ mm^2 (from which we should subtract also grooves and central hole surfaces, not available for electrodes). The area is slightly bigger on Y and Z faces because of reduced gaps, but it is shared among a higher number of electrodes.

To choice not to implement injection electrodes on the X faces is motivated by the need of reducing the overall stiffness, eliminating the extra contribution introduced by the relatively high electric fields required. For the same reason, injection

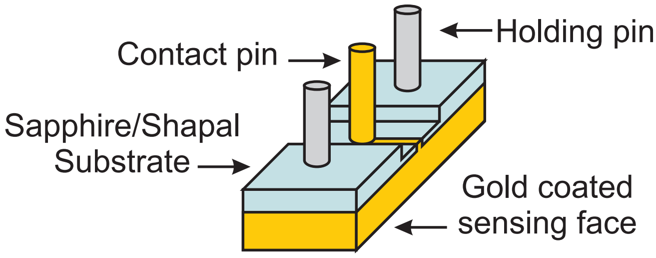

Figure 2.6 – A sketch of the electrodes design adopted on the GRS, along with the detail of the gold coated channel that provide the ohmic contact between the front gold coated sensing face and the rear connection pin. Additional pins used for mounting are shown too. Note that the gold coating stops before reaching the back face that lay on the electrode housing, so to avoid unwanted contact. Once in place, the lateral exposed dielectric surface (actually much smaller in than that shown here) would face a guard ring surface, being thus buried inside a deep groove.

electrodes have been split among Y and Z faces and recessed by 1 mm[5] with respect to the EH internal surface: thus also the overall stiffness on the DOFs orthogonal to the sensing axis is lowered, reducing the disturbances related to cross-talk effects.

In search for the highest possible thermal uniformity, the EH is made of high thermal conductive molybdenum and gold coated for electrostatic homogeneity.

For the same reason, each electrode is constituted by a bulk Shapal (a high thermal conductivity but electrically insulating ceramic) parallelepiped with gold coating on the front face and on the sides down to less than 1 mm from the back face, that is not coated to provide insulation toward the EH. In this way any exposed dielectric surface is deeply recessed inside a narrow groove of conducting material. A single track of coating is extended in a recessed channel on the back of the electrode and provides a contact point to which coaxial wires that bring signals to the readout electronics are soldered (see Figure 2.6). In this way external interferences are reduced to a minimum, as there is no interruption between the electrostatic shielding provided by the grounded EH and that provided by the coaxial cable, that enters the EH volume for several mm through a narrow hole. As already stated, in the flight model Shapal has been replaced with sapphire, both for composition (and properties) reproducibility and because it has already been tested to some extend in space. The connection design is similar but guarantees a better electrical shielding.

Figure 2.7 shows two pictures of the GRS Engineering Model Replica employed in this work.

[5]As shown in Section 2.2.1, the stiffness terms is proportional to the second derivative of the capacitance, thus scales with d^{-3}, while TM polarization depends on the capacitance itself, proportional to d^{-1}. Even though it requires higher voltage to maintain the same TM bias, increasing the electrode distance will result in a lower stiffness. Limits are set by the GRS geometry and increasing electrode capacitance toward the guard rings, that reduces its effective capacitance with respect to the TM.

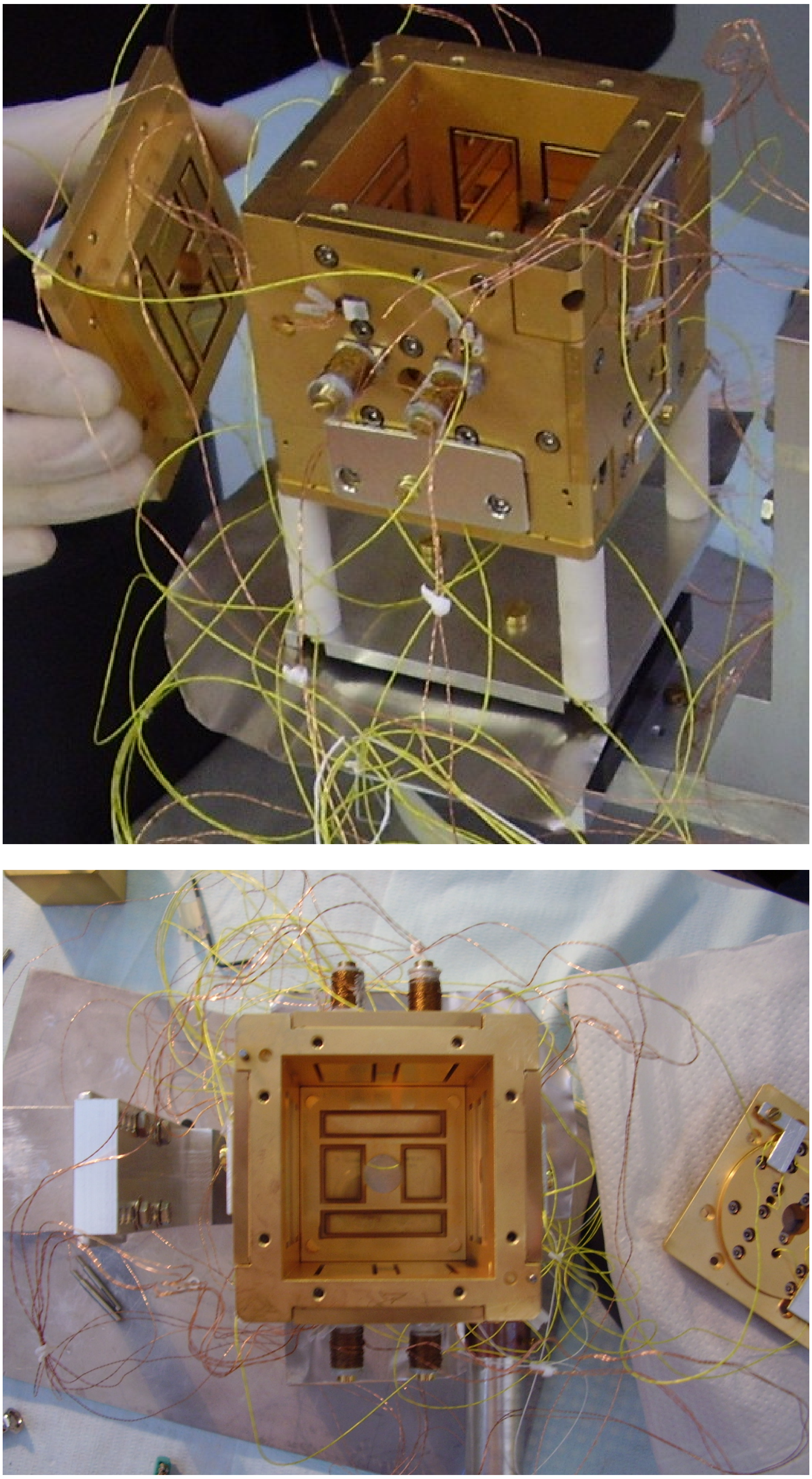

Figure 2.7 – Two picture of the GRS Engineering Model Replica currently installed in the 4-TM torsion pendulum facility.

Chapter 3

Testing GRS performances on-ground

GRS performance requirements in terms of sensitivity and maximum force noise exerted on TM, as described in Chapters 1 and 2 (see in particular Section 2.2), represent both a technological challenge and one of the most critical aspects of the LISA mission. Although one of the main aim of the LTP mission is to demonstrate the achievable purity of TM free fall in flight [22], in space missions there is very little opportunity to fix things during operation if something is not performing as expected and jeopardizes the success of the experiment. Being able to test a subsystem's performance on ground in an environment as representative as possible of the flight one is thus fundamental. For the GRS, this is particularly important both to help during the design phase to meet the requested sensitivity, and to place upper limits to the expected force noise in flight that should be as close as possible to the LISA and LTP requirements before launching.

LISA and LTP force noise isolation requirements are a well below any previous free-fall experiment; to meet such stringent requirements and assure the success of the missions, each known source of noise should be tested and characterized, and an upper limit as low as possible should be set for any unknown force.

In the following chapter we will demonstrate the suitability of torsion pendulums as extremely sensitive dynamometers. The Trento torsion pendulum facility basic characteristic and instrumental sensitivity will be pointed out before describing the overall setup and techniques we use to exploit it as GRS test bench.

Finally, current facility limits will be presented and a new torsion pendulum design will be proposed to overcome most of them. Proposed facility sensitivity and possible issues related to interpretation of the results will be discussed.

3.1 Torsion pendulums as test benches: the single TM facility

On-ground, GRS-TM interaction testing requires the ability to measure very small forces: even upper limits for LTP force noise, that are relaxed a factor 10 with respect to LISA ones, are at the fN level (as reported in Figure 1.3), about 10^{16} orders of magnitude less than gravity on Earth, and relative to a very low frequency band in the $0.1 - 30$ mHz range. This means that if on-ground measurement apparatus is coupled to the Earth gravitational field, there are two main experimental problems: first, a very small relative fluctuation of the gravitational field will be an enormous signal that will compromise your measurement; second, you would anyway need an apparatus capable of more than 15 orders of magnitude of dynamic range, that is in general a quite hard experimental challenge.

It is therefore needed to decouple the measurement process from the local gravitational field. Torsion pendulums have proved to be well suited to achieve this [23, 24]: the suspension fiber that sustains the weight of the inertial member naturally hangs parallel to local gravitational field, reducing the coupling of the inertial member rotational DOF with the Earth gravitational potential. At the same time, with a correct choice of fiber dimensions and material, you can achieve a very low torsional spring constant and high quality factor, that result in a lower torque thermal noise and thus in an increased sensitivity. Moreover, the pendulum helps in filtering out seismic noise and reduce its impact on the measurement.

A torsion pendulum based facility for testing the forces exerted by the GRS on the inside TM has been operating in Trento for several years. It consists of a single (from now on we will refer to it as *1-TM*, or *single TM* pendulum) hollow mock-up of a LISA TM suspended, inside the sensor to be tested, by a thin tungsten fiber connected to a shaft extending orthogonal from the center of one TM face (see Figure 3.1) [25].

For the reasons already explained, this setup is nearly insensitive on all degrees of freedom except the "soft" rotational one around the fiber axis.

The equation of motion of the pendulum along the sensitive (rotational) DOF ϕ is written as:

$$I\phi''(t) + \beta\phi'(t) + \Gamma\phi(t) = N(t) \tag{3.1}$$

where I is the moment of inertia of the suspended inertial member, Γ the fiber torsional spring constant, N the applied torque and β is a dissipative term. As the best model for the torsional fiber is that of internal damping [26], when moving to the frequency domain, we can define the loss angle $\delta = 1/Q$ (with Q the oscillator quality factor) and write the relation between applied torque and angle displacement Fourier transforms as:

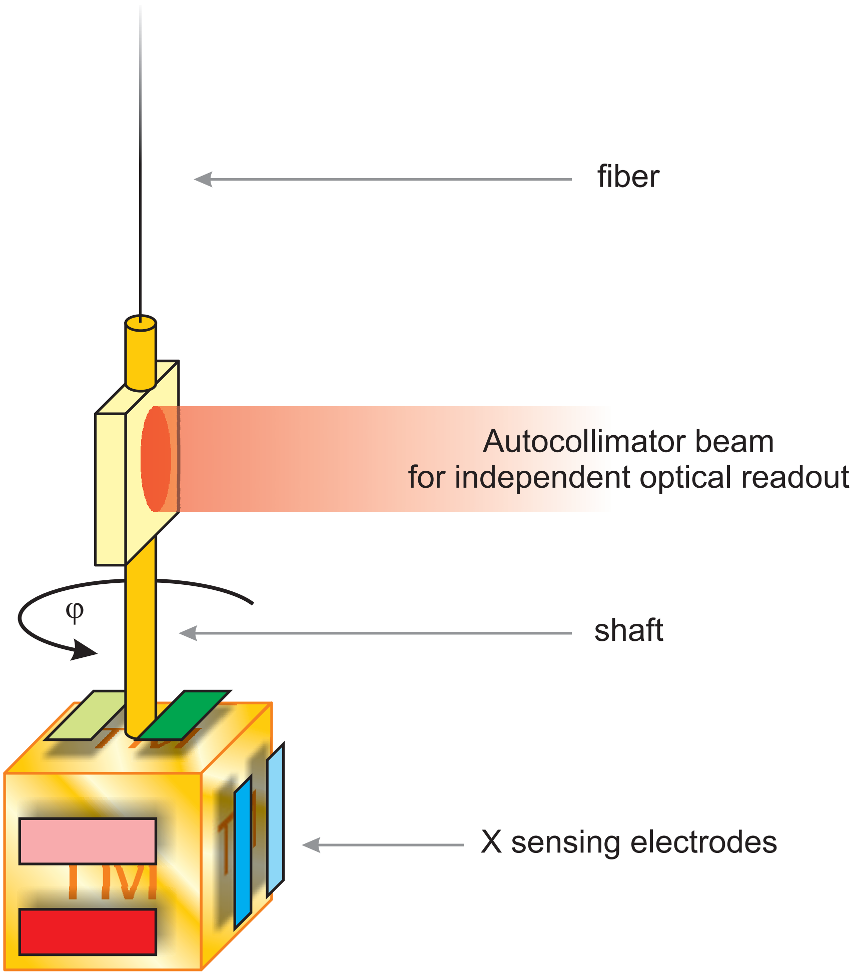

Figure 3.1 – A simple scheme of the 1-TM torsion pendulum facility operating in Trento for several years. GRS electrodes (the colored rectangles surrounding the TM) are represented without the electrode housing for clarity. The commercial autocollimator based independent readout is also shown. Any torque acting on the TM produces a deflection in the very “soft” rotational DOF and can be detected.

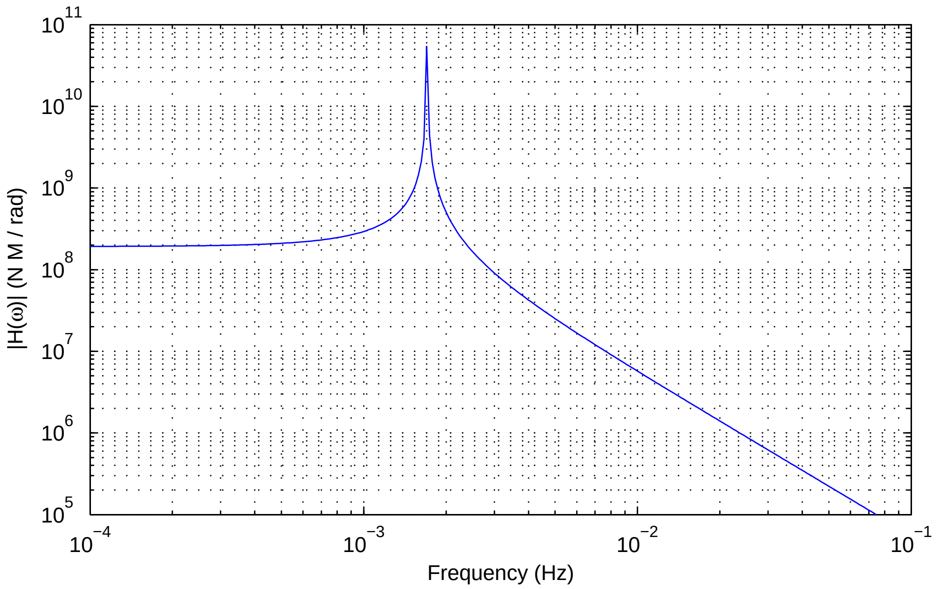

Figure 3.2 – Absolute value of the single TM torsion pendulum facility transfer function. Note the resonance peak at about 1.7 mHz, the rapid decay as ω^{-2} above resonance and the value of about Γ^{-1} in almost the whole frequency region below resonance.

$$I\omega^2\phi(\omega) + \Gamma(1+i\delta)\phi(\omega) = N(\omega) \quad \Rightarrow \quad \phi(\omega) = \frac{N(\omega)}{\Gamma(1+i\delta)+I\omega^2} \tag{3.2}$$

Exploiting the relations $I = \Gamma/\omega_0^2$, where ω_0 is the natural resonant angular frequency in the approximation of small δ (high quality factor), and introducing the pendulum transfer function $H(\omega)$, it can be rewritten in the more commonly used form:

$$\phi(\omega) = H(\omega)N(\omega); \qquad H(\omega) = \frac{1}{\Gamma(1-(\frac{\omega}{\omega_0})^2+\frac{i}{Q})} \tag{3.3}$$

This means that any external force acting at an angular frequency ω would be converted in an angular motion of the pendulum at the same frequency with a scale factor given by the above transfer function. Measuring this motion, it is thus possible, through the knowledge of the pendulum parameters, to estimate the external torque exciting the pendulum. As an example, the 1-TM pendulum transfer function is plotted in Figure 3.2.

However, the measured angular displacement signal $\phi_m(\omega)$ will be affected by a noise $\phi_n(\omega)$, so that

$$\phi_m(\omega) = \phi(\omega) + \phi_n(\omega) = H(\omega)N(\omega) + \phi_n(\omega) \tag{3.4}$$

and thus the measured torque will have a PSD given by

$$S_{N_m}(\omega) = S_N(\omega) + \frac{S_{\phi_n}(\omega)}{|H(\omega)|^2} \tag{3.5}$$

$S_N(\omega)$ is contributed by GRS, external sources and the unavoidable torque thermal noise induce by dissipation in the fiber, that has a PSD given by:

$$S_{N_{th}}(\omega) = 4K_B T \frac{\Gamma}{\omega Q} \tag{3.6}$$

where K_B is the Boltzmann constant and T the operating temperature. The instrumental noise floor is therefore:

$$S_{N_m}(\omega) = S_{N_{th}}(\omega) + \frac{S_{\phi_n}(\omega)}{|H(\omega)|^2} \tag{3.7}$$

which can be improved by reducing the angular readout noise, and providing a fiber with higher Q and lower torsional stiffness Γ. In particular, in order to reduce the latter so to make the instrument performances suitable for LISA GRS testing, it is required to employ a lightweight hollow TM. Γ depends on the fiber radius r via the relation

$$\Gamma = \frac{\pi r^4}{2L}(F + \frac{mg}{\pi r^2}) \tag{3.8}$$

L being the length of the fiber, F the elastic modulus of the material employed, m the pendulum mass and g the local gravitational field: as the fiber maximum load depends on r^2, the weight of the inertial member sets a lower limit on the suitable fiber diameter[1].

While using an hollow TM prevents us from testing bulk properties and interactions (gravitational and magnetics), it still allows for testing surface forces, that are the least known and thus more threatening, as expressed in Section 2.2.

In Figure 3.3 we show, both in angle and in torque, the effect of the mentioned contributions to the noise floor, for pendulum parameters similar to those used in the single mass facility. The left side of the measurement band is dominated by the pendulum thermal noise, that masks external contributions up to its value. The right side, on the other hand, is dominated by the readout sensitivity, unable to distinguish pendulum movement below a certain value. Because of the $1/\omega^2$ behavior of the transfer function, at higher frequencies, a bigger torque is needed to excite a pendulum response high enough to exceed the readout noise and be detected. This is clear in Figure 3.3b, where it can be seen that the torque required

[1]One may observe that the fiber Γ is also a function of the fiber length L. However, we are currently using length of order 1 m, and as Γ scales as $1/L$, substantially reducing it by increasing L would require an unrealistic long fiber. On the other hand, in practice the term $mg/(\pi r^2)$ is negligible with respect to F for tungsten fibers, even if heavily loaded. Γ thus depends on r^4, and even small reduction in the fiber radius will result in considerable decrease of the torsional spring constant.

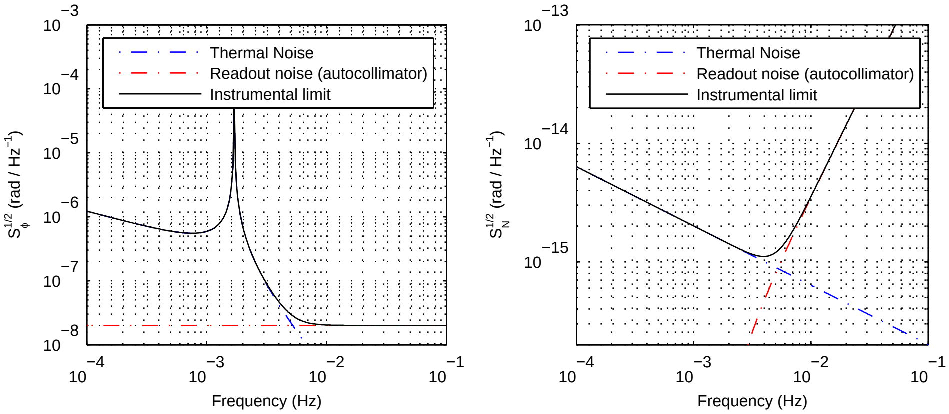

(a) Angular sensitivity

(b) Torque sensitivity

Figure 3.3 – The (autocollimator) readout and fiber thermal noise contribution to the 1-TM facility sensitivity curves are shown both (a) in angle and (b) in torque.

for a detectable pendulum response above readout noise goes as ω^2. The best torque sensitivity is reached in the crossover frequency between the two region. Here, given the fiber radius of 25 μm, the measured quality factor of about 3000 and the ambient temperature of about 300 K, the linear spectral density $S_{N_{th}}^{1/2}(\omega)$ has a value of less than 2 $\mathrm{fN\,m/Hz^{1/2}}$ around 2 mHz, that means that we are in principle able to detect a sinusoidal torque of less than 0.1 fN m with a SNR of 10 with a measure of 12 hours.

3.2 GRS characterization techniques

With such high sensitivity, this facility has proved to be very effective and has been used extensively to test GRS readout performances and actuation capabilities as well as to characterize known thermal and electrostatic effects and place relevant upper limits on unmodeled force noise sources [9, 17, 21, 22, 25, 27, 28]. Mainly three type of tests have been performed:

Readout sensitivity: as shown in Section 2.2, high sensitivity is a key feature of the GRS as it partially affect the spacecraft jitter around the TM, that translates in force noise by means of the coupling interaction. Although the electrostatic and electronic models used during the design phase to estimate the sensitivity of the GRS plus electronics system are solid and well tested, a 4 mm gap capacitive readout with such low displacement noise requirements has never been produced and needs to be tested. Rigidly binding things at the nm level to test sensor readout noise against a "still" TM is not simple. However, the pendulum transfer function heavily suppresses high frequency motion, allowing for easy identification of the low and high frequency bands in which, respectively, the real motion of the pendulum or the readout noise are predominant (see previous section and Figure 3.3), and thus estimate the white (in principle) level of the latter. With more than one available readout as in our case (see Section 4.1), by means of more sophisticated data analysis techniques id is even possible to separately estimate readout noise contributions to the observed noise in both frequency regions.

Another interesting test is cross-talk, i.e. leakage of signal coming from the TM motion in a DOF different from the observe one.

Known effect characterization: Section 2.2 lists a wide number of known effects that can convert environmental disturbances into forces acting on the TM. Even if with different levels of confidence, most of these effects have been modeled and their dependence on some relevant "scale variable" has been predicted (e.g. thermal gradients for the radiometer effect, injection voltage for the sensing stiffness, TM charge for DC biases...) . However, models need to be tested and the values of parameters involved estimated.

By proper modulation of one of the scale variables of a know noise source (e.g. the thermal gradient across the sensor for thermal related effects) and measuring the coherent response of the pendulum, we can calculate the torque induced on the pendulum at that particular frequency and attribute it to the modulated variable, thus estimating the coupling factor between it and the torque acting on the TM. This can then be compared with the predicted value, validating the theoretical model that can be used to translate the measured torque disturbance in equivalent force noise for LISA and LTP. This coherent analysis has the advantage of clearly identifying in frequency the source of the induced torque while getting rid of the pendulum noise in the remaining of the measurement band.

Unknown noise sources upper limit: when no disturbance is applied on purpose, unmodelled GRS-TM interactions, that we are interested in evaluating or upper-limiting, contribute to the pendulum torque noise together with a number of other sources. Whenever possible, we can eliminate known disturbances by proper shielding (e.g. inserting μ-metal envelopes around the GRS to shield external magnetic field) or source suppression (e.g. thermalizing the vacuum chamber to avoid temperature gradient and fluctuations). When such shielding is not possible, we still have the option of measuring the known source and, by an experimental or theoretical estimation of their coupling factor with the torque acting on the TM, subtract their effect. As a final step, we can evaluate the difference between the observed torque spectrum estimate and that of the thermal noise that we know to be due to the fiber internal dissipation mechanism and cannot be avoided. We are then left with a measured excess torque noise that we cannot reduce further based on our knowledge of noise sources and interactions: this represents the effect of uncontrolled and unknown noise sources that are acting on the pendulum. By conservatively attributing this unexplained excess noise entirely to the GRS-TM interaction, we can place an upper limit to the disturbance on the proof mass due to the capacitive sensor.

It is worth noting that even if we are interested in the excess noise with respect to foreseen thermal noise, being able to lower the latter employing suitable fibers (higher quality factor and smaller torsional stiffness, as explained in the previous Section) would result in a big advantage. The thermal noise is not only a constant that sets our zero from which to measure the excess noise (in which case its actual value, once known, would be of relatively little interest), but also directly proportional to the instrument sensitivity to external torque noise for a measure of a given length, and thus enters directly in our final uncertainty on the noise excess estimate.

In particular, consider the (theoretical) case in which there is no excess noise. To claim this, we should give an estimate of the observed power spectrum, that by hypothesis is equal to the thermal noise of the fiber. But from the statistical properties of the power spectrum, the measured value would have an uncertainty proportional to the value of the spectrum itself, and we can only state that we observe no excess noise within this level of uncertainty. The minimum lower limit we can set for the excess noise, in the case where we observe no excess with respect to the pendulum thermal limit, is thus proportional to the latter, and improving it would result in setting upper limits nearer to LTP and LISA requirements.

3.3 1-TM facility limitations

Despite the significant and accurate results obtained so far [9, 11, 21, 22, 25, 29], the single mass facility has intrinsic limitations due to the fact that it measures torques acting on the TM, while in space we will be much more interested in forces that directly affect the X translational DOF.

Although torque data taken with the 1-TM pendulum can be converted in equivalent force through models that provide a proper effective armlength, these models are effect-dependent and rely on hypothesis about the distribution of sources that in some cases can have a high degree of uncertainty.

Consider for example the case of a thermal related effect: to produce a torque, a rather complicated thermal pattern should be induced on the EH by applying suitable heaters on its exterior and alternately heating opposite corners (see Figure 3.4). Suppose we have a theoretical model for the force dF exerted on the TM by each infinitesimal GRS surface dS depending on its temperature: the induced

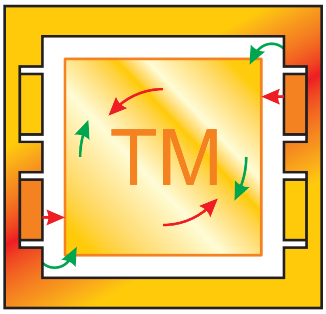

Figure 3.4 – The figure exemplifies an induced thermal pattern for torsional thermal effects investigation. Red arrows represent forces and consequent torques corresponding to hotter surfaces pushing away the TM (it can happen via a variety of effects, as explained in 2.2.2). As the thermal pattern has to produce a torque on the TM, it is required to vary from corner to corner, thus over distances smaller than the TM face. In such a configuration, and with thermal input obviously applied to the exterior of the GRS, the actual thermal gradient inside it is not easy to estimate. Moreover, green arrows shows that, if the thermal pattern is not well controlled around the corner (or this effect is not well modeled when making theoretical calculation for comparison) a suppression effect is likely to arise by means of "leakage" of heat toward surfaces that produce an opposite torque

torque can be estimated by integrating dF, computed for the internal temperature profile $T(\vec{x})$. If the model also depends on an unknown parameter p, its value can be inferred by comparing the estimated torque with the measured one. Then, the same theoretical model can be used to draw conclusions about the total force acting on the TM in the case of a different internal temperature profile, in particular one producing a net force along X. Alas, the relative distances between heaters, thermometers and surfaces which temperature are relevant for the effect (internal faces) are comparable with the scale of variation of the desired pattern; in addition, many complex features inside the GRS (grooves, holes, interfaces between different materials...) heavily modify effective thermal conductivity along different paths; all this makes it hard to give a reliable estimate of the internal temperature profile even using finite element model simulations. Moreover, border effects often neglected or roughly modeled happen to be particularly critical in a torsional configuration, in which forces leaking from the border of a face to the adjacent ones could have a relevant suppression effect applying an opposing torque with respect to that foreseen by the simple model. All this contributes to rise the uncertainty on the estimation of the parameter p, and thus the reliability of the model used to infer force noise related to the measured effect.

Another limitation comes from the fact that, as said, a torsion pendulum is only sensitive to combination of forces that exert a net torque with respect to the fiber. Given the construction geometry of the single mass facility, this corresponds to combinations of forces that exert torques with respect to the TM vertical rotational axis (that coincide with the fiber). On the contrary, any "translational" force acting on the TM (i.e. force that would produce a pure translation on a free TM) would

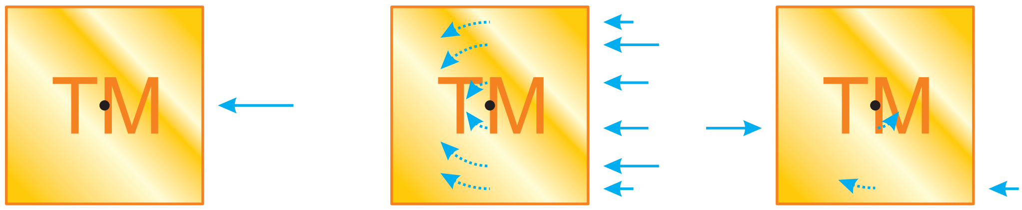

Figure 3.5 – The scheme, that represent the 1-TM torsion pendulum see from above (the black dot in the center of the TM is the torsional fiber, entering the page), shows some example of force combinations that would be invisible to this facility, but dangerous on a really free TM in space. While the right hand example, where the torques induced by two completely asymmetric forces exactly cancels out because of different arms, is quite improbable given the symmetry of the GRS, the other two cannot, for the same reason, be excluded and need investigation.

not be detected, producing only a net force that excite the swing motion of the pendulum, so stiff to be completely insensitive to forces of the order of magnitude we are investigating. As represented in Figure 3.5, these correspond to any force with a symmetric distribution with respect to a plane containing the fiber, an obvious example being a force acting orthogonally in the center of a TM face.

This means that investigating the GRS-TM interaction using the 1-TM facility we could in principle miss some contributions to the force that would act on a really free TM, that is particularly important because the most critical DOF in space would be the X translation axis, sensitive to "translational" forces instead of torques.

3.4 4-TM facility concept

Based on the deep experience gained on the 1-TM facility and the high level of sensitivity achieved, a new facility scheme capable of directly detecting forces acting on the TM has been proposed[30]: the principle is to suspend the TM off center with respect to the torsion fiber, so that any force acting on the TM along the direction orthogonal to both the fiber and the line joining it and the TM center (see Figure 3.6), would also produce a torque with an arm equal to the distance between the TM and the fiber axis. Installing the GRS with its X axis along this direction would thus allow it to be sensitive to any source of noise that would exert a force on the TM along the X axis, that is the most critical for space experiments.

In this configuration, the Z component (the one producing a rotation around the fiber) of the total torque N exerted on the pendulum by the forces $\vec{f_i}$ acting on one TM can be written as:

$$N_Z = \left(\sum_i \vec{R_i} \times \vec{f_i} \right) \cdot \hat{z} = \sum_i \left(\vec{b} \times \vec{f_i} \right) \cdot \hat{z} + \sum_i \left(\vec{r_i} \times \vec{f_i} \right) \cdot \hat{z} \tag{3.9a}$$

where $\hat{z}$ is the Z direction unity vector and, according to Figure 3.6, $\vec{R_i} = \vec{b} + \vec{r_i}$ is the vector connecting the fiber axis with the application point of the force $\vec{f_i}$; $\vec{b}$ is

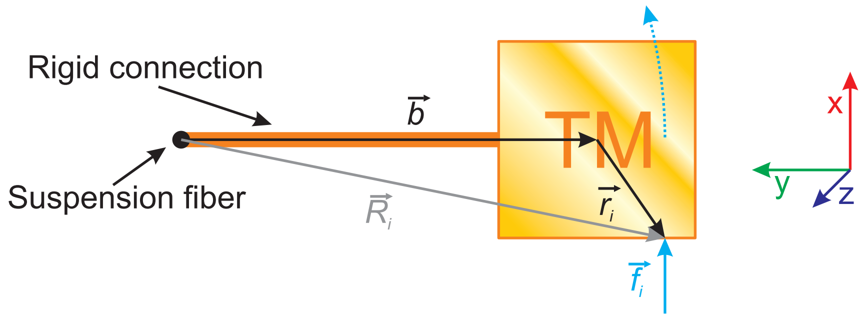

Figure 3.6 – A simple scheme illustrating the idea of a force sensitive torsion pendulum: suspending the TM off-center with respect to the fiber via a rigid connection would allow forces acting along the X axis to produce a torque with respect to the torsion fiber, thus becoming detectable even in the case their torque with respect to the TM vertical symmetry axis is null.

the vector from the fiber to the TM center on the $X-Y$ plane and $\vec{r}_i$ is that from the TM center to the application point of $\vec{f}_i$. Exploiting the properties of the triple product, and observing that $\vec{b} \times \hat{z} = b\hat{x}$, where $b = |\vec{b}|$ is the "pendulum arm":

$$N_Z = b \sum_i \vec{f}_i \cdot \hat{x} + \sum_i \left(\vec{r}_i \times \vec{f}_i \right) \cdot \hat{z} = bF_X + N_{Z,TM} \tag{3.9b}$$

Here, F_X is the net force acting on the TM along the X axis, and $N_{Z,TM}$ is the Z component of the torque calculated with respect to the TM center (that would make a really free TM only rotate, thus not affecting the X DOF).

The above expression shows that the proposed pendulum configuration, besides being sensitive to forces acting on the TM along the X direction, detects also pure torques acting on the TM, due to both X and Z components of the forces acting on the TM. We however observe that forces F_X contributing the first term in Equation 3.9b have an effective armlength equal to b, while the components that enter in the second term contribute with an effective arm less than $L/2$ (with L the TM size), and they are thus suppressed by a factor $\frac{2b}{L}$ or more, meaning about $1/5$ for the inertial member geometry proposed in this work (see Section 5.1).

When approximating the force along X by simply dividing N_Z by b, the error we make ignoring the presence of the second term in Equation 3.9b depends on hypothesis on forces distribution and characteristics.

For homogeneously distributed uncorrelated noisy forces, this result in an over-estimate of order several percent, as in summing up uncorrelated terms their relative weight due to different arms enters quadratically. If we remove the hypothesis of homogeneous distribution, in the worst (and highly improbable) case of forces acting only on the inner TM edges and along the X axis, this error can lead to an under-estimate of the X force noise of order 20%: this should be compared to the case of the 1-TM facility, where an inhomogeneous, but much more probable distribution of force acting close to the TM faces centers could potentially lead to complete insensitivity, that is a 100% underestimate.

More delicate is the problem of net coherent forces, as in this case, like for every torsion pendulum, it is always possible to find combinations of forces with a net sum different from 0 but a zero torque with respect to the fiber, or vice versa. While this possibility should be kept in mind and evaluated case by case, we observe that, contrary to the case of the single mass facility, the force distributions that would lead to complete insensitivity of the four TM facility should have a symmetry completely different from that of the GRS, and are thus less likely to arise.

In particular, when investigating coherent response to induced parameters modulation, we could in principle be worried about some kind of suppression effect, if a torque arises contrasting the one induced by the force acting along X, thus leading to an underestimate of the force itself and any related parameter (that, in search for upper limits, is the most worrying risk). However it should be considered that controlling source distributions is much simpler in this configuration than in the case of the single mass facility: going back to the example of thermal gradient related effects given in Section 3.3, to produce a net force without inducing also a torque we should uniformly (to be precise, symmetrically) heat the $X+$ and $X-$ face of the GRS. This is obviously much simpler to achieve than creating the thermal pattern required for the 1-TM facility measurements (see Figure 3.4). Moreover, the larger scale of variation of the induced thermal pattern makes it easier to calculate the effective temperature of internal surfaces, thus making the parameters derivation more accurate.

Because suspending the TM off-center with respect to the fiber will require some kind of balancing to bring the overall center of mass below the suspension point when the inertial member lays horizontally, at least one extra TM is required on the opposite side of the one used for testing. In addition, trying to maximize the sensitivity to forces with respect to torques acting on the TM, a long arm b is desirable, thus increasing the overall size of the inertial member: however, this increases also the pendulum sensitivity to environmental gravitational disturbances [24], and depending of the value of the latter it could require an enhancement of the symmetry of the structure by adding additional TMs (as reported in 5.3.2, given the pendulum sensitivity and the laboratory gravitational noise level, it was indeed measured to be necessary).

Trying to find a compromise with total inertial member weight, that limits our ability to use thin, low thermal noise fibers, we finally arrived at the proposed design for the inertial member: a symmetrical 4-mass configuration with four identical TMs installed at the ends of the arms of a cross-shaped central support, suspended by its center. This configuration is not only obviously balanced from a center of mass point of view, but in principle allows also to exactly cancel the gravitational quadrupole moment of the pendulum, thus strongly reducing its gravitational interaction with the surroundings.

In Figure 3.7 we show a conceptual design of the pendulum, along with some conventions about the axes and angles orientation that will be used from now on.

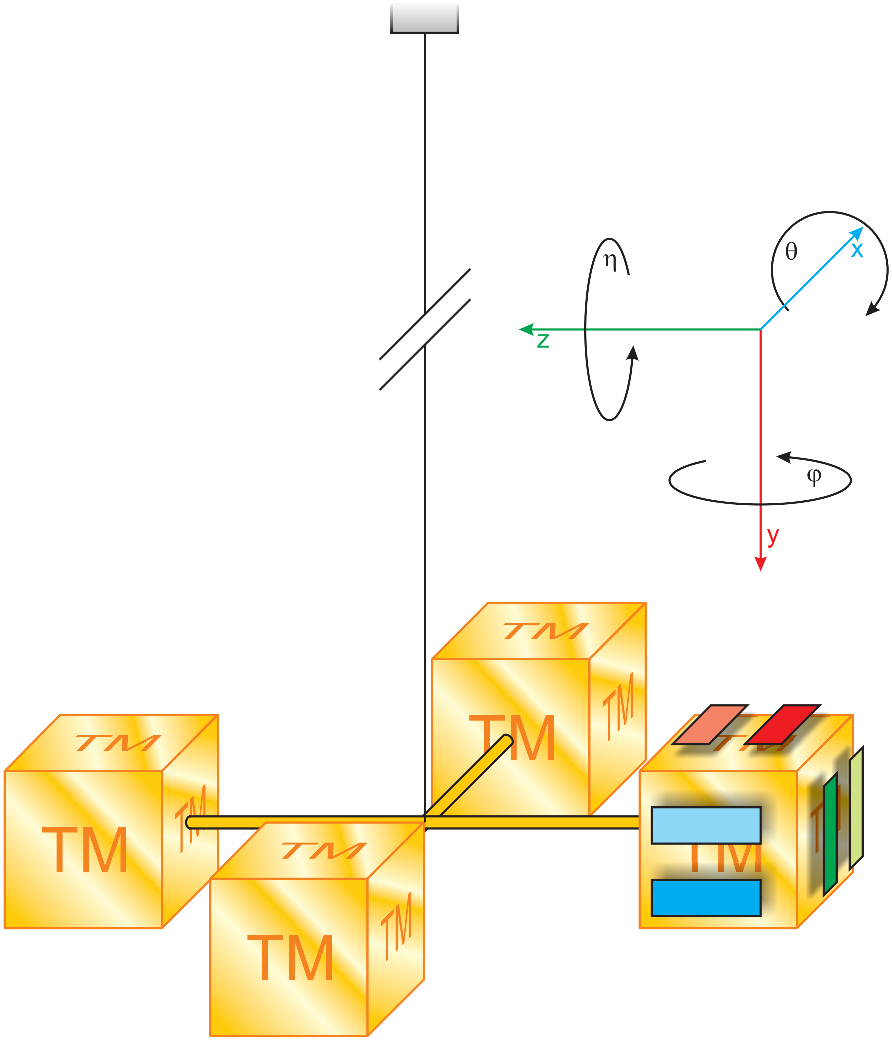

Figure 3.7 – A simple scheme of the conceptual design of the 4-TM torsion pendulum. GRS electrode layout is shown as a reference, along with conventions about DOFs labels (please note that angle direction are not conventional, as they have been chosen to have easy relation with the relevant translational GRS DOFs: in particular a positive ϕ inertial member rotation around the fiber implies a positive TM translation inside the GRS, and the same for positive pendulum tilt in η).

Chapter 4

4-TM facility

The single TM facility described in the previous chapter has been and is still very effective in testing GRS performances. Nevertheless, a more representative test capable of both getting rid of the uncertainty coming from torque-to-force conversion models and excluding threatening sources of force noise not detected by the torque-only sensitive 1-TM pendulum configuration would be highly desirable before launch of the space missions.

In this chapter we will present the torsion pendulum facility built to overcome these limitations [10]: being directly sensitive to forces acting on the TM, it allows both a more reliable, model independent estimation of the contribution of the different sources to the total force noise and an evaluation of other possible sources of force noise that do not translate into torques.

The current facility has been implemented in two steps: while the conceptual design and the most of the experimental apparatus are the same, two different inertial member and capacitive sensors setups have been used. The first was a simplified version aimed at debugging the new facility and probing its performance capabilities; the second one is the real testing setup with high precision LISA TM mock-ups and GRS integration.

While the detailed description of the two different setup will be given in the following two chapters, here we present common torsion pendulum design, characteristics and expected performances, as long as the overall structure of the whole experimental facility with auxiliary and diagnostic systems.

4.1 Torsion pendulum implementation

The core part of the whole experimental facility is obviously the torsion pendulum itself, that you can think being formed by a torsion fiber, an inertial member and one or more readout sensors.

Even if we first implemented the facility using simplified inertial member and capacitive sensors (see Chapter 5) for easier and safer debugging, we designed them to share the same basic features and physical characteristics, and so similar expected performance, of the GRS testing apparatus. We will present here common features of the two torsion pendulum assemblies and expected performance coming from common relevant characteristics.

Based on the needs and preliminary design of the GRS testing facility, both inertial members have been designed to have a weight of about 460 g, an arm of about 10 cm and a moment of inertia of about $3 \cdot 10^{-3}$ Kg m^2 (among the relevant parameters, this is actually the most different between the two inertial members, from $(2.4 \pm 0.1) \cdot 10^{-3}$ Kg m^2 for the preliminary version to $(3.7 \pm 0.05) \cdot 10^{-3}$ Kg m^2 for the final one). According to the experience gained on the 1-TM pendulum, we use for suspension a bare tungsten torsion fiber about 1 m long[1] 50 μm diameter: this is the smallest diameter that yields a theoretical breakdown limit high enough to suspend the near half-kilogram overall weight of the inertial member; several fibers were tested before suspending the pendulum, confirming that those with diameter smaller than 50 μm, that would have been desirable to enhance pendulum performances lowering the intrinsic thermal noise, have too low a load limit. Because this fiber has about the same length but twice the radius of the fiber used in the single TM facility, whose measured torsional stiffness constant Γ was $5.5 \cdot 10^{-9}$ Nm/rad, we estimated its Γ at about $8.7 \cdot 10^{-8}$ Nm/rad (see Equation 3.8 about the relation between fiber radius and torsional stiffness). The measured value based on GRS testing facility resonant frequency and estimated moment of inertia assuming that no other spring contributions (e.g. electrostatic) were present was $(7.6 \pm 0.1) \cdot 10^{-8}$ Nm/rad. In Figure 4.2 we show theoretical thermal noise of such a fiber computed according to Equation 3.6;

Given these values for fiber Γ and inertial member moments of inertia, the resonant frequencies expected for the preliminary and final versions were respectively about 0.85 and 0.7 mHz.

A two DOF commercial autocollimator is used on both implementations as an independent optical readout for calibration purposes and no-bias measurements (i.e. with capacitive sensing injection voltage set to 0, that obviously makes this readout unavailable). Autocollimator resolution is 50 nrad on both axes, while measured noise spectra is of order of 20 nrad/Hz$^{1/2}$ in the measurement bandwidth (see Fig. 4.1).

Capacitive readout in the preliminary and final implementation relies on different sensors and electronics, thus different performance levels are expected. In Figure 4.2 theoretical angular and force noise performances for final inertial member and sensors setup described in Chapter 6 are shown using both autocollimator and capacitive readout.

[1] Precisely measuring the length of the fiber once installed and loaded is not a simple task, and we did not spend much effort on that because it is of little interest

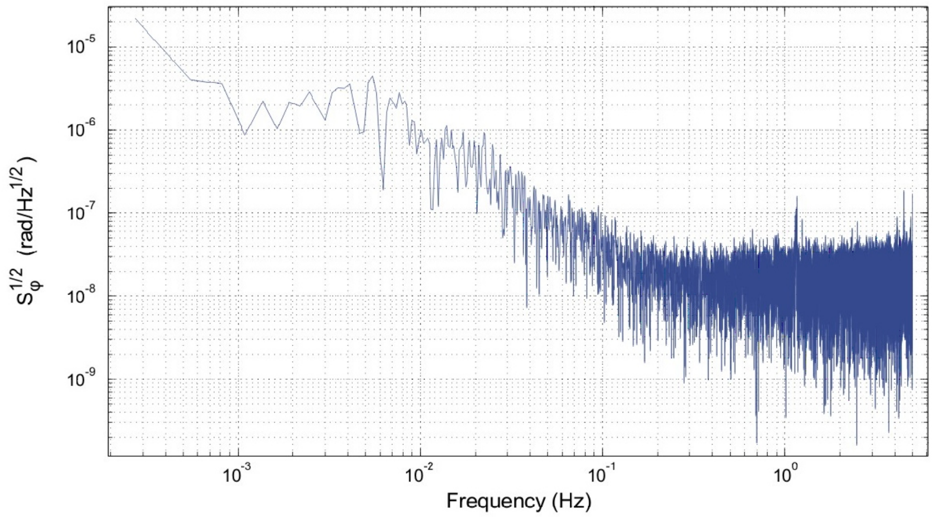

Figure 4.1 – an autocollimator readout noise power spectrum. This spectrum has been obtained fixing a mirror directly on the autocollimator front lens: at relatively high frequency the nearly white electronic noise is visible at a level of about $2\cdot10^{10-8}$ rad/Hz$^{1/2}$; at low frequencies the noise level increases, probably due to thermal and mechanical effects that induce a relative rotation between the mirror and the autocollimator.

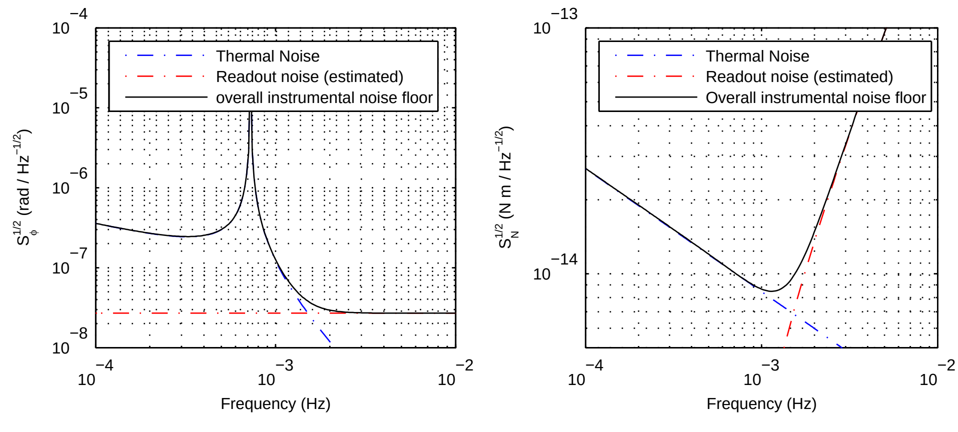

Figure 4.2 – Instrumental theoretical angular (a) and torque (b) noise performances computed for the actual GRS testing facility setup. The instrumental noise limit is given by the sum of the torsion pendulum mechanical noise, dominating a low frequencies, and the white readout noise dominating at high frequencies over the real mechanical motion of the pendulum, which is highly suppressed by its transfer function.

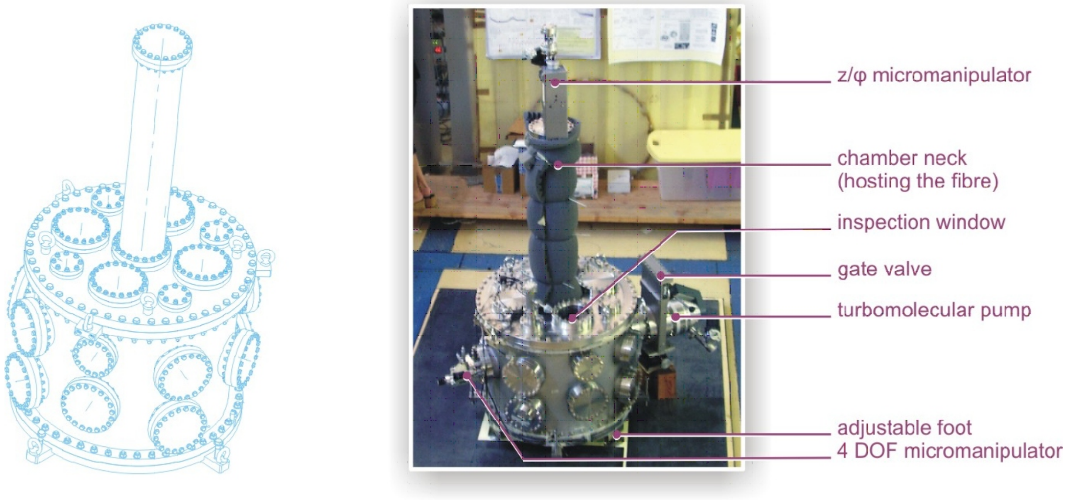

(a) (b)

Figure 4.3 – design of the vacuum vessel (a) and picture of it in an advanced integration stage (b); the chamber neck is surrounded by thermal insulating foam; the autocollimator is installed on a CF160 flange on the opposite side of the chamber and is not visible here

4.2 Auxiliary systems

The pendulum described so far, except the readout electronics and the autocollimator, is installed inside a vacuum chamber that sits on a platform partially isolated from the remaining part of the floor, reducing vibrations and tilting of the apparatus due to human activity in the laboratory.

4.2.1 Vacuum system

The pendulum is hosted in a 300 l vacuum vessel made up two parts: a cylindrical main chamber about 80 cm in diameter and 60 cm high, and a 20 cm diameter, 90 cm high neck on top of it. The vessel has 31 CF40, CF100 and CF160 flanges, as well as completely removable top and bottom lid of the main chamber itself, to allow flexible installation of different devices and easy installation, inspection and maintenance operations of the internal hardware; in addition, two glass windows have been installed and are used for inside inspection during operation (see Fig. 4.3).

The vacuum is provided by means of a 400 l/m turbo-molecular pump linked to the main chamber through a gate valve. The exhaust is connected to a secondary pumping system, made up of a turbo-molecular and a membrane pumps in chain, that lie outside the experiment platform. Tubes connecting primary and secondary pumping system are tightened and weighted down so to damp vibrations. Internal pressure is measured using a Varian UHV24 ionization gauge that operates from $1.33 \cdot 10^{-1}$ down to $2.7 \cdot 10^{-9}$ Pa.

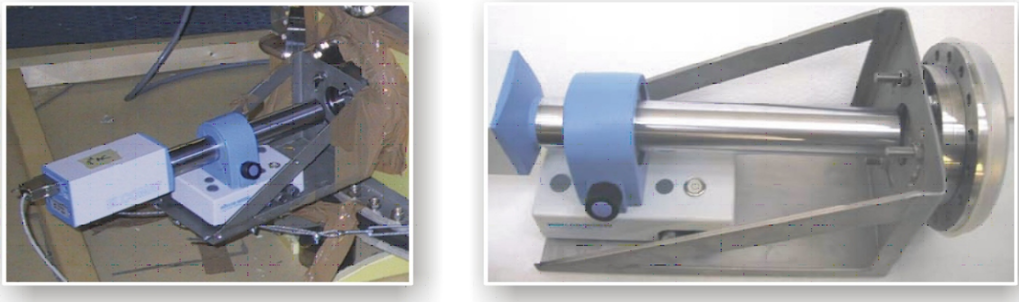

(a) (b)

Figure 4.4 – a picture of the autocollimator installed on the vacuum vessel (a) and a detail of the custom support that hold it (b): note the optical window stainless steel frame visible between the CF160 flange and the autocollimator support.

The lowest pressure reached so far is $8 \cdot 10^{-6}$ Pa, while typical values during experiment normal operation is about $2 \cdot 10^{-5}$ Pa. Though some improvements are still possible, this pressure is near LISA requirements and we remark that it is low enough to perform significant measurement without being limited by gas damping induced noise (see [18]).

The autocollimator is rigidly installed on the outside of the vacuum chamber by means of a custom support fixed to a CF160 flange; a third glass window allow the autocollimator beam to enter inside the chamber and shine on a mirror installed on the inertial member (see Fig. 4.4).

4.2.2 Suspension system

The main torsion fiber hangs from a magnetic damper that consist of an aluminum disk suspended by means of a 7 cm long, 250 μm diameter tungsten fiber (nearly 104 times more stiff than the main fiber and thus basically rigid) between two ring-shaped magnets. Any motion of the disk due to pendulum tilting will cause eddy currents to flow inside the disk itself, dissipating energy by joule effect and thus damping oscillations with a measured time constant of about 200 seconds.

The magnetic damper is then connected via a stainless steel shaft and a glass electrical insulator stage to a two DOFs micro-manipulator installed at the top of the vacuum vessel neck, allowing for precise positioning in the vertical and rotational DOF (y and ϕ respectively from here on). In addition, a mechanical Teflon damper acts on the shaft to suppress major vibrations (see Fig. 4.5).

4.2.3 Micro-positioning

The vacuum chamber lies on three μm resolution adjustable feet that provide the ability to compensate chamber tilt with μrad accuracy and mrad range in any direction . On the GRS testing facility, a number of PC-controlled micro-step translational and rotational motors have been employed to allow for precise alignment and

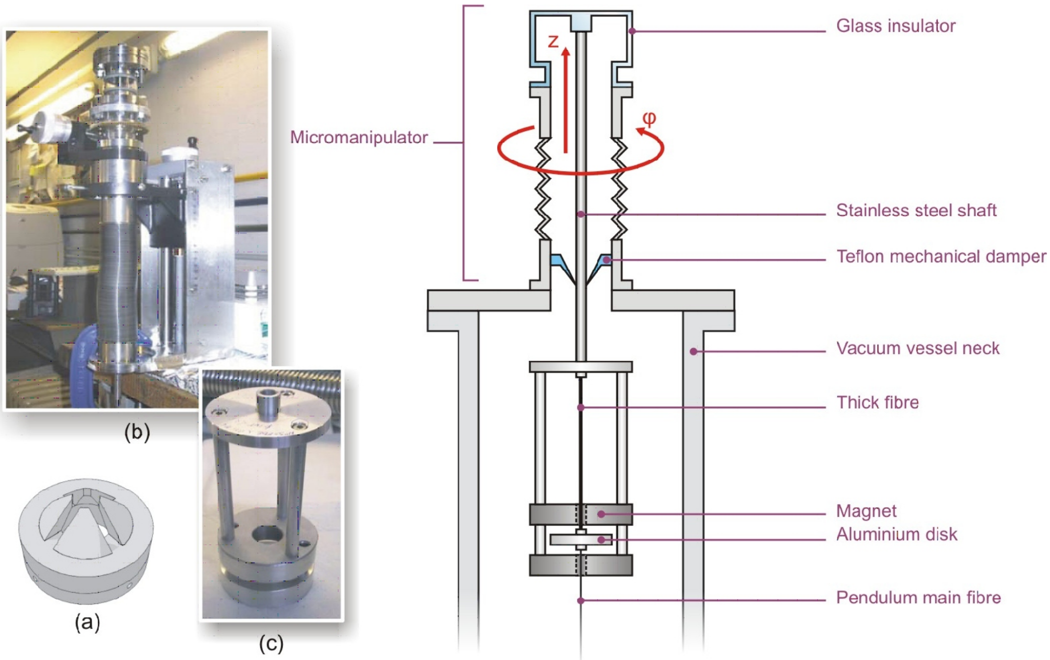

Figure 4.5 – schematic representation of the pendulum suspension system, together with a drawing of the mechanical Teflon damper (a) and pictures of the two DOFs micro-manipulator (b) and the magnetic damper frame (c) before assembling.

automated measurements: they will be described in more detail in Chapter 6

4.2.4 Charge Management Control

The cosmic ray contribution to the charging of electrically floating TM inside the sensors is negligible on ground. However, charging can still happen due to a variety of effect, the major ones being the follows:

- If the TM accidentally hits any surface, the contact potential induce a transfer of charges between them: when the surfaces are detached, the charge remains there thus resulting in a charged TM.

- An ion gauge pressure sensor needs sometime to be switched on to check vacuum level. Although TM are hidden by sensors EH, these are not completely closed and some ion produced by the pressure monitor can reach the TM and deposit their charge there.

Moreover, the representative TM environment realized within the torsion pendulum facilities offers an useful test ground for any subsystem directly related to the TM or the sensor properties. Thus, on the GRS testing facility[2], optical fibers and interfaces have been arrange for the Charge Management System developed at Imperial

[2]The Charge Management System was not available on the preliminary facility, and rough discharging of TMs was done letting them purposely touching the EH. However, residual charging due to contact potential was likely to arise.

College London[31, 32]: it is based on electrons extraction from both TM and EH by means photoelectric effect using UV light guided by suitable optical fiber to shine inside the sensor; extracted electrons are then driven by appropriate electric field to control the equilibrium potential of the TM. At present, the Engineering Model version of this system is shared between the two facilities to allow in-operation charge management[3], while a characterization and testing campaign in ongoing on the single mass pendulum [33].

4.2.5 Thermal stabilization

Variations in the mean temperature and temperature gradients can introduce noise in the experimental data through a variety of different effects that act on the pendulum's real motion as well as on the readout system calibration parameters; these effects include modification of the fiber equilibrium angle, thermal gradient related effects in the GRS (as listed in 2.2), deformations in the vacuum chamber and other structures, readout resonant frequency drifts, amplifiers gain fluctuations and so on... Vacuum chamber and first stage front end electronics are thus enclosed in a thermally insulated and stabilized room to minimize both mechanical and readout noises due to thermal fluctuations. The thermal room is made up of a modular wood frame that holds in place insulator foam walls, floor and easy removable ceiling (that is needed to maneuver the heavy vacuum vessel using a crane installed in the lab); it has two doors to access the interior and removable lateral panels to provide in/out interface for cables and tubes (see Fig. 4.6).

An heating/cooling unit controls the temperature of a water bath that exchanges heat with the interior of the thermal room via a radiator and a system of forced air. While in the preliminary facility the water temperature was set to a constant value, thus ignoring other external temperature inputs, in the GRS testing facility it is controlled by the unit via a self-calibrated PID control loop closed on a PT100 thermometer that reads the vacuum chamber neck temperature[4], insulated by an additional jacket of insulating material.

4.2.6 Diagnostics

There are three types of diagnostic systems currently installed in the facility: thermal, magnetic and low frequency tilt.

The thermal diagnostic system is composed of an array of PT100 or 4-wires thermometers, read in sequence by a multiplexing digital multimeter with controllable integration time and sampling rate. At present, we use an integration time of about 0.1 s (that according to the manual and our measurement assure the lowest

[3] Once the appropriate external optical interfaces and internal optical fibers have been arranged on the vacuum chambers, the system can indeed by easily moved between the two facility

[4] We chose the vacuum vessel neck because it is in radiative thermal equilibrium with the fiber, that we expect to be the part of the system most reactive to temperature fluctuations.

(a) (b)

Figure 4.6 – a picture of the thermal room during the assembling phase (a) and an aerial view of the apparatus inside the fully assembled (ceiling removed) room (b): note the heat exchanger with water tubes and air fun power cables in the lower right part of the picture.

noise due to optimal compensation of multimeter electronics internal drifts) and a sampling rate of 20 s, the fastest possible considering the multiplexing over 16 thermometers and the switching time between them. Resulting readout noise it about $8e-3$ K/Hz$^{1/2}$. Number and disposition of thermometers is different among the two facility implementations:

Preliminary facility

GRS testing facility: of the 16 PT 100 thermometer installed in the facility, four are distributed outside the vacuum chamber: two of them are on the upper an lower part of the chamber neck, the other two on the chamber feet that are under the autocollimator mounting and the STC. The remaining thermometers are installed on the STC $X+$ and $X-$ face (one each) and on the GRS (10 in total, over different faces).

In addition two three-axis magnetometers (10^{-8} T/Hz$^{1/2}$ nominal sensitivity[5] in the measurement bandwidth) can be placed anywhere around the vacuum vessel to monitor both magnetic fields and their gradients.

Finally a two axis tiltmeter (with 100 nrad/Hz$^{1/2}$ sensitivity around 1 mHz) is fixed on the bottom of the vacuum chamber taking advantage of the vacuum thermal stability, and monitors the low frequency tilt motion of the apparatus. Note that the pendulum itself is a much more sensitive tiltmeter, being able, depending on the sensors and electronics employed, to detect TM translation of order of few nm and

[5] Actual sensitivity is a factor ten worse, limited by acquisition system problems currently being debugged

Signal	Reading device	Type	Acq. Device	Samp. f	# ch
Capac. sensors	readout elect.	Analog	ADC board	10 Hz	2
Actuation	readout elect.	Analog	DAC board	10 Hz	2
Autocollimator		Digital	Serial Port	50 Hz	1 (2)
Thermometers	dedicated elect.	Analog	ADC board	10 Hz	3
Thermometers	digital multim.	Digital	Serial Port	0.1 Hz	1 (8)
Magnetometers	dedicated elect.	Analog	ADC board	10 Hz	6
Tiltmeter	dedicated electr.	Analog	ADC board	10 Hz	2
Pressure	ion gauge contr.	Digital	ADC board	0.1 Hz	1
Total					15 (23)

Table 4.1 – List of preliminary facility experimental input and output signals, along with their acquisition (or generating) device and sampling rate. In addition, we have digital configuration and control signals to manage (ETHZ readout electronics, UV lamps electronics…). The number in parenthesis in the last column represent effective signals, even if acquired via a single input. Sampling rate for autocollimator is hardware: routines query the COM port every 0.1 seconds.

thus, given the about 1 m long fiber, tilting of order of few nrad; anyway it is always desirable to have a redundant independent readout for debugging purposes.

4.2.7 Data acquisition system

All the data gathered during experiment operations are collected on a PC-based acquisition system via custom integrated LabView routines. Different data streams are read directly using NI ADC boards sampling at 10 Hz (such as readout electronics outputs or magnetometer signals), or using digital I/O ports to query readout instruments (temperature or autocollimator data) up to 1 Hz. The same system provides also pendulum actuation and instruments parameter control via DAC boards or I/O digital ports.

Tables 4.1 and 4.2 lists the various experimental signals, respectively, on the preliminary and GRS testing facility, along with they acquisition device and rate.

4.2.8 Clean environment

The facility site is located in a class 10000 clean room that allows for clean assembling and installation of the apparatus. With the experiment in operation, a large part of the clean room will be occupied by the thermal chamber and will not guarantee a clean environment (that will no more be necessary since all the sensitive parts of the apparatus will be enclosed in the vacuum vessel); a small part, however, will still be available and working to provide an uncontaminated storage and assembly location.

This would be requested for future testing campaigns on a flight model replica and maybe the flight model itself: in that case we should handle the hardware under stringent cleanliness requirements not to spoil the representativity of the investigation (or even not to compromise the performances, in case we test the actual Flight

Signal	Reading device	Type	Acq. Device	Samp. f	# ch
GRS	ETHZ elect.	Analog	ADC board	10 Hz	6
GRS AC act.	ETHZ elect.	Analog	DAC board	10 Hz	6
GRS DC act.	ETHZ elect.	Analog	DAC board	10 Hz	12
STC	ETHZ elect.	Analog	ADC board	10 Hz	2
GRS DC act.	ETHZ elect.	Analog	DAC board	10 Hz	4
Autocollimator		Digital	Serial Port	50 Hz	1 (2)
ORO readout	dedicated elect.	Analog	ADC board	10 Hz	6
Thermometers	dedicated elect.	Analog	ADC board	10 Hz	1
Thermometers	digital multim.	Digital	Serial Port	0.05 Hz	1 (16)
Magnetometers	dedicated elect.	Analog	ADC board	10 Hz	6
Tiltmeter	dedicated elect.	Analog	ADC board	10 Hz	2
Pressure	dedicated contr.	Digital	ADC board	0.1 Hz	1
Total					48 (64)

Table 4.2 – List of GRS testing facility experimental input and output signals, along with their acquisition (or generating) device and sampling rate. In addition, we have digital configuration and control signals to manage (ETHZ readout electronics, UV lamps electronics...). The number in parenthesis in the last column represent effective signals, even if acquired via a single input. Sampling rate for autocollimator is hardware: routines query the COM port every 0.1 seconds.

Model).

Chapter 5

Preliminary 4-TM facility

Given the potential complexity of the proposed facility and the number of new problems related to the higher number of degrees of freedom and sensors involved, we decided to build a preliminary version based on the same project but employing simpler and cheaper inertial member and capacitive sensors. This facility was a valuable test-bed for subsystem setup and performance testing, allowing us to refine the design and understand the behavior of the torsion pendulum as an instrument before being involved in actual GRS characterization. While most of the features are those already reported in Chapter 4, we will describe here the ones peculiar to this implementation before presenting the results obtained in terms of noise performances and gravitational background estimation.

5.1 Inertial member

While the torsion fiber used in the preliminary facility has the same characteristics as the one employed in GRS testing facility, inertial member and readout sensors have been redesigned for easy and fast machining and assembly, as well as for reduced cost. Nevertheless, basic features (overall shape, weight, moment of inertia, etc...) have been maintained to preserve representativity of the final experimental apparatus.

The preliminary inertial member design has been based on ideas presented in Section 3.4, simplified where possible with respect to the high precision final design with flight-representative hollow TMs that will be described in the next chapter. It is composed of four identical solid cubic TMs with 30 mm side weighting about 66.5 g. Each TM has an hole to allow its installation on one of the four 112 mm long arms of a cross-shaped compound central support. TM are kept centered around the support arms via Teflon bushings, and tightened in the chosen position by means of nuts that fix on the threaded arms. In this way TM center of mass distance from the center of the pendulum can be set at any point between about 35 and 90 mm.

Two opposite TMs are used for capacitive sensing and actuation and are insulated by means of Teflon bushings, while the other two are short-circuited to the

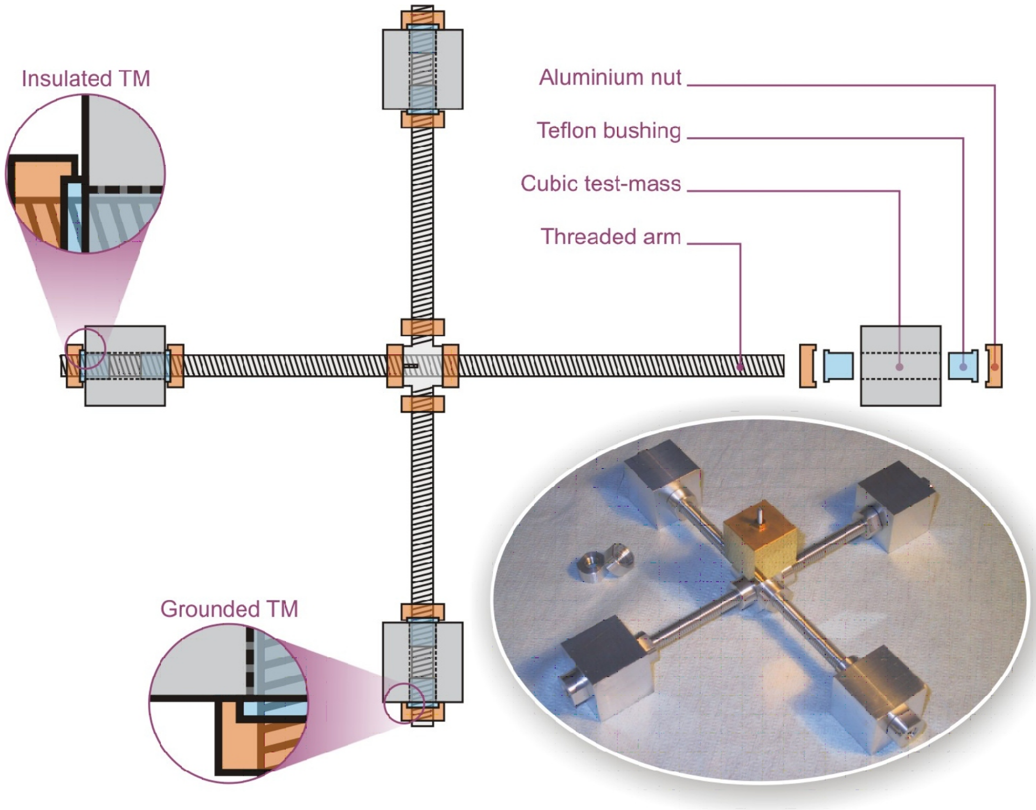

Figure 5.1 – Schematic top-view representation and a picture of the preliminary pendulum assembled.

central body by suitably shaped nuts that override the insulators (see Figure 5.1). This allows electrostatic homogeneity and avoids unwanted charging and consequent electrostatic interaction with the surroundings. For the same reason, Teflon insulating bushings are almost totally hidden in a recess of the aluminum nuts.

The whole structure (except the glass mirror) is made of aluminum, to keep the overall weight low (the assembled structure weight is 464 gr), enabling us to use a thinner torsion fiber that allow for higher sensitivity (see Section 3.1, and in particular Equation 3.6. Using aluminum also helps in providing magnetic cleanliness (i.e. low magnetic susceptibility and permanent magnetic moment). The use of aluminum nuts instead of brass ones, more common and more easily available, has indeed been decided after a first experimental run, performed using brass nuts for assembling, in which a high coupling of magnetic noise with pendulum motion has been observed. Subsequent measurements on each single element composing the pendulum have shown that the brass nuts where responsible for a permanent magnetic moment, orders of magnitude higher than those observed with other on other torsion pendulums with aluminum inertial members (see Section 5.3.1).

For the whole measurement campaign, with the exception of the runs aimed to estimate gravitational gradient noise (see Section 5.3.2), the pendulum has been assembled with all the TMs center of mass at a distance of 89.5 mm from the suspension point. Each element has been weighed and measured and the whole structure has been assembled accounting for machining imperfection and slight differences in weight and dimensions, so to minimize residual quadrupole moment and center of mass offset with respect to the ideal geometry. In this configuration, supposing the pendulum lying in an horizontal plane once suspended, the fiber perfectly centered with respect to the cross intersection and accounting only for tolerances on geometry and weight of the various elements, we calculated a moment of inertia $I = (2.4 \pm 0.1) \cdot 10^{-3}$ Kg m^2 and estimated a residual quadrupole moment of $0 \pm 6 \cdot 10^{-6}$ Kg m^2.

5.2 Capacitive readout

5.2.1 Sensors

Capacitive sensing is provided by means of two sensors based on the same readout concept of the GRS but simplified so to read a single DOF each. Because at this level we are interested in pendulum performances instead of sensor characterization, we also choose larger gaps to minimize their contributions to the pendulum noise. The two capacitive sensors are installed on opposite TMs and measure translations in the X direction. The pendulum rotational motion along Φ and swing motion orthogonal to the arm connecting the measured TM η[1] can be obtained summing and subtracting the two signals respectively (see Figure 5.2), with appropriate calibration parameters that account for different sensitivities. Note that the same DOFs are read by the autocollimator, and can be calibrated against it (see Appendix B for details).

Each sensor is composed of an *EH* (Electrode Housing) in the form of a square shaped ring that surrounds the TM: one 28x20 mm rectangular injection electrode is installed on each of the top and bottom faces, while a single 28x26 mm rectangular sensing one is located on each of the two X faces. Injection electrodes are separated from the mass by 5 mm wide gaps, while injection electrodes by 8 mm gaps. As previously stated, such large gaps have been chosen to suppress as much as possible disturbances originating in the sensors, in particular surface-related ones (whose magnitude is expected to decrease as some power of the distance), since the structures are not gold coated and the whole production process is not controlled for cleanliness and high precision finishing.

Each sensor has been manually aligned and fixed to a base aluminum plate by means of four Teflon cylindrical legs that provide both electrical and thermal insulation. Three aluminum legs are used to rise the base plate at a suitable height above the vacuum vessel bottom.

Shielding copper caps short circuited to ground have been installed on the open

[1]for a reference about facility DOFs labels see Section 3.4 and Figure 3.7

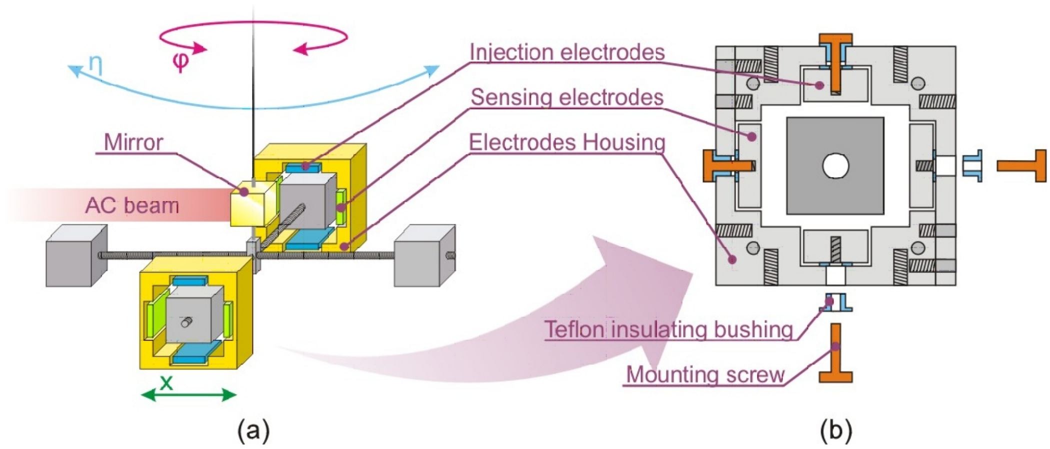

Figure 5.2 – Schematic view of the preliminary pendulum "in operation" assembly (a) with main parts and DOFs names indicated (shields are not shown for clarity), and a detailed front section of one of the capacitive sensors (b).

faces of the two sensors, so to reduce cross-talks (i.e. unwanted leakages of signal) between injection and sensing electrodes, even between to opposite sensors. Grounded copper shields around the pendulum structure (see Fig. 5.3) have also been added.

These shields are intended to screen the pendulum from all the dielectric parts present in the vacuum vessel (Teflon supports, cable shields, etc...) which could accumulate charge and interact with it. Shielding has turned out to be necessary after the first experimental runs in which the pendulum was unstable due to a negative overall spring constant (see Section 5.3.1).

5.2.2 Electronics

The readout and actuation circuitry is composed of purpose-built electronic boards (that directly connect to pairs of electrodes from the resonant capacitive bridges that read the TM position) attached in chain with commercial lock-ins and oscillators. An oscillator provides the 100 kHz injection voltage that drive the TM potential via the injection electrodes, while induced signals on the readout electrodes are compared by means of an inductive transformer, processed by a digital lock-in amplifier and sampled at 10 Hz via ADC boards by custom LabView routines running on a dedicated PC. Actuation voltages generated by DAC boards are amplified by an home made amplifier and can be sent to the sensing electrodes in DC or AC mode driven by an independent 205 Hz oscillator. (see Fig. 5.4).

Despite the fact that in the preliminary configuration we only have to monitor two channels (we measure one translation axis on each of the two TM), and thus we need only two resonant bridges, a more generic six-channel electronics box has been assembled for later, more generic usage (see Figure 5.5).

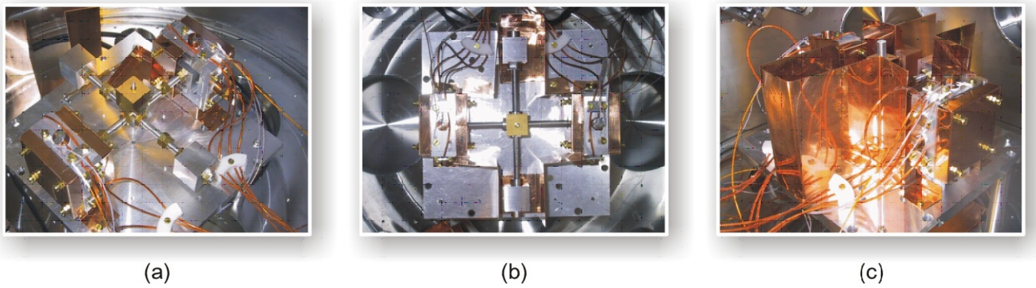

Figure 5.3 – Picture of the copper shielding caps during their installation on the two sensors (a) and top (b) and lateral (c) picture of the apparatus in the vacuum chamber with all the shields mounted. Note that picture (a) has been taken in a previous integration stage: brass nuts had not yet been substituted by aluminum ones; moreover, compensation nuts are visible in the middle of the arms: they have then been removed because accurately positioning the TMs has shown to be enough to balance the pendulum and compensate the quadrupole moment within our discrimination ability. Since one shield is partially removed, in (a) you can also see the sensors structure with two injection and two sensing electrodes.

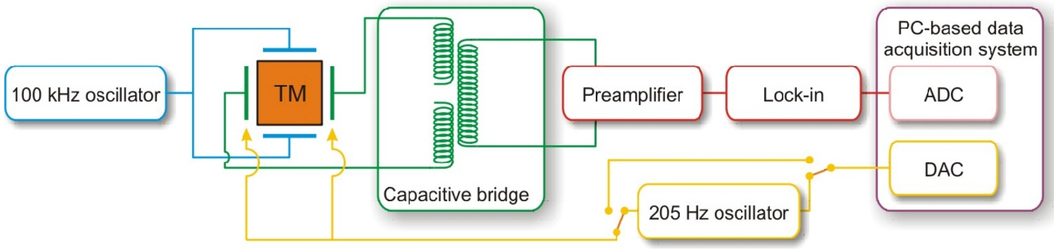

Figure 5.4 – Scheme of the readout and actuation chain.

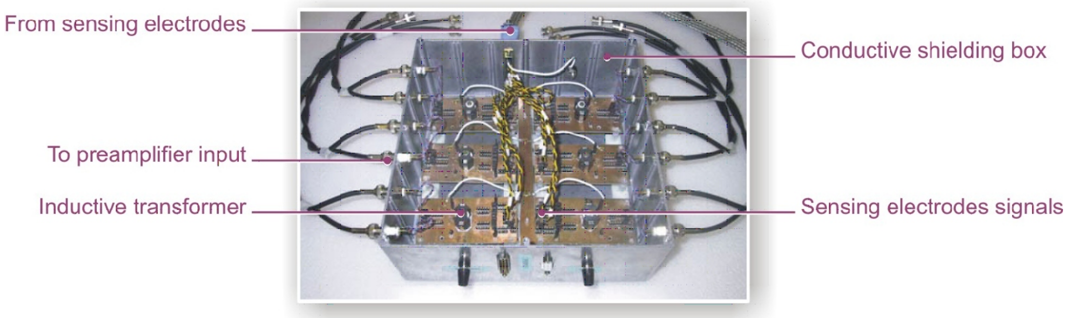

Figure 5.5 – a picture of the box that enclose the purpose-built section of the readout and actuation electronics.

The measured voltage noise of each bridge is nearly a factor 1.2 above the theoretical value of about $7.5 \cdot 10^{-8}$ V/Hz$^{1/2}$ set by the intrinsic thermal noise. Considering a measured dV/dx of order 55 V/m (where V is the voltage measured at the preamplifier) with typical injection voltage of 7 V_{RMS}, this yields a theoretical readout translational sensitivity of about 2 nm/Hz$^{1/2}$, that converts in an angular sensitivity of about 20 nrad/Hz$^{1/2}$ given an 89.5 mm long arm, reduced by an additional factor $\sqrt{2}$ accounting for the combination of two independent signals.

5.3 Experimental results

The main goals of the preliminary facility measurement campaign were to gain confidence with four-mass pendulum dynamics, readout and control, as well as investigating possible spurious noise sources not related to the GRS and to get as close as possible to the theoretical instrumental thermal noise limit set by the fiber characteristics.

5.3.1 Ultimate noise performances

As stated in Section 3.2, one of the tasks of the GRS testing facility is that of placing upper limits on the force noise coming from GRS-TM interactions. The ideal way of testing it would be installing and uninstalling GRS while keeping the rest of the facility stable enough to trust that the level of noise has not changed due to other causes. Unfortunately, this is not possible and the only comparison we can make is that between the observed noise, with the GRS installed, and the theoretical thermal noise limit of the pendulum, thus conservatively attributing any unidentified source of noise to the GRS itself. In this framework, testing the overall noise performance capability of the proposed setup in a GRS-free configuration, even if not directly employable as an estimate of the noise background for the actual GRS testing facility, is of great importance: it would be both a clue to the attainability of the limiting performance of the pendulum as an instrument and a valuable help in identifying and removing unforeseen sources of noise not related to the GRS, that could be erroneously attributed to it.

During several runs a variety of spurious effects and noise sources have been detected and removed (or reduced) in order to improve pendulum noise performances. While some of them are closely related to this preliminary prototype and not necessarily representative of what can be experienced with the GRS testing apparatus, most of them are more general and their knowledge helped to approach the thermal noise limit more quickly and reliably with the GRS testing facility. A brief list of the main steps performed to make this preliminary facility approach the thermal noise limit follows:

- The first time we suspended the pendulum it turned out to be unstable unless actuated with an "artificial" positive stiffness constant about the same order of magnitude as the fiber's one. We were not able to pin-point the exact cause, but surrounding the pendulum structure with copper grounded shields hiding all the dielectric exposed parts present in the vacuum vessel (cables, cable holders, spacers...) the negative stiffness contribution, previously estimated in about $-6 \cdot 10^{-7}$ N m/rad, was immediately removed.

- Since the very first runs (even before managing to make it stable), a strong coupling of the pendulum motion with magnetic field gradients and oscillations, that we were able to estimate using both magnetometers and single mass pendulum data, has been observed. On this basis, and supposing a very simple magnetic model (given the relatively big extension of the pendulum, we should account not only for the total magnetic moment μ_{tot}, but also for the distribution of the different contributions among the structure, that make it sensitive also to magnetic field gradients)

$$N = \overrightarrow{\mu} \times \overrightarrow{B}$$

  we estimated a μ_{tot} of about 10^{-4} A m^2. As anticipated at the end of Section 5.1, after some investigations it turned out that commercial brass nuts used to assemble the pendulum had a large residual magnetic moment. Although it was not worthwhile to perform accurate measurements, summing the estimated magnetic moments modulus of the brass nuts (ranging from about $2 \cdot 10^{-6}$ to $3 \cdot 10^{-5}$ A m^2) we obtained about10^{-4} A m^2. This is a worst-case estimation of μ_{tot}, as different contributions add randomly as vectors which are not expected to have all the same orientation; however it is compatible with the measured magnetic moment and orders of magnitude bigger than that expected for the lone aluminum structure based on experience with other pendula (typical value for the single mass pendulum were measured to be of order 10^{-7} Am^2). Moreover, contributions of aluminum elements to the total magnetic moment have turned out to be too weak to be measurable using the same technique. Substituting brass nuts with custom aluminum ones, the pendulum coupling with environmental magnetic noise was no longer observable.

- As expected, a coupling of thermal fluctuations with pendulum mechanical noise has been observed. A variety of effects have been suspected to be responsible for this: they include vacuum chamber differential thermal expansion and consequent distortions and tilting as well as fiber unwinding rate and equilibrium angle dependence on the temperature. In addition, temperature variations induce a readout noise by means of drift in capacitive bridges resonant frequency, amplifier gains, and so on. An accurate investigation of the role of different effects has not been performed, , however, including all the experiment in a thermally insulated and stabilized room helped to lower the noise floor toward the thermal noise limit. Note that in the period of operation of the preliminary pendulum we used a *passive* stabilization that set the radiator water temperature at a fixed value without monitoring the room temperature. This has been changed in the GRS testing facility, in which water temperature control loop is driven by the feedback of a PT100 thermometer installed on the vacuum chamber, thus helping to improve thermal stability and to reduce the frequency noise at the lower end of the measurement band.

- It is known that heavily loaded fibers experience an unwinding that diminishes accordingly to an exponential like law [22]. The effect is that of rotating the pendulum equilibrium angle over time, thus introducing low frequency noise and making difficult to perform long measurements due to limited dynamic range of the apparatus. Moreover, the unwinding process could introduce additional noise even at higher frequency by means of secondary mechanical effects in the fiber whose rate and amplitude are to some extent proportional to the unwinding rate. Even if unwinding rate and its derivative depend on the history of the fiber and on a lot of unknown parameters, it is clear that to make very good noise measurements we have to wait enough time to reduce the unwinding rate at a level of μrad/h or less: in our experience this means waiting one week or more since the last time the fiber has been unloaded, although slightly. Trying to speed up the process and get rid of residual unwinding and related effects, we attempted to perform a "direct baking" of the fiber, heating it by means of Joule effect. Since we had no specific apparatus for such a task, we arranged to make a current flow through the fiber by polarizing its uppermost end and tilting the pendulum to make the arms touch the grounded shields. Unfortunately this procedure causes the fiber to be unloaded in an uncontrolled and unrepeatable way, and despite obtaining one very good result lowering the unwinding rate to a nearly non measurable value (about 0.1 μrad/h) in a few hours baking, we where not able to replicate the procedure reliably. Considering both the verified potential advantage of directly baking the fiber, we developed ideas and design studies of a more sophisticated and easily controllable system, but we were not yet able to build, test and integrate them in a facility.

Evaluating the pendulum torque noise means evaluating the torque acting on it that cannot be explained by means of known sources. To do that, we perform what we call a "noise run", in which pendulum and diagnostics data are gathered after preparing the facility in the best possible conditions:

- wherever possible, the pendulum is centered with regard to the capacitive sensors to minimize displacement-proportional readout (and potentially torque) noise.

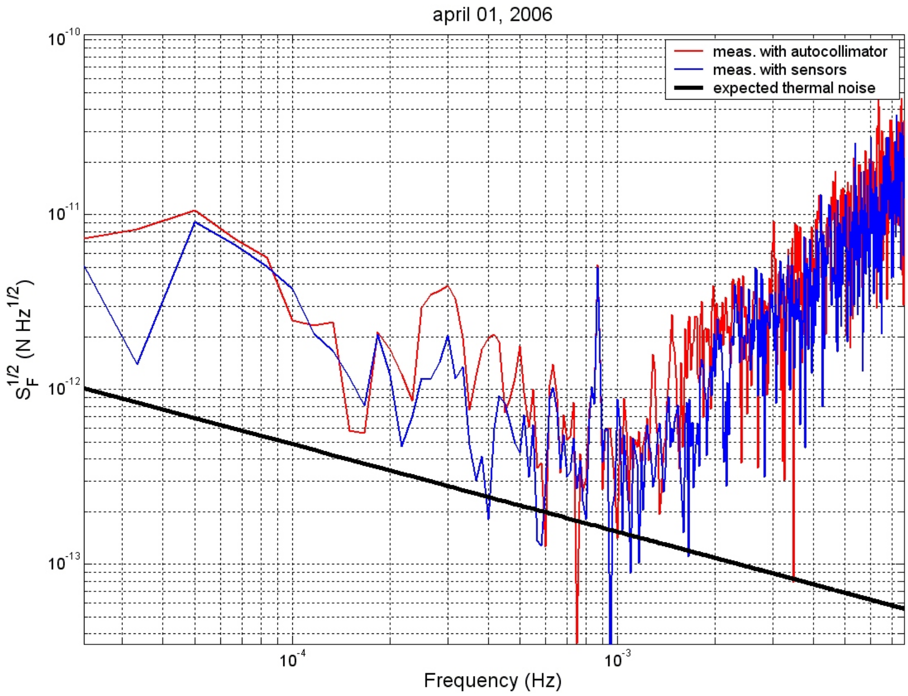

Figure 5.6 – Force noise spectra obtained by both autocollimator and capacitive sensors when the preliminary pendulum was performing at its best.

- readout chain is set-up for lowest possible dynamic range compatible with expected pendulum motion (oscillation plus drift) to improve sensitivity. This is done in practice by adjusting the amplification of the readout signal and the dynamic range of ADC boards to keep additive and digitization noise low compared to the signal itself.

- the environment is kept as quite as possible, avoiding wherever possible the production of mechanical (e.g. stepping around the experiment or moving big loads) and electromagnetic (e.g. using the crane or other electromagnetic devices) noise. For this reason we usually perform noise runs during weekends and night-times, when human activity is reduced not only in the laboratory, but in the whole university building and surroundings.

Performing all the optimizations described above we managed to get very close to the pendulum thermal noise limit compared to what we have been able to obtain with other more expensive and sophisticated apparata. The best noise run we obtained can be roughly estimated in a factor 2-3 above the thermal noise limit in the band around the pendulum resonant frequency, as shown in Figure 5.6.

5.3.2 Estimating gravitational background

Because of its extended size, one of the worrying noise source that could prevent the attainment of the thermal noise limit in the 4-mass configuration is the gravitational gradient noise, that can couple with the pendulum quadrupole and higher gravitational moments [24]. To predict the impact of gravitational noise background on the final pendulum performances is not easy, as the background itself is not constant and difficult to estimate, while the very small residual quadrupole moment of the pendulum, mostly due to machining and assembling imperfections, is hard to calculate precisely. Employing an high quadrupole moment pendulum to measure the gravitational interaction can help in estimating the gravitational background effect and give us some clue about what gravitational noise to expect on more symmetric pendula.

We therefore moved two opposite mass of the preliminary inertial member toward the suspension point, intentionally enhancing the quadrupole moment to a value of about $(9.6 \pm 0.1) \cdot 10^{-4}$ Kg m^2 (at least a factor 150 above the "compensated" one reported in Section 5.1), and performed a series of noise runs during working days, nights and weekends. Results are shown in Figure 5.7.

Gravitational noise appears to be negligible, given the preliminary pendulum sensitivity, during nights and weekends, when the gravitationally unbalanced pendulum performances are about the same of the balanced one. On the other hand, during working days it raises the overall pendulum noise of about a factor 50. This clearly suggests that the gravitational noise is mostly related to human activity, as there is a great difference between that measured during working days or during nights and weekends. Thus, observing pendulum performance in different moments of the week we could infer if it is limited by gravitational noise or not[2].

Moreover, we can also try to set a quantitative upper limit to the gravitational noise affecting the performances of a generic pendulum (in our experimental site) by scaling its estimated (or upper limited) gravitational quadrupole moment by that calculated for this unbalanced inertial member.

This information was extremely useful in view of the design and assembly of the inertial member for actual GRS testing, guaranteeing us not to be limited by gravitational noise, as:

- It showed that, already with the preliminary inertial member, the gravitational related noise was at least a factor three below the thermal noise limit during working day.

[2]What this measure actually tells us is that the gravitational background has a "modulation" between days and nights, and between working and non-working days. This can help us conclude that, in the case we observe an excess noise, it is *not* due to gravitational interaction if we don't observe the same type of modulation. Unfortunately, in case we do observe this modulation of the noise, we cannot conclude that we are actually limited by gravitational noise, as there are a number of potential noise sources related to human activity that will very likely show the same modulation

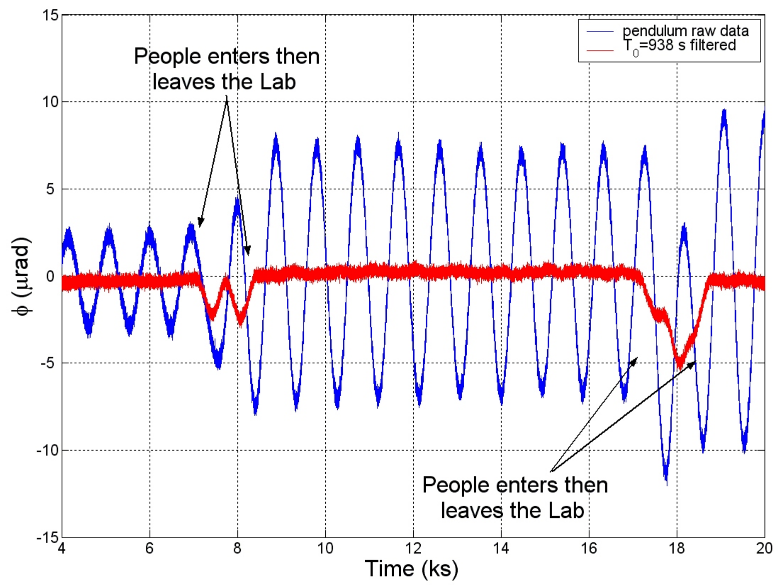

(a)

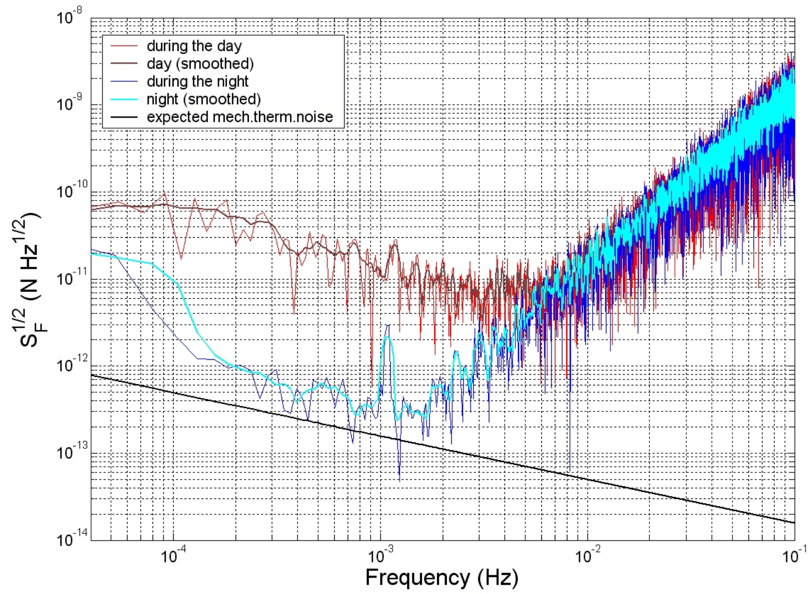

(b)

Figure 5.7 – a time series of the pendulum ϕ angle in the high gravitational quadrupole configuration during day hours (a): note the big signal induced by people moving within a few meters from the apparatus. In (b) a comparison between pendulum performances during working and non-working hours is shown: while during non-working hours the noise is comparable to the typical compensated pendulum performances, during working hours it rises by about a factor 50.

- Given the similar structure, the assembly precision of the inertial member for GRS testing has been measured to be a factor two or more better than that of the preliminary one (see D.1.1), thus guaranteeing a even smaller maximum estimated residual quadrupole moment and unwanted coupling with the laboratory gravitational noise.

- Because of the observed modulation in the gravitational-related noise, measuring the pendulum noise during nights or weekends should guarantee a further reduction of the gravitational noise of a factor 50 or more.

Chapter 6

4-TM GRS testing facility

Having gained important skills and experience building and operating the preliminary facility, we then moved to the construction of the actual GRS testing torsion pendulum. Aside from a number of minor enhancements on auxiliary systems, the major changes concern inertial member design and finishing, capacitive sensors, electronics and the mounting scheme and aligning capabilities of the whole setup.

6.1 Inertial member

The four TMs that compose the inertial member for actual GRS testing share the same design as the one employed in the single mass pendulum (see Figure 6.1): a full-size, hollow mock-up of LISA TMs, lacking only minor details not yet completely defined for the flight model (i.e. corners rounding and recesses on the Z faces for the caging mechanism).

Each of them is an hollow, 2.5 mm thick aluminum cube 46 mm in size. Provided the most threatening and most numerous sources of noise are related to surface effects, using hollow TMs allows us to reduce the total weight of the pendulum being thus able to use a thinner fiber with lower thermal noise (see Section 3.1), while retaining the ability to investigate surface properties. A cylindrical shaft 5 mm in diameter and about 10 cm in length goes perpendicularly through a 7 mm wide hole in one of the two Z faces[1], without touching it, and is anchored on the inner face by means of a quartz ring. In this way mechanical strength is retained while the shaft is electrically insulated from the TM and can be grounded separately; moreover, the dielectric quartz ring is completely hidden inside the structure, avoiding electrostatic interaction with the surroundings in case it becomes charged. On the two TMs that are not included in sensors and do not need to be biased for capacitive sensing, the quartz ring is substituted by a conductive aluminum one, grounding it through the shaft thus avoiding unwanted charging and consequent interaction with

[1]The presence of the shaft is the only thing that identify it as a Z face, meaning that according to the mounting scheme when the TM is inside the sensor, this face will be in front of the Z electrodes

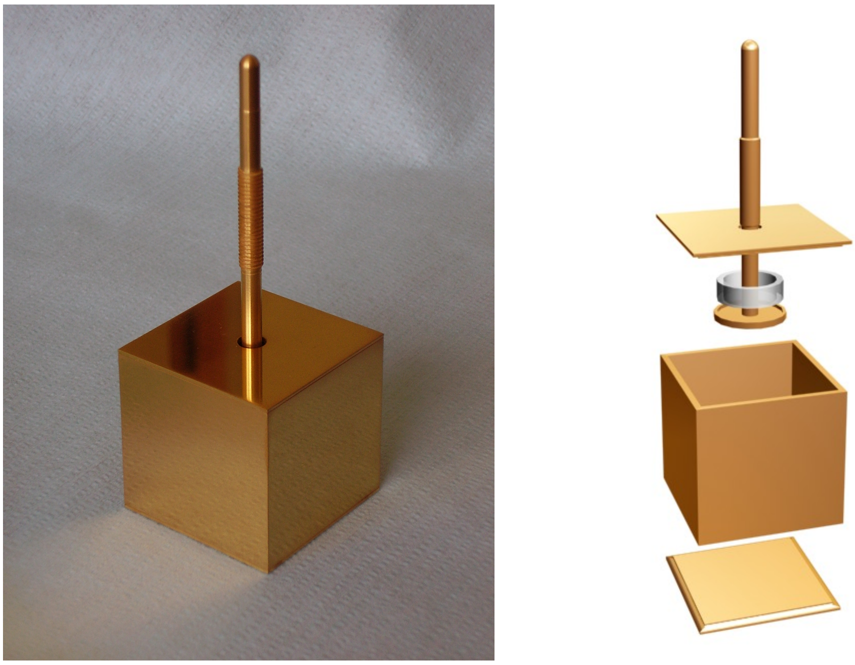

(a) (b)

Figure 6.1 – Picture (a) and 3D drawing (b) of one of the four gold coated aluminium hollow LISA TM mock-up used in the torsion pendulum

the surroundings.

A pair of aluminum cylindrical compensation masses can be moved, and blocked one against the other, along the threaded central part of each shaft to compensate imbalances in the assembled structure. At present, they are used to compensate a small construction difference between the sensing TM and the other two: each TM has a small 3 mm diameter hole on the Z face opposite to the shaft one to allow residual gas to exit the interior while in vacuum; due to an error of the provider, the two grounded TM have a bigger hole (5 mm diameter), thus resulting in a nominally uncompensated quadrupole gravitational moment of the assembled structure (note that even if the difference in the two holes is quite small, the effect is enhanced by the fact that they affect mass distribution at its extremities). Building slightly bigger compensation masses and moving them toward the exterior allowed us to obtain a null nominal quadrupole moment.

The shaft and its hole, along with the small hole on the opposite Z face, are the only major differences between the mock-ups and the real TM for what concerns exterior appearance.

The four TMs are kept in place by a 40x40x20 mm square central support that binds them on all DOFs except translation along, and rotation around their shafts: this way alignment is obtained by design (and limited by machining accuracy) on all DOFs except these two.

A vertical shaft then screws on the central support, hosting the cubic mirror used for autocollimator readout and providing a suitable interface for suspending the inertial member to the torsion fiber. In Figure 6.2 a 3D cartoon of the exploded structure and some picture of the assembled inertial member are shown. The whole structure is made up of aluminum for lightness and magnetic cleanliness (see Section 5.1) and all the parts are gold coated for electrostatic homogeneity.

To ensure accurate assembly we used a custom reference mask that provided both a reference plane for TM rotation around their shafts, and a number of stoppers to fix their distance from the center; once assembled, each TM distance from the nominal center of the structure has been measured to be 105.65 ± 0.05 mm (see Appendix D for details about alignment procedures and measuring techniques). The overall weight of the inertial member including mirror and compensation masses has been measured to be about 460 gr, while the estimated moment of inertia supposing it is laying horizontal has been calculated in $(3.7 \pm 0.05) \cdot 10^{-3}$ $\mathrm{Kg\,m^2}$.

6.2 Capacitive readout

Although the GRS is a 6-DOFs sensor capable by itself to discriminate all the degrees of freedom of the inertial member (for our purpose we can indeed consider it as a rigid body whose position in space is totally described by the 6 DOFs of one of its TM), using an additional sensor on the opposite TM as in the preliminary facility design would allow for much better instrument sensitivity. Using the GRS, TM rotations are evaluated measuring differential displacement d at a distance l between the centers of a pair of electrodes: $\phi_{GRS} \approx d_{GRS}/l$; using another sensor on the opposite TM, we can measure differential displacement of two TM at a distance L between their centers given by twice the arm, and $\phi_{Both} \approx d_{Both}/L$. Thus $\Delta\phi = \Delta d/l$ and using two sensor we can take advantage of the longer arm: if the two sensors have comparable translational sensitivity,

$$\frac{\Delta\phi_{Both}}{\Delta\phi_{GRS}} = \frac{l}{L} \approx \frac{1}{10}$$

for our geometry, in which the distance between a pair of electrodes is of order 2 cm, and the distance between opposite TMs is about 20 cm. For a detailed discussion about calibrations and angular readout reconstruction see Appendix B.

Moreover, the translation stiffness associated with the GRS (mainly electrostatic, as reported in Section 2.2) translates the pendulum tilt motion, i.e a TM translation inside the GRS, in a torque noise. This can be avoided inserting a comparable stiffness acting on the opposite side of the inertial member, so to generate a torque that cancels that originating in the GRS.

We thus decided to design and build an additional capacitive sensor to be employed on the TM opposite to the GRS: it has larger gaps to minimize its contribution to pendulum noise (because we obviously want to characterize the GRS and not our

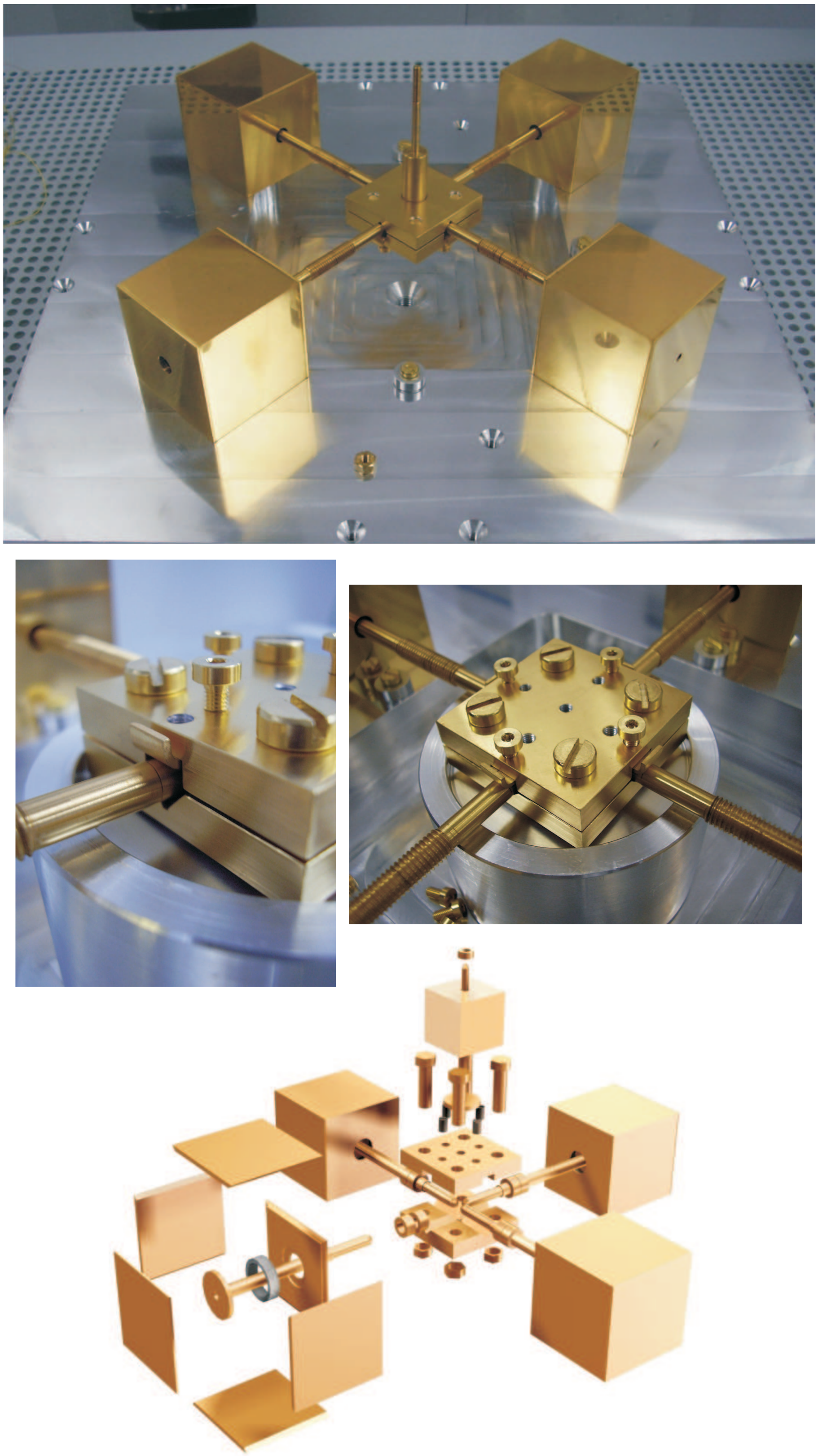

Figure 6.2 – An exploded 3D drawing and some picture of the assembled inertial member composed of four LISA like hollow TM. Note the detailed view of the central support holding the TMs shafts and assuring mounting alignment.

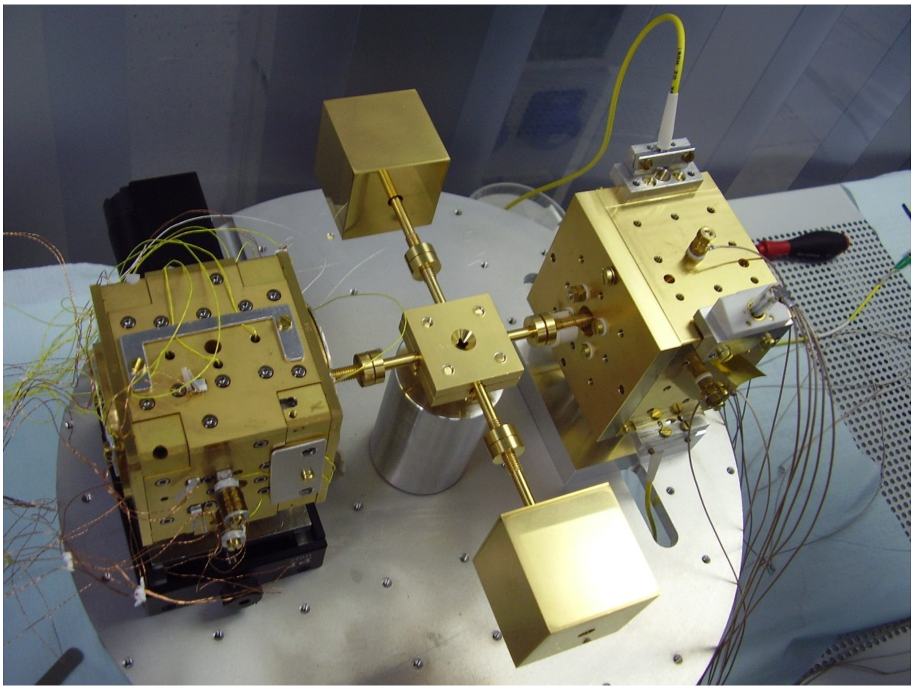

Figure 6.3 – A picture of the on-bench alignment of the capacitive sensors together with the inertial member (note that TMs inclusion in the capacitive sensors must be performed together with their installation on the base platform). It serves here to show capacitive sensors arrangement in the GRS testing facility: the GRS is visible on the left, with its X axis horizontal and perpendicular to the pendulum arm, and the Z axis parallel to the pendulum arm (actually the TM shaft pass through a Z face). The STC is installed on the opposite TM and help improve the facility angular readout sensitivity, obtained by means of a differential displacement readout of order 20 cm. Note the small coils on the GRS, that are heaters used for thermal measurement, and the yellow optical fibers, part of the additional Optical Read Out system developed by the Napoli INFN group and currently under testing in the 4-TM facility (see Appendix C.

own sensor) but, at the expense of reading only two degrees of freedom, comparable sensitivity. Controlling the injection voltage, its electrostatic stiffness can be adjusted to match that of the GRS: is has thus been called "Stiffness Compensator" (*STC*. A detailed description will be given in the next section).

The two sensors' arrangement is shown in Figure 6.3. They are installed on a 30 cm diameter round aluminum slab fixed to the vacuum chamber floor via a stack of one turntable and two orthogonal translational sleds driven by PC-controlled microstep motors. These have, respectively, about 10^{-6} rad and 10^{-8} m nominal resolutions and experienced repeatability about a factor 10 worse. The STC is mounted on top of a small aluminum platform by means of four Peek electrically and thermally insulating cylindrical legs; the platform itself lies on three adjustable support points on the big aluminum slab, allowing for alignment in rotation and height, and is firmly kept in place by means of three screws that pull it toward the bottom. The GRS interface is similar in structure and alignment capabilities, except that it has only three legs and the aluminum platform lies on a translational sled (with same performance as the two described above) oriented along the X axis that is fixed to the round slab via the same adjustable support system.

The assembled inertial member has been inserted in the two sensors at mounting time and fixed to the slab in an arbitrary, roughly-centered position; it can then be used as a guide for correct relative alignment exploiting the capacitive readout. In this way, during installation we were able to monitor and align all the degrees of freedom read by our sensors and align them within $5 \cdot 10^{-5}$ m in translation and $5 \cdot 10^{-4}$ rad in rotation (worst aligned DOFs reported).

With the two capacitive sensors aligned one with respect to the other, once the pendulum is suspended we only have to align the sensors assembly with respect to the inertial member position. Combining the positioning capabilities of rotational and translational motors described above with the ability to tilt the chamber precisely with the adjustable feet presented in Section 4.2.3, we are able to align the sensors assembly with respect to the inertial member on all the six degrees of freedom (see Appendix D for all the details concerning alignment at mounting time and in operation).

6.3 Stiffness Compensator

As stated above, reading pendulum ϕ motion using the rotational DOF of the TM inside the GRS will yield poor performance. In addition using only the GRS will result in a tilt-twist coupling effect due to its (negative) electrostatic stiffness. It acts only on one TM and has an effective arm with respect to the fiber axis, so that any swing motion of the pendulum in the x direction will result in a translation of the TM inside the GRS, a corresponding electrostatic force (by means of the electrostatic interaction) and a consequent torque exerted on the pendulum.

$$N(t) = F(t)b; \qquad F(t) = x(t)k; \qquad x(t) = \eta(t)L \qquad \Rightarrow \qquad N(t) = \eta(t)Lkb$$

thus

$$S_N^{1/2} = S_\eta^{1/2} Lkb \tag{6.1}$$

where $N(t)$ is the torque acting on the pendulum, $F(t)$ the force exerted on the TM inside the GRS due to the spring constant k and the displacement $x(t)$, b the pendulum arm (i.e. distance between the TM center and the suspension point), $\eta(t)$ the tilt angle defined in Figure 3.7 and L the length of the pendulum.

Given the geometry of our pendulum and measured GRS stiffness (that is completely dominated by the electrostatic contribution, as reported in Chapter 8), the multiplication factor between the tilt and related torque is about

$$L \cdot k \cdot b \approx 4.5 \cdot 10^{-8} \text{ Nm/rad}$$

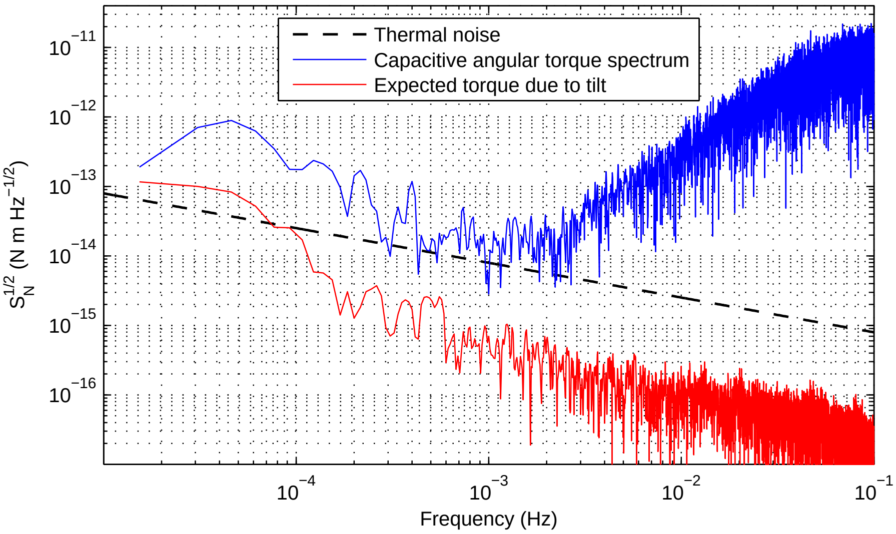

Figure 6.4 – Estimate of the uncompensated tilt-stiffness induced torque noise on the GRS testing facility; thermal torque noise is shown for comparison. It can be seen that its contribution, much smaller than the present measured excess, would only affect region below 10^{-4} Hz, and even here we find no relevant correlation.

Together with the typical tilt noise registered with the preliminary facility, this yields a tilt-induced torque noise more than one order of magnitude smaller than the thermal noise in the measurement band down to about $5 \cdot 10^{-4}$ Hz, and thus not critical for current pendulum performances (it would become so if we would be able to decrease the low frequency noise and approach thermal limit around 10^{-4} Hz. An estimate of the role of the tilt-stiffness induced torque noise is given in Figure 6.4 for a typical measured tilt noise.

For this reasons we developed an additional capacitive sensor, based on the same conceptual readout scheme of the GRS, with two main goals:

- to improve readout performance along the torsional DOF providing an additional signal with comparable sensitivity
- to compensate for the electrostatic stiffness of the IS that introduces a mechanical cross-talk between η and ϕ DOFs (this is why this sensor has been called "Stiffness Compensator", or *STC*)

Installing it on the TM opposite to the GRS will allow for both the discrimination of the rotational motion of the pendulum based only on translational data of two opposite TMs (thus taking advantage of the enhanced sensitivity due to the long arm) and the transformation of the η motion of the pendulum in a torque that compensates that arising in the GRS (exactly canceling it if the two spring constants are equal).

Trying to suppress sensor related disturbances, the STC has been designed with very large gaps. This, together with the need to (nearly) match the sensitivity of the GRS, forced us to use larger electrodes and thus drop four DOF compared to the GRS due to geometric constrains.

The STC, shown in Figure 6.5 is composed by a rectangular EH with one electrode per face. Each Y face hosts a 32×32 mm^2 injection electrode at a distance of 6 mm from the TM. X faces host 28×28 mm^2 sensing electrodes at 8 mm gaps. Z faces has the same 8 mm gaps and electrodes external dimensions, but smaller active area, because on the face toward the pendulum center there must be a hole to allow the TM shaft to enter the sensor. Thus the corresponding electrode has a 18 mm diameter hole centered with respect to the face. The opposite electrode has the same shape for symmetry reasons. The central hole on this face is closed by a removable cap that can be used for accessing the interior of the sensor if needed (for example for installation of UV light optical fibers). Each electrode is a single piece of metal with a threaded hole on the back (except for Z electrodes that have four holes): a screw coming from the outside of the STC keeps the electrode in place and provides a suitable interface for connecting it to the electronics, while insulating Macor bushes insulate the electrode and the screw from STC electrode housing. On the exterior of the STC, suitable shielding caps short-circuited to the sensor mask the screws' external ends and connection with the electronics' coaxial cables, providing continuity to the electrostatic shielding and preventing signals pick-ups.

Moreover, Z lids can be removed allowing for TM insertion. The whole structure is made of aluminum and gold coated for electrostatic homogeneity. If needed, Y electrodes can be used for sensing while biasing the TM using X or Z ones.

Although feasibility and global performance of such a large gaps sensor had already been proved by the preliminary pendulum sensors described in Section 5.2, the design described above has been obtained from an optimization procedure on a theoretical electrostatic model of the STC. We estimated the sensitivity/stiffness curve and compared it with the GRS one, matching the two as much as possible while retaining coherence with design guideline used for the GRS, such as the maximum area allocatable for electrodes compared to the TM face (see Section 2.3).

Since the gaps are relatively large compared to the electrode dimensions, in estimating expected performances of the STC we used a "corrected" model that roughly accounts for border effects, instead of the infinite parallel plate one used for GRS performances calculation (and whose results have been verified within about a 10-20% accuracy on the GRS, which however employs smaller gaps). This extended model considers for each surface that faces an extended (considered infinite) plane, an effective area obtained by increasing its linear dimensions by the value of half the gap in each direction. As sketched in Figure 6.6, this has been obtained starting from the consideration that electric fields simulated by means of FEM methods in similar situations are often reported to propagate as arcs of circumference, thus connecting to an area of the infinite plane bigger than the small surface by the gap in each direction. However, considering this whole area as the active one is clearly

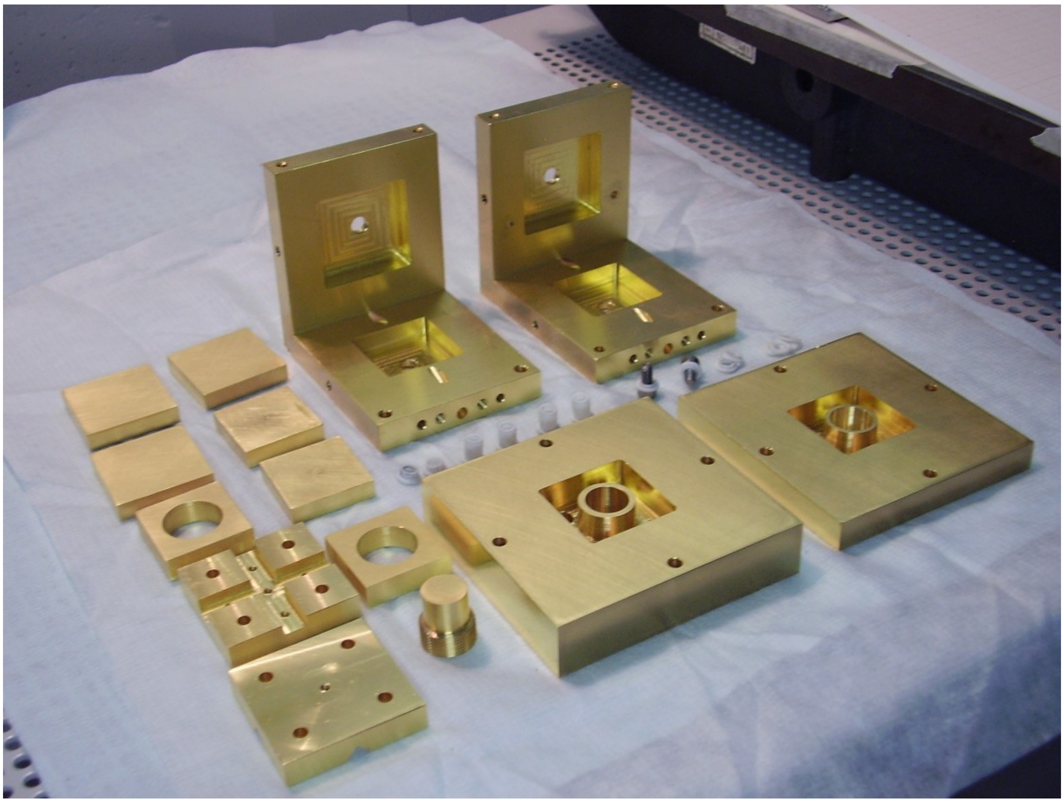

(a)

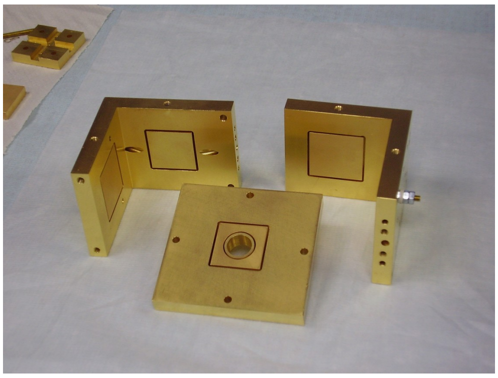

(b)

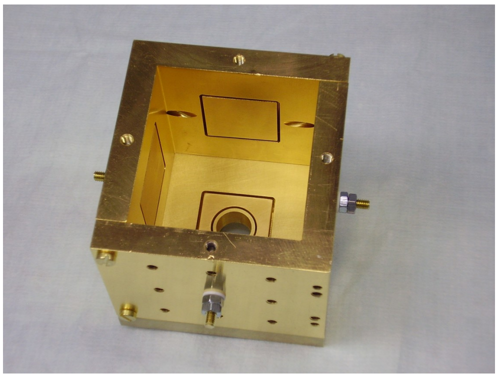

(c)

Figure 6.5 – Some pictures of the STC: composing pieces (a) and STC partially (b) and completely assembled (c).

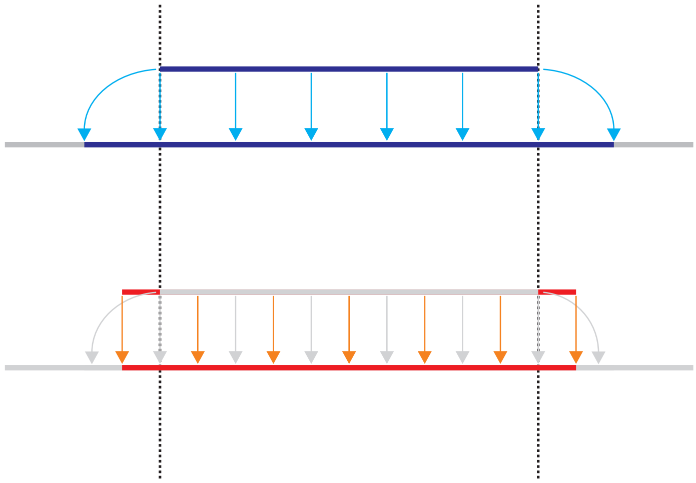

Figure 6.6 – A schematic comparison between the infinite parallel plate electrostatic model and the "corrected" one used in estimating STC capacitances accounting to some extent for border effects. Blue lines represent the maximum estimate obtained considering flux lines departing from the smaller surface (upper one) and closing on the facing bigger surface as arch of circumference: this way the interested area of the bigger surface turns out to be equal to the smaller one augmented by the gap on each side (thus two times the gap on each dimension). A reasonable correction for border effect has been obtained considering an effective area for the total capacitance that account for half this contribution, resulting equal to the smaller surface augmented by the gap on each dimension (red lines).

an overestimate, as it is equivalent to considering an ideal capacitor with both plates of that size: we thus chose to adopt the intermediate area as the effective one. As a consequence, the capacitance C of an electrode of area $A = b \cdot c$ at distance d from a bigger plane is computed as

$$C = \frac{\epsilon_0 (b+d)(c+d)}{d}$$

Table 6.1 reports the estimated values for the main quantities that characterize the STC electrostatic behavior.

In the optimization procedure, priority has been given to readout performances over matching stiffness, that has been kept small. Once we have matched GRS sensitivity obtaining at the same time a lower stiffness, it would be easy to increase the injection voltage to match the stiffness, and the resulting further increased sensitivity would be of no disadvantage[2]. On the contrary, if we were obliged to increase injection voltage to match sensitivities, we would end up with an STC stiffness exceeding the GRS one, thus introducing twist-tilt coupling again and perhaps with a bigger coefficient.

At present, a separate transformer to use a different STC injection voltage with respect to the GRS one has not yet been integrated. We are thus working with a

[2]Note that it would also be of little advantage, as the two readout noises sum up in quadrature when combined and the bigger one would result the dominating term.

Quantity	Symbol	Estimated value
Total injection electrode capac. toward TM	C_{inj}	4.3 pF
Total TM capac. toward surrounding surfaces	C_{tot}	20.9 pF
Injection ratio	$\alpha = \frac{V_{TM}}{V_{inj}}$	0.206
Single Sensing electrode capac. toward TM	C_{sens}	1.4 pF
Displacement to capac. imbalance gain	$\frac{d\Delta C}{dx}$	360 pF/m
Sensitivity (considering $S_V^{1/2} = 10^{-4}$ V/Hz$^{1/2}$)	$S_x^{1/2}$	2.5 nm/$Hz^{1/2}$

Table 6.1 – Estimate of the main quantities that characterize the STC electrostatic behavior, computed using the "corrected" model described in the text

slightly lower sensitivity and roughly 1/5 stiffness of STC compared to GRS. However this is expect to only affect readout performance slightly, and not the pendulum mechanical noise via residual stiffness as it would be noticeable only below 10^{-4} Hz, where there are currently other sources of noise dominating.

6.4 Electrostatic shielding

As observed in the preliminary facility (see Section 5.3.1), electrostatic interaction of the inertial member with possibly charged (e.g. by means of the ion gauge pressure sensor that is occasionally switched on to check vacuum level) dielectric surfaces inside the vacuum chamber (cables sheaths, spacers, supports. . .) is very likely to arise, and can be strong enough to overcome the torsional spring constant of the fiber and make the pendulum unstable.

To avoid this kind of interaction, the pendulum should be surrounded by conductive, grounded surfaces. While the two sensing TMs are enclosed in their EHs and are thus naturally shielded, the remaining part of the inertial member is exposed to this kind of interaction; this would be especially dangerous for the peripheral parts of the inertial member, TMs in particular, because a force acting there would have a big arm with respect to the fiber and so produce a relatively big torque.

We thus built around the pendulum a perimeter of grounded copper planes that mask almost every dielectric element that could be "seen" by the inertial member (see Figure 6.7).

Unfortunately, we were forced to leave some openings in the shielding enclosure (top part for mounting reasons and a side aperture for autocollimator light to reach the mirror): the only dielectric surfaces that face the inertial member in this way are however two, relatively far vacuum chamber glass windows. Although at present we observed no evidence of electrostatic interaction between them and the pendulum[3], a dedicated investigation should be eventually performed to completely exclude any relevant related effect.

[3] We also tried to build and install a conductive shield to place in front of the autocollimator window to mask it (and temporarily excluding that sensor), observing no substantial effects

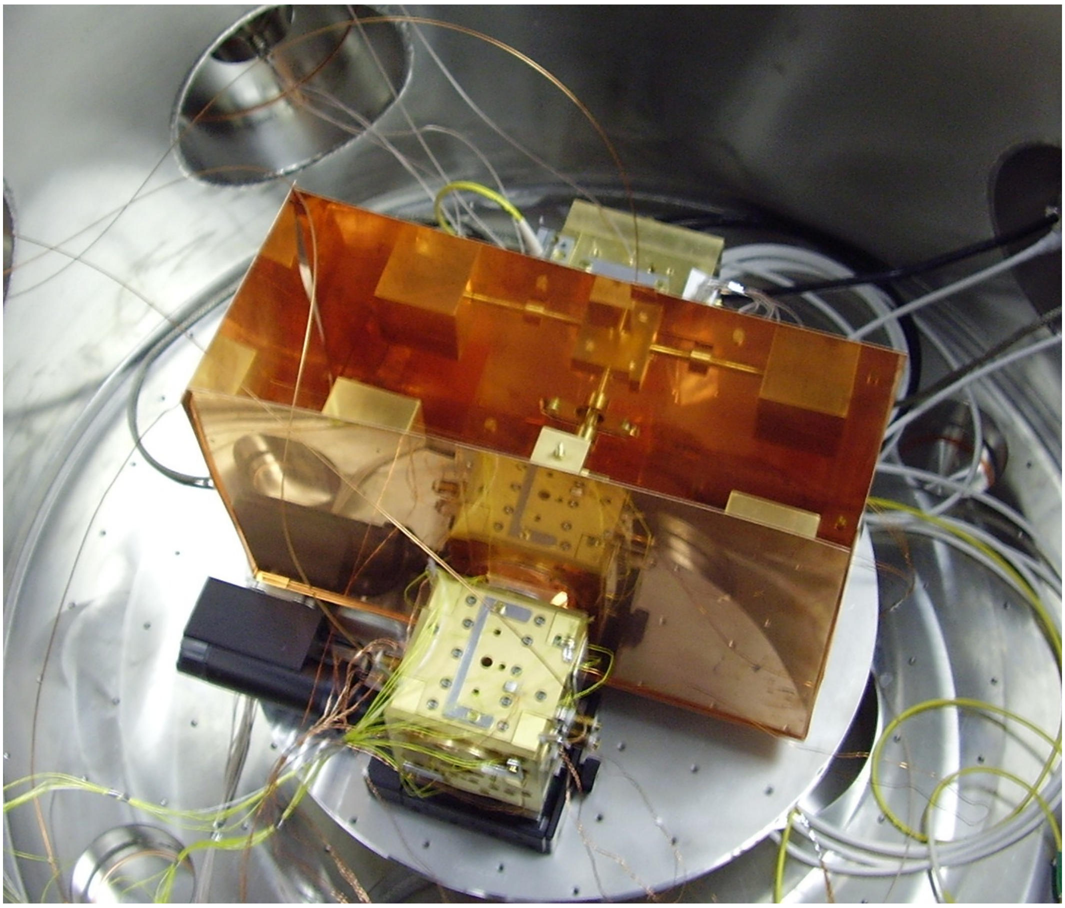

Figure 6.7 – A picture showing the copper shields installed around the inertial member to avoid interaction with possibly charged dielectric surfaces

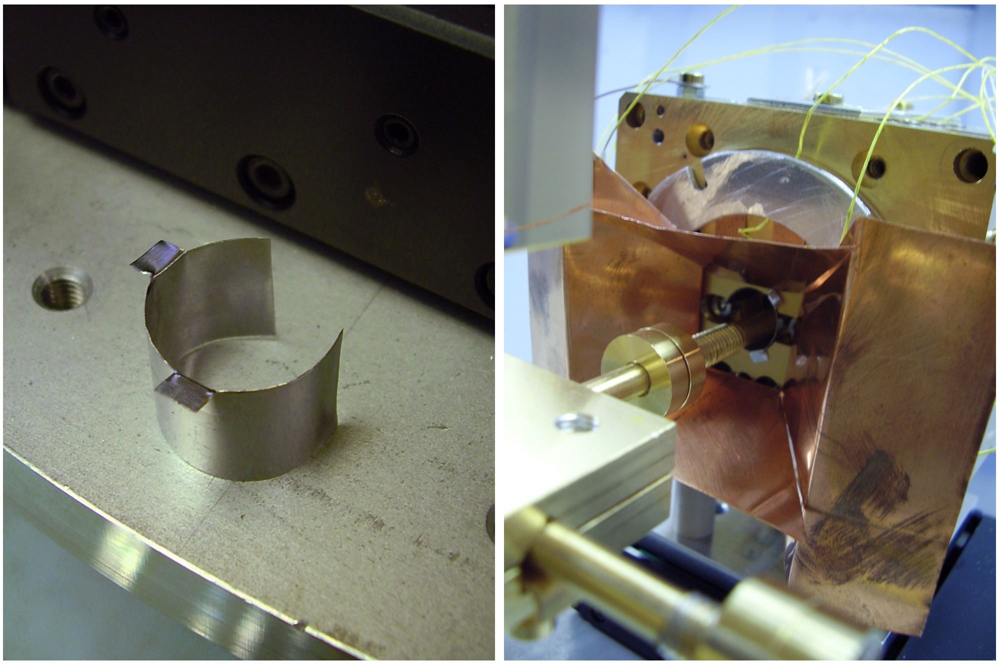

Figure 6.8 – The left picture shows the aluminum collar to be inserted in the shaft hole on the inner GRS Z face to mask the dielectric back of the Z electrodes. The right picture shows the GRS ineer Z face with conductive shields used to mask Z electrodes connection wires that comes to be very close to the shaft. The collar, here installed, is barely visible.

In addition to the external plates, we added two small shields to the side of the GRS facing the inertial member: this side has a number of wires connected to sensing and injection electrodes that come very close to the TM shaft and are thus a threatening potential source of interaction. Moreover, the GRS EH grounded guard-rings does not extend inside the hole through which the shaft passes, and this leaves it exposed to the small uncoated rear part of the electrodes. To shield these parts we added a round collar inside the hole in which the shaft passes and four copper "wings" hiding the cables. (see Figure 6.8).

6.5 Electronics

As sensing and actuation electronics (SAE) for both sensors we use an engineering model of the flight electronics developed by ETHZ. It has been designed to drive a 12-electrode, 6-channel sensor such as the GRS. However, it has two spare channels introduced both for redundancy and for compatibility with an alternative electrode configuration foreseen in an early stage design of the GRS. With small adjustments to the way the internal EEPROM manages the actuation on the two additional channels, it has been possible to adapt the ETHZ SAE to control both the six GRS channels and the two STC ones.

While retaining the full sensing and actuation (both AC and DC) functionality on the GRS channels, AC actuation has been disabled on the two spare channels, leaving them with full sensing capabilities but only DC actuation[4].

Adapting the electronics to drive both the capacitive sensors lead to a big simplification in the experimental setup and homogeneity in data acquisition.

The ETHZ SAE has a nominal voltage noise

$$S_V^{1/2} \approx 10^{-4}\ \mathrm{V/Hz^{1/2}}$$

with slightly better measured performances. The voltage output gain with respect to the difference in capacitance read for each capacitive bridge (i.e. channel) has an approximate value of

$$\frac{dV}{d\Delta C} \approx 90\ \mathrm{V/pF}$$

for 0.6 V bias voltage on the TM; the actual values range between 84 and 94 V/pF. This combines with the above value and GRS $\frac{d\Delta C}{dx} \approx 2 \cdot 300$ pF/m to yield an overall sensitivity per x channel

$$S_{x,GRS}^{1/2} = S_V^{1/2} \frac{dx}{dV} = S_V^{1/2} \frac{dx}{d\Delta C} \frac{d\Delta C}{dV} \approx 1.9 \cdot 10^{-9}\ \mathrm{m/Hz^{1/2}} \tag{6.2a}$$

For the STC, $\frac{d\Delta C}{dx} \approx 2 \cdot 180$ pF/m (according to the corrected model), and

$$S_{x,STC}^{1/2} = S_V^{1/2} \frac{dx}{dV} = S_V^{1/2} \frac{dx}{d\Delta C} \frac{d\Delta C}{dV} \approx 2.2 \cdot 10^{-9}\ \mathrm{m/Hz^{1/2}} \tag{6.2b}$$

Consider anyway that obtaining the same 0.6 V of TM voltage inside the STC would require a roughly 30% higher injection voltage (note that, as already stated, the necessary transformer has not yet been implemented).

[4] Actually "DC" means "low-frequency" actuation, as the SAE directly sends to the electrodes the input DC actuation signal after amplification and low-pass filtering at about 50Hz. This means that even using DC actuation inputs you can use a modulated signal to produce an AC actuation up to about 50 Hz. Real AC actuation is different as it takes the input signal and use its value to scale the amplitude of an internally generated high frequency signal, different for each electrode to minimize cross-talks.

Chapter 7

Upper limits on GRS related force noise

We developed the torsion pendulum facility as an instrument to detect, characterize and place upper limits on the very small force disturbances arising inside the GRS. As such, it requires the highest possible sensitivity to produce relevant results. This is important in particular when searching for unknown sources of noise: while the characterization of the modeled ones is based on the modulation of a scale parameter that can usually be amplified as much as needed to obtain the desired signal to noise ratio[1], the upper limit we can place on unknown contributions is directly related to the minimum torque noise we measure.

A theoretical lower limit to the torque noise acting on the pendulum is given by the thermal noise due to fiber dissipation (see 3.6). Operating at such a low level is however not trivial, as a number of external factors (temperature, magnetic field, tilting of the platform. . .) can intervene as a possible cause of additional torque: if identified, they can be reduced at the source, shielded and/or measured and their calculated effect subtracted from the measured data. We can also adopt strategies to reject as much as possible the pendulum rotation readout noise[2], that can be erroneously interpreted as real motion and then converted in torque noise, giving an additional, but unphysical, contribution.

All the above contributions to the noise can be subtracted from the measured torque noise, as long as they are clearly identified and not related to the GRS: after this, any unexplained excess, even if possibly due to other intervening mechanisms irrelevant to LISA and LTP, can in principle come from the presence of the GRS, and should thus be considered as an upper limit to the disturbances originating inside it.

[1] The next two chapters describe stiffness and DC-bias measurements, giving an example of the characterization of modeled sources

[2] The readout noise can be contributed by both electronic noise or real motion of the sensors with respect to the local inertial frame: in both cases, it would be erroneously interpreted as real motion of the pendulum in the inertial frame, thus resulting in a contribution to the estimated torque.

Anyway we still cannot state that the measured excess is actually due to the GRS, because it could be contributed by any missed external source as well as by pendulum noise through mechanisms that do not involve the GRS. Provided we could assure repeatability to the pendulum performances upon different integrations, a measurement campaign removing the GRS but leaving the rest of the apparatus as untouched as possible would be interesting to try to evaluate the ultimate achievable noise performances without the GRS, thus helping in better understanding the measured excess with the GRS installed.

Besides the above strategies to get rid of unwanted noise contributions, a precise evaluation of the measured excess noise is required to place an upper limit, as close as possible to both LTP and LISA requirements, on the unforeseen sources of noise that can arise in the GRS.

In this chapter we will first give a detailed overview of the data analysis techniques: data preprocessing and excess noise PSD estimation will be described in some detail, along with examples of their application to actual pendulum data.

We will then present the experimental results obtained so far with the 4-TM torsion pendulum facility: best observed noise levels during a single run will be shown to be within about a factor two from the pendulum thermal noise. Having identified a possible event that spoiled the facility performances during runs acquired after a given date, we will report on a statistical study of the pendulum average noise over a number of different noise runs, grouped in two sets: the first one corresponding to optimal facility functionality, and the second to an extended period covering some months but with limited performance. Even taking this inferior set of results as a representative value, we will place a significant upper limit to the noise force exerted by the GRS: it will be shown to be compatible with equivalent upper limits set with the 1-TM torsion pendulum via estimated conversion arm-lengths. In addition, however, it represents the first upper limit set by an instrument directly sensitive to the X force exerted by the GRS on a LISA like TM.

7.1 Data taking

Despite our efforts to suppress any external source of disturbance, at this extremely high level of sensitivity the pendulum motion is likely coupled to a number of environmental variables that are hard to control and, often, also to identify or measure. In taking data to estimate the pendulum noise we thus choose periods of time in which we expect these uncontrolled sources of noise to be reduced in number and intensity: since most of them are likely related to human activity, nights and weekends have proved to be the most quiet moments.

Moreover, preparing the pendulum for a noise run (i.e. a period of continuous data taking aimed at estimate the pendulum noise performances) requires that we center both TMs with respect to the sensors: this allows us to use higher electronics gains, so to relatively reduce the digitization and additive noises, and to suppress displacement-proportional readout noise.

To be able to correctly reconstruct the pendulum angular motion starting from the capacitive sensors voltage readouts, just before beginning the noise run we usually perform a calibration as described in Appendix B.2. This helps to get rid of long term drifts in electronics components that can spoil the validity of calibration coefficients over time. We also damp the pendulum free motion as much as possible by mean of the capacitive actuation, that is then gently released.

Finally, diagnostics systems described in 4.2 are all switched on, collecting environmental data for post-processing and correlation analysis.

7.2 Data analysis

After a very short reminder on Power Spectral Density estimation, we will introduce here the data analysis procedure we use to obtain this information from the pendulum angular motion data. As an example, we will present the described procedure applied step by step to run #20070929 [3], one of the best noise runs obtained so far[4].

7.2.1 Power spectral density estimation

Power Spectral Density, as the name says, is the quantity we use to estimate the power distribution in frequency of a signal $X(t)$. It is fundamental in stochastic data analysis, where the time series themselves do not carry an easy-to-interpret information. On the contrary, the PSD can tell how much power the signal has at a given frequency, and for a stationary process this would be a definite, characteristic and time independent function of the angular frequency ω. The "single sided" PSD S_X is defined as the Fourier transform of the autocorrelation function $R_X(\tau) = \langle X(t)X(t+\tau)\rangle$:

$$S_X(\omega) = 2\int_{-\infty}^{+\infty} R(\tau)e^{-i\omega\tau}d\tau \tag{7.1}$$

Many interesting signals in physics, and among them Gravitational Waves, have a well-defined and frequency-localized PSD that can be used to resolve them from a noisy background. Alas, stochastic processes produce random signals with intrinsic statistical variability: the outcome of an experiment only represents a statistical sample, and even under the hypothesis of stationarity, the PSD of the process that produced it cannot be simply "calculated" as a deterministic quantity, but has to be *estimated* from the experimental data.

[3]The name of the run given here represent the date in which it has been acquired, #20070929 standing for 2007, September the 29^{th}.

[4]For a more general and complete discussion on overall experimental results and average pendulum noise among different runs see Section 7.4

The tool we use for estimating the PSD of a finite length, discrete real time series is the well known Welch Periodogram, that consists of evaluating the Discrete Fourier Transform $\mathbb{X}(\omega_k)$ of the signal and computing the quantity:

$$S_X(\omega_k) \approx P_X(\omega_k) = 2\Delta T \mathbb{X}(\omega_k)\mathbb{X}^*(\omega_k) \tag{7.2}$$

where ΔT is the sampling time of the discrete time series and the asterisks indicates the complex conjugate.

As it will be useful further on in this chapter, we also recall here the definition of Cross Spectral Density (CSD) between signal X and Y:

$$CSD_{X,Y}(\omega) = 2\int_{-\infty}^{+\infty} R_{X,Y}(\tau)e^{-i\omega\tau}d\tau \tag{7.3}$$

where $R_{X,Y}(\tau) = \langle X(t)Y(t+\tau)\rangle$ is the cross-correlation function between $X(t)$ and $Y(t)$. The CSD can be estimated applying the same methods introduced for the PSD. In particular we can compute the Welch Periodogram (see Equation 7.2) in the form:

$$P_X(\omega_k) = 2\Delta T \mathbb{X}(\omega_k)\mathbb{Y}^*(\omega_k) \tag{7.4}$$

where $\mathbb{X}(\omega_k)$ and $\mathbb{Y}(\omega_k)$ are the Discrete Fourier Transform of the two signals. It can be noted that the PSD is just a particular case of the CSD, in which the two signal X and Y are actually the same: because of this, the CSD is often indicated as $S_{X,Y}$.

It is worth mentioning that, in computing the Discrete Fourier Transform of a truncated signal, data are usually weighted by a "window" function that "gently" approach zero at both ends of the selected time range so to avoid artifacts and biases due the abrupt truncation. As suggested in [10], we use a 3^{rd} order Blackman-Harris window. Please note that this window has been shown to produce a strong bias on the lowermost three point in frequency (not considering the zero-frequency one), that are usually considered not to be valid as an estimation of the process PSD. Throughout this thesis, we will use the symbol S_X to indicate both the theoretical PSD and its estimate through the Welch Periodogram P_X. Whenever relevant and not clear, the difference will be explicitly noted.

As the quantities we are interested in are in general linear quantities (deflection, displacement, etc...) and not quadratic (like the power), noise spectra are usually presented (and plotted) as Linear Spectral Densities, i.e. the square root of PSD. In Figure 7.1 we plot the estimated LSD of the angular data relative to the run #20070929 .

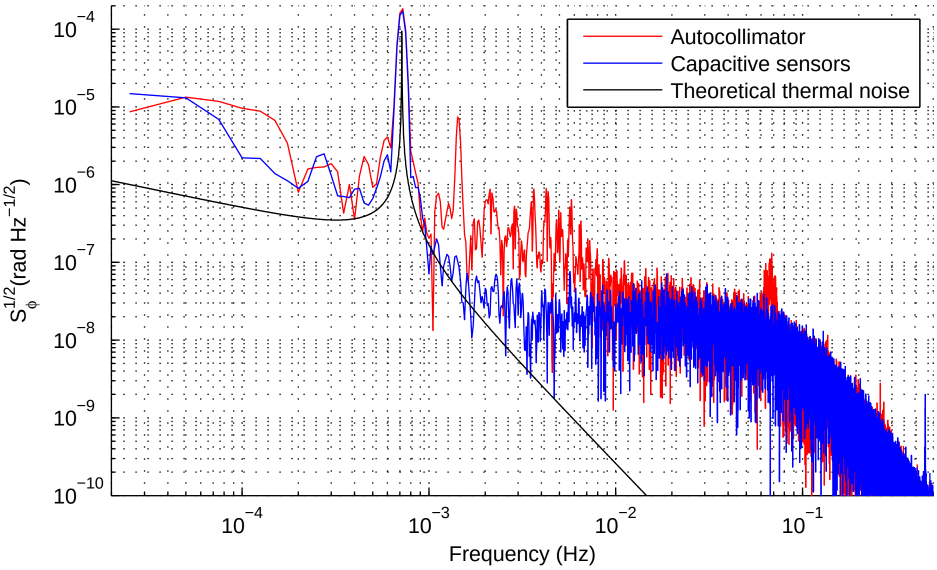

Figure 7.1 – Square root of Power Spectral Density estimation of angular data of run #20070929 , acquired with both autocollimator and capacitive sensors, is plotted as a function of the frequency, along with the theoretical thermal noise. As expected, it has a high value at resonance frequency, due to the relatively big free oscillation amplitude compared to noisy motion at other frequencies. The well visible roll-off in the experimental data around 100 mHz corresponds to the 4-pole digital low pass filtering explained in Section 7.2.2. Note how noisy the autocollimator signal is between 2 and 3 mHz: this corresponds to the pendulum best sensitivity region, and unfortunately, as we will see in 7.2.5, the autocollimator turns out to be of very little help here in enhancing the information already given by the capacitive sensors

7.2.2 Data interpolation, per-filtering and decimation

Given the high number of channels sampled and instruments read (see Table 4.2), and the present non-optimal efficiency and stability of our Microsoft Windows based software data acquisition system, we experience randomly distributed dropped points in the acquired data, on average about 1% of the total. Because of their random distribution and relatively low number, we fill them by means of simple nearest neighbor linear interpolation.

Moreover, we sample almost all sensors data at 10 Hz (although it would be possible to directly sample at a lower frequency, 10 Hz is the sampling frequency foreseen for LTP and the ETHZ Sensing and Actuation Electronics anti-aliasing filters have been deigned for such a sampling rate). Because the resulting Nyquist frequency, 5 Hz, is still much higher than the frequency band we are interested in, few mHz and below[5], we decimate the data for an easier and faster handling. In doing that, we first apply a 4-pole anti-alias low-pass IIR filter at about 100 mHz[10], and then down-sample them at a rate of 1/10, obtaining a sampling rate of 1 Hz.

The above procedure has been tested on simulated data as well as on real ones not to produce artifacts in the filter pass band. Random dropped points have been inserted in synthetic data, that have then been interpolated, filtered and decimated according to the above procedure. Figure 7.2 shows a comparison between noise spectra computed on the simulated data before and after interpolation, filtering and decimation: in the interesting frequency band there is no noticeable difference.

7.2.3 Conversion into torque

While our sensor systems give a measure of the pendulum angular deflection (see Figure 7.3a for an example), we are actually interested in the torque noise as this can be converted in equivalent force noise exerted along the X axis on the TM inside the GRS (in the 4-TM facility this conversion is almost straightforward, being it reasonable to assume that the torque is simply proportional to the force acting on the TM along X via the inertial member arm-length). The problem is thus that of estimating the torque starting from the measured angular motion.

Because we are interested in computing the PSD of the force acting on the TM, one possible way of doing that is directly in the frequency domain. As explained in Section 3.1, because the Fourier Transform of the angle deflection $\phi(t)$ is proportional to that of the torque $N(t)$ via the pendulum transfer function

$$H(\omega) = \frac{1}{\Gamma(1 - (\frac{\omega}{\omega_0})^2 + \frac{i}{Q})}$$

[5] The frequency band we can investigate roughly corresponds to LTP and LISA measurement ones. It is limited toward higher frequency by sensors readout (see Section 3.1 and Figure 3.3), while toward the bottom by just the maximum allowable time for a given measure under controlled conditions (depending on the experiment).

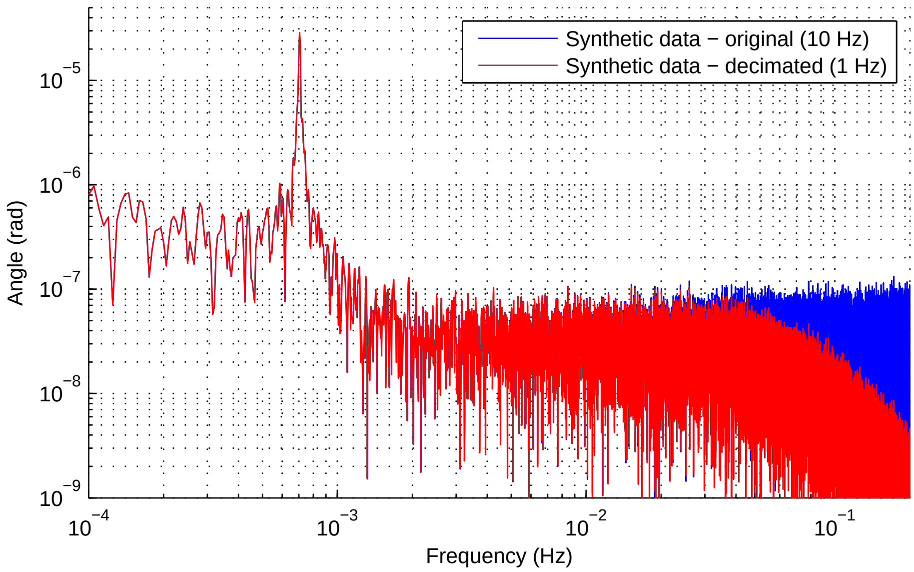

Figure 7.2 – The figure shows the comparison between spectra obtained from the same synthetic time series, before and after the data decimation technique described in Section 7.2.2. As you can see, below the well visible anti-aliasing low-pass filter roll-off, there is no noticeable difference between the two spectra.

the torque PSD can in principle be obtained dividing the angular PSD by the squared modulus of $H(\omega)$:

$$S_N(\omega) = \frac{S_\phi(\omega)}{|H(\omega)|^2} \approx \frac{P_\phi(\omega)}{|H(\omega)|^2} \tag{7.5}$$

While this is rigorous and easy to apply in principle, working with real, finite duration time series a number of problems arise:

- For a relatively high Q pendulum, the transfer function has a narrow peak at $\omega = \omega_0$, as does $S_\phi(\omega)$ (see Figure 7.1). Dividing the latter by the former will easily lead to unwanted artifacts around ω_0 unless you can give a very accurate estimate of the resonant frequency $f_0 = \omega_0/(2\pi)$ and quality factor Q (that determines the width of the peak).

- The finite duration of the signal, together with the use of a window for spectral density estimation (as briefly recalled in Section 7.2.1), will lead to a complex modification and broadening of the estimated spectrum; for Equation 7.5 to be still valid, this would require to use an "effective" transfer function whose shape depends on both the type of window and its length. This will be more evident near the resonance peak, and if we divide the angular PSD by the unmodified transfer function, this may not be canceled out correctly, leading to artifacts in the torque PSD estimation.

- The torsion pendulum is a damped oscillator which energy decays in time as $e^{-t/\tau}$, where $\tau = Q/\omega_0 \approx 2800/(2\pi/1400)$ s $\approx 6 \cdot 10^5$ s, or about 7 days. This means that the pendulum needs at least one week to "forget" its initial state and reach an "equilibrium" angular noise, much longer that any measure we usually perform. Both an excess or reduced damping before starting the noise run, as well as an exceptional isolated event that could excite the pendulum, will thus affect the whole measurement, leading to a bias in the estimate of the torque noise. This effect will be enhanced by the broadening of the peak discussed above, especially for shorter runs.

Since one of the most interesting frequency band is that around the resonant frequency ω_0, being very near to the spot in which the facility happens to have its best sensitivity, it is highly desirable to get rid of the problems explained above, that affect in particular this zone. We thus use direct estimation of the external torque in the time domain[34].

The torque estimation procedure we use is based on the application of the equation of motion in the form

$$N(t) = I\phi''(t) + \beta\phi'(t) + \Gamma\phi(t) \tag{7.6}$$

where the external torque has been written on the left to stress that it is the quantity to be computed starting from the others.

Actually, this equation corresponds to a viscous damping model, while the pendulum is more suitably described by an internal damping model as in Equation 3.2[26]. However, we cannot exploit the latter in the time domain, and so we use Equation 7.6 as an approximation; the differences in the results turns out to be negligible.

To estimate the torque acting on the pendulum at time t_i we approximate the first and second derivatives of ϕ in t_i by means of a parabolic fit to the 5 adjoining points $t_{i-2} \dots t_{i+2}$. The obtained values can be then substituted in Equation 7.6 to calculate $N(t)$. As this represents the "external" torque acting on the pendulum, this method get rids of both transients and free oscillation amplitude, giving an instantaneous estimate of $N(t)$ independent from the initial conditions (it is thus affected only by the four nearest samples). An example of angular motion conversion into external torque exploiting this technique can be seen in Figure 7.3.

Although this procedure still requires an estimation of the pendulum parameters I, ω_0 and Q, it turns out to be less critical in their value and, moreover, it removes all the other problems related to the correct transfer function estimation. This is particularly true for shorter time series, where the modification of the effective transfer function with respect to the theoretical one is bigger. Consistency of the two methods for longer time series or away from resonance has been checked. Figure 7.4, which reports a simulated time series analyzed with both techniques, clearly exemplifies the difference in performance around resonance and their consistency in the rest of the frequency band.

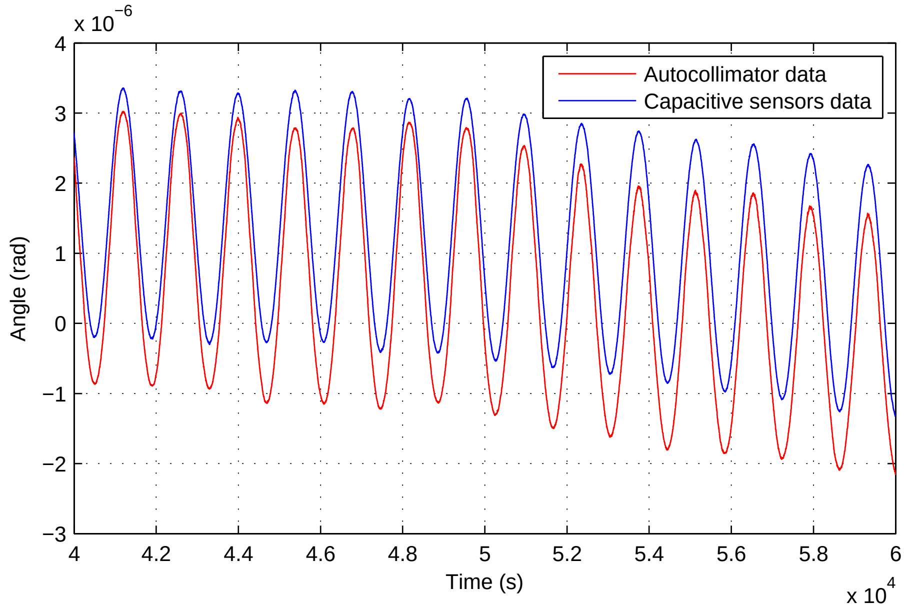

(a) Pendulum angular motion

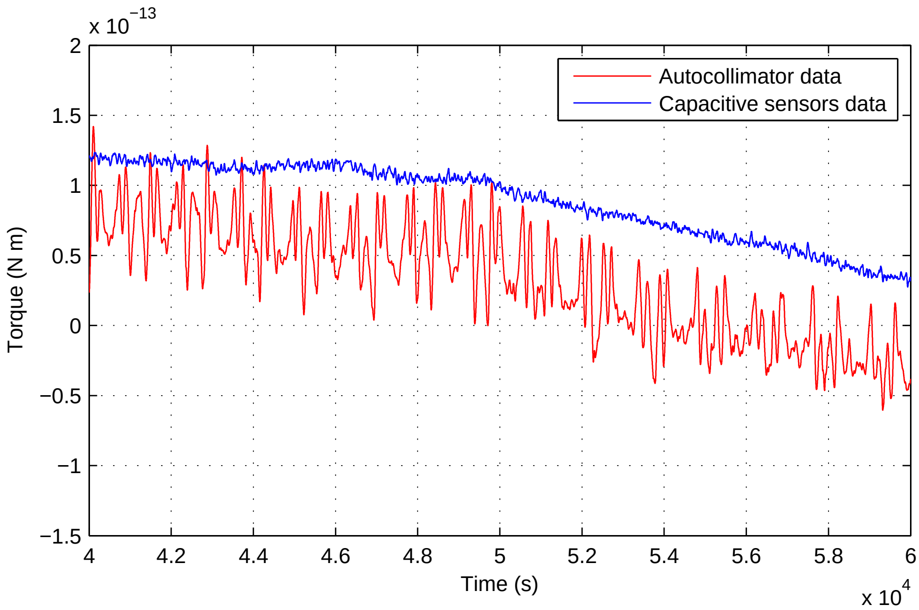

(b) Computed external torque

Figure 7.3 – 4-TM pendulum run #20070929 angular deflection time series, from both autocollimator and capacitive sensors data, is shown in (a): the $\approx$ 1400 s free mode oscillation is clearly visible. In (b), the same time series has been converted into external torque by direct application of the equation of motion (see text for details). Not to be completely masked by high frequency readout noise converted into apparent torque, data plotted here are low-pass filtered around 5 mHz: the low frequency behavior, clearly correlated with the observed angular motion, is thus visible. Note how much noisier is the autocollimator with respect to the capacitive sensors: this will be discussed later in the text.

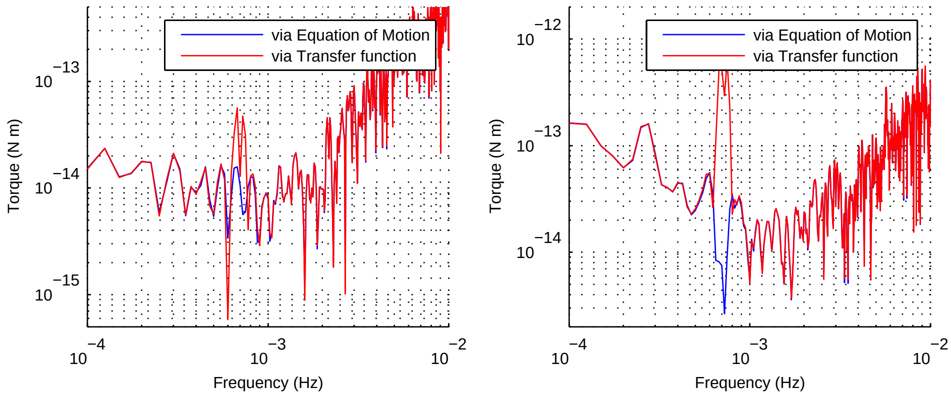

(a) Synthetic data   **(b)** Real data

Figure 7.4 – The left graph (a) shows the PSD of the external torque estimated on a $4 \cdot 10^4$ seconds synthetic time series (thus with known parameters) with both “Transfer Function” and “Equation of Motion” techniques, using exact parameters (see legend for plots explanation). While they both gives very similar results away from resonance (the two lines are actually superimposed), a clear difference is noticeable around 0.7 mHz, as the “Transfer Function” method cannot completely suppress the resonance peak. In (b), the same comparison is shown for an experimental time series of the same length

In addition to those explained above, there is another reason to chose the time domain approach. In the next section we will talk about effects related to environmental variables that can show a coupling with the pendulum motion. For the majority, the coupling effect is likely to manifest itself as an external torque acting on the pendulum. While below resonance the transfer function of the pendulum is flat (so the angle and the torque time series low frequency component are proportional), looking for a correlation of environmental variables with the measured deflection is often unphysical and will lead to a wrong result for disturbances acting around and above resonance, where the transfer function has a definite shape and torque and angle have a frequency dependent ratio (the two time series are thus no more proportional). Computing the torque in the time domain will instead provide the right signal in which to search for correlation with most of the environmental variables.

It is worth mentioning here one general possible issue related to this technique and the role of readout noise. As shown for example in Figure 7.1, the almost flat readout noise dominates the upper frequency band of the angular noise spectrum. Because the data analysis procedure doesn't distinguish between real motion and that mimicked by readout noise, the latter is converted in torque the same way as the former. However we should notice that the pendulum tends to respond poorly to high frequency torques due to its moment of inertia, and thus if we consider the high frequency readout noise as a real motion we will conclude that a huge torque is acting on the pendulum. This is more formally expressed by the shape of the transfer function reported in 3.3 and shown in Figure 4.2: because $H(\omega)$

decreases like ω^{-2} above resonance, a flat readout noise would be converted in an ω^2 like torque. After a few frequency decades, this can lead to a readout-mimicked torque several orders of magnitude bigger than in the best sensitivity region. Thus, depending on the subsequent operations performed on the torque data, this huge difference in orders of magnitude could make noticeable a number of source of error that would otherwise be negligible: errors related to numerical approximation, effects of statistical fluctuations of high frequency data (specially for shorter time series), high-frequency noise leakage in low-frequency noise estimates, and so on... To get rid of this effect, it is sufficient to low-pass the data near the lower end of the frequency band in which the white readout dominates, using a filter with a roll-off steeper than ω^{-2}.

Note that our decimation procedure explained in Section 7.2.2 already foresees a relatively hard low pass filtering of the data that prevents us to be affected by such problems.

7.2.4 Analysis of external disturbances

A number of environmental variables can in principle affect the pendulum motion through a variety of effects. Among others, these includes:

Tilt: pendulum tilting due to seismic noise and structure relaxation (or even temperature fluctuation mentioned below) can produce a torque on the pendulum via both a direct effect on the fiber suspension point being stressed, or interactions modulated by the tilt-induced inertial member translation (as for example the twist-tilt effects observed with the single mass facility [9, 22, 33], or the tilt motion coupling with the GRS stiffness described in 6.3).

Temperature: thermal and thermal-gradient fluctuations can induce a torque on the pendulum via structural distortion of the apparatus (that can affect the fiber suspension point) or changes in the fiber equilibrium angle. They can also produce electronics-calibration drifts or relative motion of the sensors with respect to the local inertial frame, introducing a fake deflection signal in the readout.

Magnetic field: the mean value of the magnetic field can exert a torque on the pendulum by direct interaction with its residual magnetic moment. Moreover, as the 4-Tm pendulum has a non-negligible spatial extension, any magnetic moment distributed away from the inertial member center, and thus moving in space upon pendulum rotation, will couple with the magnetic field gradient. Finally, induced magnetic moment and eddy currents can also have a role in the interaction.

Despite our best efforts to reduce the coupling factors as much as possible using shielding techniques and careful construction, some residual effects of these variables on the pendulum could still be at a detectable level. However, as long as we can measure them and understand what contribution they are giving to the detected torque, they can be subtracted from it and thus not affect the estimated, unexplained excess.

As explained in Section 4.2, a number of sensors are employed on the facility to measure those that we consider to be the most threatening environmental variables coupled to the torque acting on the pendulum. We can use them to search for correlations and try to subtract the effect of the monitored variables.

Although we do not always have precise or complete models to explain the effect of such variables on the pendulum motion, almost all of them are supposed to exert a torque on it, whatever the real mechanism through which it happens. Moreover, the pendulum transfer function is in practice flat below resonance, meaning that pendulum motion and exerted torque should simply be proportional. Physical variables that affect directly the (measured) angular motion, if any, should thus show an equivalent correlation with the torque time series low frequency behavior.

Different techniques are available to find the best linear combination of environmental variables that, subtracted from the torque time series, minimizes its PSD. It should however be noted that any real signal has a probability, although low, to show by chance a correlation with another one, even if they are generated by completely uncorrelated physical systems. It is thus advisable to check for evident correlation before subtracting.

This is more formally expressed by the cross-coherence function between the signals $X(t)$ and $Y(t)$:

$$\rho_{X,Y}(\omega) = \frac{S_{X,Y}(\omega)}{\sqrt{S_X(\omega)S_Y(\omega)}} \tag{7.7}$$

where $S_{X,X}$,$S_{Y,Y}$ are the PSD of the two signals, and $S_{X,Y}(\omega)$ is their cross-spectral density as defined in 7.2.1.

Intuitively, $\rho_{X,Y}(\omega)$ represents the power spectrum of the correlated part of the two signals normalized to 1 (it is easy to see that if X and Y are completely correlated, $\rho_{X,Y}(\omega) = 1$). As such, we note that it gives a frequency-dependent result, being thus able to show correlations "localized" in frequency due to a non-flat transfer function of the physical system that couples the two variables.

Let us define

$$F_\rho(\omega) = \frac{(N-1)\,|\tilde{\rho}_{X,Y}(\omega)|^2}{1-|\tilde{\rho}_{X,Y}(\omega)|^2} \tag{7.8}$$

where $\tilde{\rho}_{X,Y}(\omega)$ is the estimate of $\rho_{X,Y}(\omega)$ computed by averaging[6] N different sets of data (obviously referred to the same processes X and Y, here supposed to be stationary). It can be shown [35] that, for two signals uncorrelated by hypothesis, F_ρ represent an F distribution with 2 and $2(N-1)$ DOFs for the numerator and the

[6] This is mandatory as, for estimated signal, using only one time series it always holds $|\tilde{\rho}_{X,Y}(\omega)| = 1$ just for algebraic reasons

denominator respectively. This means that, under the null hypothesis, the two signal have a non null probability of showing some degree of correlation. Setting a suitable threshold value on F_ρ (that for a given N results on a corresponding threshold value on $|\tilde{\rho}_{X,Y}(\omega)|$) we can thus test the null correlation hypothesis between the two signals.

This warns us about our intention to subtract environmental variables from the torque time series to reduce the noise; each time we subtract a signal, even if it is uncorrelated, we will end up slightly lowering the noise just by chance. In the limit we try this with an infinite number of variables, we can completely null the noise.

Although we are far away from this limit, as the number of signals is much lower than the DOF of the time series, it is advisable to check for highly improbable values of F_ρ under the null correlation hypothesis, before subtracting a signal claiming to have found a correlation.

We thus perform this type of check comparing all the diagnostic signals (two three-axial magnetometers, a number of thermometers and the pendulum tilt signal from both capacitive sensors and autocollimator) with both the torque time series obtained by autocollimator and capacitive sensors data. In most of the cases we found no correlation at all (two example for run #20070929 example are reported in Figure 7.5); we occasionally find weak correlations that we are anyway unable to effectively subtract, as the improvement in the usually narrow frequency region in which they show up is limited, and much smaller than the spectrum degradation outside it. It is worth mentioning, however, that in the past, on the single pendulum facility, we found and effectively subtracted a number of different, significant contribution to the measured excess noise (as for example in [22]).

Finding no correlation with the signal of a given environmental monitor does not necessarily mean that the pendulum motion is not affected by that variable. This can happen for different reasons, as for example:

- The sensitivity with which we measure a given environmental variable could no be sufficient to resolve its fluctuation, that however could be high enough to affect the pendulum motion. In this case the analysis will try to correlate the torque signal with the readout noise of the instrument, obviously (hopefully!) confirming the null correlation hypothesis. This is indeed the case of the thermometers data, except for those outside the vacuum chamber: given the thermal control system performance, from high frequency to slightly above 10^{-4} Hz we are usually limited by the measuring system white readout noise at a level slightly below 10^{-2} K/Hz$^{1/2}$.

- The inputs that affect pendulum motion and environmental monitoring system can be different, as can the transfer functions toward the two. The measured signal can therefore be insufficient to reconstruct the impact that a given set of environmental variables has on the pendulum. Using once again temperature

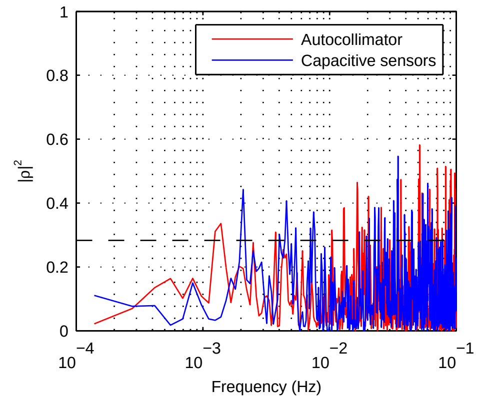

(a) Synthetic data

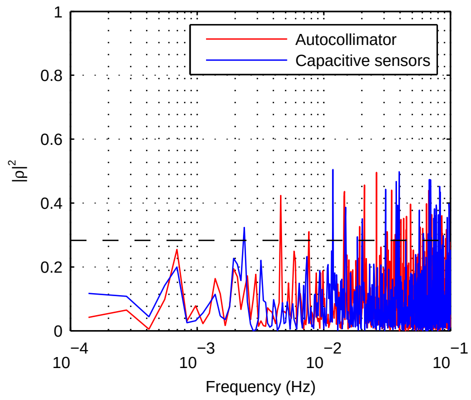

(b) Real data

Figure 7.5 – Two plot showing the modulus of the complex-coherence relative to signals acquired during run #20070929 , plotted as a function of the frequency; the 5% null hypothesis threshold is also plotted: if $|\tilde{\rho}_{X,Y}(\omega)|$ shows to be steadily above threshold in a frequency region, the two signals are very likely to be correlated there. In (a) the cross-coherence between computed external torque from both sensor and tilt signal from capacitive sensors shows no correlation at all: there are very few and isolated points above the 5% threshold. The same applies for (b), in which the cross-coherence is computed between torque data and the temperature of the vacuum chamber neck (that affects the fiber temperature via radiative thermal exchange).

as an example, we are obviously not monitoring all the possible heat input to the pendulum, nor do all the inputs that affect the thermometers necessarily have an impact on the pendulum motion, so finding no correlation does not necessarily mean that we are not limited by thermal fluctuations.

On the other hand, we want to stress that, if possible, any correlation found should undergo an experimental investigation to check for the effect, measure the coupling factor independently and propose and verify a model for the correlation (for example, if we find correlation with the magnetometers data we should measure the pendulum magnetic moment by means of purposely induced magnetic field with known time dependence; or in case we suspect a correlation with the measured tilt, we should tilt the chamber on purpose and measure the “twist-tilt” coupling coefficient…). Otherwise, it would be hard to keep the procedure under control and assure we are actually subtracting an *external* disturbance, and not a part of the GRS contributed noise we are trying to measure.

7.2.5 Readout noise reduction

Once every identified correlated source of noise has been subtracted, we obtain our best estimate of the torque acting on the pendulum based on angular data read by each sensor. An example of application of the analysis steps performed so far is given in Figure 7.6, where the estimated PSD of the torque noises computed using both the autocollimator and the capacitive readout are shown.

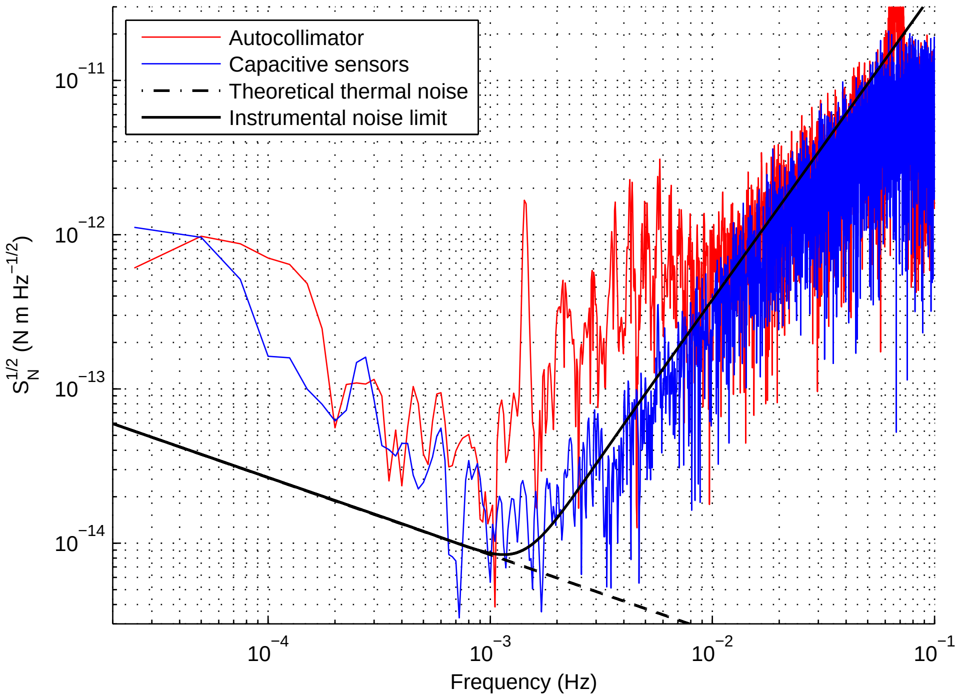

Figure 7.6 – The figure shows the estimated PSD of the torque acting on the pendulum during run #20070929 . The pendulum thermal noise and "instrumental limit", given by the sum of thermal and (capacitive) readout noises, is plotted as well (without uncertainty for clearness). As you can see, the capacitive readout appears to be in very good agreement with its calculated readout noise, and roughly a factor two from the thermal noise in the best performance region between about 1 and 2 mHz. On the other hand, the autocollimator shows a much worse level of noise, with an high (currently unexplained, but very likely due to mechanical vibration of the mounting) peak in the interesting region mentioned above. Even the low frequency noise, although difficult to estimate by eye due to the fluctuations and the low number of points, appears to be higher that those registered by the capacitive sensors.

Using each of the available sensors (that can in principle be more than two) independently to give an estimate of the observed excess noise observed is a possibility. However, exploiting their multiplicity we can undertake a further step in the attempt of setting a lowest possible upper limit on the torque experienced by the pendulum.

Each sensor reads the "real" angular position of the pendulum plus a noise, that can be contributed by both the sensor readout noise, and the residual motion of the sensor itself with respect to the local inertial frame.

$$\phi_i(t) = \phi_{real}(t) + \phi_{n_i}(t) \tag{7.9}$$

where $\phi_i(t)$ is the angular deflection read by the i-th sensor, $\phi_{real}(t)$ is the actual motion of the pendulum in the inertial reference frame and ϕ_{n_i} is the noise added by the sensor as explained above. The main difference between the two is that, while the first should in principle be read by all the sensors (supposing they are correctly calibrated), the second should be sensor-specific, although some correlation could be expected (e.g if $\phi_{n_i}(t)$ is partially due to the rigid motion of the vacuum chamber, each sensor that is fixed to it will experience such noise component). For this reason, in the derivation that follows it is more convenient to think of the angular readout of each sensor to be composed by a totally correlated part $\phi_c(t)$ among all the different sensors, and a totally uncorrelated, sensor dependent one $\phi_{u,i}(t)$, the real motion of the pendulum belonging to the correlated one.

$$\phi_i(t) = \phi_c(t) + \phi_{u,i}(t); \qquad \phi_c(t) = \phi_{real}(t) + \phi_{n,c}(t) \tag{7.10}$$

with $\phi_{n,c}(t)$ being the correlated part of the noise.

Let's now consider the realistic case of having two available sensors A and B (the capacitive readout system and the autocollimator, in our case). If we take the combination

$$\phi_\Sigma(t) = \frac{\phi_A(t) + \phi_B(t)}{2} = \phi_c(t) + \frac{\phi_{u,A}(t) + \phi_{u,B}(t)}{2} \tag{7.11a}$$

$$\phi_\Delta(t) = \frac{\phi_A(t) - \phi_B(t)}{2} = \frac{\phi_{u,A}(t) - \phi_{u,B}(t)}{2} \tag{7.11b}$$

and suppose $\phi_{u,A}(t)$ and $\phi_{u,B}(t)$ as stationary, zero mean random processes, when we compute the PSD we obtain:

$$S_{\phi_\Sigma}(\omega) = S_{\phi_c}(\omega) + \frac{S_{\phi_{u,A}}(\omega) + S_{\phi_{u,B}}(\omega)}{4} \tag{7.12a}$$

$$S_{\phi_\Delta}(\omega) = \frac{S_{\phi_{u,A}}(\omega) + S_{\phi_{u,B}}(\omega)}{4} \tag{7.12b}$$

Subtracting the second from the first of the above equations, we finally get an estimate of the pendulum angular motion PSD that exploit the readout of two partially independent sensor to get rid of the uncorrelated noise read by each of them.

While the above derivation makes it clear the mechanism through which we can reduce the estimate of the pendulum noise exploiting redundant readouts, it can be shown that the PSD of the correlated part of the signal computed as above is equal to the real part of the Cross Spectral Density (see Section 7.2.1) between the two signals:

$$S_{\phi_c}(\omega) = S_{\phi_\Sigma}(\omega) - S_{\phi_\Delta}(\omega) = Re\big(S_{\phi_A,\phi_B}(\omega)\big) \tag{7.13}$$

As in converting angular deflection in external torque, only linear operations are involved, the same applies to the torque, and we can thus estimate the external torque acting on the pendulum as the cross spectral density between the torque time series obtained by two different sensors outputs:

$$S_{N_c}(\omega) = S_{N_{real}}(\omega) + S_{N_{n,c}}(\omega) = Re\big(S_{N_A,N_B}(\omega)\big) \tag{7.14}$$

Up to now, cross spectral density analysis has been effectively used on the 1-TM facility to lower the excess noise estimation. It has also shown unexpected correlations between autocollimator and capacitive sensor "white"[7] readout noises, that have been thought to be caused by overall facility shaking due of vacuum pumps vibration, and successfully reduced.

However, applicability of CSD analysis in the 4-TM facility is at present limited: actual mounting of the autocollimator in the 4-TM facility has proved not to be effective enough in reducing mechanical vibrations and drifts. Moreover, exploiting the translational sensitivity of GRS and STC combined with the big separation between the two (that has to be compared with the separation between X electrodes of the GRS, used to measure the ϕ rotation of the single mass pendulum), the capacitive readout turns out to be much more sensitive than the autocollimator in the most interesting region just above resonance. This big difference in performances has shown to produce very noisy and difficult to interpret result in the computation of the CSD, probably because the noise of the autocollimator is so high that it masks any correlation with the capacitive sensors in certain frequency regions.

Although autocollimator mounting could be made better so to reduce mechanical vibrations and distortions related noise, recent similar upgrades on the single mass facility have shown that the level of performance achievable is probably still too poor compared to the capacitive sensors. A much better improvement could in principle come from the employment of a different, more sensitive readout, such as the Optical Read Out developed by the INFN group of Napoli, already installed in the facility

[7]Since they have a mechanical contribution, as demonstrated by CSD analysis, its unlikely that they are still white. Anyway, we intentionally use here this improper term to indicate the almost flat part of the readout noise that dominates the overall angular signal at high frequencies.

and still in a testing phase (see Appendix C).

7.2.6 Accurate spectrum estimation

When we search for excess noise, to give a significant result we should be able to make quantitative statements about the difference between the spectrum of the measured noise S_ϕ, computed applying the procedures described so far, and the thermal noise background. Unfortunately, while the latter comes from a theoretical estimation which is affected by relatively small errors on the measured pendulum characteristics, in the experimental estimation of S_ϕ each point has a relative uncertainty of 100%[8], thus making a direct comparison with the theoretical model difficult[9]. This can be seen in many of the figures presented throughout this thesis (see for example Figure 7.2): the estimated spectrum appears very noisy, and its mean level is difficult to evaluate by eye.

As a reasonably smooth model is expected to drive the process that produced the time series, we ideally would like to plot a smooth curve representing it: we however encounter the problem of deciding which features of the estimated spectrum are just statistical fluctuations and which are, instead, real features of the underlying process that should be included in the model.

A number of different strategies are possible to reduce the fluctuation of the spectral estimate and obtain a PSD which is easier to interpret:

- the Welch Periodogram provides by itself a method of reducing estimate uncertainty via averaging. The definition given in Equation 7.2 can be modified as follows:

$$P_X(\omega_k) = \frac{2\Delta T}{N} \sum_i^N \mathbb{X}_i(\omega_k)\mathbb{X}_i^*(\omega_k) \tag{7.15}$$

  meaning that, given a time series, we can divide it in N smaller segments, compute the Welch Periodogram on each of them independently and finally average the results point by point. In this way, we are considering shorter time ranges, thus resulting in a reduced frequency resolution[10]; on the other hand, the accuracy of each point is increased by a factor N, thus resulting in a less fluctuating spectral estimation, approaching the theoretical value as N increases. We note that as a results of the windowing process mentioned at

[8] To be precise the 100% uncertainty refers to the theoretical value of the spectrum. When we obtain an experimental estimation of the spectrum, we cannot assume a unity relative error on each point, because they can be much higher than the real value of the spectrum itself, resulting in an overestimate error, or much lower (down to zero!), resulting in an even worse underestimate.

[9] The same applies to estimation performed exploiting the CSD, in which the situation is even worse: each point coming from a single estimation has a completely random phase, making it almost impossible to evaluate the level of the estimated spectrum without applying some kind of averaging.

[10] For very low frequency experimental investigations such as those presented in this thesis, shortening the time range has an importance not only for the reduced capacity of resolving spectrum features, but also for placing a limit on the minimum frequency (bigger than zero) that you can investigate, since it is equal to the inverse of the data segment duration

the end of Section 7.2.1, points in the "tails" of the windows are weighted less. This suggest that we can select overlapping data segments so that each point is weighted about 1 by the average of the two (or more) windows in which it is considered: in this way we can increase the number of segments and/or their length. Overlapping fraction depends on the shape of the windows used: with the Blackman-Harris window adopted here we choose 50% overlap, determining the number of windows (and thus their length) based on the desired minimum estimated frequency (or, equivalently, frequency resolution).

- Another way of producing a smoother estimate sacrificing frequency resolution is that of performing data binning in frequency, averaging all the points belonging to the same bin. Although this method could rigorously be applied only to white spectrum, as it averages points at different frequencies and thus corresponding to different theoretical values of the spectrum, as long as the width of each bin is small enough compared to the slope of the spectrum, it can produce a robust and easy to interpret estimate. Since both this and the previous technique are based on statistical average, they provide also a method of checking consistence of adopted models. That is they allows for the computation of the standard deviation of estimated values at a given frequency, that should correspond to the estimated mean value of the spectrum divided by the number of averaged points.

- Standard least squares fitting of measured PSD values with an analytical model can help produce a smooth and easily interpretable estimate while retaining the information at the lowest frequencies. Alas, it has two possible drawbacks:

  - for the fit to be reliable, each point should be weighted with its own error, that is actually equal (or proportional) to the *unknown* theoretical value of the spectrum at that frequency (seen note 8 on page 100). A possible work-around is that of performing an iterating procedure that uses the fit result at present iteration step to assign errors to each experimental point before performing the fit again.

  - More dangerous is the problem of deciding which theoretical model to use to fit the data. A number of physical arguments (i.e. hypothesis about noise sources that produce noises with known shape, or known conversion of flat readout noise via the transfer function. . .) are available for selecting a reasonable set of functions to use for the fit, and produce statistically meaningful results on well shaped PSD estimates. When the estimated PSD presents obvious artifacts or strange shapes, however, it can be difficult both to decide if consider them as statistical fluctuation, rather than actual features of the theoretical spectrum, and to find an analytic function capable of fitting the given set of data.

- A further method has been proposed among the LTP/LISA collaboration [36] to produce smooth PSD estimate with uneven data distribution that can be better adapted to the need of investigating very low frequencies.[11] Once a set of frequencies f_i at which we want to obtain an estimate of the spectrum has been decided, for each of them we divide the original data set in segments (still allowing for a 50% overlapping) of length $L_i = 1/f_i$, so that the lowest frequency point of their Welch Periodogram exactly corresponds to f_i.[12] Then we compute the mean value of the estimates at frequency f_i obtained from the various data segments, and use it as our best estimate of the PSD at that frequency. This way we can highly reduce uncertainty on relatively high frequency points (that require shorter data segments thus allowing for averaging lots of them) while still retaining the information at low frequency (although with higher uncertainty). At present, issues about the correct choice of number and spacing of frequencies for an unbiased, non redundant estimation are under discussion.

The above methods have been tested on synthetic data to produce consistent results both among themselves and with the theoretical spectrum used for generating the data, and are in general considered to be equivalent. Fitting and data binning have been and are currently used in the 1-TM pendulum data analysis, producing stable and repeatable results [22, 33].

7.3 Setting upper limits on GRS related noise sources

The data analysis procedure described so far deals with angles and torques, that are the relevant quantities for a torsion pendulum. However, we built and use the facility to investigate GRS related disturbances, and requirements about them come in terms of force (or, better, acceleration on a 1.96 kg LISA TM).

Although simpler and more reliable than in the case of the single TM facility, we thus need to set-up assumptions and model to interpret the observed pendulum torque noise as an equivalent force noise.

As we want to set upper limits, our approach has to be conservative, preferring the risk of an overestimate of the GRS related force with respect to that of an underestimate. On the other hand, being strictly conservative would prevent us to set any limit at all, as in principle the measured torque noise can always be due to noise source configurations that would correspond to an huge (potentially infinite) force noise. These sources configurations are however exceedingly improbable, and we can thus exclude them in our effort to give a realistic and significant upper limit.

[11] DFT produces equidistant points, that result in very poor frequency logarithmic resolution at low frequencies. This method has been proposed to obtain constant logarithmic resolution.

[12] Because of the unreliability of the last three point estimated with the Blackman-Harris windows (as explained at the end of Section 7.2.1, we take the fourth smallest point as the first good one, thus requiring it to fall at frequency f_i; calculating $L - i$ to obtain this is trivial.

In the following section we will thus present results expressed in terms of force (or acceleration) computed under the following hypothesis:

- each measured excess torque acting on the pendulum, if the source is not clearly identified, can in principle be due to the GRS. Not only sources external to the pendulum, but even the STC sensor cannot be supposed to contribute to the excess noise (all the more so because it has been built with care in reducing related disturbances, employing very large gaps).

- The torque exerted on the pendulum and originating in the GRS can in principle be due completely to forces acting on the TM along the X axis. Moreover we assume them to act in the center of the TM face, or symmetrically distributed on it: their effective arm length in producing a torque on the pendulum is thus supposed to be equal to the TM distance from the suspension point (roughly 10 cm). In the worst case in which the relevant forces are acting close to the inner edge of the TM, it will result in an underestimate of the force noise of order 20% (note that this is only relevant for the conversion from torque to force, and doesn't affect the estimate of the measured excess torque).

- Any possible (and probable) contribution to the observed noise coming from torques directly applied to the TM by GRS related disturbances cannot be distinguished. However, if present, they will cause an overestimate of the X force noise, thus preserving the validity of the upper limit[13].

  Under this hypothesis, the conversion between observed torque N_{obs} and the force values $F_{GRS,max}$ presented as results (easily converted in LISA TM acceleration dividing them by the mass of 1.96 kg) is performed by simply dividing the former by the inertial member arm b[14]:

$$F_{GRS} \leq F_{GRS,max} = \frac{N_{obs}}{b} \approx \frac{N_{obs}}{0.1 \text{ m}}$$

  As such, the meaning of the force values given in the next section should be interpreted as "The maximum GRS related force noise compatible with pendulum observed noise". Obviously, nothing can be said on the minimum: whatever the excess, it could be completely due to causes other than the GRS.

[13]This is true under the hypothesis that the noise sources are uncorrelated. In principle there could be a torque noise on the TM correlated with, and exactly canceling, the effect of the force noise on the X faces, thus resulting in a null net torque on the pendulum. This however belongs to the class of the very highly improbable noise sources configurations

[14]Note that $b = 10.165$ cm; any result in torque (as the graphs shown so far) can be easily converted "by hand" (with an error less than 2%) in equivalent force arising in the GRS by simply multiplying by 10.

7.4 Experimental results

The noise estimation procedure described in the previous section has been applied to a number of data runs, each from 1 to several days in length, during several months of operation of the facility. Because of continuous debugging and improvement, we experienced long term variations in the measured noise spectra related to overall performance gain, as well as temporary degradation due to loss of functionality of some apparatus. Beside them, however, a-posteriori analysis showed that, after reaching a stable level of performance maintained for about one month, the overall facility performances underwent a quite sudden degradation both in overall performances (about a factor 2 around 1 mHz) and in repeatability.

We found that the sudden change coincided with a rearrangement of the facility, that among other interventions included modification to the pumping line. As recent investigation on the 1-TM facility showed the possibility of a noticeable residual coupling between the pump system and the torsion pendulum, actually this is one of the most probable cause: further investigations are currently ongoing.

In the following sections we will present a typical good noise run obtained during a weekend, and a statistical study on two sets of noise runs acquired so far, selected on an a-priori criterion: one set is relative to the period of best functionality of the facility, while the other include also the following period of degraded performances. At the end, we will draw conclusions about the estimation of the measured excess noise, comparing the result with those obtained with the 1-TM facility and drawing conclusions.

7.4.1 Single run torque noise analysis

We already showed in Figure 7.6 the estimated PSD for #20070929 : it can be noted that the readout noise (the high-frequency, f^2-behaved part of the plot) appears to be in optimum agreement with the expected one. Moreover, while at very low frequency the noise clearly departs from the expected pendulum thermal noise by more than one order of magnitude, there is a frequency range around $1mHz$ in which the estimated spectrum seems to be close to the expected thermal limit. However, quite big fluctuations are visible between points at adjacent frequencies: because there are no physical reason to expect them to be due to sharp features in the noise spectrum of the underlying physical process that produced the time series, they are thus interpreted as statistical fluctuations. As such, their presence makes it hard to give a quantitative estimate of how much higher the measured noise is with respect to the thermal one.

We can try to reduce the uncertainty of each point by means of any of the methods presented in Section 7.2.6: Figure 7.7 shows a comparison between Welch

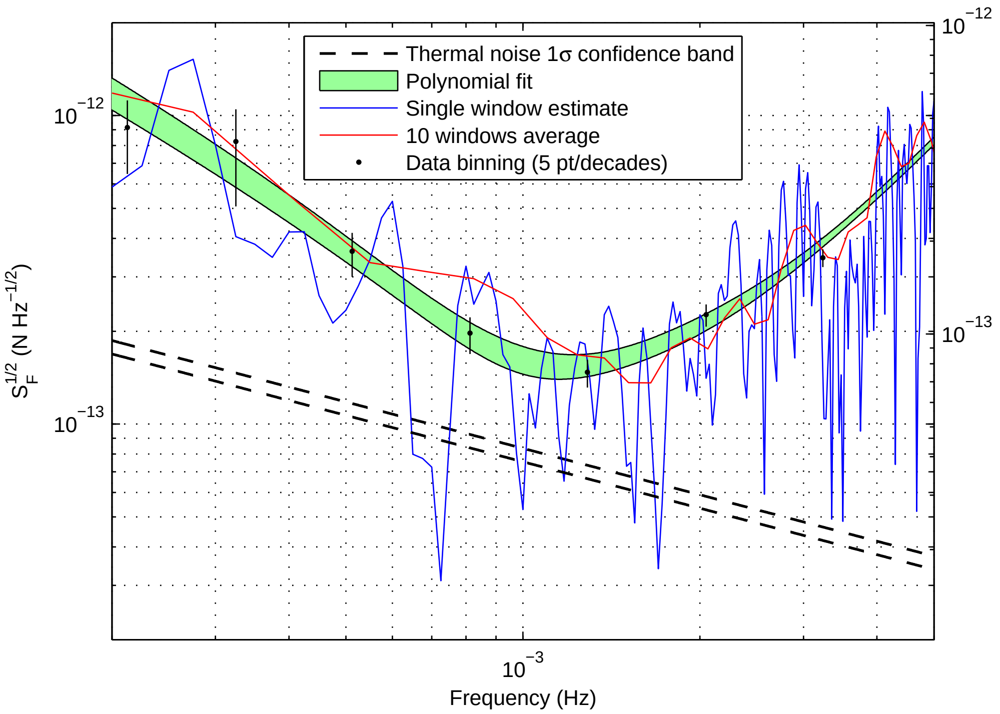

Figure 7.7 – Run #20070929 force noise data from capacitive sensors. Various smoothing techniques are plotted for comparison. While the results are consistent within the errors, the windows averaging technique shows a slight tendency to overestimate the spectrum with respect to the other techniques: a possible explanation is given in the text.

Periodogram smoothing, data binning and fitting with a polynomial model

$$S_N(f) = \frac{b}{f^2} + \frac{c}{f} + d\, f^4$$

applied to run #20070929 . The three methods give consistent results, although the window averaging one shows a slight bump just below 1 mHz.

Similar small deviation of the windows averaging method from other technique have been observed in most runs, always leading to a slight overestimate of the noise: a possible hypothesis, presently under investigation, is that occasional fluctuations in the pendulum noise spectra are overweighted by the averaging procedure. As this method divides the whole time range in smaller time windows and then averages the PSD (and not Linear Spectral Densities), if the noise level in each window is not exactly the same (as it should be for a rigorously stationary process), this method tends to prefer the highest one (as it averages the squared quantities instead of the linear one), thus resulting in an higher overall estimate of the noise with respect to a PSD computed on the whole time range. Another possible hypothesis is that of a change in phase of the noise signal from one windows to another: to make an example, if a sinusoidal signal suddenly change its phase by π at half the time range, it would give a null contribution upon integration on the whole time range because of the change in sign; on the contrary, if we divide the time range in two segments, integrate and then average quadratically, the sign difference is lost and the results will be different from zero.

Also the fitting method shows a small variability, depending on the theoretical model chosen (as for example including or not a constant term). While typically this doesn't noticeably affect the minimum estimated excess noise, usually found near the crossover frequency between the readout noise and the pendulum mechanical noise dominated regions, it strongly changes the values of the coefficients of the various terms of the polynomial, making it difficult to draw conclusion about the origin of the excess from its frequency dependence. In Figure 7.8 the 1σ confidence band obtained with two different models fitting another run (#20071002) is shown, along with each polynomial term contribution: while the overall shape of the curve and its minimum are quite similar, the contribution of the different terms (except the f^4 one coming from the conversion in torque of the readout noise) varies substantially in the two cases.

One possible explanation is that the frequency region in which we are fitting is too small to clearly discriminate the behavior of the different power law at low frequencies. While extending the frequency region in which to fit the data would probably help in better interpreting the results, we are currently unable to do that: we are limited at high frequency by the f^4 readout noise rapidly masking all other contributions, and at low frequency by the presence of sporadic relevant events disturbing the pendulum at an approximate rate of one per day. While we have well-founded reasons to attribute them to external events (as they show up in environmental monitors too, and often affect also the very stiff tilt DOF), we have not yet found their cause(s), and we are forced to remove them from the data stream thus limiting the maximum length of contiguous data.

We recall that, as stated at the end of Section 7.2.5, CSD analysis on single run data produces ambiguous and scarcely reproducible results, probably due to poor autocollimator performances. Given the big fluctuation of the CSD phase, an estimation "by eye" is not feasible and some sort of averaging is required. However, it is not easy to fit with a theoretical model similar to those used for the capacitive data (accounting for an f^4 readout term and some negative power mechanical noise ones); also data binning shows exotic structures and region of completely uncorrelated data (incompatible even with a correlated signal of the level of the pendulum thermal noise) that allows no easy interpretation. We thus do not present here any CSD analysis based on single runs, as in this condition it appears to be an unreliable tool.

In the following section we will present an excess noise estimation based on a statistical study of a set of noise runs.

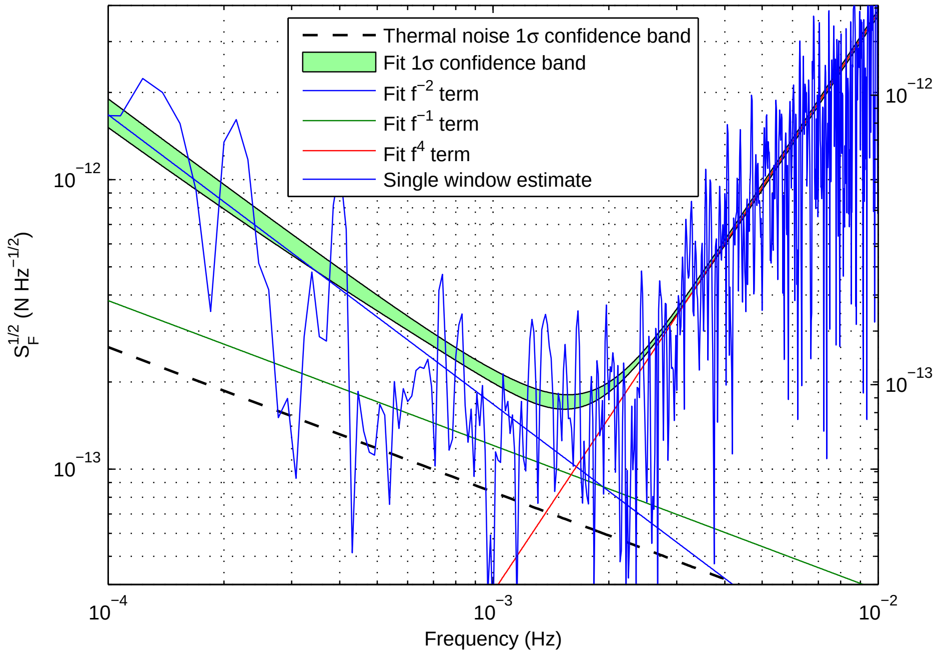

(a)

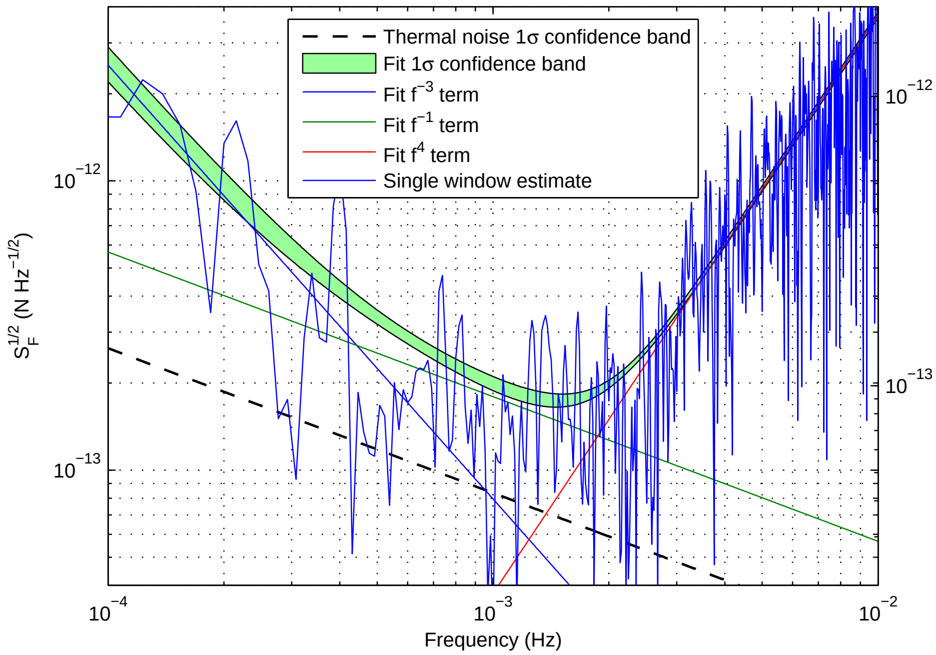

(b)

Figure 7.8 – Both figures show the result of a polynomial fit to capacitive sensors force noise data of #20071002 , along with the contribution of single terms. In (a), however, the lowest order term is f^{-2}, while in (b) it has been substituted by an f^{-3} term. It can be seen that, while this did not change considerably the overall and minimum estimate of the noise, it had a big impact on the values of the f^{-1} coefficient: the example shows that this kind of variability makes it difficult to chose a theoretical model, or point out a precise dependency from a specific term, as in so small a frequency region different combinations of terms can fit the data with similar results.

7.4.2 Estimation of the average torque noise

In analyzing side by side several sets of data in the effort of obtaining a more reliable and accurate estimate of the excess noise, we noted a clear, although not huge, change in measured noise level and stability: after some investigation, we found that it was possible to distinguish to period of time characterized by clearly different performances. Moreover, exactly in between the two periods the facility underwent a rearrangement due to overall laboratory reorganization. This included interventions on almost every external subsystem, in particular acquisition systems and pumping line, that are both probable candidates for an overall facility performance degradation (the first because of injected readout noise, the second by means of possible induced vibrations causing real pendulum motion or relative sensor displacement, as observed in the 1-TM facility [33]). While the exact cause of the increased noise is under investigation, it appears reasonable to consider the runs prior to the intervention as representative of the measured excess noise (we will refer to them as "Set1"); nevertheless, a statistical study on the whole set of run will be presented for completeness.

The noise run to include in the study were selected based on both a-priori criteria and on-inspection vetoes. In particular, these are the characteristics to used to select a run for Set1:

- being acquired before the facility rearrangement
- correspond to a weekend (Friday, Saturday or Sunday) night
- having data available from 8 p.m. to 7 a.m. This was chosen both to allow for homogeneous run length (thus resulting in easier averaging) and to avoid known potentially disturbing events, for example a daily step in the measured magnetic field at about 7:40 in the morning.
- showing no visible anomalies on inspection of environmental variable data
- showing no extraordinary noise torque isolated events ("kicks"), here meaning single spikes several orders of magnitude above the RMS torque noise value. Note that, although preventively specified, we excluded no run from Set1 based on this criterion.

Based on this criteria, six 11-hours runs were selected, and data from both autocollimator and capacitive sensors were processed as explained and demonstrated in the previous sections, then averaged obtaining a point by point mean and standard deviation; this yielded an error estimate for each point that can be compared with the theoretical values, equal to the spectrum itself (for which we have the mean as an estimator). The resulting average ratio of 0.91 between the calculated point by point standard deviation and mean is shown in Figure 7.9, and states a substantial compatibility of the data with the model of a stationary, random process.

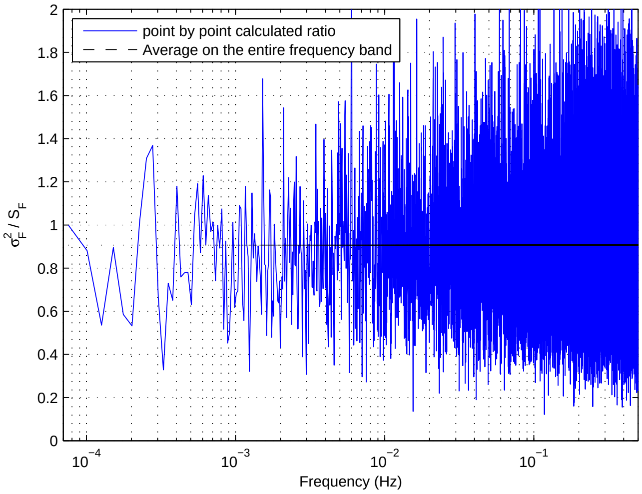

Figure 7.9 – A plot of the ratio between the standard deviation of each PSD point, result of the average of six runs, and its mean value. According to the hypothesis that the torque noise is a stationary random process, this value should be 1. The average value shown in the image by the black line is about 0.91. Not also that, although here the average value is mainly contributed by high frequency ($\gtrsim$ 10 mHz) points related to the readout system rather than to the pendulum mechanical noise, restricting the analysis points below 10 mHz yields the same result.

Figure 7.10 shows the resulting averaged spectrum for both autocollimator and capacitive sensors, obviously affected by much smaller fluctuation with respect to the single run estimates, thus allowing for a more reliable evaluation of the measured noise levels. The standard deviation of the mean is plotted as vertical bars. A fit to an empirical model well suited to the data has been drawn for capacitive sensor data; no analogous has been drawn for autocollimator data, as the excess noise reshape the overall spectrum making fitting it very hard.

We note here that, contrary to what has been said in 7.2.6 about smoothing single window data, in applying the fitting procedure to averaged data no iterative error evaluation is required: each point already comes with its error computed as standard deviation of the mean, and these are the errors to use to weight the fitted points.

In Figure 7.11, finally, the difference between the capacitive sensors data PSD and the theoretical thermal noise PSD is presented as an estimate of the excess noise. Please note that the f^4 (f^2 in the plotted LSD) behavior that dominates the high frequency region is very unlikely due to a real excess pendulum torque noise; instead, it is more probably mainly contributed by nearly white readout noise converted to an f^4 behavior by the pendulum transfer function shape. The fit, that is in good agreement with data points and relative errors, helps in making a smoother estimate and shows a minimum excess noise in the range

$$S_{F,exc}^{1/2} = 115 \div 130 \ \frac{\mathrm{fN}}{\mathrm{Hz}^{1/2}}$$

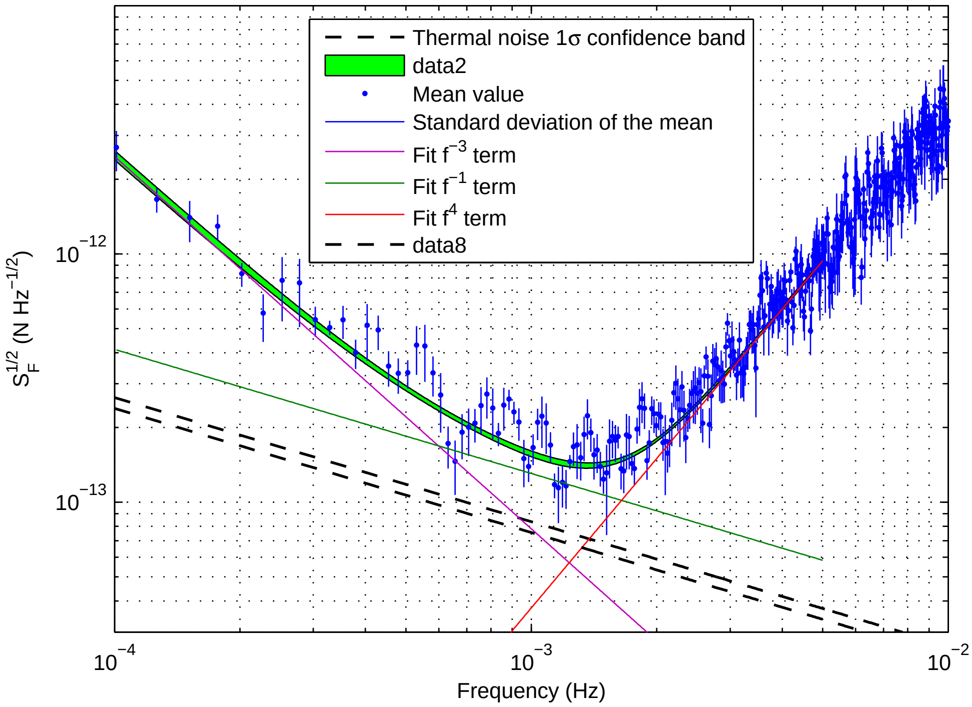

(a) Capacitive sensors

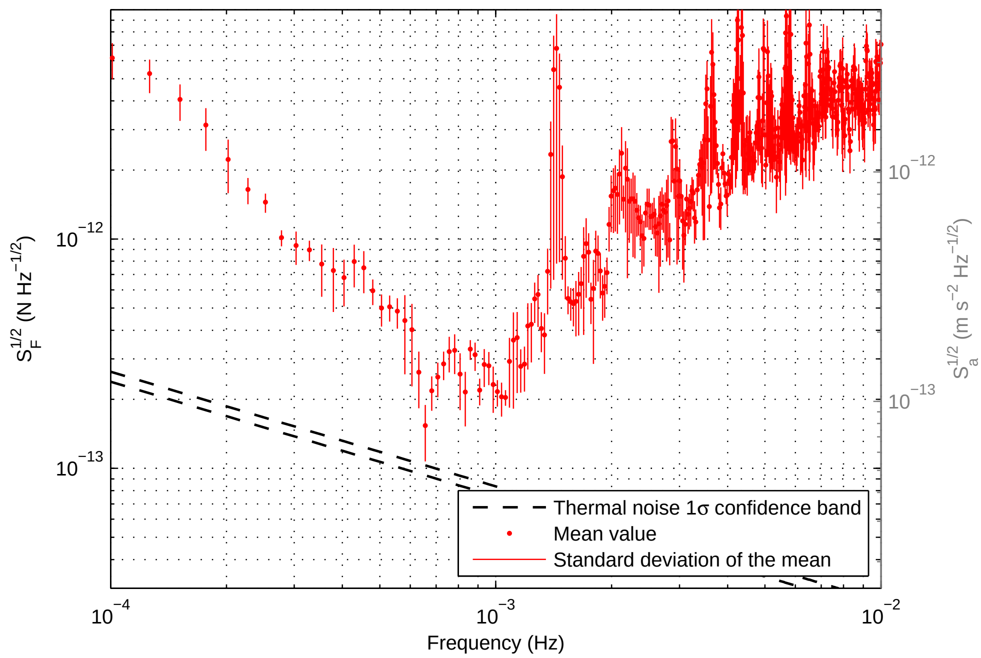

(b) Autocollimator

Figure 7.10 – In (a) and (b) we show the result of averaging capacitive sensors and autocollimator data of the six run of Set1: the advantage in term of reduction of fluctuation, as expected, is clear. Note how much noisier the autocollimator is with respect to the capacitive sensors. While we found very difficult and not useful to fit the former because of the very strange shape, we performed on the second a polynomial fit involving terms in f^{-3}, f^{-1} and f^4. The choice of the f^{-3} term was suggested by no physical reason, but only for its suitability to fit the given data at low frequency.

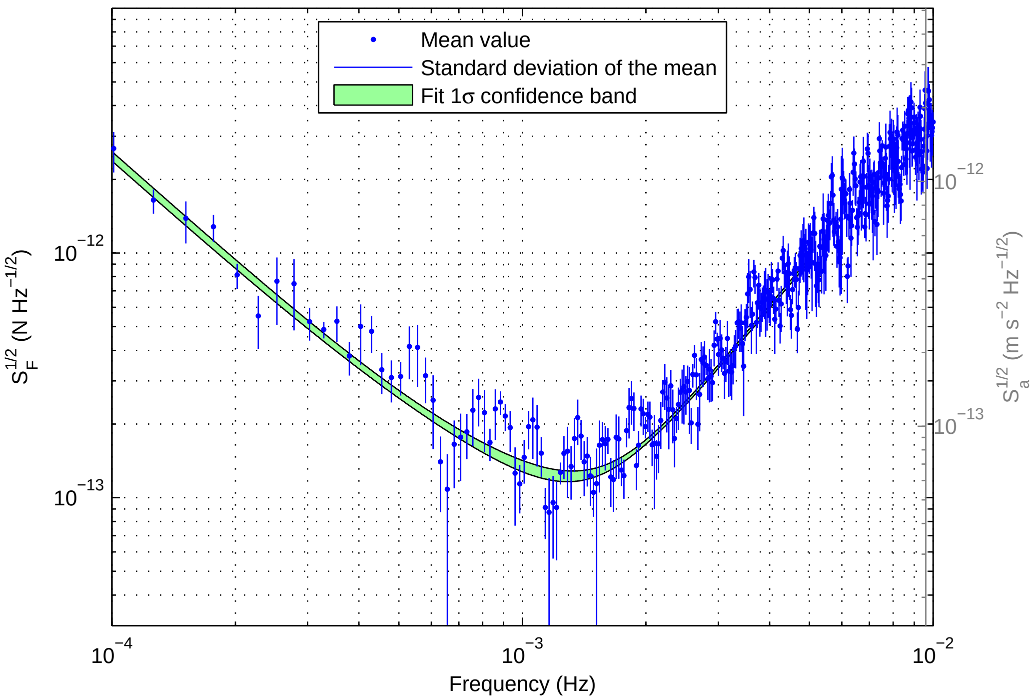

Figure 7.11 – Excess noise estimation obtained subtracting the expected fiber thermal noise from the measured torque noise. Averaged data over the six runs are shown along with a polynomial fitting. Note that the high frequency f^4 behavior is mainly contributed by readout noise and should not be interpreted as a real measured excess torque noise. As you can see, both the fit and the scattered data are consistent with a minimum excess of about $115 \div 130$ fN/Hz$^{1/2}$ slightly above 1 mHz.

at about 1.3 mHz.

Given the reduced uncertainty and the overall higher "cleanliness" of the spectra obtained by averaging, we tried to apply CSD analysis (explained in Section 7.2.5 and unsuccessfully applied to single runs, as already stated): we averaged the CSDs computed individually for each run, and then took the real part to represent the correlated part of the signal seen by both sensors, and the standard deviation of the mean as its error. In Figure 7.12, the resulting CSD shows a low frequency value almost equal to the one of the capacitive sensor data PSD, meaning that, there, capacitive sensors are measuring the real motion of the pendulum. On the other hand, CSD value around and above 1 mHz is observably lower than the capacitive sensors (and, obviously, autocollimator) one. Although slightly dependent on the model used, the fits performed here and on the capacitive sensor data PSD, based on the same model, can help us make some comparison.

For this comparison, we fitted both data sets (PSD and CSD) with the model

$$\frac{a}{f^3} + \frac{b}{f} + cf^4$$

Among the different combinations of negative power terms down to f^{-4} (we are

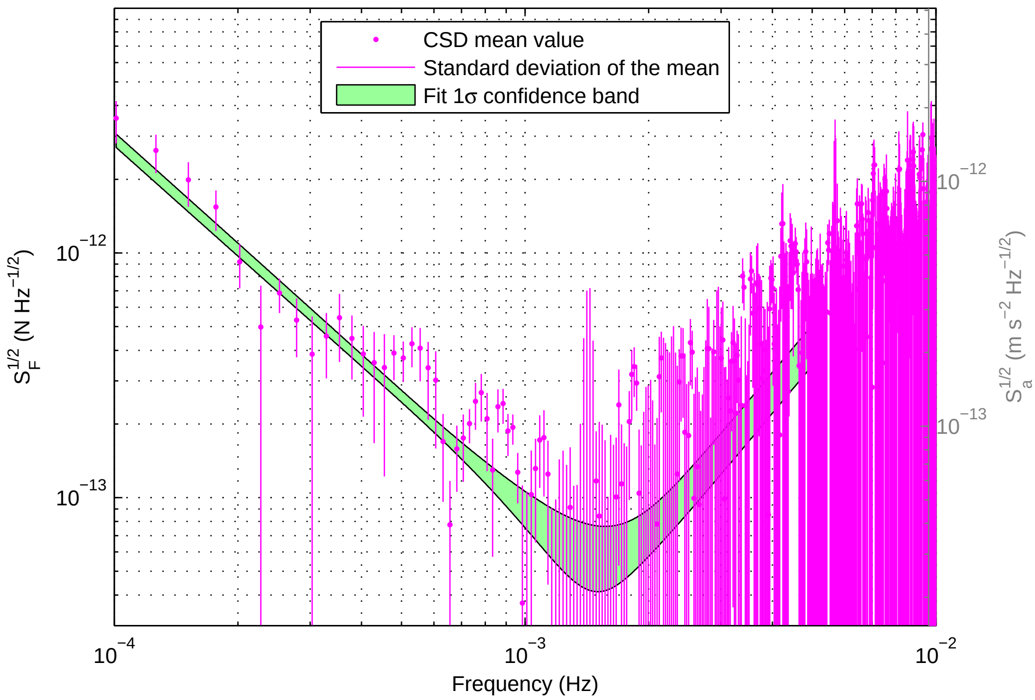

Figure 7.12 – The plot shows the noise excess estimate obtained by averaging the CSD independently obtained for each of the six different runs of Set1. A weighted fit to the model $a\,f^{-3} + b\,f^{-1} + c\,f^{4}$ is also shown: the results, especially for what concern the minimum, have shown to be model dependent and should be thus considered carefully; nevertheless, the f^4 term compared to that obtained fitting the capacitive sensors PSD (see Figure 7.11) clearly shows that CSD analysis substantially reduces the uncorrelated part of the noise. As in that case, the residual f^4 term, although somehow unexpected, is very unlikely due to a real motion of the pendulum and should rather be interpreted as a correlation in the readout noise of the two sensors, whose origin is currently under investigation.

Coefficient		PSD	CSD
a	(N^2/Hz^5)	$(6.1\pm0.5)\cdot 10^{-36}$	$(8.5\pm1)\cdot 10^{-36}$
b	(N^2)	$(17\pm1)\cdot 10^{-30}$	$(6\pm3)\cdot 10^{-30}$
c	(N^2Hz^2)	$(14.1\pm0.5)\cdot 10^{-16}$	$(3\pm1)\cdot 10^{-16}$

Table 7.1 – Comparison of the coefficients obtained by fitting the capacitive sensors torque data PSD and the capacitive sensors and autocollimator torque data CSD to the model $a\,f^{-3}+b\,f^{-1}+c\,f^4$, selected among several trials as the one that best fits the data without producing negative (unphysical) coefficients.

much more confident on the f^4 shape of the high frequency noise than on the low frequency one), it gave the best results in both data sets in terms of minimizing residuals and χ^2 without implying unphysical negative coefficients. Table 7.1 lists the coefficient obtained for the three terms of the fit in both cases.

It can be seen that there are relatively small differences among the f^{-3} and f^{-1} terms, meaning that no substantial contribution came from the sensors at low frequencies. Completely different is the situation at high frequency: the CSD f^4 term is 5 times smaller than the corresponding term coming from capacitive data fit, meaning that a big part of the high frequency readout noise visible for example in Figure 7.11 is contributed by the capacitive sensors independently. This was expected, as the CSD is aimed at extracting only correlated part of the signals: the strange thing here is the residual coefficient, that should in principle be compatible with 0 under the hypothesis of uncorrelated readout noises, but is not. As a real motion of the pendulum at those frequencies is exceedingly improbable (requiring a torque noise source increasing in power as f^4), we should look for other possible causes of correlation among the readouts: one possible explanation is a rotational vibration of the vacuum chamber with respect to the inertial frame, in which the pendulum stays almost still at high frequency. If it were so, by dividing the correlated torque noise (note that the table reports coefficients relative to the force noise PSD, that have to be multiplied by the pendulum arm b^2 to obtain the torque) by the transfer function, that for $f \gg f_0$ is

$$H(f \gg f_0) \approx \frac{1}{\Gamma\left(\frac{f}{f_0}\right)^2} = \frac{1}{I(2\pi)^2 f}$$

with I the moment of inertia, we can obtain the correspondent angular noise (supposed to be white to explain the f^4 behavior):

$$\frac{b\sqrt{(2 \div 4)\cdot 10^{-16}\ \mathrm{N^2/Hz^5}}}{I(2\pi)^2} = (1.0 \div 1.4)\cdot 10^{-8}\ \frac{\mathrm{rad}}{\mathrm{Hz^{1/2}}}$$

Still looking at the fit performed on the CSD data, we can notice that the estimate of the minimum excess noise around 1.5 mHz is reduced to:

$$S_{F,exc}^{1/2} = (40 \div 80)\ \frac{\mathrm{fN}}{\mathrm{Hz}^{1/2}}$$

A factor 2 better than using the capacitive sensors alone. However, given that both results are model dependent, and this difference only involve the small "best performance" frequency region above 1 mHz, this number should be carefully considered not to risk to underestimate the observed excess. This is particularly true as we can note that the CSD, when binned, shows periodic structures that have not yet been understood.

For comparison, Figures 7.13 and 7.14 shows the same type of analysis repeated on Set2, in which we included all the run satisfying the same conditions of Set1 except that of being acquired before the facility rearrangement. While we will not comment on them further, as they have exactly the same interpretation of those discussed so far, we observe only that the very low frequency and the readout contributed noises are almost the same as in Set1, while there is a significant performance degradation (about a factor 2) in the best sensitivity zone slightly above 1 mHz. As already explained, we expect this to be due to some external noise source became important after facility rearrangement, and currently under investigation.

7.4.3 Conclusion

Presented experimental results clearly demonstrate the 4-TM pendulum ability, via representative *force* measurements, to place upper limits on the force noise exerted by the GRS at level very close to overall LTP requirements. With respect to LISA requirements, it corresponds to a factor from 10 (just above 1 mHz) to 20 (in the band $1 - 5$ mHz) higher.

Complemented with single mass facility estimates relative to a class of disturbances with arm length of order 1 cm [33], they demonstrate overall LTP requirements fulfillment down to about 1.5 mHz, as shown in Figure 7.15. This also further lowers the gap from LISA overall requirements, limited to a factor 10 (just above 1 mHz) to 3 (at about $10^{-2} mHz$ and above).

In spite of this important result, a definite excess with respect to the theoretical instrumental lower limit, set by the fiber thermal noise in the frequency region below about 1.5 mHz, has been measured. Although we cannot exclude a GRS contribution, present facility debugging status suggests possible residual dependencies on environmental variables: clues are both observed sporadic relevant external events impacting on facility measurements, and residual high frequency readout noise correlation among different sensors, very unlikely to be due to actual torque noise.

Additional investigation is thus needed to pinpoint residual coupling (explicitly measuring coupling factors as for example twist-tilt effect or magnetic moment) and try to reach a more stable, environmental independent performance level.

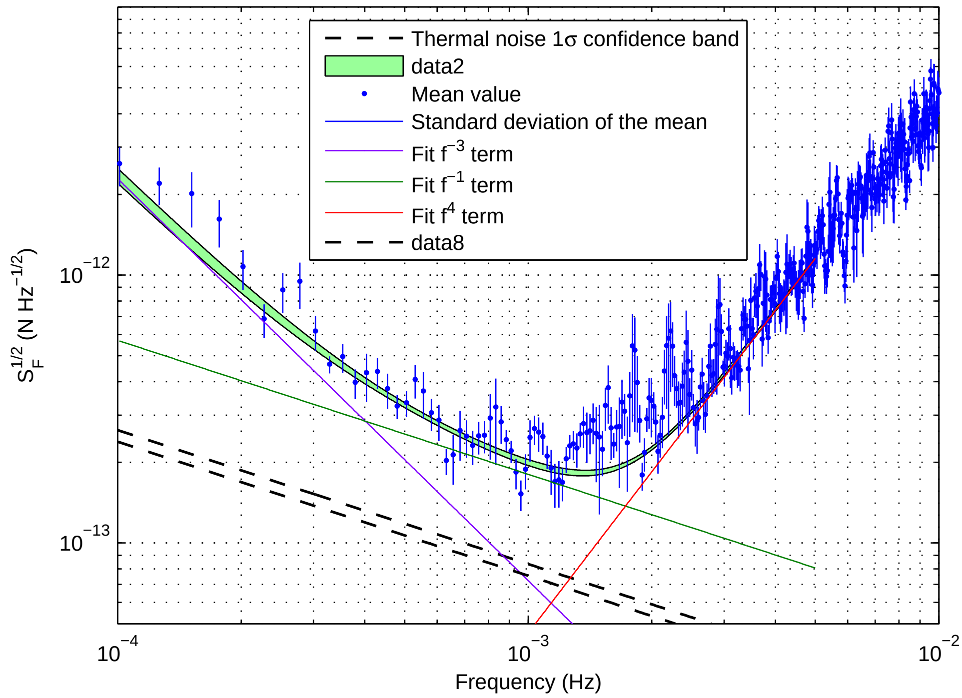

(a) Capacitive sensors

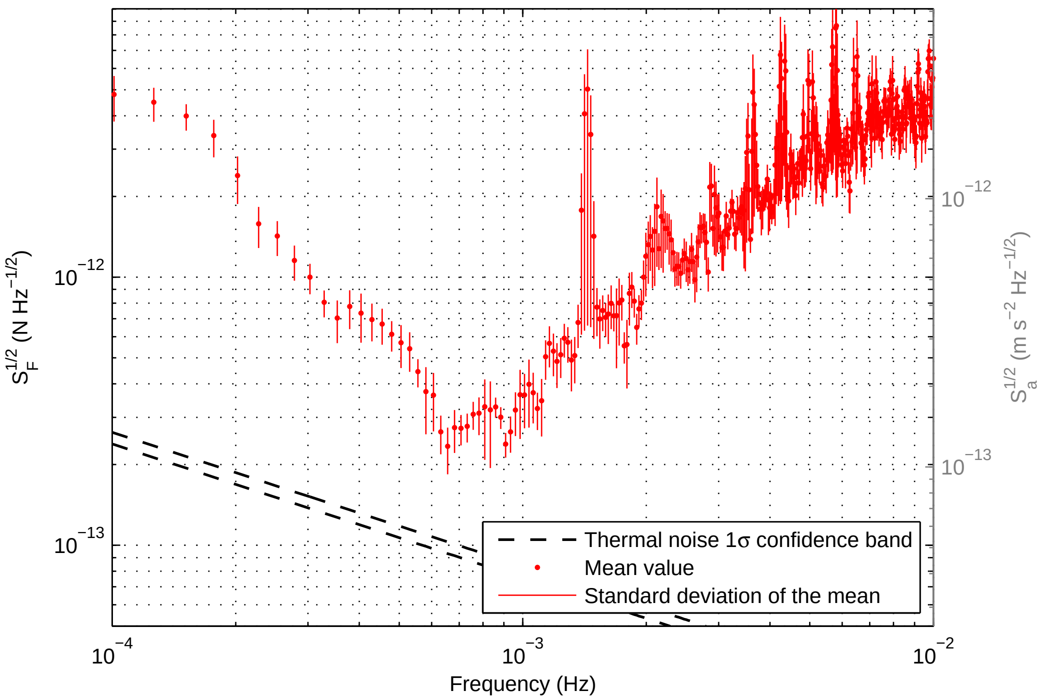

(b) Autocollimator

Figure 7.13 – In (a) and (b) we show the result of averaging both autocollimator and capacitive sensors data among runs belonging to Set2. They should be compared to results shown in Figure 7.10, and same consideration apply. We note that very low frequency mechanical noise and high frequency readout noise appear not to be substantially changed, while there is a net, although not huge, degradation of performances in the best sensitivity region around 1 mHz.

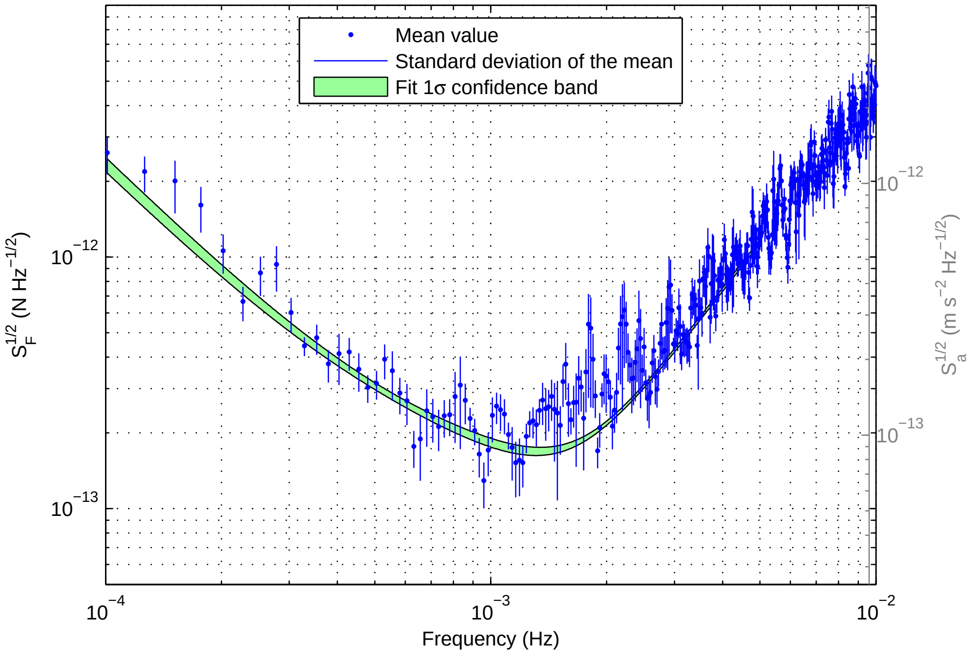

(a) Capacitive sensors

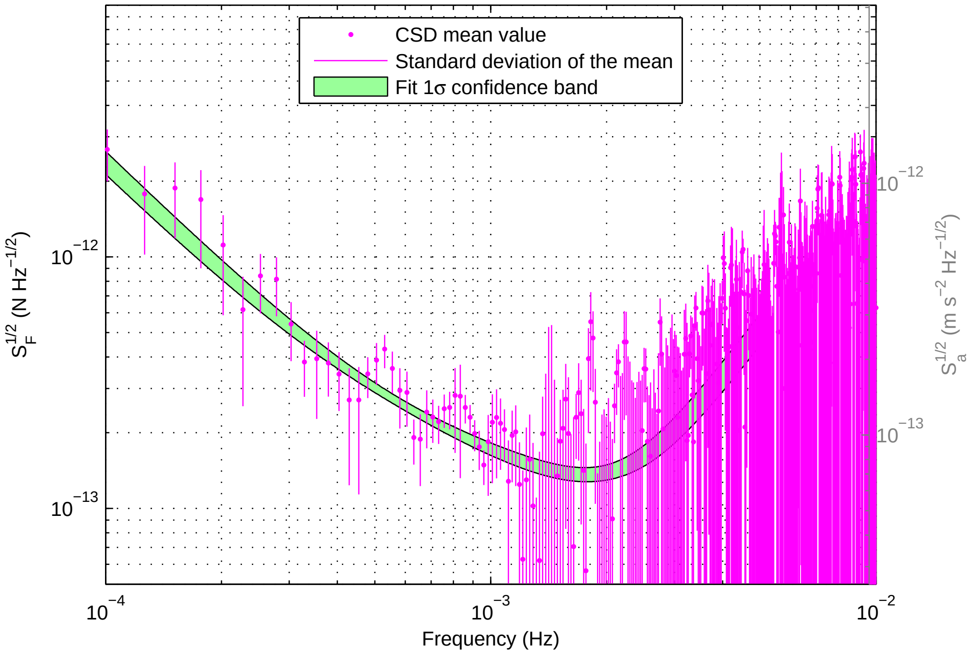

(b) Autocollimator

Figure 7.14 – Set2 average torque noise PSD (a) and cross spectral density (b) difference from the theoretical thermal noise; the latter represents the best estimate of the excess measured torque noise in the mid-low frequency region not dominated by the f^4 term. Both figures should be compared to Figures 7.11 and 7.12 showing the same analysis computed on Set1, and same comments found there apply for their interpretation. While the very low frequency noise (below 10^{-3} Hz) is almost equal in the two set, above 10^{-3} Hz Set2 shows an evident degradation both in readout-dominated noise and in the minimum excess estimation, about a factor two higher than that of Set1.

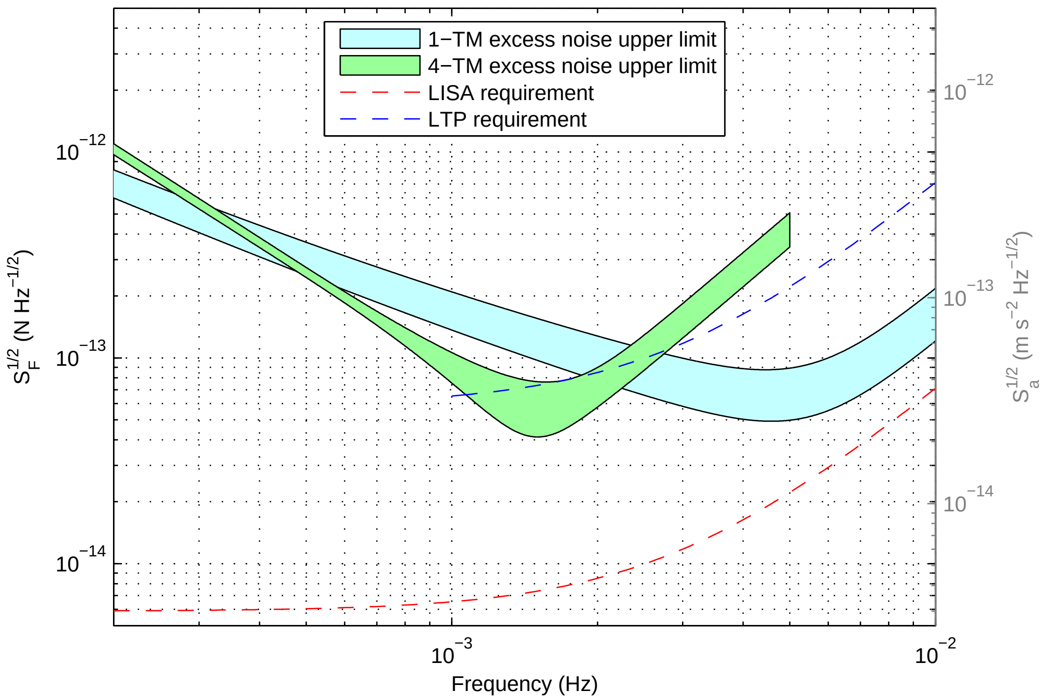

Figure 7.15 – Upper limit set by independent 4-TM and single 1TM facilities campaigns, compared to LTP and LISA noise budgets. Joining the result of the two facility it is possible to place upper limits to GRS related disturbances within LTP requirements at about 1.5 mHz and above.

Moreover, environmental monitor performance improvement would be desirable, as our ability to measure most of the potentially relevant variables is currently limited by instrumental noise.

In addition, improving the auxiliary optical readout system would be of further help, as the autocollimator performances limits the present ability of cross correlation analysis with the more sensitive capacitive sensors. Current proposal is to employ the Optical Readout System already installed into the facility but still in a debugging phase (see Section C).

By extensively employing the presented data analysis techniques to extract relevant information from the pendulum total measured torque, this study also allow us to demonstrate their effectiveness and the possibility of exploiting them for LTP data analysis.

Chapter 8

GRS related force gradient: the "stiffness"

To search for unmodeled force gradient effects and to confirm the GRS electrostatic model (already investigated with the single mass pendulum) through a direct force detection, we measured the "stiffness" that couples the GRS to the TM. As introduced in Section 2.2, it has an important role in the noise model as it converts spacecraft-TM relative position noise in TM acceleration noise.

Magnetic and gravitational effects, that can cause relevant interactions between the GRS and the TM in LTP and LISA, are related to the bulk properties of the TM and will not be measurable with the hollow mock-up employed in the facilities. According to the present noise budget[10], we thus expect the electrostatic force to be the dominant spring-like term among the modeled ones detectable with both torsion pendulums. This is in agreement with previous measurements performed with the single-mass pendulum that, based on estimates derived from rotational stiffness measurement through an equivalent arm, found measurable but small excess [28]. The 4-TM facility offers now the opportunity for a further investigation by means of directly measuring the force (and force gradient) acting between the GRS and the TM along the X axis, increasing the level of representativity of the threatening interactions that can jeopardize the LTP and LISA missions.

A comprehensive and exhaustive study of the role of the various parameters that affect the electrostatic interaction is scheduled but has not yet been performed. We present here a measure of the overall GRS-TM spring-like coupling together with a study of its dependence upon the applied sensing bias, that is foreseen to be the most relevant contribution when actuation fields are switched off [10].

8.1 Electrostatic model and the origin of the electrostatic stiffness

The capacitive readout requires high frequency polarization of the TM inside the grounded EH. Moreover, as listed in Section 2.2.1, a number of different effects can contribute to an RMS variation of the potential of the TM or surrounding surfaces. Thus there is a voltage drop between the TM itself and the surrounding EH, and the resulting electric fields gives rise to attractive forces. Along with an average value, these forces have in general a non-zero gradient and, according to Section 2.2, to first order they can be modeled as "stiffnesses".

Although this type of interaction has already been formalized in Equation 2.20, a simple example can help understanding the underlying mechanism: the TM, along with facing EH walls, is a capacitor with capacitance C_{tot} contributed by all the surrounding surfaces. However, if we adopt the electrostatic model and assumptions introduced in Appendix A, the only capacitances that are functions of x are those relative to the $X+$ and $X-$ faces. Thus the force along X corresponding to a voltage drop V between the TM and the EH has the form:

$$F_X = \frac{1}{2}V^2\left(\frac{\partial C_{X+}}{\partial x} + \frac{\partial C_{X-}}{\partial x}\right) \tag{8.1}$$

where $C_{X\pm}$ and their derivatives are defined as in Equations A.1, with A the area of a TM face.

Substituting Equation A.1b in Equation 8.1 and computing for $x = 0$ shows that no electrostatic force acts on the TM when it is centered[1]. However, a force gradient is still present, and can be easily shown by series expansion of Equation 8.1 around $x = 0$:

$$\begin{aligned} F_X(x) &= F_X(0) + F'_X(0)x + \frac{1}{2}F''_X(0)x^2 + \ldots \approx \\ &\approx \frac{1}{2}V^2\left(\frac{\partial C_{X+}}{\partial x}(0) + \frac{\partial C_{X-}}{\partial x}(0) + \left(\frac{\partial^2 C_{X+}}{\partial x^2}(0) + \frac{\partial^2 C_{X-}}{\partial x^2}(0)\right)x\right) \end{aligned} \tag{8.2}$$

[1]Actually, it should be noted that here $x = 0$ means the point in which $\sum_i \frac{\partial C_i}{\partial x} = 0$ (C_i being the surrounding surfaces capacitances toward the TM), that in an ideal design should exactly coincide with the point in which the capacitances between TM and opposing electrodes are equal, thus yielding a null displacement readout signal. Actually, the "sensing zero" and "force zero" points may not coincide, due to both geometrical factors (machining and aligning imperfections) or asymmetric interaction (e.g. between the TM and nominally grounded surrounding surfaces, that actually have different potentials). In Section 9.3 we give a measure of this difference. Anyway we can always make them coincide at least in principle, by adding an offset to the sensing output.

Using again Equations A.1:

$$F_X(0) = \frac{1}{2}V^2\left(\frac{C_X}{d} + \frac{-C_X}{d}\right) = 0 \tag{8.3a}$$

$$F'_X(0) = \frac{1}{2}V^2\left(\frac{2C_X}{d^2} + \frac{2C_X}{d^2}\right) = 2V^2\frac{C_X}{d^2} \tag{8.3b}$$

$$\ldots$$

and finally

$$F_X(x) \approx 2V^2\frac{C_X}{d^2}x \tag{8.4}$$

This simple example deals only with equipotential EH faces to show the mechanism that gives rise to the "stiffness". As shown by Equation 2.20, when computing the calculation in realistic situations, we should account for different potentials of the various surfaces surrounding the TM, affected by the mechanisms listed in Section 2.2.1. The interaction between TM and each surrounding surface (where one surface is a portion of EH with homogeneous electrical characteristics) should then be evaluated separately, and the different contribution summed over all the relevant surfaces. Moreover, stray biases on the EH also affects the TM potential in a position dependent way. When evaluating their effect, the first order expansion should account also of V_{TM} derivative with respect to x (as shown by Equation 2.20c. Note anyway that the electrostatic interaction always give rise to a *negative* spring constant, thus making a free TM unstable. In the torsion pendulum facilities, it opposes the fiber spring constant, and the pendulum remains stable as long as the latter is bigger.

In the following we list the main foreseen sources of electrostatic stiffness.

8.1.1 Sensing stiffness

As the TM voltage V_S due to sensing bias is a sinusoidal signal of frequency $f = 100$ kHz and amplitude $V_{S,0} = \alpha V_{inj}$ (with α defined in Section 2.1), we can write

$$V_S(t) = V_{S,0}\sin(2\pi f t) \qquad \Rightarrow \qquad V_S^2(t) = \frac{V_{S,0}^2}{2}\left(1 - cos(4\pi f t)\right) \tag{8.5}$$

An off-center (i.e. $x \neq 0$) TM will thus experience a net displacement-proportional force along X, together with a zero-mean sinusoidal force at twice the sensing bias frequency. As the latter is in a frequency region of absolutely no interest and produce no detectable motion of the TM because of its inertia, we can neglect it and consider only the zero-frequency term. According to Equation 8.4 and considering that the injection TM voltage is independent of x as long as we consider C_{tot} to be so[2], it gives rise to a spring-like force

[2]It is a very reasonable approximation because of the compensation effect due to the EH completely surrounding the TM: as this moves to one side, corresponding capacitances increase while

$$F_X(x) \approx V_{S,0}^2 \frac{C_X}{d^2} x = k_{sens} x \tag{8.6}$$

that is the same expression we found in 2.20a.

8.1.2 TM charge

In space, the TM will be continuously hit by cosmic rays that can lead to accrual of a charge Q (see Section 2.2.1). Also in the laboratory a variety of mechanisms can cause a charge Q to accumulate on the TM.

Charge residing on the TM induces a voltage drop $V_Q = Q/C$ with respect to the EH. Besides coupling with the stray voltages to produce a net force, 2.20b shows that this term also contributes to the total electrostatic stiffness with both a linear and a quadratic term. From rough preliminary estimates based on typical observed stray voltages values, the linear term is expected to be small compared to the quadratic one, but since it depends on the particular stray voltage distribution it needs experimental investigation.

8.1.3 DC Biases

DC-biases contribute to the total stiffness via a variety of effects: they directly contribute the RMS voltage drop between the EH and the TM, they polarize the TM and they couple to the TM charge. As expressed by Equation 2.20c, the overall dependency of the stiffness on DC-biases distributions is complicated and difficult to estimate a-priori. However, given the expected RMS values of stray voltages of order 100 mV, it should constitute few percents of the sensing one: experimental investigations are still ongoing.

As we will see in the next chapter, DC-biases are much more dangerous for they contribute to the net force, when coupling with TM charge.

8.2 Measurement technique

Measuring pendulum overall stiffness with or without the GRS would be the most natural way of measuring the GRS contribution. However, this is not only unpractical, but it also prevents us from individually measuring the various contributions.

Instead, a number of different techniques can be exploited to estimate the overall interaction as well as the single contributions, thus leading to a more detailed confirmation of the models that underlie the noise budget estimation and apportioning.

In the following we will describe the techniques employed for measuring overall stiffness, and that related to sensing bias and charge, while in Section 8.3 we will present the result of this preliminary investigation.

the opposite ones decrease. For TM movements about the geometrical center of the EH, this is a second order effect.

8.2.1 Global stiffness

As introduced in Section 3.2, the general technique for investigating a known source of force on the TM consists in the modulation of a scale parameter (i.e. a parameter to which the known effect is proportional) and the analysis of the coherent motion of the pendulum to compute the torque acting on it (that in the 4-TM facility is dominated by the force exerted on the TM along the X axis). In this case, as the force has the form $F_X = -kx$, the scale parameter we modulate is the displacement x between the TM and the GRS.

To better understand the measurement technique, let us consider the following picture: the inertial member experiences a number of external torques N_i, including that due to the fiber. They can be expanded to the first order in the limit in which the pendulum motion around the resulting equilibrium point ϕ_0 is small compared to the scale of variation of the torque themselves. The GRS is then aligned in such a way that with $\phi = \phi_0$ the TM position is in the equilibrium point of the GRS related stiffness, and its readout shifted to read 0 in this position. Finally, the autocollimator is fixed with respect to the local inertial reference frame, and is assumed to read the angle ϕ. Setting $\phi_0 \equiv 0$[3] (that means adding a suitable offset to the autocollimator readout), and expanding in series:

$$N_{tot}(\phi) = \sum_i N_i(\phi) \approx \sum_i \left(N_i(0) + \left.\frac{\partial N_i}{\partial \phi}\right|_{\phi=0} \phi \right) = \sum_i \left.\frac{\partial N_i}{\partial \phi}\right|_{\phi=0} \phi$$

where $\sum_i N_i(0) = 0$ by definition of ϕ_0. Thus, $\sum_i \frac{\partial N_i}{\partial \phi}\big|_{\phi=0}$ can be thought of as a torsional spring constant Γ_{tot} so that

$$N_{tot}(\phi) \approx -\Gamma_{tot}\phi$$

If we define Γ as the torsional spring constant obtained by summing all the N_i contributions except those related to the GRS, the equation of motion becomes:

$$I\phi''(t) + \Gamma\phi(t) = N_{GRS} \tag{8.7}$$

Where N_{GRS} are all the source of stiffness not included in Γ, i.e. those arising in the GRS.

On the other hand, the contribution given by the GRS translational stiffness (as defined in the previous section) when the TM is offset by x with respect to the its equilibrium point, can be expressed as a rotational spring constant by means of the relations that hold in the small angle approximation, and expanded to the first order

[3] We observe that the above assumptions about the zeros of sensing readouts and stiffnesses serve to simplify the following calculation. However, they are not necessary from a practical point of view because of the modulation-demodulation technique we use to extract the signal, that gets rid of any DC contribution coming from readout or position offsets.

as above:

$$\phi \approx \frac{x}{b}; \quad N = bF; \qquad \Rightarrow \qquad -bK_{GRS}x = bF_{GRS} = N_{GRS} \approx -\Gamma_{GRS}(\phi - \tilde{\phi}) \quad (8.8)$$

where b is the pendulum arm and $F_{GRS} = -K_{GRS}x$ is the force arising in the GRS due to its spring-like coupling K_{GRS} with the TM. $\tilde{\phi}$ is the position of the GRS itself, until now supposed to be zero.

Substituting the expression for the GRS contribution in Equation 8.7:

$$I\phi''(t) + \Gamma\phi(t) = -\Gamma_{GRS}\left(\phi(t) - \tilde{\phi}(t)\right) = -K_{GRS}b^2\left(\phi(t) - \tilde{\phi}(t)\right) \quad (8.9)$$

where $\tilde{\phi}$ has been expressed as a function of t as it can be changed in time moving the GRS position $\tilde{x}(t) = b\tilde{\phi}(t)$.

The quantity

$$\phi(t) - \tilde{\phi}(t) = (x(t) - \tilde{x}(t))/b$$

is proportional to the TM X position read by the GRS (x^{GRS}), and so the torque acting on the pendulum. However, as $\phi(t)$ depends on $\phi(t) - \tilde{\phi}(t)$ through the unknown parameter Γ_{GRS}, it is not possible to know in advance how to move $\tilde{x}(t)$ to obtain the desired modulation of $\phi(t) - \tilde{\phi}(t)$. Moreover, the GRS is installed in the facility and we cannot remove it to measure Γ, that is on its own unknown.

It is thus much more convenient to rewrite Equation 8.9 as:

$$I\phi''(t) + (\Gamma + \Gamma_{GRS})\phi(t) = I\phi''(t) + \Gamma_{tot}\phi(t) = \Gamma_{GRS}\tilde{\phi}(t) \quad (8.10)$$

Here, the effective stiffness $\Gamma_{tot} = \Gamma + \Gamma_{GRS}$ needed to solve the equation of motion of the pendulum is exactly the physical one acting on it, that can be easily estimated by measuring the period T_0, and the scale parameter of the external torque is $\tilde{\phi} = \tilde{x}/b$, independent of the pendulum motion and easy to modulate as desired by simply moving the GRS.

The GRS position is changed by means of the translational sled installed under the GRS itself (see Section 6.2). Although the PC-controlled motor we use for this purpose is equipped with an encoder that reads its movement, because of material elasticity and mechanical play together with the significant weight to be moved, we are not guaranteed that it corresponds to the exact displacement of the GRS. We can however measure the position in an independent and more accurate way by simply computing the difference between the angle read by the autocollimator and that read by the GRS itself:

$$\phi^{GRS} = \phi - \tilde{\phi} \qquad \Rightarrow \qquad \tilde{\phi} = \phi - \phi^{GRS}$$

To investigate the sensor-TM stiffness we modulate its equilibrium point $\tilde{x}$ (and thus $\tilde{\phi}$) by modulating the GRS position along the X axis: the EH is driven in a square-wave like motion around it central position, thus applying a square-wave force on the TM and a corresponding square wave torque on the pendulum.

The square wave has been chosen for simplicity of control, and if needed allows for a deeper check of the effect under investigation exploiting the relation between the different harmonics. A square wave signal $S_\omega(t)$ at frequency ω can be written as

$$S\omega(t) = \frac{4}{\pi}\sum_n \frac{\sin\left((2n+1)\omega t\right)}{2n+1}$$

Thus modulating the GRS position with a square wave at frequency ω_{mod} we expect a coherent motion of the pendulum at ω_{mod} and all its odd harmonics, with decreasing amplitude. The external torque can then be calculated via coherent demodulation of the deflection angle and division by the pendulum transfer function (see Equation 3.3. Dividing it by the measured displacement of the GRS at the same frequency, we can finally measure the stiffness constant:

$$\Gamma_{GRS} = \frac{N(\omega)}{\tilde{\phi}(\omega)} = \frac{bF_{GRS}(\omega)}{\tilde{x}(\omega)/b} = b^2\frac{F_{GRS}}{\tilde{x}} = b^2 k,$$

that is

$$k = \frac{1}{b^2}\frac{N(\omega)}{\tilde{\phi}(\omega)}. \tag{8.11}$$

8.2.2 Sensing stiffness

By moving the GRS and detecting the coherent torque acting on the pendulum, the above technique clearly measures the overall coupling of GRS and TM. However, it is also interesting to evaluate the magnitude of the single effects contributing to the global GRS stiffness, both to check the reliability of the noise model and to place upper limits to unforeseen interactions.

While magnetics and gravitational effects cannot be investigated with the hollow TM employed in the facility, we are sensitive to all electrostatic contributions, the main one being the "sensing stiffness" due to TM polarization for capacitive sensing. The scale parameter of this effect is clearly the injection bias V_{inj}, because the effect is directly proportional to its square, as shown by 2.20a.

Although it would be possible to directly modulate V_{inj}^2, Equation 8.10 shows that this would result in a modulation of the total stiffness too, complicating the analysis.

As an alternative, we can repeat the measurement described in Section 8.2.1 with different values of V_{inj}, and perform a linear fit to Γ_{GRS} as a function of V_{inj}^2. In this way, the advantage coming from coherent analysis is retained, as the signal is still modulated by GRS motion along X; at the same time, because the injection voltage is constant during each "run", there is no modulation of the overall spring constant and we simply have to account for a different free-mode period from run to run. The parameter extracted from the linear fit will represent the GRS stiffness dependence on the applied injection bias, and the residual one due to other effects.

8.2.3 Charge related stiffness

As shown by Equation 2.20b, electrostatic stiffness depends on TM charge via both a quadratic and a linear term. While the first is in principle defined by the sensor geometry, the second comes from the coupling of the TM charge with stray DC-biases, and can give us informations about the characteristics of their distribution.

TM charge can be simulated by means of suitable biasing potential applied to electrodes orthogonal to the measurement ones. In analogy with the sensing bias scheme, this has the effect of changing the TM potential by a value $V_m(t)\alpha_m$ (with α_m the ratio between polarizing electrodes and total TM capacitances), thus mimicking a charge

$$\frac{Q_m(t)}{C_{tot}} = \alpha_m V_m(t) \Rightarrow Q_m(t) = \alpha_m V_m C_{tot}$$

on the TM[4]. This technique is used in the DC-biases measurement scheme presented in the next chapter to measure the interaction of simulated TM charge with DC-biases, where the modulated stiffness arising as a secondary effect is used to find the stiffness equilibrium point at which to perform the measurement, and thus reduce systematic errors.

As an alternative, TM charge can be changed by means of the Charge Management System introduced in Section 4.2.4, thus creating a more representative situation of what will happen in space.

We did not yet perform a specific measure of stiffness dependence on the TM charge.

8.3 Results

We present here measurements of the total stiffness as a function of the sensing RMS bias $\tilde{V}_{inj}$. This will allow us to evaluate the sensing bias contribution to the overall stiffness. These measurements have been performed on an almost discharged TM ($V_{TM} < 5$ mV).

As described in the previous section, the measurement has been performed moving the GRS with respect to the TM by means of the installed translational stage (see Section 6.2). In this situation, the angular readout resulting from the combination of the capacitive sensors is clearly compromised, and the autocollimator

[4]Note that in this case we are not actually simulating a total TM charge, that remains unchanged. Rather, by polarizing some electrodes on Y or Z faces we are attracting charges there, leaving charges of the opposite sign on the X faces and thus effectively simulating a TM charge for what concerns electrical interactions on the remaining faces, X in particular.

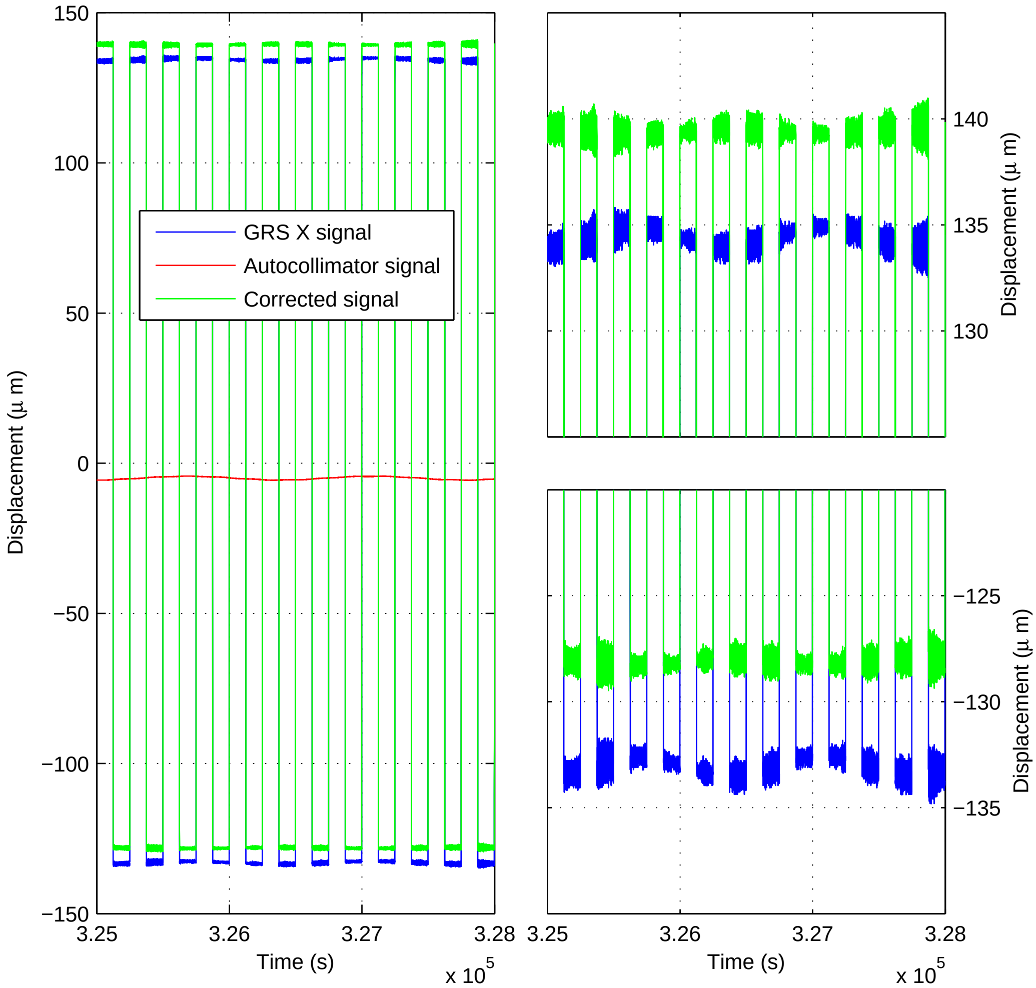

Figure 8.1 – Correction of the GRS displacement signal to correctly compute its actual position, as explained in the text. The blue and red lines show, respectively, the GRS signal and the autocollimator one, multiplied by the pendulum arm to convert it in TM displacement. The green line shows the difference of the two, i.e. the GRS absolute position.

signal has to be used. Moreover, as we performed the measure for GRS position modulation amplitude up to about 400 μm, the electronics could not be operated in science mode (high gain, low dynamic range), and was switched to non-science one (low gain, increased dynamic range), thus reducing readout performances. For each GRS position modulation amplitude, the injection bias has then been changed among five different values: 4.25, 3.25, 2.25, 1.25, and 0.25 V. We avoided switching it completely off as in this case the GRS readout would not have been available, and consequently no control on the GRS actual displacement could have been done. As explained in 8.2.1, the real GRS translation has been reconstructed by the difference between its signal and the autocollimator one: Figure 8.1 shows an example of displacement signal reconstruction starting from GRS and autocollimator readouts.

We thus obtained a total of 25 group of experimental points, each group being

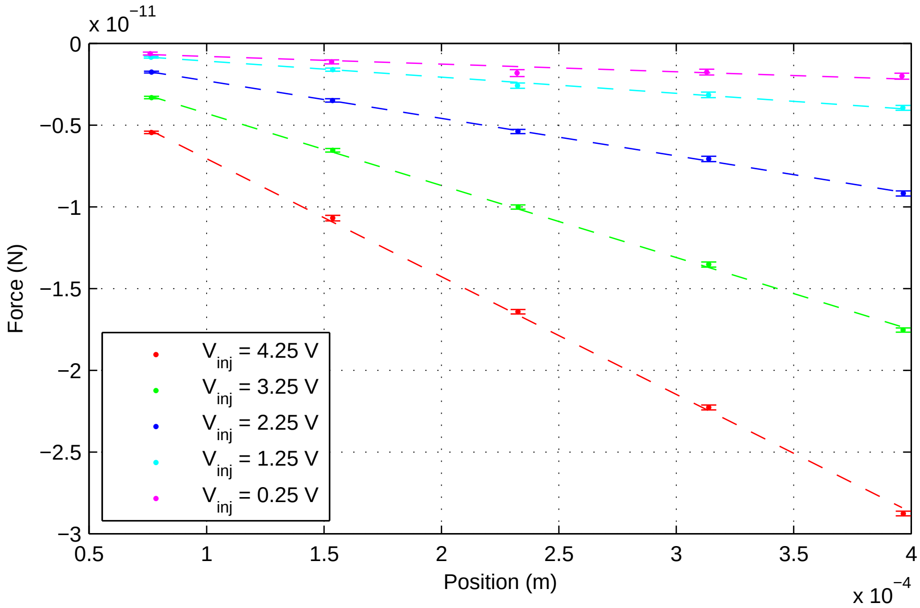

Figure 8.2 – Measure of the force exerted on the TM by the GRS as a function of the relative displacement, for different value of the injection bias. As expected, the linear behavior agrees with the model of a spring-like interaction.

defined by a GRS position modulation amplitude and an injection voltage. For each point the torque acting on the pendulum has been evaluated by means of coherent demodulation of the deflection signal, that has then been divided by the calculated transfer function (that, being away from resonance, is not affected by the uncertainties expressed in 7.2.3). The same demodulation technique applied to the corrected signal of Figure 8.1 has been used to evaluate the actual GRS position modulation amplitude for each point; analyzing both modulated quantities in the same way allows for a more reliable comparison of the two.

The pendulum torque has been converted into equivalent force acting on the TM inside the GRS by simply dividing for the pendulum arm b.

Figure 8.2 shows the measured force as a function of the GRS modulation amplitude: the points are well aligned along straight lines, each corresponding to a different injection voltage. The slope of each line represent the GRS stiffness, obviously increasing as the injection voltage increase.

If we plot the measured slope as a function of V_{inj}^2, we can evaluate the total GRS related stiffness dependence on the injection bias, obtaining an estimate of the residual stiffness by extrapolating the fitted data to 0 (we note that, as the dependence is quadratic in V_{inj} and we have measurement from $V_{inj}^2 = 18.0625\ \mathrm{V}^2$ down to about $0.0625\ \mathrm{V}^2$, we are not extrapolating that far from the measurement interval). Such a plot is presented in Figure 8.3, where the linear fit give a stiffness

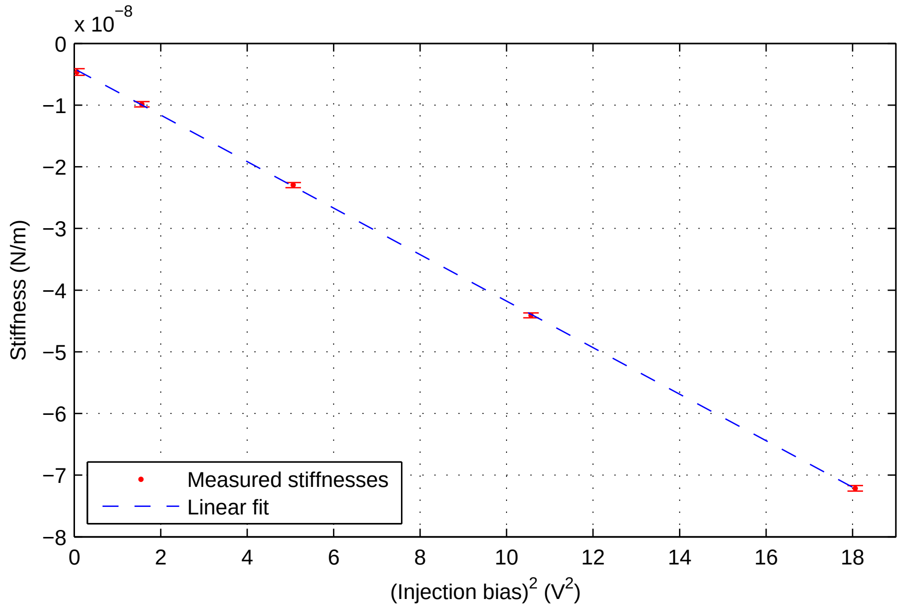

Figure 8.3 – Measured stiffness coupling between GRS and TM as a function of the sensing injection bias squared. The relation is linear as predicted by the noise model, and the derivatives agree within about 20% with the theoretical one.

dependence on V_{inj}^2 equal to

$$K_{GRS}(V_{inj}) = aV_{inj}^2 + b \Rightarrow \begin{cases} a = (-3.77 \pm 0.03) \cdot 10^{-9} \ \dfrac{\mathrm{N}}{\mathrm{V}^2\,\mathrm{m}} \\ b = (-4.1 \pm 0.3) \cdot 10^{-9} \ \dfrac{\mathrm{N}}{\mathrm{m}} \end{cases}$$

corresponding to a stiffness

$$K_{GRS} = (-60.32 \pm 0.5) \cdot 10^{-9} \ \frac{\mathrm{N}}{\mathrm{m}}$$

for a nominal injection bias of 4 V needed (based again on electrostatic model calculation) to obtain a TM oscillating voltage of amplitude about 0.6 V as required for LTP and LISA.

The slope a should be compared with the theoretical value

$$a = -\frac{C_{Xf}}{d^2}\alpha_{inj}^2 \approx -4.8 \cdot 10^{-9} \ \frac{\mathrm{N}}{\mathrm{V}^2\,\mathrm{m}}$$

and is thus about 20% smaller than expected. We should anyway consider that this calculation is strongly dependent on the value of α, which in turns depends on the total capacitance C_{tot} of the TM toward the surrounding surfaces. This is one of the most difficult parameter to be evaluated for the TM mock-ups used in the torsion pendulum facilities, as the presence of the shaft give a contribution that cannot be easily modeled with the infinite parallel plane model. In term of C_{tot}, the observed difference could be explained accounting for a TM capacitance toward the surrounding surface of about 34 pF instead of the calculate value of 31 pF. This difference is within the usual 10% accuracy assumed for the electrostatic model.

On the other hand, we note that the residual measured stiffness b represents slightly more than 5% of the sensing one at $V_{inj} = 4$ V, thus irrelevant for LISA. The equivalent DC-Biases RMS value to obtain the same effect can be roughly estimated to be of order 100 mV: these results are comparable with previous ones obtained with the single mass torsion pendulum [28].

Chapter 9

Stray electrostatics inside GRS: DC-Biases

Although grounded and gold coated in search for electrostatic homogeneity, conducting surfaces facing the TM could present a spatially and time varying potential. This can be due to electrochemical potential variations and differences in the Fermi levels that can arise as a consequence of different impurities, alloy components concentrations or different orientations of adjacent crystalline domains.

Even on a nominally uniform sample, these surface potential variations can show up with values from few mV up to about 100 mV, and coherence lengths ranging from a few μm (that is likely the case for differences among adjacent crystallites) to several mm (in case of inhomogeneities in alloy or contaminants concentration)[16, 19, 37, 38]. While on the typical physical scale of GRS geometry, μm size variations are likely to average to 0, larger patches can cause a net field to arise through the sensor. Moreover, these voltage spatial variations are not guaranteed to be stable over time, and can cause relevant fluctuations in the measurement bandwidth.

Given the lack of reliable theoretical models and the strong dependence of actual values and coherence length on the specific sample (composition, deposition technique, handling, contamination. . .) it is mandatory to have a experimental estimate of this voltage variations both in time and space.

In addition, as introduced in Section 2.2.1, electrodes surface also experience voltage fluctuations due to thermal noise arising in the readout and actuation electronics as well as dielectric losses in the bulk electrode insulating material. These effects sum up and couple with the previous ones, and can produce a contribution to the overall stiffness or noisy force exerted on the TM. Although the models used in estimating them are more reliable, they need an experimental confirmation as well as an estimate of the actual values of the parameters involved.

To be able to place upper limits on the related TM acceleration, it is thus necessary to carry out an on-ground experimental characterization of surface potentials variations (that we are used to refer to as “DC-biases”, as their slowly varying values are expected to be bigger than their in-band fluctuations) and related effects.

As we will show in the next section, we can compensate DC-biases effect, or at least that coming from their mean (i.e. very slow varying) value, by applying suitable voltages to the electrodes so as to produce a canceling force. Employment of this technique is foreseen in space, and the torsion pendulum is also a valuable test bench to verify it [17] and check for its applicability for typical DC-bias values.

Although thorough characterization campaigns and compensation technique demonstration have already been performed with the single-mass torsion pendulum [17], the new 4-TM facility offers the unique opportunity to confirm those results and search for unexpected effects by directly measuring the *force* induced along the X sensitive axis by DC-biases related interactions. This will result in an increased level of representativity and a lower risk of unmodeled effects manifesting in space.

At present, a full DC-bias characterization campaign with the 4-TM facility, including all the possible parameters measurements and compensation techniques, has not yet been performed. We instead measured and compensated the DC-Biases effect directly producing a net force along the X axis. This is the most worrying effect of DC-biases because, as explained in 2.2.1 and expressed by 2.24, it can couple with the noisy TM charge caused by cosmic ray impacts producing a noisy TM acceleration.

This is the first measurement of the *force* related to DC-Bias effects on a LISA-like TM inside a representative GRS prototype, and a first demonstration of the effectiveness of the compensation technique applied to a translational DOF.

9.1 DC bias as a noise source

DC-biases couple with TM voltage and voltage fluctuations resulting in both an electrostatic stiffness, as discussed in the previous chapter (see in particular Section 8.1.3) and a random noisy force. While in Section 2.2.1 we presented a global picture of how all these sources of noise interact each other, we will try to give here a more intuitive understanding of the interaction associated with different possible DC-bias configurations. It will be of help also to better understand the measurement and compensation techniques explained in the next section.

Let us thus analyze a simple case: consider EH surfaces to have a null uniform and constant potential, and the only surfaces affected by DC-biases to be the four X sensing electrodes, however supposed to have each an uniform potential V_i. We will also assume the design geometry to be perfectly symmetrical, and thus all electrode capacitances to be equal. Finally, we will make use of capacitance relations A.1a (using as A the area of a single X electrode) and the approximation of the electrostatic force to the first order in x expressed by A.4.

Example 1: if the pair of $X+$ electrodes have equal and opposite potential $\pm V_{DC}$,

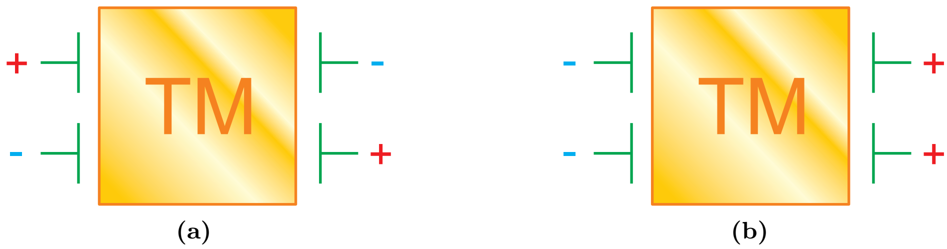

Figure 9.1 – Two example representing simple DC-biases configurations that produce (a) a stiffness or (b) a net force (the latter only in the case $V_{TM} \neq 0$).

and the same happens to the $X-$ electrodes, as sketched in Figure 9.1a, the first term of Equation A.4 nulls and only a stiffness term survives:

$$F_X(x) \approx \frac{C_X}{d^2}\left(2(V_{TM}-V_{DC})^2 + 2(V_{TM}+V_{DC})^2\right)x = 4\frac{C_X}{d^2}\left(V_{TM}^2+V_{DC}^2\right)x \tag{9.1}$$

where we note that $V_{TM} = V_{TM,0}$ (defined in Section 2.2) as in this configuration

$$\sum_i V_i C_i / C_{tot} = 0$$

This DC-bias combination thus gives rise to a stiffness term V_{DC}^2 in addition to the one due to the TM voltage, but the net exerted force is 0 and so is the net TM polarization. Equation 9.1 shows that as we introduce any modification in the EH surfaces voltage, a corresponding contribution to the total stiffness is unavoidable.

Example 2: let us now consider a similar configuration, but with both $X+$ electrodes at potential $+V_{DC}$ and opposing one at $-V_{DC}$ (see Figure 9.1b). The contribution to the TM polarization $\sum_i V_i C_i / C_{tot}$ is still null, and calculating Equation A.4 for the new voltage configuration:

$$\begin{aligned} F_X(x) \approx \frac{1}{2}\frac{C_X}{d}&\left(2(V_{TM}-V_{DC})^2 - 2(V_{TM}+V_{DC})^2\right) + \\ &+\frac{C_X}{d^2}\left(2(V_{TM}-V_{DC})^2 + 2(V_{TM}+V_{DC})^2\right)x = \\ &= -4\frac{C_X}{d}V_{TM}V_{DC} + 4\frac{C_X}{d^2}\left(V_{TM}^2+V_{DC}^2\right)x \end{aligned} \tag{9.2}$$

As long as the TM voltage is different from 0, a net force proportional to both V_{TM} and V_{DC} arises, and if any of the two (or both) fluctuates over time, it will result in a TM acceleration noise: this force term is the most threatening and the one we must compensate in space, as it couples with TM charge that affects TM potential. Moreover, a stiffness term is still present.

Eample 3: we can now think that each electrode has a voltage V_{DC}, so that the

TM polarization is different from 0. Performing calculations similar to those that brought to Equation 9.1, we find:

$$F_X(x) \approx 4\frac{C_X}{d^2}\left(V_{TM,0} + \left(\frac{4C_X}{C_{tot}} - 1\right)V_{DC}\right)^2 x \tag{9.3}$$

where the force is again null, but the stiffness is still present, with an additional contribution given by the increased TM voltage due to polarization by the surrounding surfaces at potential V_{DC}.

We remark that the above examples are simplified. The real DC-bias distributions would be much more complicated, so the resulting effect would be a superposition of those above. Moreover, interaction terms between the different effects can arise: for example, if we superimpose the configurations of the second and third examples, the force due to the characteristics of the former, being proportional to V_{TM}, can mix with the TM voltage contribution coming from the latter. In order to give a more clear picture, we also considered in the calculation only DC-biases related effects, excluding for example the contribution to the stiffness given also by grounded surfaces when the TM has a voltage different from 0. Finally, we did not consider here the effects of the TM being off center on other DOF: their role will be shown in the next section.

However, these examples help understanding the problems related to DC-biases and sketch the possible interactions due to different DC-biases configurations. While the first and the third examples demonstrate that DC-biases RMS and mean values affect the stiffness and the TM polarization, from the second one it is clear that, for a net force to arise, there should be a DC-bias "imbalance" along the X axis.

Recalling Section 2.2.1 we can observe that the second example exactly corresponds to the situation hypothesized to define ΔX in Equation 2.21a, whose expression has been obtained for a generic stray voltage distribution.

The definition of

$$\Delta X = \left|\frac{\partial C_X}{\partial x}\right|^{-1} \sum_i \frac{\partial C_i}{\partial x} V_i \tag{9.4}$$

(equal to $\left|\frac{C_X}{d}\right|^{-1} \sum_i \frac{C_i}{d} V_i$ according to the electrostatic model presented in Appendix A) helps to represent a generic DC-biases distribution imbalance relevant for the force acting along X on a charged TM, as if it was an equivalent distribution of equal voltage values affecting only the X sensing electrodes according to the scheme presented in the second example. As will be shown in the next section, this suggest an operational way of measuring a generic distribution ΔX by means of compensating its effects purposely applying a suitable voltage to the X electrodes.

9.2 Measurement technique

As we saw in the previous section, the force exerted on a centered TM in the presence of an appropriate DC-bias imbalance is proportional to the TM potential and to the imbalance itself, summarized by the parameter ΔX defined in Equation 9.4.

The usual coherent signal detection approach used to characterize known sources of disturbance thus suggests we should modulate the TM potential and analyze the response of the pendulum at the same frequency, that will be proportional to ΔX. In analogy with what we do for sensing bias, this can be achieved by means of a suitable sinusoidal polarization voltage $V_m \sin(\omega_m t)$ applied to Y electrodes, that would induce a consequent TM voltage modulation $\alpha_Y V_m \sin(\omega_m t)$, where $\alpha_Y = C_Y/C_{tot}$, C_Y being the sum of all the Y electrodes capacitances toward the TM. Y electrodes have been chosen because Y is the only axis along which the pendulum is completely insensitive to both forces and stiffnesses[1].

It is interesting to note that, as suggested in 8.2.3, from the point of view of the X faces this is seen has a modulated charging of the TM: when polarized, indeed, Y electrodes attract charges on the corresponding TM faces, leaving a charge of opposite sign on the remaining ones. Although induced in a different way, the procedure suggested here thus measures exactly the coupling between DC bias X imbalance ΔX and TM charge, that is what we are worried about in LTP and LISA according to Equations 2.24.

Rewriting Equation 2.3 including the TM modulation term:

$$\begin{aligned} F_X =& \frac{1}{2}\sum_i \frac{\partial C_i}{\partial x}\left(V_{TM} + \alpha_Y V_m \sin(\omega_m t) - V_i\right)^2 \\ =& \frac{1}{2}\sum_i \frac{\partial C_i}{\partial x}\big(V_{TM}^2 + \alpha_Y^2 V_m^2 \sin^2(\omega_m t) \\ &+ V_i^2 + 2V_{TM}\alpha_Y V_m \sin(\omega_m t) - 2V_{TM}V_i - 2V_i\alpha_Y V_m \sin(\omega_m t)\big) \end{aligned} \tag{9.5}$$

Exploiting the relation $\sin^2(\omega_m t) = (1 - \cos(2\omega_m t))/2$ and grouping terms by

[1] Although the pendulum is also insensitive to Z translations, asymmetries in forces applied along this axis would translate in torques that the pendulum would detect. Using Z electrodes to apply the relatively strong electric fields needed to polarize the TM is thus not recommended. Moreover, even if symmetrical, it would induce an additional electrostatic rotational stiffness term.

modulation frequency:

$$F_X =$$

$$\frac{1}{2}\sum_i \frac{\partial C_i}{\partial x}\left(V_{TM}^2 + V_i^2 - 2V_{TM}V_i + \frac{\alpha_Y^2 V_m^2}{2}\right) \tag{9.6a}$$

$$+ \alpha_Y V_m \sin(\omega_m t)\sum_i \frac{\partial C_i}{\partial x}(V_{TM} - V_i) \tag{9.6b}$$

$$- \frac{\alpha_Y^2 V_m^2}{2}\cos(2\omega_m t)\frac{1}{2}\sum_i \frac{\partial C_i}{\partial x} \tag{9.6c}$$

We now define the TM coordinates $\overrightarrow{r}_0 = (x_0, \phi_0, \eta_0)$ (here including all relevant DOFs) as the point in which $\sum_i \frac{\partial C_i}{\partial x} = 0$[2]). When extracting the coherent torque signal at frequency ω_m, only term 9.6b will contribute. Expanding it in series around $\overrightarrow{r}_0$ up to the first order in all the relevant variables (see discussion in Appendix A):

$$F_{X,\omega_m} = -\alpha_Y V_m \sin(\omega_m t)$$

$$\Bigg(- V_{TM}\sum_i \left.\frac{\partial C_i}{\partial x}\right|_{\overrightarrow{r}_0} \tag{9.7a}$$

$$+ \sum_i \left.\frac{\partial C_i}{\partial x}\right|_{\overrightarrow{r}_0} V_i \tag{9.7b}$$

$$- \sum_i \left.\frac{\partial^2 C_i}{\partial x^2}\right|_{\overrightarrow{r}_0} (V_{TM} - V_i)(x - x_0) \tag{9.7c}$$

$$+ \sum_i \left.\frac{\partial^2 C_i}{\partial x \partial \phi}\right|_{\overrightarrow{r}_0} V_i(\phi - \phi_0) \tag{9.7d}$$

$$+ \sum_i \left.\frac{\partial^2 C_i}{\partial x \partial \eta}\right|_{\overrightarrow{r}_0} V_i(\eta - \theta_0)\Bigg) \tag{9.7e}$$

The first term is zero by definition of the "zero force" point $\overrightarrow{r}_0$ about which we are expanding in series. The second represents exactly what we want to measure, being proportional to $\Delta X = \left|\frac{\partial C_X}{\partial x}\right|^{-1} \sum_i \frac{\partial C_i}{\partial x} V_i$. As for the remaining terms, they can in principle introduce systematic errors in the measure of ΔX. Anyway we note that, according to the electrostatic model introduced in Appendix A,

$$\left.\frac{\partial^2 C_i}{\partial x \partial \phi}\right|_{\overrightarrow{r}_0} = \left.\frac{\partial^2 C_i}{\partial x \partial \eta}\right|_{\overrightarrow{r}_0} \leq 2C_i \frac{l}{d^2} = \frac{2l}{d}\left.\frac{\partial C_i}{\partial x}\right|_{\overrightarrow{r}_0}$$

[2]This point should by design coincide with the sensing zero, in which the electrodes capacitances toward the TM are all equal. However, due to machining and assembling imperfections this may not be true. In the following we will give a measure of this difference

where l is at maximum half the TM size, thus $2l/d \sim 10$. When the TM is in the "sensing zero" ($x = 0$, $\phi = 0$, $\eta = 0$), terms 9.7d and 9.7e has to be multiplied by ϕ_0 and η_0 whose values are expected to be $\lesssim 10^{-3}$ (for a measure of ϕ_0 with the same sensor see [9]), thus becoming two order of magnitude smaller than term 9.7b. Potentially more dangerous is term 9.7c, as

$$\left.\frac{\partial^2 C_i}{\partial x^2}\right|_{\vec{r}_0} = \frac{2C_i}{d^2} = \frac{2}{d}\left.\frac{\partial C_i}{\partial x}\right|_{\vec{r}_0} = \frac{2}{4 \cdot 10^{-3}\ \mathrm{m}}\left.\frac{\partial C_i}{\partial x}\right|_{\vec{r}_0}$$

and we have no estimate for x_0. However, we note that the TM voltage modulation gives rise to a $2\omega_m$ component of the signal described by term 9.6c: once expanded in series around $\vec{r}_0$ it turns out to be only proportional to $(x - x_0)$:

$$-\frac{\alpha_Y^2 V_m^2}{4}\cos(2\omega_m t)\sum_i \frac{\partial C_i}{\partial x} = -\frac{\alpha_Y^2 V_m^2}{4}\cos(2\omega_m t)\sum_i \left.\frac{\partial^2 C_i}{\partial x^2}\right|_{\vec{r}_0}(x - x_0) \tag{9.8}$$

This suggests that we can exploit the $2\omega_m$ signal to move to $x = x_0$, thus nulling at the same time term 9.7c, and then perform a more accurate estimate of ΔX. Supposing to have nulled the $2\omega_m$ component, and that terms 9.7d and 9.7e are negligible, measuring the pendulum motion amplitude A_{ω_m} at frequency ω_m we can evaluate ΔX:

$$-\alpha_Y V_m \left|\frac{\partial C_X}{\partial x}\right| \Delta X = -\alpha_Y V_m \sum_i \left|\frac{\partial C_i}{\partial x}\right| V_i = F_{X,\omega_m} = \frac{N_{\phi,\omega_m}}{b} = \frac{1}{b}\frac{A_{\omega_m}}{|H(\omega_m)|} \tag{9.9}$$

from which

$$\Delta X = -\frac{1}{\alpha_Y V_m b}\left|\frac{\partial C_X}{\partial x}\right|^{-1} \frac{A_{\omega_m}}{|H(\omega_m)|} \tag{9.10}$$

where b is the pendulum arm and $H(\omega_m)$ its transfer function at frequency ω_m.

ΔX produced by unknown DC-bias distributions can not only be measured, but also compensated, nulling the overall effect. As shown by 2.23, any value of ΔX can be obtained applying a compensation voltage V_{comp} to each X electrode, with appropriate signs. Thus, once we have measured a value ΔX_{meas}, we can calculate the V_{comp} needed to produce a net $-\Delta X_{meas}$:

$$-\Delta X_{meas} = -4V_{comp} \Rightarrow V_{comp} = \frac{\Delta X_{meas}}{4} \tag{9.11}$$

Applying $+V_{comp}$ to $X+$ electrodes and $-V_{comp}$ to $X-$ we can null the overall ΔX. At the same time, this combination would not modify the overall TM polarization, here including the contribution from the pre-existing DC-biases. On the other hand, it can raise the overall RMS voltage drop between the TM and the surrounding EH housing, thus adding a contribution to the overall stiffness.

We want to stress here that we are not necessarily canceling the pre-existing DC-bias combination at the level of individual electrostatic domains: it would indeed be possible only if the imbalance was evenly and uniformly distributed on the X electrodes surfaces, as the compensating bias we are applying. In this case we would exactly null the single "charge patches" (actually a whole electrode each) themselves. However. in the presence of a generic (and realistic) distribution, we would compensate by applying a different combination of "charge patches" that sums to the previous one canceling the average field that the charged TM feels (but for example not canceling the pre-existing distribution RMS value).

This compensation technique also suggests a way of measuring ΔX more directly with respect to the one presented so far: applying Equation 9.10 requires the knowledge of the pendulum transfer function, and parameters α_Y and $\left|\frac{\partial C_X}{\partial x}\right|$ from the electrostatic model, that have their own uncertainties. Exploiting the explained compensation technique we can instead apply different compensation voltages ΔX_{comp} until we null the ω_m signal, obtaining exactly the opposite of the ΔX we wanted to measure.

The estimate of the required ΔX_{comp} can be obtained both by means of Equation 9.10 or performing a linear fit on the result of at least two measurements with different applied compensation voltages and extrapolating to zero to directly find the value that nulls the effect. In both cases, if the computed values do not exactly null the ω_m angular motion component, the procedure can be iteratively repeated. In this way, the ability to measure and compensate the ΔX imbalance is only limited by the instrument angular sensitivity at the modulation frequency and the resolution we have in controlling applied voltages.

It is worth making here one more remark about this measurement technique applied to the 4-TM pendulum: as we know, the pendulum configuration is not only sensitive to forces along the X axis, but also to pure torques acting on the TM. As there exists an equivalent combination of DC-biases, obtained from a derivation analogous to the above one, that produces a torque on the TM instead of a force, when modulating the TM voltage we will actually measure both effects, although with the reduced sensitivity to torque discussed in Section 3.4. Anyway, there is no means to distinguish the two effects in both the x_0 determination (that would also be influenced by distance from ϕ_0) and ΔX (that would add to the similarly defined $\Delta\phi$). Keeping this in mind, in the following we will consider only the ΔX imbalance to contribute to the pendulum measured torque, while still accounting for 2ω signal amplitude dependence on $\phi - \phi_0$ (in addition to $x - x_0$).

We mention that described methods have a number of possible variations aimed at separating DC-biases contributions coming from different GRS elements (guard rings, X electrode,...). A more general discussion about the measurement and compensation techniques, along with consideration on their applicability in space on a completely free TM and a report on the results obtained on the single mass facility can be found in [9].

9.3 Results

Before exploiting the measuring technique described so far, we centered the TM inside the GRS within about 1 μm in translation and 100 μrad or less in rotation on all DOFs (except Θ and Y, along which we have limited alignment capabilities and resolution, as explained in D.2.1: anyway the effect is negligible for what has been previously said.) using the technique presented in D.2.1 and performed a calibration as in Appendix B.2.

We then applied a 5 V, 4 mHz[3] sinusoidal bias to the four Y sensing electrodes, and measured the $2\omega_m$ pendulum coherent response for different values of the mean TM position along X and Φ inside the GRS. An example of the pendulum time-series during the measure is given in Figure 9.2a, along with the same time-series filtered at the free oscillation and ω_m frequencies, in which the induced ω and $2\omega_m$ signals become evident.

As we are sensitive to both torque and forces, but have no means to distinguish between the two contributions, we measured the $2\omega_m$ pendulum response amplitude scanning different points of the $x - \phi$ space, in a region spanning from about -100 to $+100$ μm in X and -1 to 1 mrad in Φ.

In each position, the capacitive signals were acquired for at least one hour, and demodulated two cycles per time at twice the modulation frequency, thus 8 mHz (see 9.2b). Resulting points were not averaged further as they corresponds to slightly different coordinates due to pendulum position fluctuations in time. Given the noise in the pendulum rotation signal, estimated at about $6 \cdot 10^{-8}$ rad/Hz$^{1/2}$, each point had an associated error of about ± 10 nrad in the measured signal amplitude. The TM position error is determined by the lone GRS translational and rotational signal noises: about $2 \cdot 10^{-8}$ m/Hz$^{1/2}$ in x and $4 \cdot 10^{-7}$ rad/Hz$^{1/2}$ in ϕ, resulting in uncertainties of order, respectively, ± 2 nm and ± 40 nrad for each point (both dominated by real motion, being above the GRS readout sensitivity). We then performed a bilinear fit to the measured values and find the locus of points in which the $2\omega_m$ signal amplitude was expected to be 0. Figure 9.3 shows the results of this measurement.

Although the fit was enough to calculate and move to one of the point in which the second harmonic of the polarizing signal was 0, the dependency of the $2\omega_m$ oscillation amplitude $A_{2\omega_m}$ on the X TM displacement inside the GRS gives us a first occasion to check the electrostatic model. According to this and Equations 9.8

[3] According to what have been seen in Chapter 7, our best sensitivity (lower pendulum noise) region is slightly higher than 1 mHz, thus below the frequency chosen here. As we will show, however, the ultimate accuracy in measuring and compensate ΔX is not limited by the pendulum sensitivity, and increasing the frequency allowed us for a faster experiment.

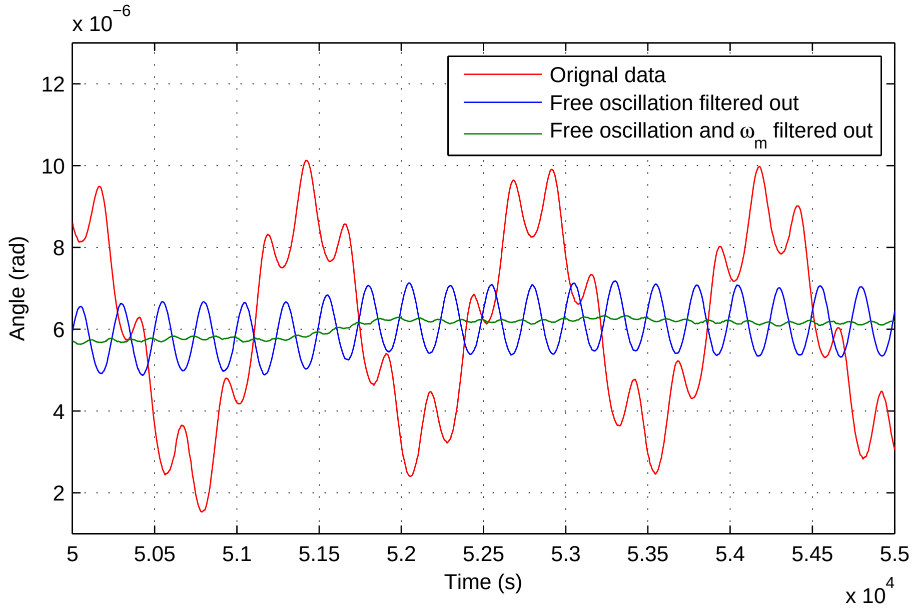

(a) Time series

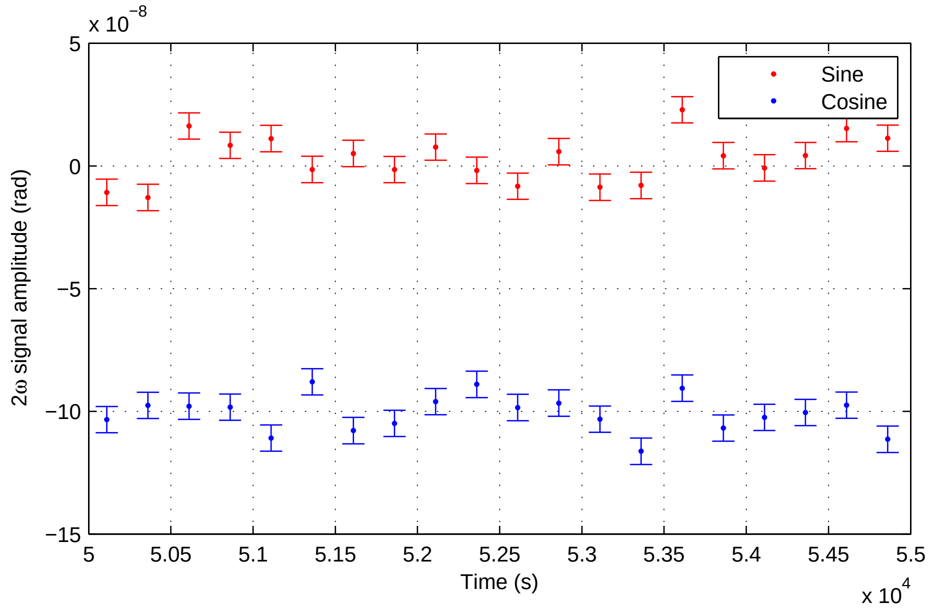

(b) Demodulated signal

Figure 9.2 – (a) 5000 seconds of 4-TM pendulum data taken while evaluating $2\omega_m$ torque component for a single position in the $X - \phi$ space (see 9.2. Free oscillation and ω_m components have been filtered out to show the much smaller, but noticeable, residual $2\omega_m$ pendulum coherent deflection, meaning that in this case we were not "centered"(see the text for details). (b) results of coherent demodulation analysis on the same time range. As expected, cosine component is in phase and measures the amplitude of the signal, while in quadrature sine component measures 0.

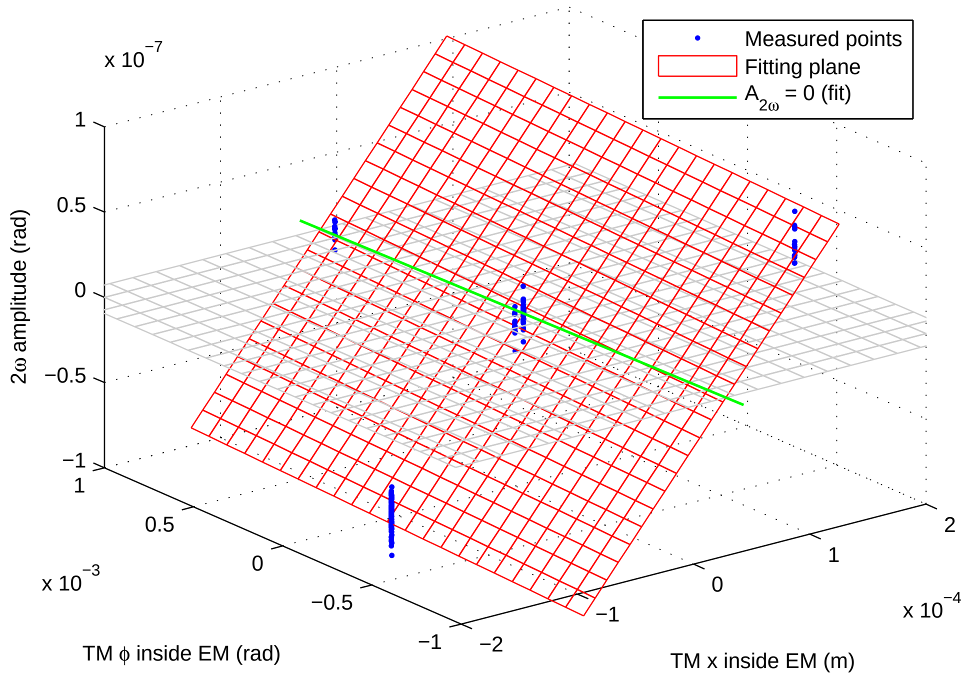

(a) 2ω signal bilinear fit

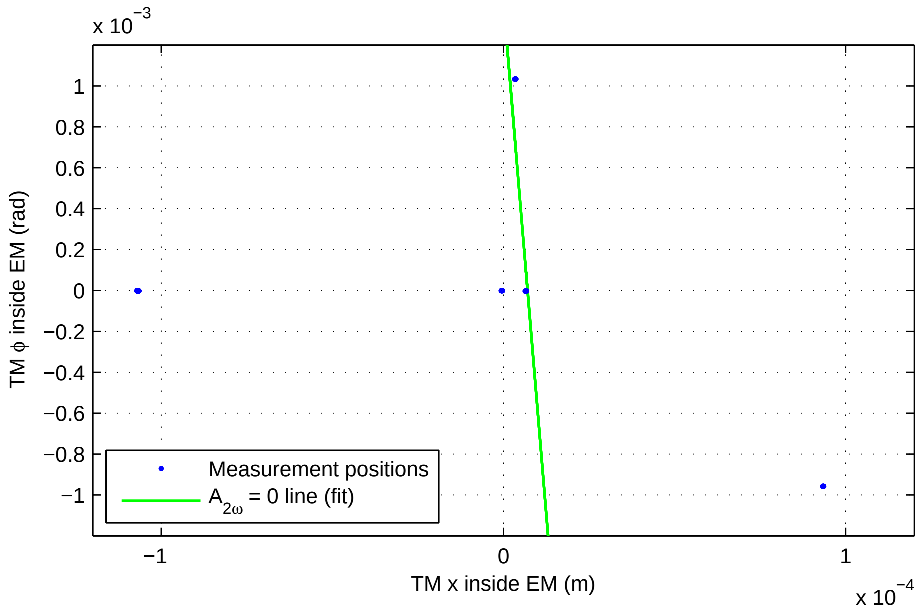

(b) Locus of 0 force points

Figure 9.3 – (a) shows a 3D representation of the plane resulting from a bilinear fit of the pendulum $2\omega_m$ coherent deflection as a function of the TM X and Φ positions: it is evident that the plane is almost parallel to the Φ axis, meaning that the dependence on ϕ is very weak. This is confirmed also by (a): the locus of the TM positions for which the $2\omega_m$ amplitude should be 0 (i.e. the intersection of the fitting plane with the $X - \Phi$ one) is plotted along with the position used for the measurements. Given the difference in the axis scales, it is clear that the dependence on ϕ is very small compared to that on x. Please note that what appear as single points in both graphs is actually a group of tens of nearby points resulting from a single measure of the type presented, for example, in Figure 9.2

and 3.3:

$$\frac{\partial A_{2\omega_m}}{\partial x} = H(2\omega_m) b F_{2\omega_m}(x) = H(2\omega_m) b \alpha_Y^2 V_m^2 \frac{C_{Xface}}{d^2} \approx 970 \ \frac{\mu\text{rad}}{\text{m}} \tag{9.12}$$

with C_{Xface} representing the capacitance between one TM X face and the EH. This value has to be compared with the result of the fit described above:

$$\frac{\partial \tilde{A}_{2\omega_m}}{\partial x} = (869 \pm 6) \ \frac{\mu\text{rad}}{\text{m}} \tag{9.13}$$

where the tilde represents "measured value". The ratio between the latter and the former is ≈ 0.9, thus compatible with the electrostatic model whose uncertainty is 10-20%.

Despite the fact that we were unable to tell what the actual value of the "*force* zero" point was, as our measurement depends also on the distance from ϕ_0, we note that the dependency on ϕ is much smaller than that in x:

$$\frac{\partial A_{2\omega_m}}{\partial \phi} = (4.3 \pm 1) \cdot 10^{-6} \tag{9.14}$$

This was expected because of both the reduced pendulum sensitivity to torque and the smaller value of the second derivative of capacitances with respect to ϕ instead of x: in particular, from the analogous interaction term dependent on ϕ it holds:

$$\frac{\partial A_{2\omega_m}}{\partial \phi} = H(2\omega_m) \frac{\alpha_Y^2 V_m^2}{4} \sum_i \frac{\partial^2 C_i}{\partial \phi^2}$$

Subdividing the TM faces in small surfaces of height L (the TM size, equal to 46 mm) and width dl, and integrating among the four X and Y faces, we get

$$\sum_i \frac{\partial^2 C_i}{\partial \phi^2} = 4 \int_{-L/2}^{L/2} \frac{\partial^2 C_{Xface}/L}{\partial x^2} dl = \frac{\partial^2 C_{Xface}}{\partial x^2} \frac{L^2}{3} = \frac{2}{3} \frac{\partial^2 C_{Xface}}{\partial x^2} L^2$$

The ratio between the two above coefficients should thus be

$$\frac{\partial A_{2\omega_m}}{\partial x} / \frac{\partial A_{2\omega_m}}{\partial \phi} = 6 \frac{b}{L^2} \approx 280 \ \text{m}^{-1}$$

to be compared to the measured ratio of $203 \pm 50 m^{-1}$.

This means that x_0 changes little as the TM ϕ position changes inside the EH: we chose to keep $\phi = 0$, yielding $x_0 = 7 \pm 0.5$ μm. As by design this point should coincide with the sensing 0, its value gives us clues about machining imperfections, that result to be compatible with the expected 10 μm.

We then measured the pendulum motion at $\omega = \omega_m$ applying $\Delta X_{comp} = 0$, +160 and -160 mV (i.e. a single electrode compensation potential $|V_{comp}| = 0$, +40 and -40 mV) by means of the actuation electronics. For each compensation value, data was taken for a number of modulation cycles ranging from a minimum of 15 to a maximum of about 70. As the error associated to each point based on GRS noise estimation seemed to be overestimated[4], we averaged the points, and took the standard deviation of the mean as the error.

Without converting the results in force, we finally performed a linear fit to the data, obtaining an estimate of $\Delta X_{comp} = (-119.9 \pm 0.06)$ mV to null the pendulum response. As our resolution in applying DC compensation is limited by the DAC resolution to about 0.6 mV[5] and 119.9 mV/4 = 29.975 mV, we applied 30 mV per electrode (with appropriate signs) and thus a total $\Delta X_{comp} = -120$ mV, obtaining a measured residual ΔX of about -0.11 ± 0.07 mV. Results are shown in Figure 9.4. We note that the difference is compatible with the excess compensation applied because of the DAC limited resolution; equivalently we can note that, although not exactly null (as expected), the experimental point measured with the applied compensation falls on the previous fit, as is easily visible in Figure 9.4a, thus demonstrating the accuracy of the measurement and the reliability and precision of the compensating technique. Here the 2ω component, measured as a check, is also visible, and is compatible with 0 within 1-2 standard deviations depending on the measurement (its fluctuations being due to the stability in time of the TM position about the zero force point).

As mentioned in the previous section, an alternative approach would have been that of measuring the pendulum response with no compensation applied, computing the corresponding ΔX exploiting Equation 9.10 and directly applying an opposite compensation bias. The theoretical derivative of the pendulum deflection amplitude with respect to ΔX,

$$\frac{\partial A_{\omega_m}}{\partial \Delta X} = \alpha_Y V_m b \left| \frac{\partial C_X}{\partial x} \right| H(\omega_m) \approx 7.06 \text{ rad/V} \tag{9.15}$$

is in perfect agreement with the measured value of

$$\frac{\partial \tilde{A}_{\omega_m}}{\partial V} = (7.117 \pm 0.002) \, \frac{\mu\text{rad}}{\text{V}}$$

Using the theoretical value of Equation 9.15, the measured signal amplitude of 853 ± 1 nrad would have converted in a corresponding $\Delta X = 120.8 \pm 0.07$ mV, in agreement with the previous result (note that the change in signs depends on the fact that this is the measured imbalances, while the previous one is the compensation). We stress that the uncertainty of 0.07 mV reported here comes from the mere conversion of the uncertainty in the amplitude measurement via the scale factor $\frac{\partial A_{\omega_m}}{\partial \Delta X}$:

[4] Actually we had reasons not to trust this estimation: we should indeed extrapolate the pendulum background noise at the modulation frequency as the measurement peak was not present. Unfortunately, we had no clean data streams long enough to resolve clearly the peak, that broadened out resulting in a rough estimate of the background noise.

[5] The voltage output noise has been measured to be ≈ 125 μm with 10 V output [39]

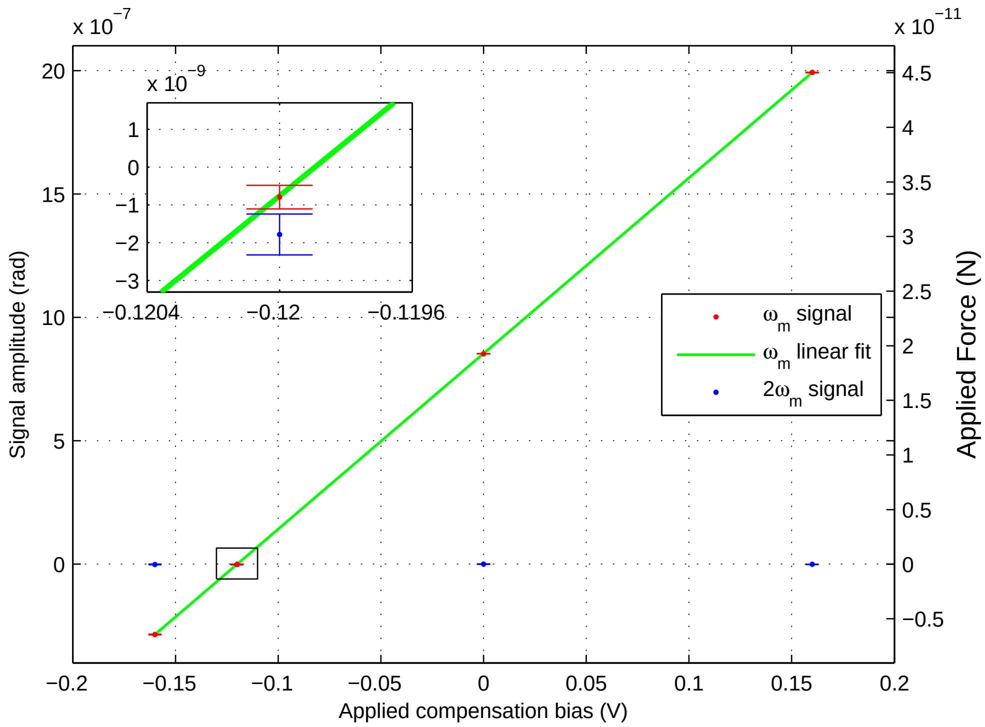

(a)

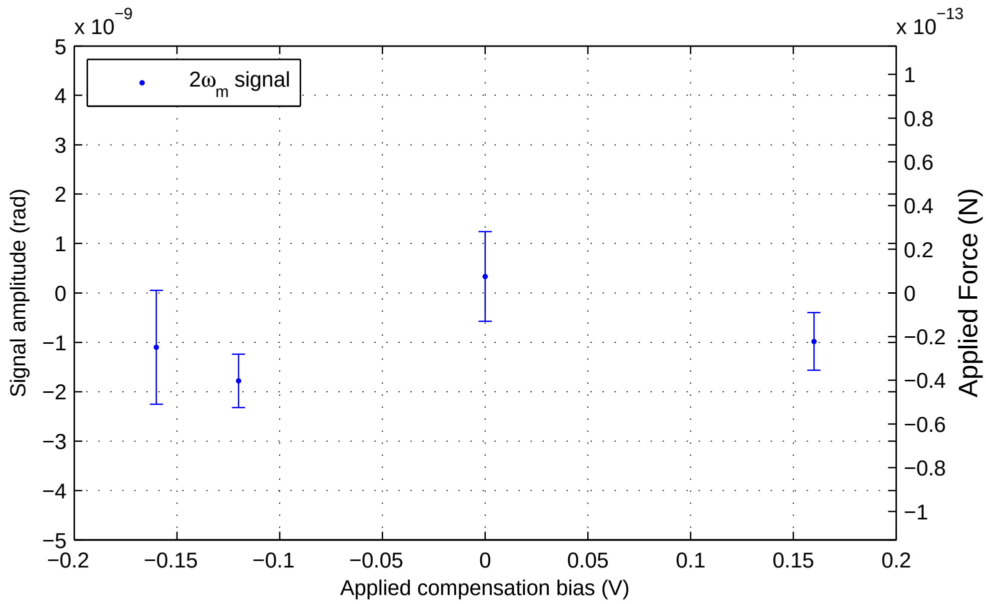

(b)

Figure 9.4 – Measurement of DC-biases imbalance ΔX. The coherent pendulum deflection amplitude, along with a least square linear fit, is shown as a function of the applied compensation bias. (a) shows the full data set, with angular deflection converted into applied force via the pendulum transfer function reported in the right Y axis; a zoomed view around the measured compensation bias (indicated by the black rectangle) is presented in the upper left corner, to better appreciate the residual uncompensated polarization. Near null $2\omega_m$ signal is also reported in (b), in which the Y axis has been expanded to better appreciate signal values, fluctuations and error bars.

this does not really mean that we are attributing this uncertainty to the calculated ΔX value, that is expected to be dominated by the uncertainty on the models used in Equation 9.15, and thus of order 10-20% or more. We anyway reported that small error because it gives an idea of what we obtains using the Equation 9.15 as a pure conversion factor: the very good agreement here, coming actually from a series of different measures (we could have done this calculation starting from any of the data points shown in Figure 9.4a, obtaining substantially the same result) seems to suggest that in this particular case we are overestimating the uncertainty of our model.

The measured ΔX imbalance value is compatible with analogous $\Delta\phi$ imbalance measurement performed with the single TM torsion pendulum [25], that corresponds to very similar compensation voltage values to be applied to each electrode, although with a different sign configuration.

It's worth remarking that the demonstrated compensation capability better than 1 mV makes the force noise coming from DC-biases imbalance coupling with TM charge negligible for LISA.

Chapter 10

Conclusions

While promising to be one of the milestones of a completely virgin astronomy, potentially rich of discoveries and exciting new science, the LISA space borne gravitational wave observatory is calling for new technological and scientific skills to prepare the steep way to its success. Existing instruments and physical knowledge have to be pushed beyond their present limits, and new ones has to be provided to maximize the scientific outcome of LISA pioneer effort in observing the deeper mystery of our universe.

In this framework, the Gravitational Reference Sensor provided by the Trento LISA group has been asked to fulfill unprecedented requirement in terms of combined high displacement sensitivity and reduced disturbances on the measured reference Test Mass. The validity of the proposed design and the accompanying noise model thus require severe ground testing both for accuracy of estimates and completeness of foreseen possible interaction and noise sources.

The Trento group itself developed a dedicated torsion pendulum facility, in use since several years, capable of both high accuracy investigation of known interactions and high sensitivity search for unexpected ones, at the 10 $\mathrm{fN/Hz^{1/2}}$ level in the critical low frequency LISA sensitive band down to 10^{-4} Hz.

Approaching the needed sensitivity to validate the sensor for LTP, the LISA precursor demonstration mission, and pushing down further its own performances to get close to LISA requirements, this instrument is however facing its intrinsic limits in representativity of obtained results, being only sensitive to torque acting on the TM and inferring the relevant force estimates via theoretical models.

The need for a next generation instrument capable of overriding this limitations and reducing as much a possible the panorama of threatening untested sources of noise, potentially jeopardizing the success of the space missions, clearly arose. Based on heritage of early torsion pendulum facility designs and on the deep experience gained on the operating facility, we thus built a new force sensitive torsion pendulum facility whose commissioning and first relevant, highly representative measurement are the object of this thesis.

Taking the first steps from a simplified version of the apparatus that demonstrated within a factor three the attainability of theoretical design performances, cleared the way from possible major issues (as feared coupling to laboratory gravitational noise) and helped in tuning up the complex set of readout, diagnostics and auxiliary systems, we built a new torsion pendulum facility employing a four LISA like Test Masses inertial member to obtain sensitivity to net forces exerted by the GRS on its inside TM.

Taking advantage of this unprecedented characteristic, we obtained the first-ever results directly exploiting sensitivity to force acting on the TM:

- We employed the 4-TM torsion pendulum facility for a partial preliminary verification of both GRS-TM coupling and stray voltages imbalances measurement and compensation, demonstrated here within less than 1 mV accuracy; previously performed with the single mass torsion pendulum, they have been confirmed in a more representative force sensitive setup. Although not representing full characterization campaigns, results were found to be in agreement with previous estimates, thus reducing the probability of unforeseen effects and confirming the validity of theoretical models used to extrapolate force noise estimates from 1-TM torsion pendulum torque measurements.

- By bringing the pendulum to operate less than a factor two from its theoretical noise floor in the $1-2$ mHz instrument best sensitivity band, we were able to set relevant upper limits below $100 fN/Hz^{1/2}$ to the force exerted on the TM by the GRS. It was both the lower-ever limit set at this level around 1 mHz, and the first one measured by an instrument directly sensitive to forces.

- In the effort of extracting the most relevant estimates from pendulum noise data, we also tested and compared on real data a variety of data analysis tools and techniques that will be employed for LTP, thus providing valuable feedback to the data analysis development activity.

- The search for the most reliable excess noise estimate brought us to an comprehensive analysis of facility performances over an extended period of time: beside giving us the occasion for checking measured data statistical consistency with hypothesis needed to correctly interpret data analysis results, this allowed us for pointing out possible upgrades and debugging activities that could bring to improvements of the obtained results, hopefully filling the remaining gap between the expected background noise and the measured one and allowing for further lowering the upper limit on the GRS related disturbances.

Even more important than the achievement of the above valuable results, is the fact that the work presented in this thesis brought to the availability of a new instrument capable of enhancing both present upper limits value and representativity, as long a testing unknown potentially dangerous effects that could have remained hidden to the single torsion pendulum facility.

In particular, one of the first and more interesting campaign already scheduled for he next months is the characterization of thermal related effects: radiation pressure, radiometer effect and thermal activated outgassing. Given their strong dependence on sensor geometry and the possible arise of hard to model mechanisms due to non negligible border effects, their investigation can largely benefit from the 4-TM facility scheme of measurement, that allows for both an easier control of the relevant parameters and a more straightforward interpretation of the measured quantities.

Looking at it central role in upcoming testing campaigns, during the present work we both spotted the need for further debugging and identified possible short term upgrades aimed at further increasing the facility performances and lowering the measured excess noise:

- although the facility showed an appreciable level of insulation from external variables, our inability to effectively find any evidence of correlation even with those known to most likely affect pendulum motion is often due to many of the diagnostics being limited by their own readout noise: debugging and enhancing them to bring their noise floor below actual variables fluctuation could help in identifying any residual couplings and reduce its effects by means of both more effective shielding or post processing subtraction.

- Observed sporadic exceedingly big (probably mechanical) disturbing events, very unlikely originated inside the facility itself, suggest the need for a dedicated investigation and consequent better insulation or setup of suitable environmental conditions to perform ultimate sensitivity noise runs.

- Poor autocollimator performances spoiling the ability to extract valuable information by cross correlation analysis with much better capacitive sensor readout ask for finding an alternative secondary readout of comparable or better performances. ORO system already installed in the facility and currently under testing could represent a very effective solution, allowing at the same time for its in-deep testing based on everyday usage and for an enhancement of the facility angular readout performances.

With LTP launch scheduled in less than two years and the GRS Flight Model replica expected to be available for testing within the next few months, the most relevant and innovative results are expected to come with upcoming measurements campaigns. Stay tuned!

Appendix A

Electrostatic Model

By comparison of the results obtained by FEM simulation, the currently adopted simple model of infinite parallel plate capacitors (used so far for the design and optimization of the GRS) has demonstrated to be valid within an accuracy of 10%-20%, and it is precise enough for most of the estimate we need.

In particular, according to this electrostatic model, facing conducting surfaces have a capacitance

$$C = \frac{\epsilon_0 A}{d}$$

where ϵ_0 is the vacuum dielectric constant, A the overlapping area[1] and d the distance of the two. This means that border effects are neglected, and parallel translation of plates don't affect capacitance, except in the case that the overlapping area changes.

Moreover, because we deal with very small angle of rotation of the TM, it's easy to demonstrate [11] that at the first order we can still express the capacitance with the same formula, provided we substitute d with the mean distance between the plates. Note that this mean distance is in general a function of the TM rotation, and so the capacitance: this is indeed at the base of the angular sensing scheme, as explained in Section 2.1 and sketched in 2.2.

As most of the time we are interested in forces acting along X, we will end up with capacitance derivatives with respect to this variable. It can be noted that, according to the above model:

- if TM rotation and translations are small, at first order only surfaces distributed on the X faces have $\frac{\partial C}{\partial x} \neq 0$
- in the same approximation, these surfaces derivatives with respect to Z, Y and Θ are identically null

[1] Actually the only exception to this model is the estimate of the injection electrodes capacitance. As they are recessed by a non-negligible fraction of their size (about 1 mm) with respect to the guard rings surface, a small correction has been applied to account for field lines ending on the guard rings, thus reducing the real capacitance between the electrodes and the TM.

- it could be observed that as we consider a subdivision of one X face in smaller surfaces, among a translation in Z or Y some of them will change their overlapping to the TM, thus effectively changing their capacitance. However, provided the translations are "small", this concerns only surfaces facing the edges of the TM, and can be considered a border effect

This suggest that we will be interested only in derivatives of capacitances distributed on the X faces. For one of this surfaces of area A facing a TM displaced by x from its nominal central position, it holds:

$$C_{X\pm} = \frac{\epsilon_0 A}{d \mp x} \tag{A.1a}$$

$$\frac{\partial C_{X+}}{\partial x} = -\frac{\partial C_{X-}}{\partial x} = \frac{C_X}{(d+x)^2} \quad \Rightarrow \quad \left.\frac{\partial C_{X+}}{\partial x}\right|_{x=0} = -\left.\frac{\partial C_{X-}}{\partial x}\right|_{x=0} = \frac{C_X}{d} \tag{A.1b}$$

$$\frac{\partial^2 C_{X+}}{\partial x^2} = \frac{\partial^2 C_{X+}}{\partial x^2} = \frac{2C_X}{d+^2} \quad \Rightarrow \quad \left.\frac{\partial^2 C_{X+}}{\partial x^2}\right|_{x=0} = \left.\frac{\partial^2 C_{X+}}{\partial x^2}\right|_{x=0} = \frac{2C_X}{d^2} \tag{A.1c}$$

where $d = 4 \cdot 10^{-3}$ mm represents now the nominal gap between the TM and the EH along X, the subscripts $X+$ and $X-$ indicate if the surface belongs to the positive of negative EH X face and we defined $C_{X+}(0) = C_{X-}(0) = C_X$. We can also introduce here the "sign" function σ which value is 1 if the considered surface belongs to the $X+$ face, and -1 if it belongs to the $X-$ one: this way, we can write

$$\left.\frac{\partial C_{X\pm}}{\partial x}\right|_{x=0} = \sigma \frac{C_X}{d} \tag{A.2}$$

whichever the surface we are referring to.

The derivative values in zero have been reported as, being interested on the interaction that the TM undergoes when in its nominal position inside the GRS, it will often be useful to perform a series expansion of Equation 2.3 (V_{TM} dependence from x via polarization effects due to stray biases is here explicitly indicated) for small TM displacements x around its centered position:

$$F_X(x) = \frac{1}{2}\sum_i \frac{\partial C_i}{\partial x}\big(V_{TM}(x) - V_i\big)^2 \approx F_X(0) + F'_X(0)x =$$

$$\frac{1}{2}\sum_i \left.\frac{\partial C_i}{\partial x}\right|_{x=0}\big(V_{TM}(0) - V_i\big)^2 \tag{A.3a}$$

$$+\frac{1}{2}\sum_i \left.\frac{\partial^2 C_i}{\partial x^2}\right|_{x=0}\big(V_{TM}(0) - V_i\big)^2 x \tag{A.3b}$$

$$+\sum_i \frac{\partial C_i}{\partial x}\big(V_{TM}(0) - V_i\big)\left.\frac{\partial V_{TM}}{\partial x}\right|_{x=0} x \tag{A.3c}$$

that, exploiting relations A.1, can be rewritten:

$$
\begin{aligned}
F_X(x) \approx & \\
& \frac{1}{2}\sum_i \frac{C_{X,i}}{d}\big(V_{TM}(0) - V_i\big)^2 && \text{(A.4a)}\\
& + \sum_i \frac{C_{X,i}}{d^2}\big(V_{TM}(0) - V_i\big)^2 x && \text{(A.4b)}\\
& + \left.\frac{\partial V_{TM}}{\partial x}\right|_{x=0} \sum_i \frac{C_{X,i}}{d}\big(V_{TM}(0) - V_i\big) x && \text{(A.4c)}
\end{aligned}
$$

Appendix B

Calibrations

The general relation linking a pendulum DOFs χ_i and the sensor channel j output voltage V_j variations is of the form:

$$\Delta V_j = \Delta \chi_i \frac{\partial V_j}{\partial \chi_i} = \Delta \chi_i \frac{\partial(\Delta C_i)}{\partial \chi_i} \frac{\partial V_j}{\partial(\Delta C_i)} \tag{B.1}$$

Here $\frac{\partial(\Delta C_i)}{\partial \chi_i}$ is the channel j capacitance imbalance derivative with respect to χ_i, that is set by construction; $\frac{\partial V_j}{\partial(\Delta C_i)}$ is the electronics channel j output voltage derivative with respect to the capacitance imbalance, that is a parameter of the electronics and proportional to the TM 100 kHz polarization $V_{TM,inj}$; the latter, on is own, is a function of the bias voltage V_{inj} applied to injection electrodes via the parameter

$$\alpha = \frac{C_{inj}}{C_{tot}}$$

being C_{inj} the total capacitance of injection electrodes toward the TM and C_{tot} the total TM capacitance toward surrounding surfaces.

In principle, knowing the matrices of the parameters involved in Equation B.1 for each i and j allows for their inversion and reconstruction of the pendulum DOFs starting from channels outputs. However, GRS and STC electrostatic models are accounted for an accuracy not better than 10%, and sensing electronics come with channels nominal sensitivities that may depend on the actual cabling, temperature and overall operating conditions. It is thus necessary to calibrate the output voltages with respect to another reference instrument to get a correct angular readout of the pendulum position.

Despite we don't have an independent readout on all the pendulum degrees of freedom, the commercial autocollimator installed on the facility (see Section 4.1), although slightly worse in angular sensitivity with respect to the capacitive sensors assembly, provides this absolute reference for ϕ and η and, exploiting the fact that the parameters shown in Equation B.1 are not all independent for different i and j, can be used as a starting point for the calibration of most of the capacitive outputs.

In the following section we will present the detailed procedure used to calibrate the capacitive readouts together with some example of the result obtained.

B.1 Preliminary facility

As mentioned in Sections 5.2 and 6.2, the main angular capacitive readout ϕ_{cap} on both facilities is obtained as a combination of translational readouts of opposing TMs. A different combination of the same signals provides also inertial member translation along X axis, or pendulum tilt angle η_{cap}, being the two linked via the pendulum length L. These signals can thus be directly calibrated against the η and ϕ values read by the autocollimator.

Here we will describe the detailed calibration procedure for the preliminary facility. GRS facility procedures, that slightly differs because of the different number of DOFs provided by the capacitive sensors, will be presented in the next section.

The preliminary facility employs a pair of single DOFs capacitive sensors on opposite TMs. Suppose we know their (calibrated) displacement output x_1 and x_2, ϕ_{cap} and x_{cap} could be easily computed as

$$\phi_{cap} = \arctan\left(\frac{x_1 - x_2}{2b}\right) \approx \frac{x_1 - x_2}{2b} \tag{B.2}$$

$$x_{cap} = \frac{x_1 + x_2}{2} \tag{B.3}$$

where b is the arm of the pendulum and thus $2b$ is the distance between the sensors. Figure B.1 can help in understanding the meaning of these signals combinations; as a check, consider that with a pure rotation the two displacement would be equal and opposite, thus $x_{cap} = 0$, while with a pure translation they would be exactly equal, yielding $\phi_{cap} = 0$.

The above relations can be expressed in matrix form

$$\begin{pmatrix} \phi_{cap} \\ \\ x_{cap} \end{pmatrix} = \begin{pmatrix} \frac{1}{2b} & -\frac{1}{2b} \\ \\ \frac{1}{2} & \frac{1}{2} \end{pmatrix} \begin{pmatrix} x_1 \\ \\ x_2 \end{pmatrix} = \begin{pmatrix} \frac{1}{2b}\left(\frac{\partial V_1}{\partial x_1}\right)^{-1} & \frac{1}{2b}\left(\frac{\partial V_2}{\partial x_2}\right)^{-1} \\ \frac{1}{2}\left(\frac{\partial V_1}{\partial x_1}\right)^{-1} & \frac{1}{2}\left(\frac{\partial V_2}{\partial x_2}\right)^{-1} \end{pmatrix} \begin{pmatrix} V_1 \\ \\ V_2 \end{pmatrix} \tag{B.4}$$

Where Equation B.1 has been partially used together with the assumption that there are no cross-talks between different sensors (i.e. $\frac{\partial V_i}{\partial x_j} = 0$ if $i \neq j$).

As the autocollimator provides independent calibrated readouts ϕ_{ac} and η_{ac}[1], we

[1] Actually, autocollimator mounting doesn't guarantee alignment of its axis with Φ and E. Anyway, this correction can be easily done offline exploiting the characteristics free resonance frequencies of the pendulum along the two DOFs: as we aspect no oscillating signal at torsional resonant frequency to be present in η data, and the same for tilt signal in ϕ data, we can apply a rotation matrix to the autocollimator signals till we found no leakage of a free motion in the opposite DOF. In practice, this is done nulling in η data the torsional oscillating signal, as this can be easily made

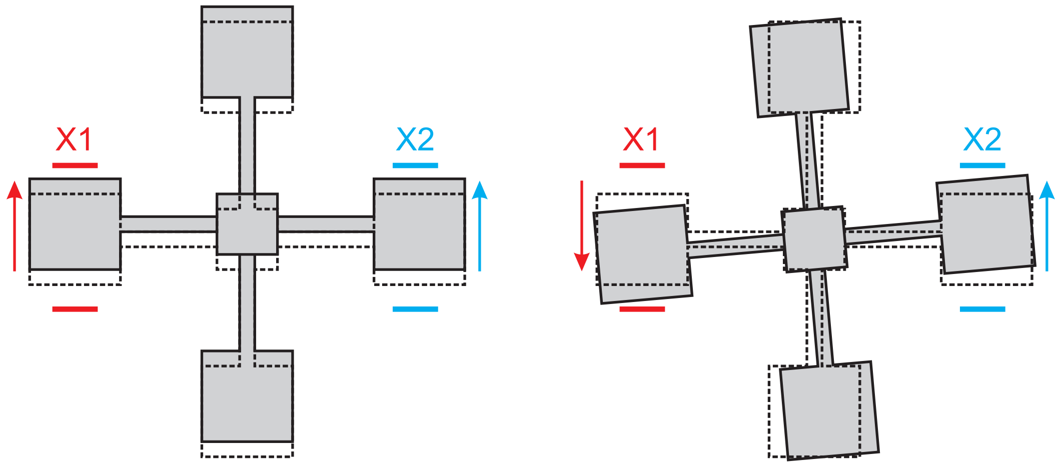

Figure B.1 – An illustration showing how capacitive sensors $x1$ and $x2$ translational data can be combined to obtain both the inertial member rotation angle phi and its translation x (actually equal to the $L\eta$, where L is the length of the pendulum and η its tilt angle). If the inertial member translates, both sensors reads the same displacements and their mean value represent the measured inertial member translation. If the inertial member rotates, the signal on the two sensors have opposite sign, and their difference divided by their separation measures the angle of rotation.

can set them to be equal to those read by the capacitive sensors

$$\begin{pmatrix} \phi_{cap} \\ x_{cap}/L \end{pmatrix} = \begin{pmatrix} a_{11} & a_{12} \\ a_{21} & a_{22} \end{pmatrix} \begin{pmatrix} V_1 \\ V_2 \end{pmatrix} \stackrel{!}{=} \begin{pmatrix} \phi_{ac} - \phi_0 \\ \eta_{ac} - \eta_0 \end{pmatrix} \tag{B.5}$$

where ϕ_0 and η_0 accounts for the arbitrary autocollimator zero set by mounting, and are subtracted to its signals (instead of summed to the capacitive ones) because we want to use the sensors centers as a reference. We also used the relation $x = L\eta$, for which some conditions are actually needed:

- the approximation of small angles should apply, so that

$$L \sin(\eta) \approx L\eta$$

- signals used for calibration should be slow induced tilts (i.e. much slower than the natural resonant frequencies involved in the η dynamics): this way the pendulum will tilt as a whole with respect to the camber (actually the chamber will tilt with respect to the pendulum, that remains vertical!), and any potential "high frequency" resonant oscillation can be filtered out, neglecting that the pendulum is actually a double one with a complex dynamics;

- it should be possible to consider any X motion of the inertial member relative to the sensors assembly due to a change in the relative tilt angle η, while in principle it could also be due to real X displacement, that is not read by

big enough to resolve required autocollimator axis rotation better than 10^{-2} rad the autocollimator. This is certainly possible when we perform a calibration, purposely inducing a tilt signal as big as to overcame by orders of magnitude any pure X translation (that by construction should not be present and can thus be due only to vibrations or deformation of the structure).

Note that "big" here doesn't conflict with the first assumption made: we are indeed speaking about induced tilts of order 10^{-3} rad, that means that relative error made applying the small angle approximation is of order 10^{-6}.

Although the four matrix coefficients a_{ij} are not independent, as can be seen comparing Equations B.4 and B.5, we can consider them to be so and solve the two rows of the above system independently. Because we deal with measured noisy signals, each equation is obviously not exactly solved for a single value of the variables, but instead a bilinear least-squares fit on the time series is performed:

$$\phi_{ac}(t) = a_{11}V_1(t) + a_{12}V_2(t) + \phi_0 \tag{B.6a}$$

$$\eta_{ac}(t) = a_{21}V_1(t) + a_{22}V_2(t) + \eta_0 \tag{B.6b}$$

Consider anyway that, for the calculated a_{ij} coefficients to be reliably calculated considering each single equation independently instead of the system of the two, both $\phi(t)$ and $\eta(t)$ should not be constant: otherwise signals triplet taken at different moments (e.g. $\{\phi_{ac}(t_1) - \phi_0, V_1(t_1), V_2(t_1)\}$ and $\{\phi_{ac}(t_2) - \phi_0, V_1(t_2), V_2(t_2)\}$ if fitting ϕ data) would be proportional and there will be infinite equivalent combinations of $V_1(t)$ and $V_2(t)$ that minimize the squared residuals with respect to $\phi_a c(t) - \phi_0$.

As an example, consider that no η motion is present: the inertial member ϕ rotation can be obtained by x_1/b, $-x_2/b$, or $\alpha x_1/b + \beta x_2/b$ provided $\alpha + \beta = 1$. The result of the bilinear fit would be any of these possible solutions, the actual one being only chosen by statistical fluctuations. On the contrary, if a ϕ motion is present, only the linear combination $(x_1 - x_2)/2b$ will rejects it and minimize the sum of the squared residuals, resulting the output of the bilinear fit procedure.

A typical calibration procedure thus consists in exciting both twist and tilt motion of the pendulum, and performing a bilinear fit to both ϕ_{ac} and η_{ac} using V_1 and V_2. In doing that, we adopt some watchfulness:

- To change ϕ, we use the natural oscillation of the pendulum after setting it to a relatively big amplitude

- To change η, we step on and off the facility platform with a relatively low frequency (several tens of seconds), trying to avoid to excite the pendulum natural swing frequency. There is another reason to do so in addition to those already explained speaking about the role of pendulum dynamics: because of different electronics and filtering, autocollimator and capacitive readouts can indeed have a relative delay that is negligible compared to the pendulum twist period of about 1400 s or our induced signal one of order 50 s, but could be a noticeable fraction of the swing one of about 2 s: if at strong signal at such a frequency is present, we could end up trying to fit time series with a big delay, with consequent poor results.

- While the tilt signal amplitude is limited to what we can obtain stepping on the platform, we have a certain freedom on the twist one: anyway it is advisable to keep the voltage signals induced by the two motion to comparable values so to maximize the efficiency of the orthogonalization mechanism explained above.

Once the for coefficients have been obtained from the bilinear fit, we can thus finally reconstruct the capacitive signals by means of Equation B.5.

As shown by Equation B.4, coefficients obtained by independent fitting of η and ϕ are not independent as they are calculated as different combinations of a number of physical parameters involving the pendulum geometry, the sensors electrostatic models and the electronic characteristics. The number of unknowns is higher than the number of independent estimate of the parameters, and thus exact calculations of the firsts starting from the lasts is not possible. However the relations can be exploited to estimate some of them (considered to have a bigger uncertainty) assuming the others as better known. Consider for example we want to estimate the length of the pendulum and the distances b_1 and b_2 (that can in principle be different) of the TMs from the suspension center. From the fitting procedure we obtain actual values for the coefficients:

$$a_{11} = \frac{1}{2b_1}\left(\frac{\partial V_1}{\partial x_1}\right)^{-1} \qquad a_{12} = \frac{1}{2b_2}\left(\frac{\partial V_2}{\partial x_2}\right)^{-1}$$
$$a_{21} = \frac{1}{2L}\left(\frac{\partial V_1}{\partial x_1}\right)^{-1} \qquad a_{22} = \frac{1}{2L}\left(\frac{\partial V_1}{\partial x_1}\right)^{-1}$$

Alas, no combination of this coefficient can completely resolve any parameter:

$$\frac{a_{21}}{a_{11}} = \frac{b_1}{L} \qquad \frac{a_{22}}{a_{12}} = \frac{b_2}{L}$$

The combination $\frac{a_{21}a_{12}}{a_{11}a_{22}}$ will yield the ratio between b_1 and b_2. We can alternatively choose to trust our previous knowledge of L (obtained for example from the pendulum tilt resonant frequency), to obtain estimates for b_1 and b_2. However, even supposing the two pendulum arms b_1 and b_2 to be equal, we will obtain two slightly different values (because of experimental uncertainties) for the same quantity b/L, but it will not help in estimating the values of b and L separately.

B.2 GRS testing facility

The way DOFs are calibrated in the GRS testing facility is similar to that presented in the previous section, except that here we have a number of additional readout, partially dependents, that requires small modifications and provide the ability to read additional DOFs.

As in the preliminary facility, the only absolute reference is the autocollimator that reads ϕ and η, and thus this two DOFs are the most immediate to calibrate. However, while the STC provides only one channel x_s that is sensitive to the TM translation along X, the GRS provides two of them, x_1 and x_2. Among the possible solutions to handle the extra signal, the one we adopted is to consider each of them separately and calibrate it together with x_s against the autocollimator.

Each of the two pairs of signals (V_1, V_s) and (V_2, V_s) is processed exactly as described in the previous section, obtaining the translational sensitivities of each channel. x_s channel sensitivity is thus measured twice, and the mean value is taken as the best estimate (provided the two values are compatible within the errors, otherwise the calibration is considered to be wrong). The final estimate of the pendulum rotation angle ϕ is computed combining all the three signals:

$$\phi_{cap} = \frac{1}{2b}\left(x_s - x_{GRS}\right) = \frac{1}{2b}\left(x_s + \frac{x_1 + x_2}{2}\right) \tag{B.7}$$

The same holds for η:

$$x_{cap} = \frac{1}{2}\left(x_s + x_{GRS}\right) = \frac{1}{2b}\left(x_s + \frac{x_1 + x_2}{2}\right) \tag{B.8}$$

In Figure B.2 we show an example of ϕ signal calibration.

It's worth noting that, being the GRS X electrodes vertically off-center with respect to the TM (see Figure 3.7), a slightly different conversion arm compared to x_s should be used for both x_1 and x_2 to obtain η.

$$\eta_{cap} = \frac{1}{2L}\left(x_s + x_{GRS}\right) = \begin{cases} \frac{1}{2L}\left(x_s + \frac{L}{L+r}x_1\right) \\ \frac{1}{2L}\left(x_s + \frac{L}{L-r}x_2\right) \end{cases} \tag{B.9}$$

Where $2r$ is the distance between the two GRS X electrodes centers on one face. Thus, in analogy with the previous section and indicating with superscript "1" and "2" the coefficients obtained from the calibration exploiting, respectively, x_1 and x_2

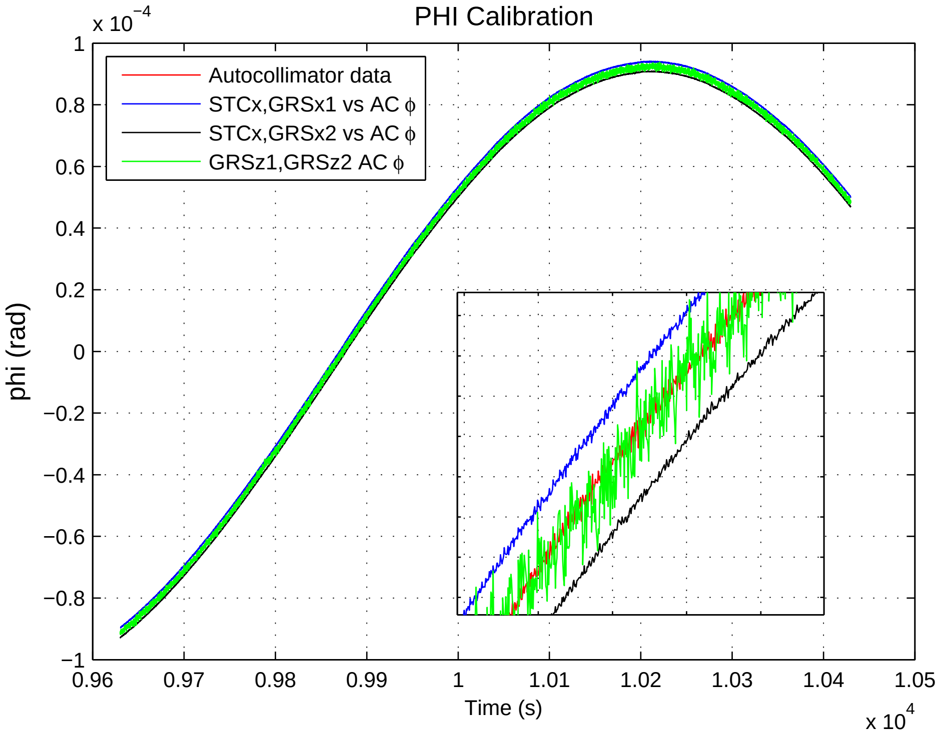

Figure B.2 – Autocollimator ϕ signal used to calibrate capacitive angular readout. The rotational signal can obtained as a combination of different displacement ones: STC X channel and one or the other of the GRS ones (showed in blue and black), or even using only the two GRS Z electrodes, as it will be done in flight (showed in green). Notice however that this last option exploit a much smaller arm between the two displacement readouts used to reconstruct the ϕ signal, thus resulting in an evident higher noise. We note that the small but noticeable offset between the different signal is due to offset in the electronics on in the actual TM rotation along η: being constant it doesn't have any impact on the measurement performed.

signals:

$$a^1_{11} = \frac{1}{2b_s}\left(\frac{\partial V_s}{\partial x_s}\right)^{-1} \qquad a^1_{12} = \frac{1}{2b}\left(\frac{\partial V_1}{\partial x_1}\right)^{-1}$$
$$a^1_{21} = \frac{1}{2L}\left(\frac{\partial V_s}{\partial x_s}\right)^{-1} \qquad a^1_{22} = \frac{1}{2(L+r)}\left(\frac{\partial V_1}{\partial x_1}\right)^{-1}$$

$$a^2_{11} = \frac{1}{2b_s}\left(\frac{\partial V_s}{\partial x_s}\right)^{-1} \qquad a^2_{12} = \frac{1}{2b}\left(\frac{\partial V_2}{\partial x_2}\right)^{-1}$$
$$a^2_{21} = \frac{1}{2L}\left(\frac{\partial V_s}{\partial x_s}\right)^{-1} \qquad a^2_{22} = \frac{1}{2(L-r)}\left(\frac{\partial V_2}{\partial x_2}\right)^{-1}$$

From which you can obtain:

$$\frac{a^{12}_{21}}{a^{12}_{11}} = \frac{L}{b_s} \qquad \frac{a^1_{22}}{a^1_{12}} = \frac{L+r}{b} \qquad \frac{a^2_{22}}{a^2_{12}} = \frac{L-r}{b}$$

where b and b_s are the pendulum arm on the GRS and STC sensors respectively, and values with superscript "12" represent average values between the corresponding coefficients that measure exactly the same quantities in the two calibrations (e.g. $a^{12}_{11} = (a^1_{11} + a^2_{11})/2$). As in the previous section, the above values can be used to estimate some of the parameters supposing known some other. For example, supposing r to be well known (note that this implies not only precision of machining and assembling, but also a reliable electrostatic model as the effective center of the electrode from a capacitive point of view is not guaranteed to correspond to its geometrical center), you can resolve the remaining three parameters:

$$-2r\left(\frac{a^1_{22}}{a^1_{12}} - \frac{a^2_{22}}{a^2_{12}}\right)^{-} 1 = b \rightarrow \frac{b}{2}\left(\frac{a^1_{22}}{a^1_{12}} + \frac{a^2_{22}}{a^2_{12}}\right) = L \rightarrow L\frac{a^{12}_{11}}{a^{12}_{21}} = b_s$$

Note also that, in principle, x_1 and x_2 are sensitive to TM rotation inside the GRS, even if it doesn't corresponds to a motion of the TM geometrical center (that on the contrary is measure by the STC). Anyway, such a rotation can happen only as an oscillation of the inertial member around the lowest fiber suspension point, and can thus easily filtered out from the signal at the beginning of the fitting procedure[2].

The same bilinear fit technique can be used to calibrate a variety of channels against autocollimator ones or capacitive previously calibrated ones. In particular:

[2]Please note that, as explained in the previous section, a low pass filter is already foreseen to suppress the swing motion. Moreover, this inertial member high frequency swing happens a such an high frequency (about 2 Hz, being the rigid shaft few centimeters long) that even if unfiltered its contribute would almost average to 0 on the timescale of a typical calibration.

	GRS						STC		AC	
	x1	x2	y1	y2	z1	z2	xs	zs	ϕ_{ac}	η_{ac}
ϕ	C						C		R	
		C					C		R	
					C	C			R	
η	C	C								R
θ			C	C	R	R		R		
X	C						C			R
		C					C			R
Y										
Z					R	R		C		

Table B.1 – The table lists all the facility DOFs, and readouts that can be used to reconstruct them. Each line refers to a calibration operation, where the reference signal is indicated by "R" and the calibrated one(s) by a "C".

- x_1 and x_2 can be calibrate against η_{ac}, as they read the η via the TM rotation inside the GRS (note that this is equivalent to accounting for the parameter r in the above analysis, and constitutes only a cross check).
- GRS z_1 and z_2 can be calibrate against ϕ_{ac}, that they read as a TM rotation
- z_1 and z_2 linear sensitivities obtained from the previous calibration can be exploited to reconstruct the inertial member translation along Z, an thus calibrate the STC z_s channel.

Table B.1 lists all the available channels and the combinations of them that can be used to calibrate different DOFs.

As an example, we report here the output of the calibration routine during a typical calibration run.

```
*************************SUMMARY*************************
*                                                       *
*- Geometrical and phisical factors used for calculation -*
*                                                       *
*  Simple pendulum length = +1.229e+000 m (4.497e-001 Hz) *
*    Torsion pendulum arm = +1.056e-001 m               *
*        X electrodes arm = +1.075e-002 m               *
*        Z electrodes arm = +1.525e-002 m               *
*      Alpha factor for EM = +1.360e-001                *
*    Alpha factor for STC = +1.940e-001                 *
*    EM Injection voltage = +8.500e+000 V               *
*   STC Injection voltage = +8.500e+000 V               *
*                                                       *
*- EMx1 and STCx vs PHI calibration ----------------------*
*                                                       *
* /phi\   /-5.328e-004\   /+1.362e-004 -2.432e-004\ /EMx1\*
* |   | - |           | = |                       | |    |*
* \eta/   \-3.337e-004/   \-1.139e-005 -2.094e-005/ \STCx/*
*                                                       *
* dV/dX1 = +3.475e+004 +- 0.013 % (from PHI calibration)  *
*        = +3.571e+004 +- 0.147 % (from ETA calibration)  *
* dC/dX1 = +2.134e+002 pF/m ( +2.89e+002 expected)        *
*        = +2.193e+002 pF/m ( +2.89e+002 expected)        *
*                                                       *
* dV/dXs = +1.946e+004 +- 0.011 % (from PHI calibration)  *
*        = +1.943e+004 +- 0.121 % (from ETA calibration)  *
* dC/dXs = +8.224e+001 pF/m ( +1.08e+002 expected)        *
*        = +8.212e+001 pF/m ( +1.08e+002 expected)        *
*                                                       *
*- EMx2 and STCx vs PHI calibration ----------------------*
*                                                       *
* /phi\   /-5.296e-004\   /+1.369e-004 -2.411e-004\ /EMx2\*
* |   | - |           | = |                       | |    |*
* \eta/   \-3.340e-004/   \-1.143e-005 -2.109e-005/ \STCx/*
*                                                       *
* dV/dX2 = +3.458e+004 +- 0.013 % (from PHI calibration)  *
*        = +3.560e+004 +- 0.147 % (from ETA calibration)  *
* dC/dX2 = +1.926e+002 pF/m ( +2.89e+002 expected)        *
*        = +1.983e+002 pF/m ( +2.89e+002 expected)        *
*                                                       *
* dV/dXs = +1.963e+004 +- 0.011 % (from PHI calibration)  *
```

```
*        = +1.929e+004 +- 0.121 % (from ETA calibration)  *
* dC/dXs = +8.296e+001 pF/m ( +1.08e+002 expected)        *
*        = +8.152e+001 pF/m ( +1.08e+002 expected)        *
*                                                         *
*- EMz vs PHI calibration --------------------------------*
*                                                         *
* |phi| - |-5.361e-004| = |+1.592e-003 -1.582e-003| /EMz1\*
*                                                   |    |*
*                                                   \EMz2/*
*                                                         *
* dV/dZ1 = +2.060e+004 +- 0.014 % (from PHI calibration)  *
* dC/dZ1 = +1.232e+002 pF/m ( +1.74e+002 expected)        *
*                                                         *
* dV/dZ2 = +2.072e+004 +- 0.018 % (from PHI calibration)  *
* dC/dZ2 = +1.160e+002 pF/m ( +1.74e+002 expected)        *
*                                                         *
*- STCz vs EMz calibration -------------------------------*
*                                                         *
* |teta| = -1.291e-004 x STCz + +8.616e-006               *
*                                                         *
* dV/dZs = -7.745e+003 +- 0.007 % (from EMz comparison)   *
* dC/dZs = +3.056e+001 pF/m ( +?????+??? expected)        *
*                                                         *
*- EMx vs ETA calibration --------------------------------*
*                                                         *
* |eta| - |-3.050e-004| = |-1.217e-003 +1.213e-003| /EMx1\*
*                                                   |    |*
*                                                   \EMx2/*
*                                                         *
* dV/dX1 = -3.821e+004 +- 0.331 % (from ETA calibration)  *
* dC/dX1 = -2.347e+002 pF/m ( +2.89e+002 expected)        *
*                                                         *
* dV/dX2 = -3.835e+004 +- 0.331 % (from ETA calibration)  *
* dC/dX2 = -2.135e+002 pF/m ( +2.89e+002 expected)        *
*                                                         *
***********************************************************
```

Appendix C

ORO

An high sensitivity optical readout (*ORO*) system is being developed by the INFN group in Napoli. It is able to discriminate up to all the TM six DOFs by means of laser optical levers detected by quadrant photodiode (the system is modular, with three optical levers guaranteeing full DOFs reconstruction), and is proposed as as independent, more sensible redundant readout solution for the drag free control loop during the LISA mission [40]. Although readout performances have been partially demonstrated on benchc[41], both a more representative readout noise characterization and a calibration and operation procedures test would be desirable: the 4-Tm torsion pendulum offers a precious test bench thanks to its high level of vibrational noise insulation and its flight representative setup with one almost free DOF. The ORO system has thus been integrated on the STC sensor by means of suitable interfaces with the aim of testing its capabilities in terms of readout noise and setting up centering and calibration procedures. In addition, it can serve as an additional high sensitivity readout for combined sensor readout noise rejection (see Section 7.2.5).

C.1 Operating concept

Development of the ORO system is not part of this thesis, and detailed descriptions could be found in [40]. However, we will briefly introduce here its operating principle to better understand how it has been integrated in the facility and how it can be used.

The ORO is based on a combination of optical levers shining on different TM faces: each of them is composed by an infrared laser beam that bounces on a TM face with an incident angle different from 0, and is then detected by means of a quadrant photodiode, able to measure the spot position of the incoming beam. The position in which the beam hit the photodiode changes upon face translation along its normal and rotation around the two axis orthogonal to the normal. Combining two optical levers shining on opposite faces, with suitable orientations, it is thus possible to discriminate these three DOFs. An example of the working scheme, in

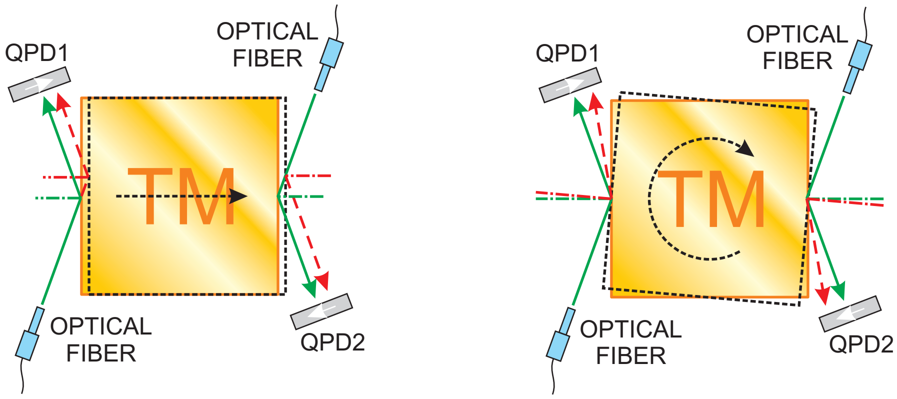

(a) TM translation

(b) TM rotation

Figure C.1 – Operating principle of the Optical Read Out system, based on optical levers each composed by a quadrant photodiode (QPD in the drawings) and an infrared laser launched by a suitable optical fiber. Employing two optical levers shining on two opposite TM faces is possible to discriminate one TM translation (exemplified in (a)) and two rotations (one is exemplified in (b), the other can be discriminated comparing spots displacement along the direction orthogonal to the drawing).

which both TM translation and rotation around one axis are considered, is given in Figure C.1.

Additional levers are required to discriminate all the six DOFs of a free TM.

The ORO system has been demonstrated on bench to be capable of a translational sensitivity of order 10^{-9} m/Hz$^{1/2}$ at 1 mHz, and decreasing as $1/f$. The corresponding rotational sensitivity should be of order 10^{-8} rad/Hz$^{1/2}$ for the same frequency.

C.2 Integration of ORO in the 4-TM facility

ORO performances have been demonstrated on bench within about a factor five from its nominal sensitivity, employing a fixed target. Testing it on an almost-free TM in a representative flight setup will be highly desirable for both verifying actual performances and setting up calibration procedure. Moreover, possible related force noise should be tested.

The ORO system has thus been integrated in the 4-TM facility, exploiting the STC (see Section 6.3) sensor. As the simplified, two optical lever configuration presented above is sufficient to test the system and provide a readout for the 4-TM torsion pendulum, suitable mounting interfaces as well as passing holes have been provided on the STC to allow the two lasers to enter the sensor, shine on the TM $X+$ and $X-$ faces and exit again hitting the two quadrant photodiodes. This way ORO system is capable of discriminating the pendulum ϕ rotation angle, its η tilt angle (that are the same two read by the autocollimator) and the TM X translation inside the EM. Figures C.2 presents a sketch of the integration scheme and some

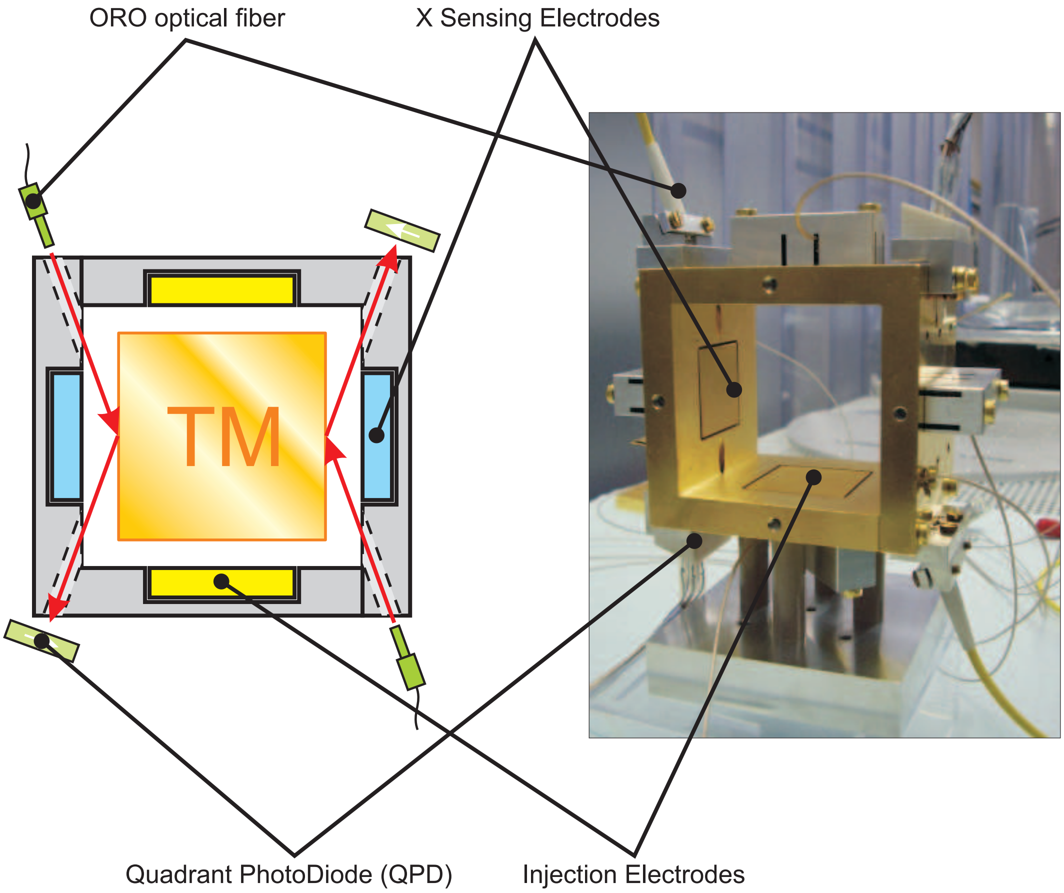

Figure C.2 – A scheme of the ORO installation in the 4 TM facility exploiting the STC as mounting support. Relevant features are highlighted on both the scheme and the picture of the STC, here without the $Z+$ and $Z-$ lids.

pictures of the system installed on the STC.

Along with dedicated hardware and design details, ORO integration on the 4-TM facility required the setup of both on-bench and in-operation aligning procedures to ensure the ability to operate it within its relatively small dynamic range while retaining the ability to operate the capacitive sensors in their best sensitivity conditions. A description of this procedures and dedicated hardware can be found in Appendix D.

The ORO readout is currently under testing, and calibration procedures have to be set-up. Besides verifying its performances and setting upper limits of the related force noise, once fully operational we plan to use it to replace the autocollimator as independent readout system, to exploit the readout noise rejection capabilities of the cross correlation data analysis presented in Section 7.2.5; we will thus be able to take full advantage of its increased sensitivity with respect to the autocollimator, whose performances limit at present the advantages coming from the joint data analysis with the more sensitive capacitive sensors setup.

Appendix D

Alignments

Assembling and alignment precision plays an important role in our effort to make the pendulum operate at its ultimate sensitivity limit, and are required to accurately measure GRS parameters. In particular, inertial member assembly accuracy impacts on its symmetry and, consequently, on its gravitational coupling to the environmental gravitational noise (see Section 3.4 and 5.3.2). At the same time, sensors alignment is required to assure they can operate simultaneously near they dynamic range center, thus in the best sensitivity conditions.

In the following two sections we describe in detail the procedures used for the GRS testing facility to assemble the pendulum inertial member and sensors, and those adopted to center the inertial member with respect to the sensors assembly.

Alignment procedures for the preliminary facility are much more simple, as less accuracy was required and fewer degrees of freedom were available both as readout and as alignment possibilities. They will thus not be described here.

D.1 On-bench assembling and centering procedures

D.1.1 Inertial member

Mock-ups of LISA TM have been provided by a commercial partner that states assembly precision of about 10 μm on assembled structure. However, combining them in an highly symmetric compound structure is not easy: the central support holds them exploiting less than $1cm$ of the about 10 cm long shaft, thus requiring very high accuracy assembly considering the factor 10 or more of TM position error amplification.

Among the different proposed alternatives for the central support, we chose the solution that foresaw by design alignment of the highest number of DOFs. It is a square support composed of two main parts: a bottom one with four V-shaped grooves in which TM shafts lay, tightened by one screw pushing from the top part when the two are assembled together. Small aluminum plates are inserted between the screw head and the shafts to reduce friction and asymmetric stress on the shaft

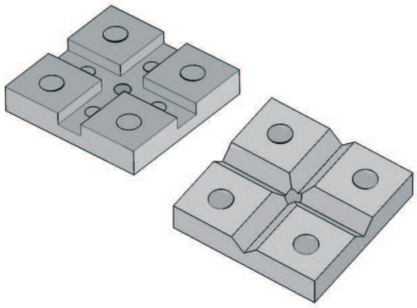

(a)

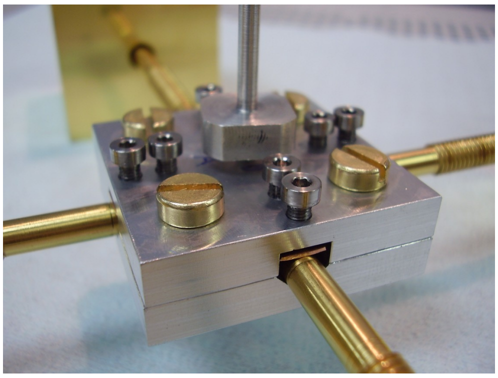

(b)

Figure D.1 – Some cartoons (a) and pictures (b) of the GRS testing facility inertial member central support, that holds the four TM mock-ups and provide their alignment along all the DOFs except rotation around and translation along their shafts.

that may compromise alignment when tightening. The structure, shown in Figure D.1, was machined on a very high precision (about several μm nominal) numerical controlling milling cutter.

The foreseen solution to correctly align TMs along the residual DOFs was an assembly mask constraining TM and central support position so to impose correct distances. However, that would have resulted in an over-binding of some component, that is not desirable if requesting high accuracy assembly because different constrains are likely to conflict each other. Moreover, binding the whole structure at once would require a mask composed of a single machined piece (as using an assembled mask would lead to assembly errors the same order of magnitude of the ones we want to correct): using such a mask lead to the problem of disentangling the mask and the assembled inertial member once tightened, with possible damage to the gold coated surfaces.

To get rid of these problems we setup a procedure based on alternate alignment of different arms of the cross shaped inertial member exploiting always the same three reference points. Using the mask shown in Figure D.2 we adopted the following procedure, sketched in Figure D.3:

1. we roughly assembled two opposing TM (*TM1* and emphTM2) together with the central support

2. holding them against point "A" and "B", we assembled *TM3* on the other arm pushing it against point "C" and thus fixing its distance from the central support, whose position was bound by that of TM1 and TM2

3. we then rotated the structure 180, and applied the same technique to *TM4*. Now TM3 and TM4 distance from central support were based on the same reference

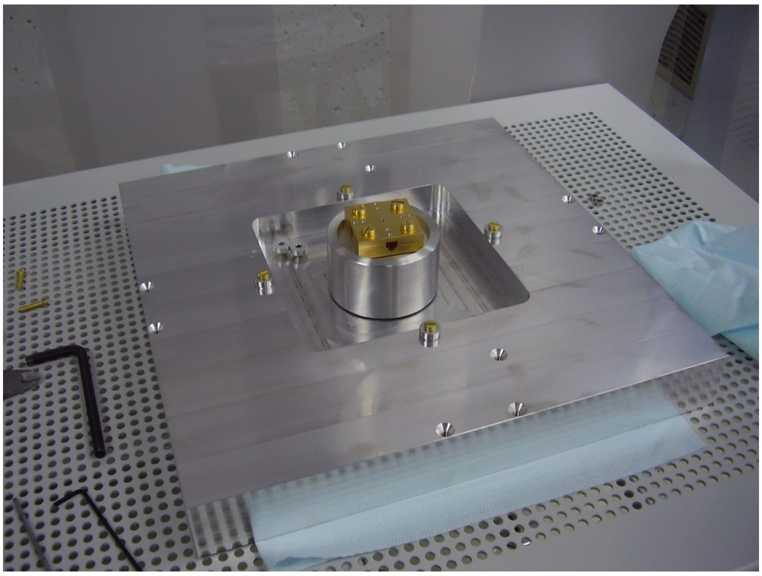

Figure D.2 – Picture of the assembly mask used for aligning the inertial member.

4. we rotate the structure 90 and applied the same procedure to TM1
5. we rotate again the structure 90 and applied the same procedure to TM2

at each aligning step, TM lower faces were kept in contact with the high precision finishing plane of the assembly mask, so to provide also alignment along the rotational DOF around their shaft.

After assembling the inertial member we measured it to evaluate the achieved assembly accuracy. The assembly mask plane served as a reference for estimating relative TM rotation (fixed by the central support machining quality and single TM assembly accuracy) with respect to the two horizontal axis: with one edge of the lower face touching the plane, the distance between this and the opposite edge was roughly estimate, when appreciable, to be less than 0.1 mm in the worst case, thus yielding an angle smaller than 2 μrad. A simple solution for measuring distances between TM was instead unavailable, as we had no measuring tool precise enough to measure more than 20 cm long distances with the accuracy of some fractions of a millimeter, enabling at the same time to avoid scratching the surfaces.

The solution was found in using a commercial scanner with an optical resolution of 800 dpi, corresponding to a pixel size of about 30 μm to acquire and compare images of the inertial member. In such a device, the image is obtained moving a linear array of sensible elements coupled with a suitable lens (that we will call X axis) along the direction orthogonal to the array (Y axis), using a precise microstep motor. The shape of each pixel is thus not necessarily square (i.e. the distance between the sensible elements could be different from the motor steps size), and some type of calibration is necessary[1]. We thus tried at first a calibration of the instrument

[1]In principle, we should also check for uniformity of pixel dimensions in different zones of the

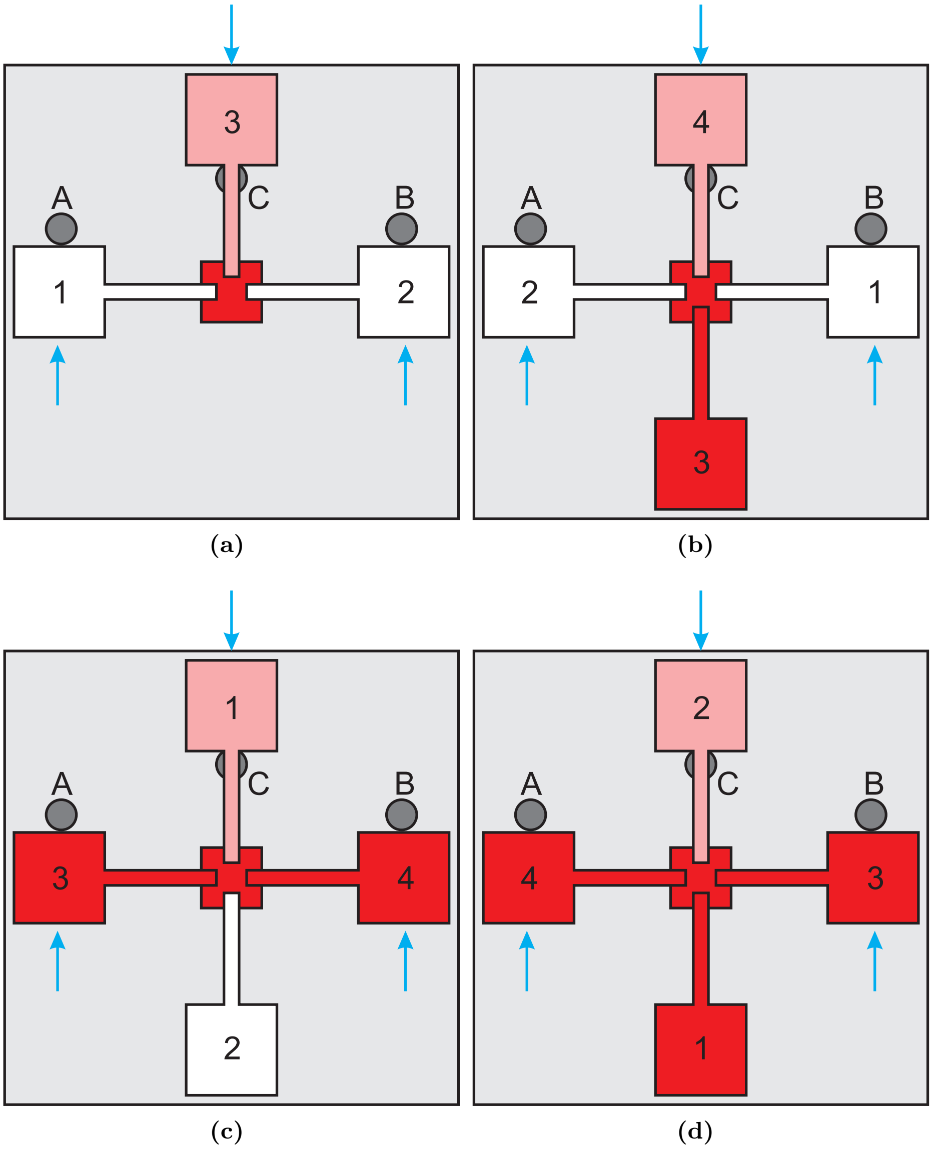

Figure D.3 – Schematic cartoon of the inertial member assembly procedure. In (a) TM1 and TM2 are roughly assembled and used as a reference against stoppers "A" and "B" for assembling TM3 against stopper "C"; in (b) the structure is then rotated 180 and procedure repeated for TM4; in (c) and (d) structure is rotated again and procedure repeated for TM1 and TM2. At each step, already aligned TMs are represented as filled in red, and TM currently being aligned in pink. Blue arrow represent pressure point to keep TMs against stoppers.

acquiring the image of a graph paper sheet, obtaining very small deviation along the two axis: in therms of scale factor between the measured size and the nominal one, they were 1.0095 for X and 1.0019 for Y. However, a relative calibration between X and Y obtained by comparison of the same quantities measured along different axis, acquiring 4 image of the inertial member rotated by 90 each, shows a different relative scale ($X/Y = 1.0200$ on average instead of 1.0075): this was probably due to the fact that the lens in front of the linear array is such that it scales object based on their distance from the scanning plane (that is very likely to happen as sensitive arrays are in general very compact in dimension, and the image need to be reduced and projected on them); this obviously doesn't happen on the other axis, in which you have a pure translation of the array. Because the graph paper was lying on the scanner plane, while the inertial member was slightly higher because it was too big for the plane width and was lying on scanner lateral plastic borders, this explains why we found a different scaling factor for one X axis and thus a different relative one between the two.

We thus measured various distances to check the assembly accuracy, correcting them for the relative scale an then applying Y axis calibration to obtain actual values in *mm*. As an example, in table Table D.1 we list the most significant among them: the distance between internal edge of opposing TM (i.e. the pendulum arms, except from a constant), measured on both "top" and "bottom"[2] side of the inertial member has been measured, and both raw and corrected values are reported. It can be observed that arms measured using top edges are equal within few cents of a mm, while on the other side the difference between the two is ten times more: that was because the top side was actually laying on the plane during assembly (it was assembled upside down because TM shafts tightening screws are accessible from the bottom side), and the stoppers, raised few mm above the plane, were in practice pushing against the "top" (but actually bottom during alignment) edges of the TMs. The "top" edges were thus the ones actually bound by the assembling mask, while the difference in the edges distances on the other side gives clues about the geometrical precision of the TMs (considering here all kind of assembly and machining imperfections), that are probably worst than what stated by the manufacturer. Anyway the demonstrated assembling accuracy is high enough to reduce the sensitivity to previously measured gravitational noise below the thermal torque noise, thus not representing a limiting factor for the facility performance.

One important observation should be done about this measurements: when performing the final assembly of the inertial member, we had to include GRS and STC top lids as the TMs shafts had to pass trough them before being tightened to the central support. Given their size, this (and any other simple, although less precise)

image. However, as we are always using the same portion of the scanner plane to perform the measurement, we expect these effects, if present, to be very small as they affect only the few pixels that are not common to two compared measures

[2] this names refers to the inertial member suspended to the fiber

rot.	Arm 1 Top X	Arm 1 Top Y	Arm 2 Top X	Arm 2 Top Y	Arm 1 Bottom X	Arm 1 Bottom Y	Arm 2 Bottom X	Arm 2 Bottom Y
0	161.71	*164.95*		164.97	161.73	*164.96*		164.72
90		165.03	161.83	*165.07*		165.04	161.54	*164.77*
180	161.78	*165.02*		164.94	161.77	*165.00*		164.73
270		165.19	161.85	*165.09*		165.03	161.56	*164.79*
Aver.		165.05		165.02		165.01		164.75
Cal.		**165.36**		**165.33**		**165.32**		**165.06**

Table D.1 – The table shows data of two different sets of measurement performed on scanned inertial member images (units are mm): columns 2 to 5 corresponds to arm 1 and arm 2 measured with the "top" side of the inertial member toward the scanner plane; depending on the inertial member rotation on the corresponding image, each arm has been measured along X or Y. In the Y column, *emphasized* numbers represent corresponding X measurement converted to Y units for comparison. The same applies for columns 6 to 9, obtained from a different set of images with the "bottom" side of the inertial member toward the scanner. Last two line shows averaged values over the four inertial member rotations and conversion to actual value via application of the Y calibration obtained scanning the graph paper. As you can see, average values for the two arm lengths on the "top" side differ for 0.03 mm, while in the other case the difference is about ten times bigger.

procedure is no longer applicable. We thus repeated the alignment couple of time without the sensor lids, verifying that we were able to replicate the same results, and the assumed them to be valid also for the final, not measured, assembly.

D.1.2 GRS

The GRS has been assembled as part of a previous work, and as been installed in the facility without disassembling and reassembling it. The procedure will thus not be described here. However, the machining ad assembling procedures aimed at an accuracy of order 10 μm. The only check we did based on "force zero" position measurement (see Section 8.3) confirmed this overall geometrical precision.

D.1.3 STC

Due its nature of auxiliary sensor that doesn't need to be characterized, and the bigger gaps that makes little misalignments more easily negligible, the STC requirements in terms of assembly precision are relaxed.

While in assembling the STC EH we only exploited the alignment provided by the screws that hold together the four parts (two half of the main body plus two lids), a bit more attention was dedicated to installation of the electrodes.

1 mm thick Teflon spacers were placed in the grooves between each electrode and the EH before tightening it with the rear screw, while the spacing bushing was responsible for correct alignment of the electrode exposed face with the corresponding EH one, both in tilt and in distance from the TM.

D.1.4 ORO

As already said, ORO radout (see Section C) in installed in the facility exploiting the STC as mounting support for quadrant pohotodiodes and optical fibers. Its small dynamic range required an accurate alignment of the elements to assure than both laser spots hit photodiodes in the center for a reasonably centered position of the TM. Note that, on the other hand, the STC itself is insensitive to the two TM rotations seen by ORO, and the only precise relative alignment between the two has to be performed along the TM X axis.

We thus built a dedicated support able to rigidly suspend, inside the STC, the TM to be used as a reference for correct ORO alignment. Being the STC insensitive on most DOFs, rough centering between it and the TM was performed by means of spacers. Then then ORO photodiodes and optical fibers were installed in such positions to read an almost centered signal on all DOFs.

This way, the assembly STC+ORO became a 5-DOFs sensor.

D.1.5 Sensors assembly

In operation, we ideally want the two opposite TM to be centered in their respective sensors (here including the ORO that, as previously stated, in conjunction with the STC constitutes a 5-DOFs sensor. This obviously implied than the two sensors have a relative alignment such that it exist a position of the inertial member that simultaneously bring both TM in their centers. To obtain this, we decided to perform an on bench sensor alignment to be no more changed during operation (except for the motorized GRS X position).

Each of the two sensors was thus installed on a small rectangular base plate by mean of suitable plastic legs, that served for both thermal and electrical insulation. On a common circular aluminum slab, two set of three adjustable contact points (the rounded ends of screws trespassing the slab upside down) were prepared: with each sensor base laying on its own set of three contact point, the sensor inclination and height could then be adjusted by threading the screws more or less, thus rising or lowering each contact point.

At the same time, suitable blocks were installed all around the sensors bases, to serve as reference for base translation and rotation on the horizontal plane.

The inertial sensor, on its own, were rigidly suspended in roughly centered position with respect to the slab and its opposite TM inside the sensors.

Exploiting this complete set of handles, we were thus able to iteratively aligning STC+ORO assembly and GRS with respect to a common reference, the inertial member. This assured that there was a position of the inertial member in which both sensors would have been reasonably centered: assuring the inertial member to be exactly in this position once suspended to the fiber is a matter of in-operation centering procedures, to be described in the next sections.

D.2 In-operation centering procedures

As explained in the previous section, during assembling we fixed the relative positions between the sensors (ORO, STC and GRS) along most of the possible DOFs (actually, all but one, that is the GRS translation along X controlled by a motorized translational sledge), so that during operations only a global centering of the sensors assembly with respect to suspended inertial member is required and possible (with the already mentioned exception).

Despite the efforts to precisely align all the sensors with a common zero using the assembled inertial member as a reference, we were unable to perform this operation with accuracy better than readout errors, and at the end of the procedure there was a measurable difference between different sensors zeros along some DOFs.

Although these misalignments are most of the time unimportant, being GRS and ORO the two sensors that require the better alignment (the former to avoid position-dependent effects and readout degradation, the latter for its limited dynamical range) the difference in their zeros were incompatible with a simultaneous operation in the best conditions.

We will thus describe two different alignment procedure that aim to center at best, respectively, GRS or ORO readouts. Note that while the GRS has a big dynamical range and, although not centered, can still be used in science-mode when the ORO is aligned at best, the opposite is not true: ORO dynamical range is too small and we completely loose its signal when centering the GRS.

D.2.1 GRS

Neglecting for a moment the GRS alignment along the X axis, that has a dedicated actuator and can be adjusted independently, we have to align the sensors assembly as a whole with respect to the suspended inertial member along six DOFs (three translations and three angles). The list of the available "actuators" we can use for this task follows, along with a brief comment on which DOFs they affect:

- The three adjustable vacuum vessel feet can be used to tilt the chamber, thus affecting η and θ DOFs: the pendulum hangs indeed always vertical, while the sensor assembly tilts together with the vacuum vessel. Unfortunately, because of the about 1 m long suspension fiber, any tilt of the chamber corresponds to a proportional displacement of the inertial member with respect to the sensors assembly in X and Z.

- The vertical micromanipulator (see Section 4.2.2) moves up and down and rotates the suspension point, and thus can be used to adjust both Y and, roughly, ϕ positions.

- The translational stages under the round slab on which the sensors are installed can be used to align X and Z, correcting in case also displacements introduced tilting the vacuum vessel.

- The rotational stage on top[3] of the two translational ones allows for a fine adjustment of the ϕ angle.

- Finally, the translational stage installed under the GRS allows for its precise alignment along X

Although a crosstalk between different DOFs is almost always present due to machining and assembly inaccuracies, where not explicitly mentioned it is intended to be small and thus unimportant when making the final, small corrections to the alignment.

As shown by the above list, we have a full set of “handles” to align inertial member and sensors along all the six DOFs. However, we cannot adjust the different DOFs one at the time, and we then set up the following procedure that allowed us to converge to complete alignment as fast and reliably as possible. Note that the following procedure is intended to e valid starting for a precise alignment from a reasonably centered position: in case of huge misalignments the best sequence of operation, if it exists, should be decided ad hoc.

- The first step consists in adjusting the vacuum chamber feet trying to make the calibrated GRS $x_1 - x_2$ and $y_1 - y_2$ (proportional to η and θ, respectively) to 0. In doing that, you will likely have to follow the consequent inertial member translations by means of the X and Z motorized stages. If you don't already have a calibration for these channels, you should work directly with the output voltages; because channels 1 and 2 of the same DOF have different displacement gains, the only think you can do in this case to be sure that the corresponding angle is 0 is to set both signal to 0 (while in the previous case you only have to make the calibrated signal symmetric with respect to 0), exploiting also the translations along X (bottom motorized stage) and Y (top micomanipulator). Same considerations applies to other DOFs alignment.

- If necessary, finalize Y alignment: Y, η and θ alignment are completed.

- With X and Z reasonably aligned from previous steps, use the rotational stage to set GRS $z_1 - z_2$ to 0, so to have GRS walls parallel to those of the TM.

[3]Here two choices, installing it on top or below the two translational stages, were possible. We opted for the former because in this case the rotation will always have as a center the sensors assembly one (provided the two were well aligned at mounting time), while in case of an (improbable) big rotation the two translational stages will no more be parallel to X and Z (defined by the sensor assembly rotation); this is anyway a quite easy correction to take in account when aligning. On the contrary, installing the rotational stage at the base of the stack would have caused the center of rotation to be offset with respect to sensors assembly in case of a (probable because of vacuum vessel tilt) quite big translation in X or Z, making it difficult to manage a subsequent alignment in ϕ.

- Use the bottom X and Z actuators to set STC x and GRS $z_1 + z_2$ channel to 0. Note that relative Z distance between the two sensors is fixed on-bench, and at this stage only one of the two (thus GRS one for obvious reasons) can be precisely aligned.

- Finally, use the GRS X translational stage to seto to 0 $x_1 + x_2$

During the whole procedure, the pendulum is kept at his equilibrium angle, with critical damping and allowing enough time between subsequent steps for it to reach, in case, it new equilibrium position (affected by the positions of the sensors via the various source of stiffness described in the text).

If the corrections are small, crosstalks between different DOFs other than those explicitly mentioned are unlikely to affect the final alignment. Anyway, they always represent a small fractions of the corrections applied, and iteratively repeating the above procedure will rapidly bring to convergence.

Note that our alignment range (i.e. the maximum amount of correction we can apply) in η and θ is not set, as could be expected, by feet maximum excursion or X and Y translational stage range. It is rather set by the magnetic damper described in Section 4.2.2: tilting the chamber too much will indeed cause the internal shaft to hit the magnets holding structure nulling the effects of the damper and introducing an erratic behavior on the tilt motion due to unstable constrain.

Also, alignment in Y cannot generally be expected to be much better than about 10 μm: this is due both to difficulties in actuating the micromanipulator by hand up to such an accuracy, and to the dependence of the heavy loaded fiber elongation on even small temperature fluctuations, that makes the alignment being derive change within some μrad in a relatively short time.

D.2.2 ORO

Alignment procedures used for centering at best the ORO signal are very similar to those exposed in the previous section. We just mention here few major differences that should be taken in account:

- The STC+ORO assembly is still insensitive to TM θ rotation, ths we have no control on this DOFs. Luckily, being insensitive, we don't even really need to be centered, as long as the offset remain in a reasonable range for cross talk and border effects not to became a problem.

- Centering of the Y DOF require the injection on the STC to be moved to a different pair of electrodes, while using the Y as sensing ones. This can be done by swapping connections outside the vacuum chamber. Note anyway that we have no independent calibration and we can only try to "center at best", with only very rough estimate of how much of center we are.

- we cannot independently control STC X translational: it must be adjusted moving the entire base platform, and subsequently correcting GRS position if needed.

Bibliography

[1] P. Bender *et al.* LISA: System and Technology Study Report. Technical Report LISA ESA-SCI(2000)11, ESA (2000).

[2] S. Vitale *et al.* LISA Technology Package Architect Final Report. Architect Final Report ESTEC 15580/01/NL/HB, ESTEC (2002).

[3] S. Anza, M. Armano, E. Balaguer *et al.* The LTP experiment on the LISA Pathfinder mission. *Classical and Quantum Gravity*, **22**(10):S125–S138 (2005).

[4] A. Einstein. Die Grundlage der allgemeinen Relativitätstheorie. *Annalen der Physik*, **49**(769):769 (1916). doi:10.1002/andp.200590044.

[5] R. A. Hulse and J. H. Taylor. Discovery of a pulsar in a binary system. *Astrophys. J. Lett.*, **195**:L51 – L53 (1975).

[6] A. Abramovici, W. E. Althouse, R. W. P. Drever *et al.* LIGO: The Laser Interferometer Gravitational-Wave Observatory. *Science*, **256**(5055):325–333 (1992). doi:10.1126/science.256.5055.325.

[7] C. Bradaschia, R. D. Fabbro, A. D. Virgilio *et al.* The VIRGO Project: A wide band antenna for gravitational wave detection. *Nucl. Instrum. and Methods A*, **289**(3):518–525 (1990).

[8] J. Hough, S. Phinney, T. Prince *et al.* LISA and its in-flight test precursor SMART-2. *Nuclear Physics B Proceedings Supplements*, **110**:209–216 (2002).

[9] L. Carbone. *Ground based investigation of force noise sources for LISA*. Ph.D. thesis, University of Trento (2005).

[10] D. Bortoluzzi, M. Benedetti, L. Carbone *et al.* Inertial Sensor Ground Testing and Noise Model for LISA. Final Technical Report for ESA S2-UTN-RP-3001, UTN (2006).

[11] M. Hueller. *Geodesic motion of LISA test masses: development and testing of drag-free position sensors*. Ph.D. thesis, University of Trento (2003).

[12] R. Dolesi, D. Bortoluzzi, P. Bosetti *et al.* Gravitational sensor for LISA and its technology demonstration mission. *Classical and Quantum Gravity*, **20**(10):S99–S108 (2003).

[13] W. J. Weber, D. Bortoluzzi, A. Cavalleri *et al.* Position sensors for flight testing of LISA drag-free control. In M. Cruise and P. Saulson, editors, *Gravitational-Wave Detection. Proceedings of the SPIE*, volume 4856 of *Presented at the Society of Photo-Optical Instrumentation Engineers (SPIE) Conference*, pages 31–42 (2003). doi:10.1117/12.458564.

[14] W. J. Weber, A. Cavalleri, R. Dolesi *et al.* Position sensors for LISA drag-free control. *Classical and Quantum Gravity*, **19**(7):1751–1756 (2002).

[15] H. M. Araújo, A. Howard, D. N. A. Shaul *et al.* Electrostatic charging of cubic test masses in the LISA mission. *Classical and Quantum Gravity*, **20**(10):S311–S319 (2003).

[16] C. C. Speake. Forces and force gradients due to patch fields and contact-potential differences. *Classical and Quantum Gravity*, **13**(11A):A291–A297 (1996).

[17] W. Weber, L. Carbone, A. Cavalleri *et al.* Possibilities for measurement and compensation of stray DC electric fields acting on drag-free test masses. *Advances in Space Research*, **39**(2):213–218 (2007).

[18] W. J. Weber. Private Communication.

[19] C. C. Speake, R. S. Davis, T. J. Quinn *et al.* Electrostatic damping and its effect on precision mechanical experiments. *Physics Letters A*, **263**(4-6):219–225 (1999).

[20] T. J. Sumner and G. Rochester. LISA Inertial Sensor Charge Management System. Technical Report LTP-TN-ICL-001, Imperial College London (2002).

[21] L. Carbone, A. Cavalleri, G. Ciani *et al.* Thermal gradient-induced forces on geodesic reference masses for LISA. *Physical Review D (Particles and Fields and Gravitation and and Cosmology)*, **76**(10):102003 (2007). doi:10.1103/PhysRevD.76.102003.

[22] L. Carbone, G. Ciani, R. Dolesi *et al.* Upper limits to surface-force disturbances on LISA proof masses and the possibility of observing galactic binaries. *Physical Review D (Particles, Fields, Gravitation, and Cosmology)*, **75**(4):042001 (2007). doi:10.1103/PhysRevD.75.042001.

[23] C. D. Hoyle, U. Schmidt, B. R. Heckel *et al.* Submillimeter Test of the Gravitational Inverse-Square Law: A Search for ıLargeȷ Extra Dimensions. *Phys. Rev. Lett.*, **86**(8):1418–1421 (2001). doi:10.1103/PhysRevLett.86.1418.

[24] Y. Su, B. R. Heckel, E. G. Adelberger *et al.* New tests of the universality of free fall. *Phys. Rev. D*, **50**(6):3614–3636 (1994). doi:10.1103/PhysRevD.50.3614.

[25] L. Carbone, A. Cavalleri, R. Dolesi *et al.* Achieving Geodetic Motion for LISA Test Masses: Ground Testing Results. *Phys. Rev. Lett.*, **91**(15):151101 (2003). doi:10.1103/PhysRevLett.91.151101.

[26] P. R. Saulson. Thermal noise in mechanical experiments. *Phys. Rev. D*, **42**(8):2437–2445 (1990). doi:10.1103/PhysRevD.42.2437.

[27] L Carbone *et al.* Upper limits on stray force noise for LISA. *Class. Quantum Grav.*, **21**(5):S611 (2004).

[28] L. Carbone, A. Cavalleri, R. Dolesi *et al.* Characterization of disturbance sources for LISA: torsion pendulum results. *Classical and Quantum Gravity*, **22**(10):S509–S519 (2005).

[29] D. Nicolodi. *Toward a third generation torsion pendulum for the femto-newton level testing of free fall in the laboratory.* Master's thesis, University of Trento (2007).

[30] L. Carbone, A. Cavalleri, G. Ciani *et al.* Torsion pendulum facility for direct force measurements of LISA GRS related disturbances. In S. M. Merkowitz and J. C. Livas, editors, *LASER INTERFEROMETER SPACE ANTENNA: 6th International LISA Symposium*, volume 873, pages 561–565. AIP (2006). doi:10.1063/1.2405099.

[31] P. J. Wass, L. Carbone, A. Cavalleri *et al.* Testing of the UV discharge system for LISA Pathfinder. In S. M. Merkowitz and J. C. Livas, editors, *LASER INTERFEROMETER SPACE ANTENNA: 6th International LISA Symposium*, volume 873, pages 220–224. AIP (2006). doi:10.1063/1.2405047.

[32] Y. Jafry and T. J. Sumner. Electrostatic charging of the LISA proof masses. *Classical and Quantum Gravity*, **14**(6):1567–1574 (1997).

[33] D. Tombolato. *A Laboratory Study of Force Disturbances for LISA Pathfinder Free-Fall Demonstration Mission.* Ph.D. thesis, University of Trento (2008).

[34] S. Vitale, M. Armano, L. Carbone *et al.* Achieving the mid-low end of the LISA band. In S. M. Merkowitz and J. C. Livas, editors, *LASER INTERFEROMETER SPACE ANTENNA: 6th International LISA Symposium*, volume 873, pages 507–514. AIP (2006). doi:10.1063/1.2405092.

[35] M. B. Priestley. *Spectral Analysis and Time Series* (1981).

[36] M. Trobs and G. Heinzel. Improved spectrum estimation from digitized time series on a logarithmic frequency axis. *Measurement*, **39**(2):120–129 (2006).

[37] J. B. Camp, T. W. Darling, and R. E. Brown. Effect of crystallites on surface potential variations of Au and graphite. *Journal of Applied Physics*, **71**(2):783–785 (1992). doi:10.1063/1.351358.

[38] C. C. Speake and C. Trenkel. Forces between Conducting Surfaces due to Spatial Variations of Surface Potential. *Phys. Rev. Lett.*, **90**(16):160403 (2003). doi:10.1103/PhysRevLett.90.160403.

[39] D. Tombolato. Private Communication.

[40] F. Acernese, E. Calloni, R. D. Rosa *et al.* An optical readout system for the drag-free control of LISA. *Classical and Quantum Gravity*, **22**(10):S279–S285 (2005).

[41] F. Acernese, R. de Rosa, L. di Fiore *et al.* Some Progress In The Development Of An Optical Readout System For The LISA Gravitational Reference Sensor. In Merkovitz, S. M., Livas *et al.*, editors, *LASER INTERFEROMETER SPACE ANTENNA: 6th International LISA Symposium*, volume 873 of *American Institute of Physics Conference Series*, pages 339–343 (2006). doi:10.1063/1.2405065.